SYNTHESIS AND CHARACTERIZATION OF NOVEL CHALCOPHOSPHATE MATERIALS

Matthew A. Gave

A DISSERTATION

Submitted to
Michigan State University
in partial fulfillment of the requirements
for the degree of

DOCTOR OF PHILOSOPHY

Department of Chemistry

2008

ABSTRACT

SYNTHESIS AND CHARACTERIZATION OF NOVEL CHALCOPHOSPHATE MATERIALS

By

Matthew A. Gave

Metal chalcophosphate compounds have received significant attention due to the presence of some industrially relevant physical properties such as spontaneous ferroelectric ordering,[1-3] reversible phase changes,[4] nonlinear optical properties,[5] and photoconductivity.[6] These compounds contain a chalcogenide (Q = S, Se, or Te) that is directly bonded to oxidized phosphorous to form various $[P_xQ_y]^{z-}$ anions. The identity and relative concentration of the metal ion has a dominant effect on the structure and properties of the resultant compound, and is not simply a requirement for charge balance.

In this work, several novel chalcophosphate materials are presented, and some insights are provided into the nature of the molten reactions that form them. The novel compounds have the general formula $MM'[P_xQ_y]$ where M = Cu, Ag,[2] Tl,[7] K[8], or Cs,[9] M' = Bi or Hg, and Q = S, or Se. The synthetic conditions required to produce each compound are detailed and so are the structural features of the crystallographic refinement. These crystalline compounds are also characterized by other spectroscopic techniques including Uv/vis and Raman, thermal analysis, and electronic structure calculations.

The reactions to produce these compounds were characterized by high temperature nuclear magnetic resonance, and from these data, the presence of a significant quantity of free radicals in the melts and syntheses of chalcophosphate-

containing materials is demonstrated. Additionally, the melt was found to have relatively low viscosity, and there was evidence that the species that exist in the molten liquid have small (several Å) radii and may be related to the species that are observed in the room temperature crystalline compounds.

1. Bourdon, X.; Maisonneuve, V.; Cajipe, V. B.; Payen, C.; Fischer, J. E., *J. Alloys Compd.* **1999,** 283, 122-127.

2. Gave, M.; Bilc, D.; Mahanti, S.; Breshears, J.; Kanatzidis, M., *Inorg. Chem.* **2005,** 5293-5303.

3. Maisonneuve, V.; Cajipe, V. B.; Simon, A.; VonDerMuhll, R.; Ravez, J., *Phys. Rev. B.* **1997,** 56, 10860-10868.

4. Chung, I.; Do, J.; Canlas, C. G.; Weliky, D. P.; Kanatzidis, M. G., *Inorg. Chem.* **2004,** 43, 2762-2764.

5. Bridenbaugh, P., *Mater. Res. Bull.* **1973,** 8, 1055-1060.

6. Galdamez, A.; Manriquez, V.; Kasaneva, J.; Avila, R. E., *Mater. Res. Bull.* **2003,** 38, 1063-1072.

7. Gave, M.; Malliakas, C. D.; Weliky, D. P.; Kanatzidis, M. G., *Inorg. Chem.* **2007,** 46, 3632-3644.

8. Gave, M.; Weliky, D. P.; Kanatzidis, M. G., *Inorg. Chem.* **2007,** Accepted.

9. Gave, M.; Canlas, C.; Iyer, R. G.; Kańatzidis, M. G.; Weliky, D. P., *J. Solid State Chem.* **2007,** 180, 2877-2884.

ACKNOWLEDGEMENTS

The efforts of a number of people have been invaluable to complete the work contained herein. In particular, I was taught many of the standard techniques to form and to study various materials by Joseph B. Wachter, James R. Salvador and R. G. Iyer. I am also grateful to Christos Malliakas and Hanna Lind for many useful discussions and assistance with various aspects of crystallography. Without the dedication of Kermit L. Johnson, it would have been impossible to collect the NMR spectra. The expertise of John L. McCracken in the collection and interpretation of electron paramagnetic resonance spectra is also appreciatively acknowledged. Carly Wunderlich and Matthew Field are also acknowledged for their dedication and hard work in the lab. Last, but certainly not least, are the efforts of my advisors Mercouri G. Kanatzidis and David P. Weliky. It was an honor to have the chance to learn from both.

TABLE OF CONTENTS

LIST OF TABLES

LIST OF FIGURES

LIST OF TERMS AND ABBREVIATIONS

Ferroelectric – Ferroelectricity results when displacement of charged ions results in an overall dipole moment. This situation arises when ions cooperatively move in the same direction. This can occur spontaneously, from the inter-ionic forces, or due to the application of a coercive electric field.

Antiferroelectric – Antiferroelectricity results when the displacement of multiple charged ions results in a canceling of the dipole moment that would be produced if only one of the mobile ions were present.

Ferrielectric – Like ferroelectricity, ferrielectricity is a dipole moment that results from motion of ions. With ferrielectricity, there are multiple ions that move in such a way that the dipole moment is partially, but not fully, canceled out.

Spontaneous polarization – Spontaneous polarization is when ferro- or ferri- electricity occurs in the absence of a coercive electric field.

Photoelectric response – When light impinges on material, some electrons are released from the surface of that material. This effect is the photoelectric response.

SHG – Second harmonic generation is a non-linear optical process that results in the wavelength of light being halved. Two photons with a given wavelength are effectively combined into one photon with half of the initial wavelength.

Flux – A flux is an inorganic solvent and is typically solid at room temperature. The purpose of using a flux is to increase the mobility of the reactants by providing a relatively non-viscous liquid in which the reactants can diffuse. The composition of the flux can be tailored to alter the chemical properties of the melt, i.e. Lewis acidity or basicity

NMR – Nuclear magnetic resonance.

EPR – Electron paramagnetic resonance.

DTA – Differential thermal analysis.

SOJT – Like the first order Jahn Teller distortions, second order Jahn Teller distortions involve a reduction in orbital degeneracy. The distortion in both cases occurs because degenerate orbitals are unevenly occupied. For first order distortions, the degeneracy occurs between orbitals on the same atom. In the second order case, the orbitals are located on two different, but proximate, atoms.

CHAPTER 1

INTRODUCTION

The earliest example of high temperature synthesis of inorganic materials is from the Bronze Age, perhaps 4000 B.C. By trial and error, copper was mixed with other metals such as tin and arsenic and heated over a flame to form new alloys with superior physical properties. High temperature or solid state chemistry continues to contribute to the development of new inorganic materials including semiconductors, high performance refractory ceramics, and superconductors. Despite the long history of solid state chemistry, discovery of new compounds and materials is still accomplished primarily with exploratory synthesis; i.e. trial and error variation of the elemental stoichiometry and heating profile.

Patterns of reactivity in solid state reactions have been derived empirically following the high temperature synthesis by considering the results of a reaction retroactively. Though this may be perceived as a limitation to the chemistry that the chemistry can only be understood by trial-and-error, it is also a tremendous asset because exploratory synthesis remains crucial to discovering compounds with unimagined structures and physical properties.

Much as they have been for the past 6 millennia, many solid state materials are produced through high temperature syntheses. These syntheses may or may not be done at a high enough temperature to melt any of the reactants. True "solid state" reactions that do not involve melting the reactants have pejoratively described as "heat-and-beat" or "shake-and-bake" methods because this type of synthesis often involves prolonged times at high temperature, followed by grinding in a mortar and pestle, and repeating this procedure until a homogenous final product is formed. In binary solid state reactions, the product compound is formed at the interface between the two solids. In order for the

reaction to go to completion, interfaces between the reactants must be replenished until no starting material remains.[1] For this reason, the repeated cycle of heating and grinding is necessary.

Though this repeat cycle is somewhat limiting because the reactions can take a significant amount of time to go to completion, it has the benefit of providing convenient points throughout the reaction where reaction progress can be monitored. For example, the kinetics of the reaction between NiO and Al_2O_3 to form $NiAl_2O_4$ are known to obey elementary reaction kinetics.[1] This determination was feasible because it was possible to identify and quantitate the reactants and the products at various points in the reaction progress.

In syntheses where the reactants are in the molten state, the pathway of the reaction is potentially much different, and the identification of the species present is inherently much more challenging due to the difficulty of applying spectroscopic or diffraction-based techniques at high temperature. There is typically no experimental data about the species that exist at high temperature and this lack of data is a contributing factor to the poor understanding of the reaction chemistry whenever melting is involved in the reaction. A few noteworthy reports have been published using high temperature X-ray diffraction,[2-5] Raman[6-9] electron paramagnetic resonance (EPR),[10-14] and nuclear magnetic resonance (NMR)[15-20] and these experiments provided some information about the identities of the species present during the course of the reactions at high temperature.

Relative to melt chemistry, reactions in the solution phase may be more predictable because the molecular reactants tend to remain relatively intact in the course of the reaction. The primary goal of the solution phase synthesis is to link these building

blocks together and to make other modifications to the molecular structure or other modifications to the functional groups. For example, a common way to synthesize target peptides is to sequentially link together the requisite amino acids.[21] Because many solid state reactions either use elemental starting materials or provide sufficient energy to break apart molecular precursors, there is often little predictability of the high temperature chemistry. For example, crystalline P_4S_{10} is a molecular super tetrahedron composed of four corner shared PS_4 tetrahedra and has been used as a reactant in a number of syntheses,[22-24] but this supertetrahedral structural moiety has not been observed in any solid state product compounds. Presumably, this moiety cannot exist in a high temperature melt although this hypothesis has not been confirmed experimentally.

Recently, so called flux methodologies have been developed, and offer more control over solid state syntheses that are molten. Fluxes are solvents in which reactions may proceed. These tend to be liquids at high temperature but solids near room temperature. Some recent examples are alkali metal chalcogenide fluxes,[25] alkali metal polychalcophosphate fluxes,[26] and alkali metal halide fluxes.[27,28] The composition of the flux can be varied to tailor the properties of the flux to produce a desired compound. For example, in reactions utilizing the alkali metal polychalcophosphate flux method, the amount of excess elemental P relative to the metal and chalcogen can be changed to affect the stabilization of more oxidized P-containing species (i.e $[PQ_4]^{3-}$ with a P^{5+}) or a less oxidized P-containing species (i.e. $[P_2Q_6]^{4-}$ with two P^{4+}). With this increased relative amount of P, the oxidizing chalcogen is putatively used up before all of the P atoms can be oxidized to the 5+ oxidation state, and instead have only been oxidized to the 4+ oxidation state. Having such control over the reaction allows for certain aspects of

the structure of the resultant product to be targeted, and therefore the trial-and-error methodology is somewhat enhanced.

The structures of these compounds contain an assortment of $[P_xQ_y]^{z-}$ (Q = S, Se, Te) anions, and some ability to choose the type of anion present in the final compound has been demonstrated by varying the reaction stoichiometry, or by related flux methodologies.[15,26,29] It was proposed that the products formed in these reactions may be affected by the equilibrium between $[P_xQ_y]^{z-}$ anions, and therefore this particular type of solid state synthesis may have some resemblance to solution chemistry because of the presence of a small number of discreet species that exist at high temperature.

Chalcophosphate materials are excellent candidates for the elucidation of chemical reactivity and reaction mechanisms due to the following: (1) it has been proposed that the flux stoichiometry affects the dynamic equilibrium between various chalcophosphate moieties, and this equilibrium is potentially measurable or its effects observed, [26] (2) many of the reactions result in highly crystalline products that can be characterized crystallographically and, (3) there is an abundance of ^{31}P in the melts and resultant compounds and so ^{31}P nuclear magnetic resonance can be used to provide structural information at room temperature and up to ~600 °C.[30-32]

Various chalcophosphate compounds are interesting not only because of the possibility of providing some information about the underlying reaction mechanisms of solid state or melt chemistry but also because of potentially useful physical properties such as ferroelectric ordering,[33-38] reversible glass-to-crystalline phase changes,[15,39-42] and magnetic phenomena.[43-45]

In this work, several new compounds and their physical properties are presented and insights into the underlying reaction mechanisms are proposed. In Chapter 2, the new compounds $CuBiP_2Se_6$, $AgBiP_2Se_6$,and $AgBiP_2S_6$ are presented, and the Cu/Bi antiferroelectric sublattice ordering is discussed.[35] In Chapter 3, The new compounds $Tl_3Bi_3(PS_4)_4$, $TlBiP_2S_7$, $TlBiP_2S_6$, $Tl_3Bi(PS_4)_2$, α-$TlBiP_2Se_6$, and β-$TlBiP_2Se_6$ are presented, and the reaction stoichiometries required to produce each as the dominant crystalline compound are given.[46] In Chapter 4, ultra high field (21 T) NMR measurements of some of the reported Tl/Bi/P/S compounds are displayed.[47] In Chapter 5, the new compounds $K_3Bi_3(PS_4)_4$, $K_{1.5}Bi_{2.5}(PS_4)_3$ and $K_9Bi(PS_4)_4$ are presented, and the modulated crystalline structure of $K_{1.5}Bi_{2.5}(PS_4)_3$ is detailed.[48] In Chapter 6, materials related to the mineral argyrodite are presented, and the composition dependant phase change that occurs is compared to the existing Argyrodite materials where the phase change occurs as a function of temperature. In Chapter 7 the new compound $Cs_4P_2Se_{10}$ is presented, and this is the first new compound that was discovered by *in situ* high temperature NMR syntheses.[49] In Chapter 8, evidence for the presence of significant concentrations of free radicals in chalcogenide-containing melts is given, as well as discussions into the potential of these radicals to play a significant role in synthetic reactions.[50] In Chapter 9, the high temperature NMR data are compared in reference to the available room temperature ^{31}P NMR data, and some conclusions about speciation in the melt are drawn. In Chapter 10, solid solutions of $Cu_3PSe_{4-x}S_x$ and $Fe_2P_2Se_{6-x}S_x$ are presented, and the distribution of the chalcogen atoms is discussed.

REFERENCES

1. West, A. R. Solid State Chemistry and its Applications; Wiley: New York, New York, 1984; pp 6-7.

2. Okamoto, Y.; Madden, P. A. *J. Phys. Chem. Solids* **2005,** 66, 448-451.

3. Polonka, J.; Xu, M.; Li, Q.; Goldman, A. I.; Finnemore, D. K. *Appl. Phys. Lett.* **1991,** 59, 3640-3642.

4. Sugiyama, K.; Nomura, K.; Waseda, Y.; Andonov, P.; Kimura, S.; Shigematsu, K. *Z. Naturforsch. A* **1990,** 45, 1324-1327.

5. Waseda, Y.; Shinoda, K.; Sugiyama, K.; Takeda, S.; Terashima, K.; Toguri, J. M. *Jpn J Appl Phys 1* **1995,** 34, 4124-4128.

6. Finkman, E.; Defonzo, A. P.; Tauc, J. *B. Am. Phys. Soc.* **1974,** 19, 212-212.

7. Scott, J. F.; Remeika, J. P. *Phys. Rev. B.* **1970,** 1, 4182-4185.

8. Yano, T.; Shibata, S.; Maehara, T. *J. Am. Ceram. Soc.* **2006,** 89, 89-95.

9. Zhang, X.; Wan, S. M.; Zhang, Q. L.; Yin, S. T.; You, J. L.; Chen, H.; Wang, A. H. *Acta. Phys. Sin.-Ch. Ed.* **2007,** 56, 1152-1155.

10. Sampath, P. I. *J. Chem. Phys.* **1966,** 45, 3519-3525.

11. Gardner, D. M.; Fraenkel, G. K. *J. Am. Chem. Soc.* **1956,** 78, 3279-3288.

12. Gardner, D. M.; Fraenkel, G. K. *J. Am. Chem. Soc.* **1954,** 76, 5891-5892.

13. Koningsberger, D.; Van Wolput, J.; Rieter, P. *Chem. Phys. Lett.* **1971,** 8, 145-147.

14. Warren, W. W.; Dupree, R. *Phys. Rev. B.* **1980,** 22, 2257-2275.

15. Chung, I.; Do, J.; Canlas, C. G.; Weliky, D. P.; Kanatzidis, M. G. *Inorg. Chem.* **2004,** 43, 2762-2764.

16. Maxwell, R.; Eckert, H. *J. Phys. Chem.* **1995,** 99, 4768-4778.

17. Maxwell, R.; Eckert, H. *J. Am. Chem. Soc.* **1993,** 115, 4747-4753.

18. Maxwell, R.; Eckert, H. *J. Am. Chem. Soc.* **1994,** 116, 682-689.

19. Maxwell, R.; Erickson, H.; Eckert, H. *Z. Naturforsch. A* **1995,** 50, 395-404.

20. Schmedt, A. J.; Meise-Gresch, K.; Eckert, H.; Holand, W.; Rheinberger, V. *Glass. Sci. Technol.* **2000,** 73, 90-97.

21. Frängsmyr, T.; Malmström, B. G. Nobel Lectures, 1981-1990; World Scientific: Singapore ; River Edge, NJ, 1992.

22. Aitken, J. A.; Canlas, C.; Weliky, D. P.; Kanatzidis, M. G. *Inorg. Chem.* **2001,** 40, 6496-6498.

23. McCarthy, T. J.; Kanatzidis, M. G. *Chem. Mat.* **1993,** 5, 1061-1063.

24. Loken, S.; Tremel, W. *Eur. J. Inorg. Chem.* **1998,** 283-289.

25. Kanatzidis, M. G. *Chem. Mat.* **1990,** 2, 353-363.

26. Kanatzidis, M. G. *Curr. Opin. Solid. St. M.* **1997,** 2, 139-149.

27. Gencer, F.; Abell, J. S. *J. Cryst. Growth* **1991,** 112, 337-342.

28. Abell, J. S.; Gencer, F. *Physica C* **1991,** 185, 441-442.

29. Chung, I.; Karst, A. L.; Weliky, D. P.; Kanatzidis, M. G. *Inorg. Chem.* **2006,** 45, 2785-2787.

30. Canlas, C. G. Ph.D. Thesis, Michigan State University, East Lansing, MI, 2004.

31. Canlas, C. G.; Kanatzidis, M. G.; Weliky, D. P. *Inorg. Chem.* **2003,** 42, 3399-3405.

32. Canlas, C. G.; Muthukumaran, R. B.; Kanatzidis, M. G.; Weliky, D. P. *Solid State Nucl. Magn. Reson.* **2003,** 24, 110-122.

33. Bourdon, X.; Maisonneuve, V.; Cajipe, V. B.; Payen, C.; Fischer, J. E. *J. Alloys Compd.* **1999,** 283, 122-127.

34. Carpentier, C. D.; Nitsche, R. *Mater. Res. Bull.* **1974,** 9, 1097-1100.

35. Gave, M.; Bilc, D.; Mahanti, S.; Breshears, J.; Kanatzidis, M. *Inorg. Chem.* **2005,** 5293-5303.

36. Maisonneuve, V.; Cajipe, V. B.; Simon, A.; VonDerMuhll, R.; Ravez, J. *Phys. Rev. B.* **1997,** 56, 10860-10868.

37. Simon, A.; Ravez, J.; Maisonneuve, V.; Payen, C.; Cajipe, V. B. *Chem. Mat.* **1994,** 6, 1575-1580.

38. Vysochanskii, Y. *Ferroelectr.* **1998,** 218, 629-636.

39. Chrissafis, K.; Kyratsi, T.; Paraskevopoulos, K. M.; Kanatzidis, M. G. *Chem. Mat.* **2004,** 16, 1932-1937.

40. Gidon, S.; Lemonnier, O.; Rolland, B.; Bichet, O.; Dressler, C.; Samson, Y. *Appl. Phys. Lett.* **2004,** 85, 6392-6394.

41. Ohta, T. *J. Optoelectron. Adv. M.* **2001,** 3, 609-626.

42. Wachter, J. B.; Chrissafis, K.; Petkov, V.; Malliakas, C. D.; Bilc, D.; Kyratsi, T.; Paraskevopoulos, K. M.; Mahanti, S. D.; Torbrugge, T.; Eckert, H.; Kanatzidis, M. G. *J. Solid State Chem.* **2007,** 180, 420-431.

43. Chondroudis, K.; Kanatzidis, M. G. *Inorg. Chem. Commun.* **1998,** 1, 55-57.

44. Odile, J. P.; Steger, J. J.; Wold, A. *Inorg. Chem.* **1975,** 14, 2400-2402.

45. Taylor, B.; Steger, J.; Wold, A.; Kostiner, E. *Inorg. Chem.* **1974,** 13, 2719-2721.

46. Gave, M.; Malliakas, C. D.; Weliky, D. P.; Kanatzidis, M. G. *Inorg. Chem.* **2007,** 46, 3632-3644.

47. Gave, M.; Johnson, K.; Kanatzidis, M. G.; Weliky, D. P. *Solid State Nucl. Magn. Reson.* **2007,** Accepted. DOI 10.1016/j.ssnmr.2007.11.002.

48. Gave, M.; Weliky, D. P.; Kanatzidis, M. G. *Inorg. Chem.* **2007,** 46, 11063-11074.

49. Gave, M.; Canlas, C.; Iyer, R. G.; Kanatzidis, M. G.; Weliky, D. P. *J. Solid State Chem.* **2007,** 180, 2877-2884.

50. Gave, M.; Kanatzidis, M. G.; Weliky, D. P. **2007,** In preparation.

CHAPTER 2

ON THE LAMELLAR COMPOUNDS $CuBiP_2Se_6$, $AgBiP_2Se_6$ AND $AgBiP_2S_6$. ANTIFERROELECTRIC PHASE TRANSITIONS DUE TO COOPERATIVE Cu^+ AND Bi^{3+} ION MOTION.

INTRODUCTION

Alkali metal selenophosphate compounds with group 15 elements such as AMP_2Se_6 (A = K, Rb, Cs, M = Sb, Bi) exhibit closely related structures with a covalently bonded anionic $[MP_2Se_6]^-$ framework and alkali metals as counterions.[1,2] There have been several discussions in the literature regarding the influence of cation size on the structure of the anion which highlight the general tendency that for a given stoichiometry, larger counterions favor lower dimensionality in the the anions.[2-4] Alkali metal interactions with the $^1/_\infty[BiP_2Se_6]^{1-}$ framework are predominantly electrostatic in nature. In the case of $KSbP_2Se_6$ three different interconvertible forms (α-, β- and amorphous) were identified.[1] The conversion from one form to another is connected to the ability of K^+ ions to move inside the structure. Given the same ionic charge of coinage metals (i.e. Cu, Ag) with those of the alkali ions, it is often useful to consider the former as pseudo alkali ions. Therefore, in general it becomes interesting to explore the relationship of alkali metal compounds to analogous compounds with Cu and Ag. By substituting the less electropositive Ag or Cu for an alkali metal, significant changes in the crystal and electronic structure are expected not only due to the counterion effect[4] but also due to the stronger Ag-Q and Cu-Q interactions compared to the electrostatic A-Q interactions (Q = chalcogen element). This is clearly manifested in marked reductions in size of the energy band gap as observed for example in $A_{0.5}M_{1.75}GeQ_4$ (A = Ag, Cu, Na; M = Pb, Eu; Q = S, Se).[5] Exploring coinage metal/alkali metal interactions could allow the manipulation of structures and the possible tuning of the optical and electronic properties.

In this context, we targeted for study $CuBiP_2Se_6$, $AgBiP_2Se_6$, and $AgBiP_2S_6$. The first two phases have been described briefly and were claimed to possess photoconductive properties, however, structural characterization has not been reported.[6] Furthermore, Cu and Ag in these types of compounds can become mobile and cause the materials to undergo unusual phase transitions. This is observed in the related layered compounds of $CuInP_2S_6$,[7-11] $CuInP_2Se_6$,[12-14] $AgAlP_2Se_6$,[13] $CuCrP_2Se_6$,[12,13] and $CuVP_2S_6$.[8,15] These compounds show interesting physical properties such as ferri- and ferroelectricity with high spontaneous polarization,[14,16,17] as well as strong second harmonic generation,[10] and photoelectric response.[6,18,19]

Here we describe $CuBiP_2Se_6$, $AgBiP_2Se_6$, and $AgBiP_2S_6$ which represent the coinage metal analogs of the $ABiP_2Q_6$ group. The stronger and more covalent interactions of Cu^+ and Ag^+ ions with the framework $[BiP_2Se_6]^{1-}$ coupled with their small size, results in a distinctly different lamellar motif from those of the alkaline metal counterparts. Interestingly, $CuBiP_2Se_6$ exhibits temperature induced anti-ferroelectric phase transitions associated with motion of Cu^+ ions in the structure whereas $AgBiP_2Se_6$ is already at this anti-ferroelectric state at room temperature.

EXPERIMENTAL SECTION

Reagents

Chemicals were used as obtained unless otherwise noted: bismuth chunks (99.999%, Tellurex Inc., Traverse City, MI.), selenium shot (99.999%, Tellurex Inc., Traverse City, MI), sulfur (sublimed flowers, Alfa Aesar, Ward Hill, MA), phosphorous

(amorphous red, MCB Reagents, Gibbstown, NJ), electrolytic copper dust (Fisher Scientific, Pittsburgh, PA), and silver powder, prepared as below. Selenium and bismuth were ground in an agate mortar and pestle to ~100 mesh.

Synthesis

Preparation of Silver Powder: Silver powder was prepared by cutting a silver coin (31g) into centimeter sized pieces, which were subsequently dissolved in 200mL concentrated nitric acid by stirring overnight. The solution was then neutralized by addition of ammonium hydroxide. Finely divided silver particles were obtained after addition of 10g of sodium borohydride to the solution which were isolated by filtration, washed with water, and dried in a 100°C oven.

$CuBiP_2Se_6$: A mixture of Cu (0.1580 g. 2.5 mmol), Bi (0.5179 g. 2.5 mmol), P (0.1549 g. 5.0 mmol), and Se (1.1816 g. 15.0 mmol) was loaded into a fused silica tube and flame-sealed at a reduced pressure of $<10^{-4}$ mbar. The mixture was heated to 700°C over 12h and held for 12h, followed by cooling to 50°C at a rate of 15°C/h. An inhomogeneous grey metallic ingot (approximately 80% product, 20% Bi_2Se_3 / Cu_3PSe_4) was isolated that fractured into graphite like layers composed of air-stable black plates. Microprobe analysis of single crystals gave an average composition of $Cu_{1.0}Bi_{1.0}P_{2.2}Se_{5.8}$. Attempts to prepare the related compound $CuBiP_2S_6$ compound were unsuccessful.

$AgBiP_2Se_6$: A mixture of Ag (0.2532 g., 2.35 mmol), Bi (0.4918 g., 2.35 mmol), P (0.1466 g. 4.7 mmol), and Se (1.1205 g. 14.2 mmol) was loaded into a fused silica tube and flame-sealed at a reduced pressure of $<10^{-4}$ mbar, and was heated with the same

profile as above. An inhomogenous grey metallic ingot (approximately 80% product, 20% $AgBiSe_2$) was isolated that fractured into graphite like layers composed of air-stable black plates. Microprobe analysis of single crystals gave an average composition of $Ag_{1.1}Bi_{1.0}P_{2.0}Se_{5.9}$.

$AgBiP_2S_6$: A mixture of Ag (0.1803 g., 1.7 mmol), Bi (0.3463 g., 1.7 mmol), P (0.1565 g. 5.1 mmol), and S (0.3203 g. 10.0 mmol) was loaded into a fused silica tube and flame-sealed at a reduced pressure of $<10^{-4}$ mbar. The mixture was heated to 850°C over 12h and kept there for 24h, followed by cooling to 50°C at a rate of 15°C/h. A homogenous grey metallic-like ingot was obtained, but was coated with amorphous red phosphorous powder. Upon fracturing, the ingot cleaved in a graphite-like manner to form black plates. Microprobe analysis gave an average composition of $Ag_{1.0}Bi_{1.0}P_{2.1}S_{6.0}$. The phase was pure by powder X-ray diffraction, although it is likely that some amorphous elemental phosphorous was present. A similar synthesis with Cu instead of Ag did not result in the compound $CuBiP_2S_6$.

Powder X-ray Diffraction

All samples were assessed for phase purity using powder X-ray diffraction. Powder patterns were obtained using an Inel CPS 120 powder X-ray diffractometer with monochromatized Cu Kα radiation (λ = 1.540598 Å) operating at 40 kV and 20 mA equipped with a position-sensitive detector with a 2θ range of 0 - 120° and calibrated with a LaB_6 standard.

Single Crystal X-ray Diffraction

Intensity data for single crystals of $CuBiP_2Se_6$ and $AgBiP_2Se_6$ were collected on a Bruker SMART platform CCD diffractometer using Mo Kα radiation operating at 40 kV and 40 mA. The crystals were manually isolated from the reaction ampoule. Individual frames were collected with a 10 s exposure time and a 0.3° omega rotation. The SMART software was used for data collection, and SAINT software was used for data extraction and reduction. An analytical absorption correction to the data was performed and direct methods were used to solve and refine the structures with the SHELXTL[20] software package.

Intensity data for $AgBiP_2S_6$ was collected on a Stoe IPDS II diffractometer with Mo Kα radiation operating at 50 kV and 40 mA on with a 34 cm image plate. The crystal used for data collection was manually isolated from the reaction ampoule. Individual frames were collected with a 60 s exposure time and a 0.5° omega rotation. The X-SHAPE and X-RED[21] software packages were used for data extraction and reduction and to apply an analytical absorption correction. The SHELXTL software package was used to solve and refine the structure. The parameters for data collection and the details of the structural refinement can be found in Table 2-1 and the fractional atomic coordinates for each compound are shown in In all cases the atoms were refined to full occupancy.

Table 2-1. Crystallographic data, experimental and refinement Details for the $CuBiP_2Se_6$, $AgBiP_2Se_6$, and $AgBiP_2S_6$.

	$CuBiP_2Se_6$	$CuBiP_2Se_6$	$CuBiP_2Se_6$	$AgBiP_2Se_6$	$AgBiP_2S_6$
Temperature, K	298	173	97	298	298
Crystal system	Trigonal	Rhombohedral	Rhombohedral	Rhombohedral	Triclinic
Space group	*P*-31*c*	*R*-3	*R*-3	*R*-3	P-1
λ, Å (Mo Kα)	0.071073	0.071073	0.071073	0.071073	0.071073
a, Å	6.5410(9)	6.5591(10)	6.5532(16)	6.6524(13)	6.3833(13)
b, Å	6.5410(9)	6.5591(10)	6.5532(16)	6.6524(13)	7.1439(14)
c, Å	13.263(3)	79.385(18)	39.762(13)	39.615(15)	9.5366(19)
α, °	90	90	90	90	91.89(3)
β, °	90	90	90	90	91.45(3)
γ, °	120	120	120	120	94.05(3)
Z	2	12	6	6	2
Crystal dimensions, mm	0.18 x 0.18 x 0.04	0.16 x 0.15 x 0.02	0.16 x 0.15 x 0.02	0.24 x 0.22 x 0.07	0.31 x 0.18 x 0.09
D_{calc} g/cm^3	5.462	5.445	5.445	5.595	4.377
μ, mm^{-1}	42.513	42.381	42.383	41.116	24.26
R_{int}, %	5.8	6.5	5.8	5.8	3.2
total reflections/ independant	1678/220	8151/1626	2947/799	3000/498	4155/2136
final R/Rw, %[a]	5.5/13.9	9.1/21.2	5.0/11.7	4.5/9.9	4.2/9.2

[a] $R = \Sigma(|F_o| - |F_c|)/\Sigma|F_o|$. $R_w = [\Sigma w(|F_o| - |F_c|)^2/\Sigma w|F_o|^2]^{1/2}$

Table 2-2. Fractional atomic coordinates and U(eq) values for $CuBiP_2Se_6$ at 298 K with standard deviations in parenthesis.

atom	x	y	z	U_{eq}[a]	Symmetry
Bi	1.3333	0.6667	0.75	15(1)	2d
Se	1.3322(3)	0.3031(3)	0.6180(1)	20(1)	12i
Cu	1	1	0.75	186(8)	2a
P	1.6667	0.3333	0.6652(6)	10(2)	4f

[a] $U_{(eq)} = (\Sigma_i\Sigma_j U_{ij} a_i^* a_j^* a_i \cdot a_j)/3 \times 1000$

Table 2-3. Fractional atomic coordinates and U(eq) values for $CuBiP_2Se_6$ at 173 K with standard deviations in parenthesis.

atom	x	y	z	U_{eq}[a]	Symmetry
Bi(1)	0.6667	0.3333	0.0412(1)	17(1)	6c
Bi(2)	0.3333	-0.3333	0.1222(1)	15(1)	6c
Se(1)	0.7200(4)	0.0410(4)	0.1031(1)	19(1)	18f
Se(2)	1.0312(4)	0.7015(4)	0.0196(1)	22(1)	18f
Se(3)	0.3503(4)	0.0099(4)	0.1473(1)	16(1)	18f
Se(4)	1.0271(4)	0.3363(4)	0.0638(1)	20(1)	18f
P(1)	1.3333	0.6667	0.0558(1)	15(2)	6c
P(2)	0.6667	0.3333	0.1385(1)	11(2)	6c
P(3)	0.6667	0.3333	0.1104(1)	13(2)	6c
P(4)	1.3333	0.6667	0.0275(1)	14(2)	6c
Cu(1)	2	1	0.1369(2)	91(4)	6c
Cu(2)	0	0	0.0430(3)	178(9)	6c

[a] $U_{(eq)} = (\Sigma_i\Sigma_j U_{ij} a_i^* a_j^* a_i \cdot a_j)/3 \times 1000$

Table 2-4. Fractional atomic coordinates and U(eq) values for $CuBiP_2Se_6$ at 97 K with standard deviations in parenthesis.

atom	x	y	z	U_{eq}[a]	Symmetry
Bi	0	0	0.0907(1)	10(1)	6c
Se(1)	0.3761(2)	0.3877(2)	0.1273(1)	12(1)	18f
Se(2)	0.3389(2)	1.0230(2)	0.0386(1)	9(1)	18f
Cu(1)	0.3333	0.6667	0.0535(1)	13(1)	6c
Cu(2)	0.3333	0.6667	0.0761(13)	47(9)	6c
P(1)	0.6667	0.3333	0.1128(1)	9(1)	6c
P(2)	0.6667	1.3333	0.0561(1)	7(1)	6c

[a] $U_{(eq)} = (\Sigma_i\Sigma_j U_{ij} a_i^* a_j^* a_i \cdot a_j)/3 \times 1000$

Table 2-5. Fractional atomic coordinates and U(eq) values for $AgBiP_2S_6$ at 298 K with standard deviations in parenthesis.

atom	x	y	z	U_{eq}[a]	Symmetry
Bi	0	0	0.0880(1)	23(1)	6c
Se(1)	0.3749(2)	0.3761(2)	0.1278(1)	26(1)	18f
Se(2)	0.3431(2)	0.0328(2)	0.0379(1)	24(1)	18f
P(1)	0.6667	0.3333	0.0555(2)	18(1)	6c
P(2)	0.6667	0.3333	0.1123(2)	18(1)	6c
Ag(1)	0.3333	-0.3333	0.0723(1)	64(1)	6c

[a] $U_{(eq)} = (\Sigma_i\Sigma_j U_{ij} a_i^* a_j^* a_i \cdot a_j)/3 \times 1000$

Electron Microscopy

A JEOL JSM-35C scanning electron microscope equipped with a Tracor Northern energy dispersive spectroscopy detector was used for quantitative microprobe analysis. Data were collected using an accelerating voltage of 25 kV and a collection time of 60 s.

Differential Thermal Analysis

Differential thermal analyses were performed with a Shimadzu DTA-50 thermal analyzer. A portion of the ingot obtained from the reaction weighing ~ 25mg was finely ground and sealed in a quartz ampoule under reduced pressure. An equivalent mass of alumina was sealed in an identical ampoule to serve as a reference. The samples were heated to 800 °C at a rate of 10 °C/min, cooled to 150 °C at a rate of 10 °C/min, reheated to 800 °C at a rate of 10 °C/min, and then cooled to room temperature at a rate of 10 °C/min.

Solid State UV/Vis Spectroscopy

Optical band gaps were determined using Kubelka-Munk theory[22-24] on data collected by diffuse reflectance UV/Vis spectroscopy on finely ground sample portions of the ingot at room temperature. A background was collected before each scan using $BaSO_4$. A spectrum was collected for the region of 200-2500 nm with a Shimadzu UV-3101 PC double-beam, double-monochromator spectrophotometer.

Method of electronic structure calculations

Electronic structure calculations were performed using the self-consistent full-potential linearized augmented plane wave method (LAPW)[25] within density functional theory (DFT),[26,27] using the generalized gradient approximation (GGA) of Perdew, Burke and Ernzerhof for the exchange and correlation potential.[28] The values of the atomic radii were taken to be: 1.8 a.u. for P atoms, 2.2 a.u. for Se and Cu atoms, and 2.6

a.u. for Bi atoms, where a.u. is the atomic unit (0.529 Å). Convergence of the self-consistent iterations was performed for 20 k points inside the irreducible Brillouin zone to within 0.0001 Ry with a cutoff of -6.0 Ry between the valence and the core states. Scalar relativistic corrections were included and a spin-orbit interaction was incorporated using a second variational procedure.[29] The calculations were performed using WIEN2K program.[30]

RESULTS AND DISCUSSION

Syntheses

$CuBiP_2Se_6$ and $AgBiP_2Se_6$ formed as black crystal plates that were manually isolated from the reaction ampoule. It was not possible to obtain pure compounds as the former always contained Bi_2Se_3 and Cu_3PSe_4 and the latter $AgBiSe_2$ as minor phases. Presumably, some phosphorous in the reaction to produce $AgBiP_2Se_6$ was either vaporized or remained attached to the walls of the reaction vessel, thus allowing for the mixture of the target phase as well as a phosphorous-poor ternary phase. The bulk samples were grey metallic in appearance and broke into graphite-like layers upon cracking. In our hands, a procedure given for these compounds in an earlier report could not be repeated.[6]

Neither the use of P_2Se_5 nor RbCl/LiCl flux were successful in producing pure phases of the desired compounds. In each attempt, as much as a 20% Bi_2Se_3/Cu_3PSe_4 or $AgBiSe_2$ impurity was found by powder X-ray diffraction. Attempts to prepare $CuBiP_2Se_6$ and $AgBiP_2Se_6$ by quenching stoichiometric melts to room temperature or in

ice water were not successful in producing the desired product as a single phase and resulted only in known binary/ternary compounds. The persistent impurities are likely the result of their extreme stability.

$CuBiP_2Se_6$ and $AgBiP_2Se_6$ are semiconductors with a room temperature energy gap E_g of 1.2 and 1.4 eV respectively, Figure 2-1A,B. Bi_2Se_3 present in $CuBiP_2Se_6$ has a band gap of 0.35 eV and is likely the cause of the high residual absorbance below the band gap of $CuBiP_2Se_6$. The other impurity phase, Cu_3PSe_4, has a band gap of 1.3 eV and, therefore, the absorption edge is nearly collinear with the absorption edge of $CuBiP_2Se_6$. $AgBiSe_2$ is an impurity in $AgBiP_2Se_6$ and has a band gap of 0.5 eV which can be seen at lower energy than the absorption edge of the $AgBiP_2Se_6$. The suitable energy gap and high crystal symmetry could result in stable photoexcited carriers with high mobility. Preliminary reports suggest that these materials can generate photoexcited carriers.[6] Therefore these systems could be attractive for investigations as possible solar energy materials. The band gaps of the related $KBiP_2Se_6$ phases are somewhat larger than those reported here at 1.6 eV for the α- and 1.3 eV for the β- phase.[31]

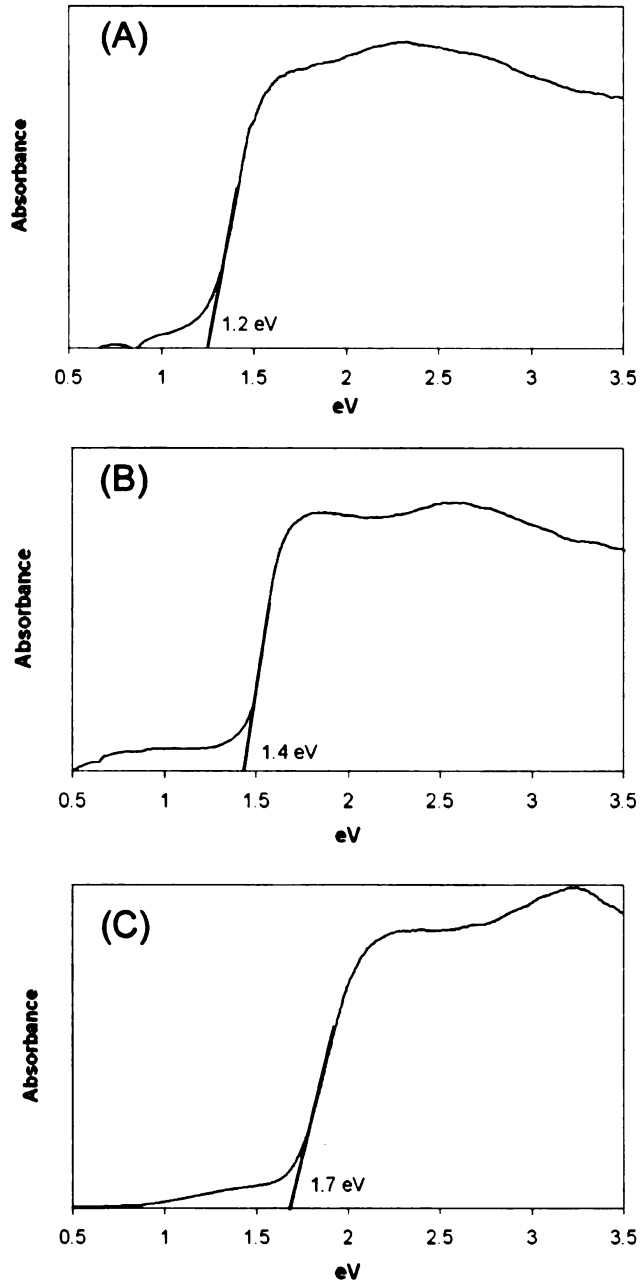

Figure 2-1 The optical absorption spectra of (A) $CuBiP_2Se_6$, (B) $AgBiP_2Se_6$ and (C) $AgBiP_2S_6$. The high residual absorbance below the band gap in (A) is likely the result of a Bi_2Se_3 impurity. The residual absorbance in (B) is the result of $AgBiSe_2$, and the residual absorbance in (C) is likely Bi_2S_3.

DTA analysis of sample portions of the ingot containing $CuBiP_2Se_6$ and $AgBiP_2Se_6$ melt incongruently at 475 °C and 480 °C, respectively. A broad endothermic

region in both cases suggested that the title phases form a eutectic mixture with the corresponding impurity phases. No deviation was observed from the baseline at the melting points of the impurities. Powder X-ray diffraction of the sample portion after two heating cycles indicated that the title compounds were obtained in approximately the same yield and were accompanied by the same impurities.

The synthesis of $AgBiP_2S_6$ could only be accomplished in the presence of an additional equivalent of phosphorous. In each attempt with the stoichiometric ratio of the elements, phosphorous was oxidized to the 5+ state and produced ternary compounds containing $[PS_4]^{3-}$ units (e.g. Ag_7PS_6, Ag_3PS_4). Apparently, the extra equivalent of phosphorous helps to achieve the P^{4+} containing $[P_2S_6]^{4-}$ anions from which $AgBiP_2S_6$ could form. The material was found to melt at 590 °C by DTA. A parallel attempt to produce $CuBiP_2S_6$ using extra phosphorous in the synthesis was not successful, instead producing the very stable phases Cu_3PS_4 and $BiPS_4$. A band gap of 1.7 eV was determined spectroscopically for $AgBiP_2S_6$, Figure 2-1C.

Structure Description

Not surprisingly, the phases reported here do not adopt the same structure as their alkali containing analogs $KBiP_2Se_6$ and $RbBiP_2Se_6$ which feature pseudo one-dimensional structures. Because of the smaller size of Cu^+ and Ag^+ ions, the $[BiP_2Se_6]^{1-}$ anion favors a two-dimensional structure that interacts strongly with the coinage metals and "traps" them inside it. This structure is similar to other Cu and Ag selenophosphates containing group 13 metals (e.g. Al^{3+}, In^{3+} etc).

$CuBiP_2Se_6$ and $AgBiP_2Se_6$: These compounds have the lamellar $Fe_2P_2Se_6$ structure type. This structure is a modification of the CdI_2 structure where $^1/_3$ of the metal sites are replaced with a $[P_2Se_6]^{4-}$ anion with the P-P bond axis along the layer normal. Each layer has the thickness of one $[P_2Se_6]^{4-}$ unit, and the structures contain well defined van der Waals gaps. Because of differences in the stacking sequence (i.e. positions on the slabs relative to each other) the two compounds are not isomorphous and, at room temperature, adopt hexagonal and rhombohedral space groups respectively.

The structures are closely related to those of $CuCrP_2Se_6$ and $CuInP_2Se_6$ with the same $[P_2Se_6]^{4-}$ anion lattice bridged by the metal cations. This $Fe_2P_2Se_6$ slab motif is generally adopted by compounds with transition M^{2+} metal ions, or a combination of M^+/M^{3+} ions (e.g. Cu/Al, Ag/In, Cu/Cr etc.) which have no valence electrons (i.e. have a $d^ns^0p^0$ configuration). When transition M^{2+} metals are replaced with main group elements, which formally possess ns^2 configuration (e.g. Pb^{2+}, Sn^{2+}), the lamellar $M_2P_2Se_6$ structure type changes to a three-dimensional one.[32,33] Therefore it is interesting that in $CuBiP_2Se_6$ and $AgBiP_2Se_6$ where an intermediate situation exists i.e. half the metal sites are Bi^{3+} ($6s^2$) the lamellar $Fe_2P_2Se_6$ motif is preserved.

The $[P_2Se_6]^{4-}$ anions in the room temperature structure of $CuBiP_2Se_6$ and $AgBiP_2Se_6$ are bridged by an ordered arrangement of alternating coinage metal and bismuth metal centers, Figure 2-2. Each anion has three coinage metal and three bismuth ions as its nearest metal neighbors, Figure 2-3. The Cu^+ ions in $CuBiP_2Se_6$ have an octahedral coordination environment of Se atoms, Figure 2-4A. This is unusually high for

Cu since it is well known that in chalcogenides, Cu prefers low coordination sites such as tetrahedral, trigonal planar or even linear. In fact, by inspecting the results of the crystal structure refinement, there is strong evidence that the apparent high coordination environment of Cu is misleading. As suggested by the very high anisotropic thermal parameter of Cu^+ ions, $U_{11} = U_{22} = 175(11)$, and $U_{33} = 209(18)$, it is likely that this is the result of dynamic averaging due to atomic motion in an oversized cavity. This suggests that the actual position of Cu is a disordered arrangement of various off-center positions. By moving off center, the Cu^+ ions can achieve a lower coordination environment.

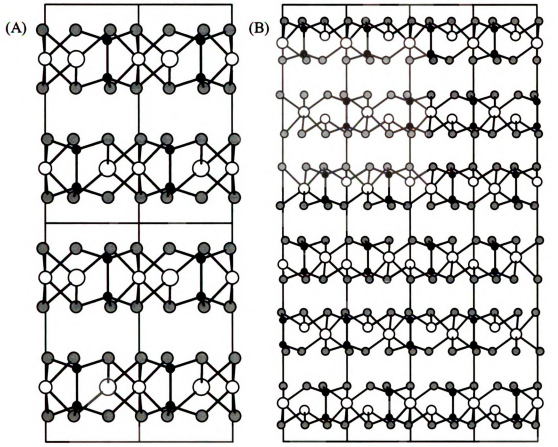

Figure 2-2 The layered structures of (A) $CuBiP_2Se_6$ and (B) $AgBiP_2Se_6$ (room temperature) as viewed down the [110] direction. Small hollow spheres are Cu(Ag) atoms, large hollow spheres are Bi atoms, solid black spheres are P, and solid grey spheres are Se.

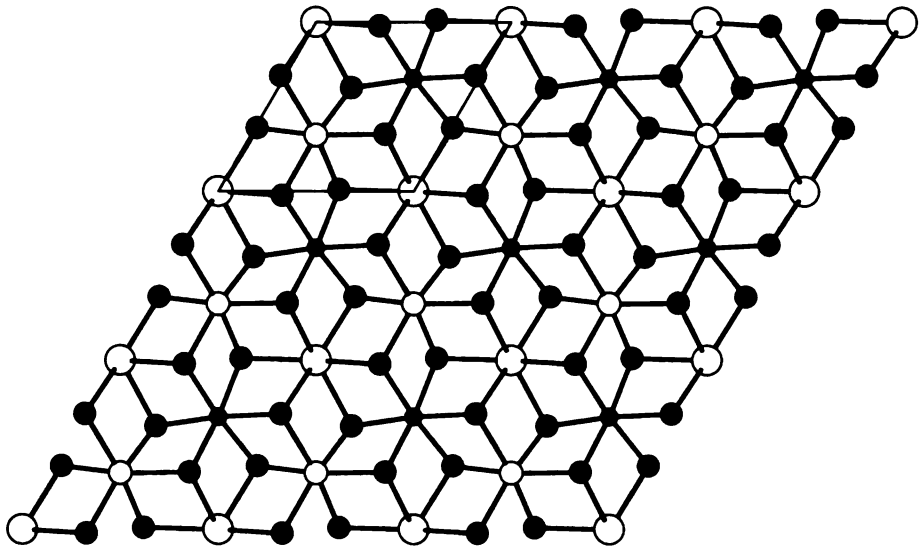

Figure 2-3 View of a single $CuBiP_2Se_6$ layer down the c-axis ([001] direction) showing the ordered arrangement of the Bi^{3+} and Cu^{+} ions. The same arrangement exists in $AgBiP_2Se_6$.

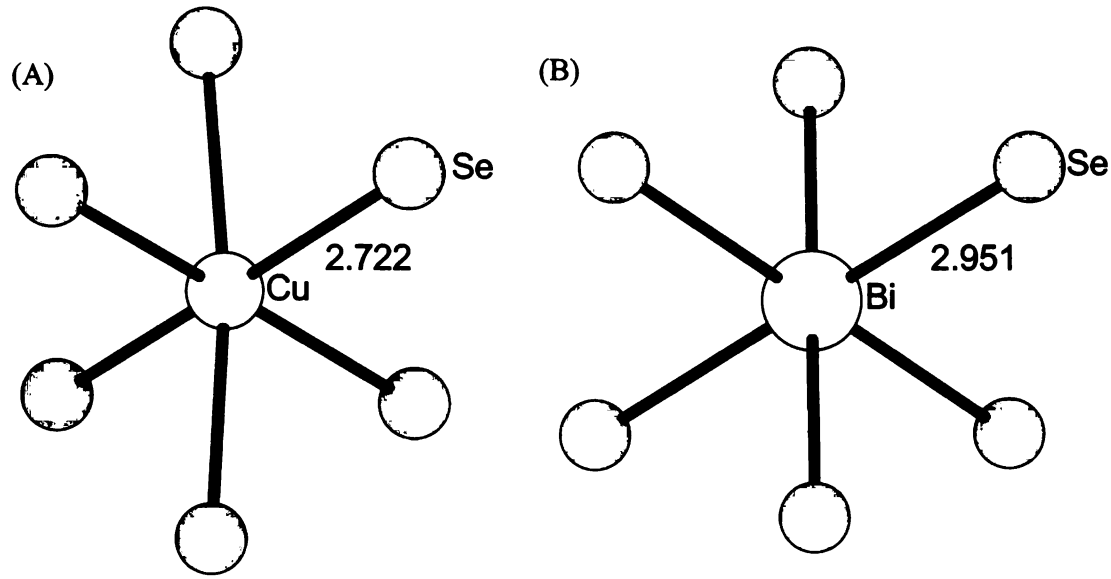

Figure 2-4 The immediate coordination environment of (A) Cu^{+} and (B) Bi^{3+} in $CuBiP_2Se_6$ at room temperature.

The Bi site is nearly octahedral with Bi-Se bond lengths of 2.950(2)Å, and Se-Bi-Se bond angles ranging from 88.37(6)° to 91.79(7)°. The so-called $6s^2$ lone pair on Bi is thus not stereochemically expressed, Figure 2-4. The expression of the lone pair would be manifested as a distortion of the octahedral Bi-Se coordination. The P-Se distance is 2.187(3) Å, and the P-P distance is 2.251(16) Å. In contrast to the Cu analog, Ag^+ ion disorder is not evident in $AgBiP_2Se_6$ where these ions are already situated in an off-center position inside a Se-based octahedron.

The positions of Ag^+ ions in $AgBiP_2Se_6$ are distorted from an octahedral environment by an elongation of three of the Ag-Se bonds, thus shifting the Ag^+ ions along the c-axis away from the center of the layer by 0.4 Å, Figure 2-5A. All Ag^+ ions are ordered at room temperature, in contrast to the disorder observed in $CuBiP_2Se_6$, described above. The Bi site is a slightly distorted octahedron with Bi-Se bond lengths of 2.9487(15) Å to 2.9550(15) Å and Se-Bi-Se angles ranging from 79.70(5)° to 95.35(4)°, Figure 2-5B The Bi^{3+} ions are shifted only 0.2Å off the center of the octahedron in the opposite direction along the layer normal of the Ag^+ ions, Figure 2-5B. The $6s^2$ lone pair of Bi seems to be stereochemically expressed, as evidenced by the slight distortion of the Bi coordination environment from the ideal octahedron. The Ag-Se bond lengths are 2.762(2)Å, with presumably weak bonding to the other side of the Se cage 3.032(3)Å away. The P-Se distances range from 2.186(2) Å to 2.193(2) Å, and the P-P distance is 2.251(9) Å.

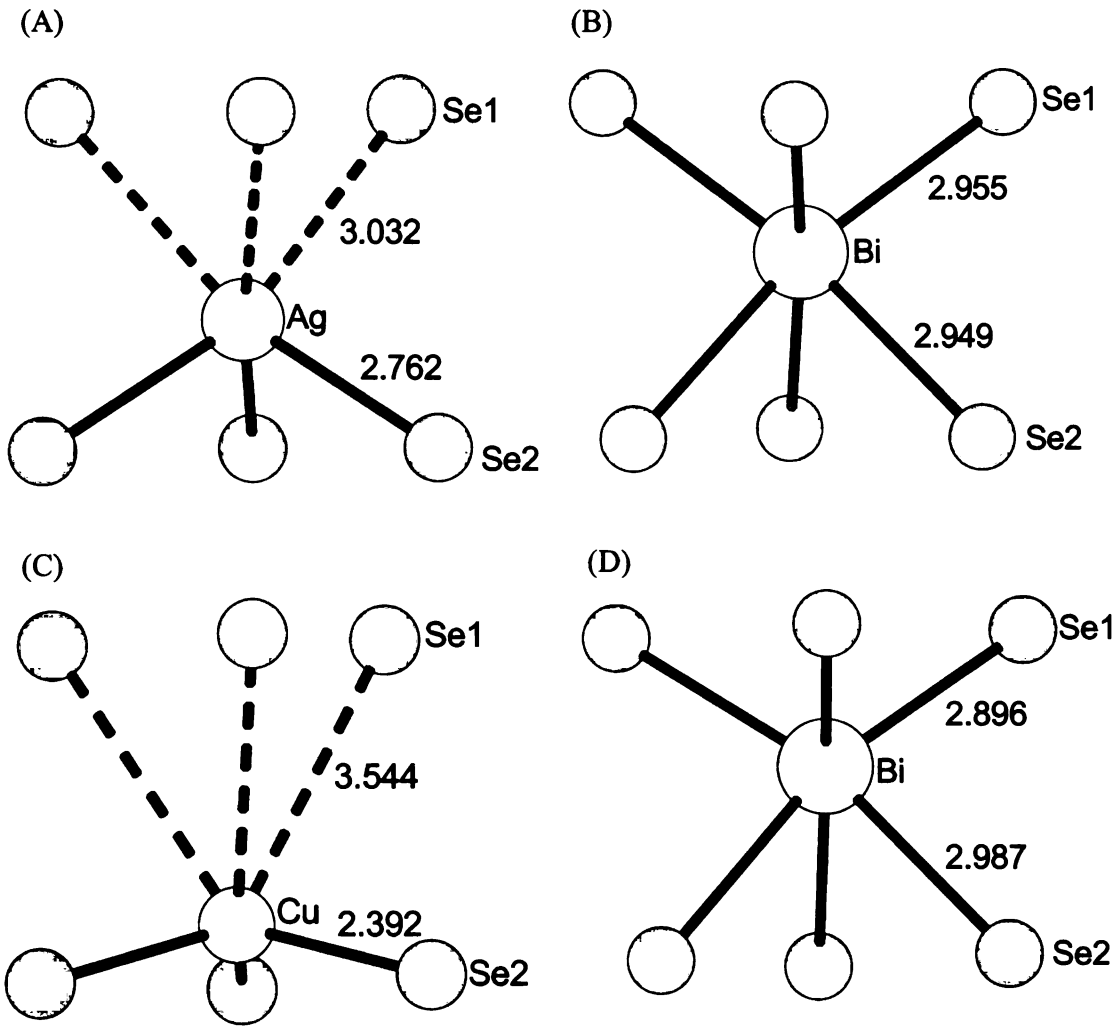

Figure 2-5. The immediate coordination environments of (A) Ag^{+} and (B) Bi^{3+} atoms in $AgBiP_2Se_6$ at 298K; (C) Cu and (D) Bi atoms in $CuBiP_2Se_6$ at 97K.

Temperature Induced Cu^{+} Sublattice Ordering

The oversized cavity of the Cu^{+} ions in $CuBiP_2Se_6$ and the possible dynamic disorder in these cavities prompted us to investigate the possibility of ordering at lower temperatures. For $CuBiP_2Se_6$ we refined the structure at three different temperatures (97, 173 and 298 K) and indeed discovered ordering in the form of two well defined anti-ferroelectric transitions as the Cu^{+} ions move and settle off-center of the octahedral sites,

Figure 2-6.

The anti-ferroelectric order of Ag^+ ions observed in $AgBiP_2Se_6$ at room temperature is achieved in $CuBiP_2Se_6$ as the sample is cooled to < 97 K. On its way to the fully ordered state the system passes through a series of intermediate structures with some slabs being fully ordered and others disordered. The low temperature structure (97K) has six layers per unit cell, Figure 2-6C. Adjacent layers are shifted with respect to each other by 1/3 along the *a*- or *b*-axes.

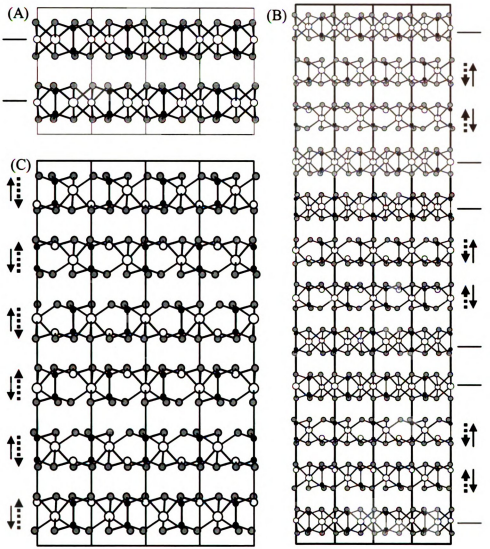

Figure 2-6. The (A) 298K (B) 173K, and (C) 97K structures of $CuBiP_2Se_6$ viewed down the [110] direction. The direction of the displacement of the copper atoms is indicated with a dashed arrow, and the direction of the bismuth atoms is indicated with a solid arrow. The atoms in the layers marked with a horizontal line have not yet ordered.

As the temperature is lowered from 298 K to 173 K a new unit cell with a six fold superstructure along the c-axis was observed. The refinement of the structure at 173 K suggested an intermediate structure in the phase transition as seen in Figure 2-6B. The

Cu^+ ions in six of the twelve "$CuBiP_2Se_6$" layers move in a direction parallel to the c-axis and towards the triangular face of the octahedral Se-cage. This motion is such that Cu^+ ions in adjacent slabs move in opposite directions and towards the same van der Waals gap. This results in an anti-ferroelectric arrangement. In the remaining layers, the Cu^+ ions are still disordered within the selenium cage and exhibit a very high thermal displacement parameter.

At 97 K, the transition of the Cu^+ ions to a fully ordered state is nearly complete with about 85% of the Cu^+ ions are in a well defined off-center position: 1.16 Å away from the center of the octahedron along the 3-fold axis, Figure 2-5C. The remaining 15% of Cu^+ ions are still disordered within the layer as before, but have been omitted for clarity, Figure 2-6C. Presumably at a lower temperature, all of the Cu^+ ions would be ordered.

The Cu^+ ion motion creates a dipole moment inside the $CuBiP_2Se_6$ slab and a new trigonal pyramidal coordination environment with Cu-Se distances of 2.3917(17) Å, Figure 2-5C. The long Cu···Se distances to the opposite side are 3.544(1) Å. Within a single slab, all of the Cu^+ ions move the same direction, thus generating a dipole along the direction perpendicular to that layer. At the same time, however, the Bi^{3+} ions within the same layer displace in a similar manner but in the opposite direction of the Cu^+ ions, Figure 2-5D. This motion is possible presumably from the stereochemical expression of the $6s^2$ electrons on Bi. The displacement of Bi^{3+} ions is 0.31 Å from the octahedral center and it creates an almost equal but opposite dipole moment. It is interesting that these ions which bear thrice the charge of the Cu^+ ions move only about one third the

distance. This gives rise to a formal antiferrolectric arrangement inside the slab and results in an intra-slab dipole moment cancellation.

Other examples where temperature dependent Cu atom ordering has been reported, include $CuInP_2S_6$ (315K),[7-11,17] $CuCrP_2Se_6$ (40K),[13] $CuInP_2Se_6$ (240K)[8,13,14,17] and $CuVP_2Se_6$ (20K).[8,15] In $CuInP_2Se_6$, the motion of Cu^+ and In^{3+} ions is such that a net dipole moment remains and a ferroelectric phenomenon is produced. The Cu^+ ions in $CuInP_2Se_6$ move 1.18 Å off center in the same direction along the slab-normal, whereas the In^{3+} ions do not move appreciably. This causes a net dipole moment in the slab which then induces the corresponding moments in adjacent slabs to align ferroelectrically.

At 1.16 Å the magnitude of the displacement of the Cu^+ ions at room temperature in $CuBiP_2Se_6$ is comparable to that in $CuInP_2Se_6$. This large Cu^+ ionic displacement in $CuBiP_2Se_6$ and in $CuBiP_2Se_6$ may be attributed to the degree of covalency between the Cu and Se atoms. The ordering at low temperatures is likely the result of a second order Jahn-Teller coupling involving the copper d-orbitals, and the selenium orbitals *(vide infra)*.[34-36]

A conversion to a disordered arrangement of coinage metal was not evident in either Ag analog. It is possible, however, that above room-temperature, a disordered paraelectric phase exists. The reasons for the differences in behavior observed between $CuBiP_2Se_6$ (antiferroelectric) and $CuInP_2Se_6$ (ferroelectric) could be traced to the existence of the stereochemically active lone pair in Bi^{3+}. The stereochemical expression of this excess electron density along a particular direction from the Bi^{3+} atom is the

driving force for shifting it off the octahedron center, a counteraction that cancels the Cu-induced dipole moment. The inability of In^{3+} to behave similarly obviates the need for a comparable shift in its octahedral cage, thereby allowing the Cu-induced dipole moments to induce ferroelectric behavior in $CuInP_2Se_6$. This implies that in isostructural $CuMP_2Se_6$ systems (where M is trivalent metal) we could expect ferroelectric ordering only when M lacks a ns^2 lone pair and presents an exact size fit in the octahedral cage.

Structure of $AgBiP_2S_6$

This compound, though layered, exhibits a different structure type, Figure 2-7. Half of the $[P_2S_6]^{4-}$ units lie with their P-P axis normal to the layer as in the structures described above whereas the other half are rotated so their P-P bond axis is nearly parallel to the layer, Figure 2-8. The $[P_2S_6]^{4-}$ anion normal to the layer coordinates to four Ag^+ and two Bi^{3+} ions. The anions lying parallel coordinate to four Bi^{3+} and two Ag^+ ions. This is a contrast to the selenium-containing analog that has only a perpendicular arrangement of $[P_2Se_6]^{4-}$ anions thus forming octahedral chalcogenide cages, which in $AgBiP_2S_6$ are absent. Ag^+ ions are instead coordinated by a highly distorted tetrahedron of S atoms within the same layer, and have only weak Ag-S interactions across the van der Waals gap, Figure 2-9A. The Bi^{3+} ions are coordinated by six S atoms with bond distances ranging from 2.752(2) to 3.106(2) Å, Figure 2-9B. This is a highly distorted coordination environment for Bi and clearly there is one side of the coordination sphere that is devoid of S atoms. This suggests the inert lone pair ($6s^2$) of Bi is strongly stereo-chemically expressed. Of the Bi environments presented herein, this

coordination geometry has the greatest degree of distortion. The S atoms spanning the putative lone pair (S3, S5, S6) have large S-Bi-S bond angles of 129.57(6)° to 152.06(6)°. The S-Bi-S angles that do not span the lone pair have smaller bond angles: 72.86(7)° to 88.77(6).°

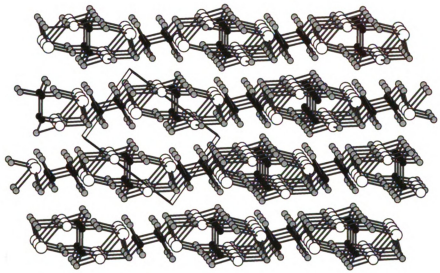

Figure 2-7. Structure of $AgBiP_2S_6$ viewed down the *a*-axis showing the lamellae.

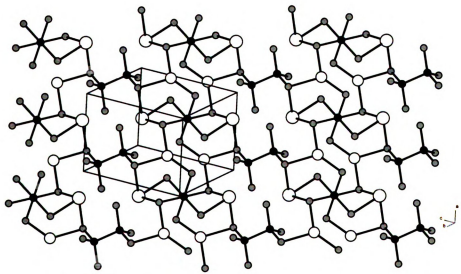

Figure 2-8. View of a single layer of $AgBiP_2S_6$. The P-P distance ranges from 2.212(4)Å to 2.225(5)Å, and the P-S distances range from 1.993(3) Å to 2.044(3) Å.

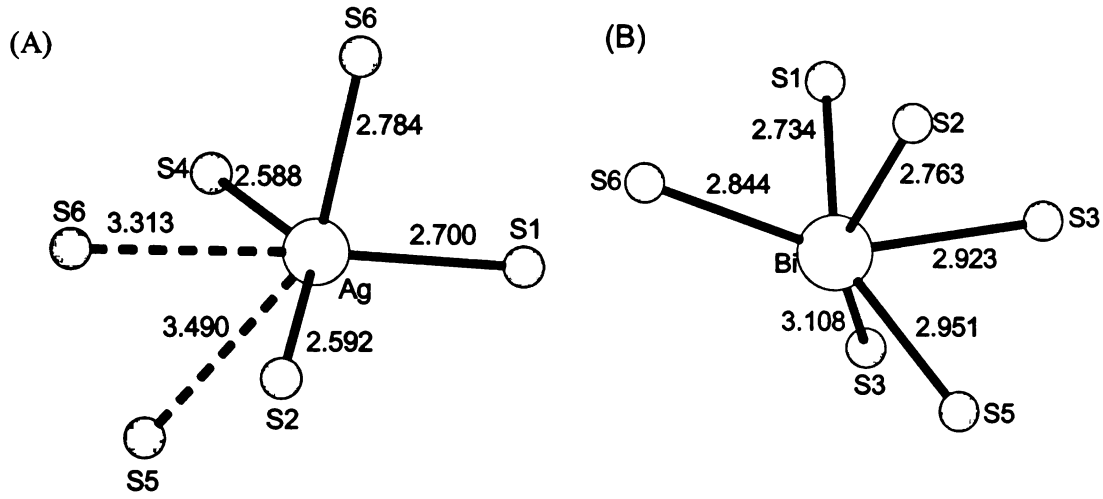

Figure 2-9. The immediate coordination environments of (A) Ag^{+} and (B) Bi^{3+} in $AgBiP_2S_6$.

The inability of $AgBiP_2S_6$ to be isostructural to its Se analog could have its origins in the large size of Bi for the available S-based octahedral cage as well as its increased tendency to stereochemically expresses its lone pair of electrons. Being smaller in size, the S atoms cannot fully satisfy the coordination shell of Bi resulting an a highly distorted geometry. Differences in the observed bonding environment of Bi^{3+} ions in the sulfide and selenide containing structures are common as for example in Bi_2S_3 (distorted octahedral) vis a vis Bi_2Se_3 (perfect octahedral). The large size of Bi^{3+} ions must play a dominant role to destabilize the $Fe_2P_2Se_6$ structure type given that the analogous compounds with smaller In^{3+}, $AgInP_2S_6$,[13] is in fact structurally closely related to $AgBiP_2Se_6$ and not $AgBiP_2S_6$.

Electronic structure calculations

In order to understand the differences between the antiferroelectric (the structure

at 97K) and paraelectric (the structure at 298K) phases of $CuBiP_2Se_6$ we performed electronic structure calculations for both forms. The band structure results show that both phases are semiconductors, Figure 2-10A,B and Figure 2-11A,B. The paraelectric phase is a direct band gap semiconductor with an energy gap of ~0.66eV at the Γ point and also has an indirect gap of the same size ~0.66eV with the valence band (VB) maximum along the H-A direction of the Brillouin zone, Figure 2-10B. The antiferroelectric phase is an indirect gap semiconductor with a much greater band-gap value of ~1.1eV, Figure 2-10A. The substantial increase in the gap is due to the restructuring of the top VB states which are shifted down in energy. There is, however, a modification of all the VB states in going from the paraelectric to antiferroelectric phase, Figure 2-10B,A. The total energy comparison shows that the antiferroelectric phase lies lower in energy by ~0.13eV/f.u. than the paraelectric phase (f.u.= $CuBiP_2Se_6$). The VB maximum occurs along the Γ-L direction in the Brillouin zone of the antiferroelectric phase. This phase transition can be classified as a second order Jahn-Teller distortion (see below).

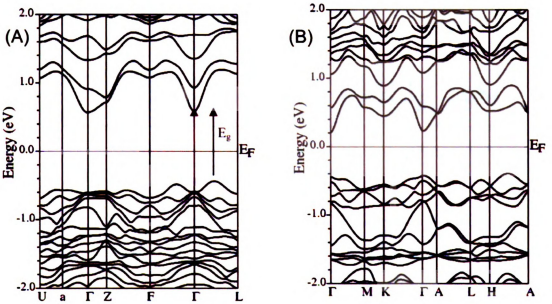

Figure 2-10. Band structure of $CuBiP_2Se_6$: (A) antiferroelectric phase and (B) paraelectric phase.

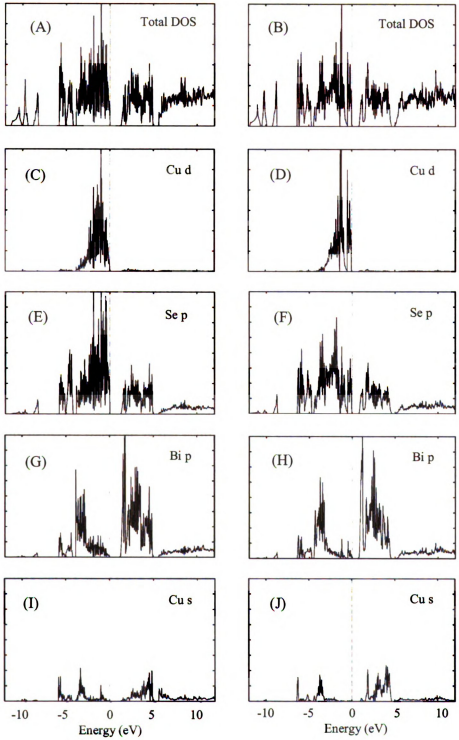

Figure 2-11. Total and partial atomic DOS: (A), (C), (E), (G), (I) antiferroelectric phase and (B), (D), (F), (H), (J) paraelectric phase.

In order to understand the atomic nature of the energy states we can inspect the partial DOS. We find that the VB states between (-4.0eV, 0eV) have strong Cu d and Se p hybridized character, Figure 2-11C,D,E, and F and to a smaller degree Bi p and Se p hybridized character, Figure 2-11G,H. This suggests that there are strong covalent interactions between the Cu-Se and Bi-Se atoms, consistent with the chalcophilic nature of both metals. The paraelectric to antiferroelectric transition affects all the states (Cu d, Se p, and Bi p). Namely, the conduction band states in the range (1.0eV, 5.0eV) consist mostly of Bi p character with small contributions from P p character, Figure 2-11G,H. In the (-3.0eV, 0eV) energy interval the Bi p states hybridize more extensively with the Se p states in the antiferroelectric phase than in the paraelectric phase.

The DOS plots suggest that the observed electronic optical absorption observed in the visible spectrum of $CuBiP_2Se_6$ (and by extension for $AgBiP_2Se_6$) are mainly due to excitations between filled Se based p-orbitals and vacant Bi-based p-orbital states. The semiconducting energy gap is defined from the band maximum occurring along the Γ-L direction to the bottom of the unoccupied band at the Γ point, leftmost arrow in Figure 2-10A. There is however another closely lying direct energy gap at the Γ point which is only slightly larger at ~1.3 eV, right arrow in Figure 2-10A. It is possible that the relatively sharp rise in optical absorption observed experimentally at ~1.45 eV (Figure 2-1A) may involve both direct and indirect transitions given these similarly spaced energy gaps. In fact, because the direct energy gap is expected to exhibit a greater absorption probability than the slightly smaller indirect gap, we may expect decent photoconductivity in these materials and this conclusion is consistent with the previously reported results.[6]

Since experimentally we observe a phase transition from the para- to antiferroelectric state in the 298-97K temperature interval, we wanted to check the relative stability of the antiferroelectric and hypothetical ferrielectric phases at 0K. The ferrielectric phase which is not observed is defined by a model in which all Cu^{+} ions in all layers move in the same direction along the c-axis so that the same Cu-Se bond distances are achieved as in the antiferroelectric phase. Similarly, all Bi^{3+} ions in every layer are displaced in the opposite direction to the Cu^{+} ions. We find that the total energy of the ferrielectric phase is higher by ~0.19 eV/f.u. This is consistent with the experimental results showing that the antiferroelectric phase is the ground state. Therefore, chemical bonding energetics dominates the Cu ion motion in $CuBiP_2Se_6$.

It is interesting to explore the driving force behind the off-center structural instabilities of Cu(Ag) and Bi^{3+} ions in these compounds. It is known that symmetry-breaking instabilities can occur as a result of a second-order Jahn-Teller d^{10}-s coupling between the conduction and valence band states.[37] Calculations carried out by Burdett *et. al.*[34] and Wei *et. al.*[38] for instabilities in the tetrahedral and octahedral symmetries support this idea. In the tetrahedral and octahedral symmetries the d-s mixing is not allowed. The mixing is allowed only if distortions from these symmetries occur and is accompanied by a lowering of energy. In contrast, in $CuBiP_2Se_6$ which have trigonal symmetry the d-s mixing is allowed even in the paraelectric (undistorted) phase, Figure 2-11J. The band calculation indicated only a small increase in the d-s mixing in the range (-1.5 eV,-0.5 eV) for the antiferroelectric phase Figure 2-11I. More importantly, as can be seen from the DOS, the states responsible for the lowering in the energy of the antiferroelectric phase involve mostly d-p mixing which is symmetry-allowed.

Consequently, a second-order Jahn-Teller effect associated with the d-p mixing is the driving force for the off-center displacement of Cu^+(and Ag^+) ions in these compounds, which create 3 short Cu-Se2 bonds and 3 long Cu-Se1 bonds. The stabilization of the Se1 p orbitals is then achieved by shorter Se1-Bi bonds due to the concomitant Bi displacement in the opposite direction to Cu(Ag). The displacement of the Bi atom in the opposite direction which tends to cancel the intra-layer dipole moment is most likely assisted by the stereochemical expression of its $6s^2$ lone pair. The so-called lone pair could then occupy the space opposite to the direction of motion. Interestingly, in $CuInP_2Se_6$, which develops a ferroelectric phase, the lack of a lone pair in In^{3+} significantly reduces the ion's ability to shift in the opposite direction which fails to cancel the incipient dipole moment created by the Cu^+ ions. The In^{3+} ion moves by 0.2 Å which is not adequate to cancel the much larger movement of 1.2 Å of the Cu^+ ions (i.e. a 6 fold difference). This compares with a 0.3 Å shift for Bi^{3+} against a ~4-fold opposite shift (1.16 Å) for Cu^+.

Although the above considerations explain well the driving force for intra-layer ordering, they do not address the issue of why an inter-layer antiferroelectric ordering of the dipole moments associated with the $Cu^+(Ag^+)$ and Bi^{3+} displacements are observed. It is clear that due to the displacement of the $Cu^+(Ag^+)$ and Bi^{3+} ions in opposite directions, the net dipole moment inside a single $CuBiP_2Se_6$ slab is considerably reduced, but perhaps not minimized. There is likely some residual dipole within a layer since the motion of the Cu^+ and Bi^{3+} ions does not differ by exactly a factor of three as the difference in formal charge would dictate. This greatly reduces the dipole-dipole coupling

between the layers which in general favors an inter-layer ferroelectric coupling.

In order to explore the origin of the antiferroelectric interlayer ordering (as seen in experiment), we have carried out crystal orbital Hamilton population (COHP)[39] analysis of the Se-Se interlayer bonds. COHP partitions the band structure states into bonding, nonbonding and antibonding character, whereas the integrated COHP (ICOHP) gives the energy contribution of a bond to the total energy. We find that in the para and ferroelectric phases, ICOHP is positive decreasing the total energy (indicating anti-bonding character), whereas in the antiferroelectric phase ICOHP is small and negative lowering the total energy. This suggests that the stability of the Se···Se interlayer van der Waals contacts may be responsible for the observed antiferroelectric ordering in these compounds.

CONCLUDING REMARKS

The coinage metal containing phases reported here are distinctly two-dimensional. Although the dimensionality is invariant upon switching from copper to silver, substantial differences exist between $CuBiP_2Se_6$ and $AgBiP_2Se_6$ with regard to the behavior of the two metals in their respective compounds. The coinage metal interaction with the anionic $[BiP_2Se_6]^{1-}$ framework is very strong relative to the corresponding alkali metal $ABiP_2Se_6$ analogs and, in fact, dominates the properties of the compounds. This includes a dramatic reduction in the energy gap and a tendency for structural distortion. The $[BiP_2Se_6]^{1-}$ framework adopts the lamellar $Fe_2P_2Se_6$ structure type motif which is apparently stable enough to force the coinage metals, which tend to prefer lower coordination, into octahedral sites of Se atoms. In turn, the coordination preference of the coinage metal is

satisfied by a motion towards one of the faces of the Se-based octahedron. The apparent tendency of the $[BiP_2Se_6]^{1-}$ framework to adopt the lamellar $Fe_2P_2Se_6$ structure type suggests that smaller alkali metals such as Na^+ and Li^+ may produce isostructural compounds to $CuBiP_2Se_6$ and $AgBiP_2Se_6$. A local dynamic hopping mechanism of Cu^+ ions is the basis for the antiferroelectric, second order Jahn-Teller type instability that sets in with reduced thermal energy. A ferroelectric state in $CuBiP_2Se_6$ fails to develop because of counteracting opposite shifts in the Bi^{3+} ion sublattice. Based on this work we conclude that in the lamellar system $CuMP_2Se_6$ (M=trivalent metal) several systems could exhibit ferroelectric or antiferroelectric phenomena depending on the ability of M to undergo local motion. It would be interesting to explore whether motional frustration sets in due to competing interactions in mixed metal phases e.g. $CuIn_{1-x}Bi_xP_2Se_6$.

REFERENCES

1. Breshears, J. D.; Kanatzidis, M. G. *J. Am. Chem. Soc.* **2000,** 122, 7839-7840.

2. McCarthy, T. Ph.D. Thesis, Michigan State University, East Lansing, MI, 1994.

3. Chondroudis, K.; Hanko, J. A.; Kanatzidis, M. G. *Inorg. Chem.* **1997,** 36, 2623-2632.

4. Kanatzidis, M. G. *Phosphorous Sulfur* **1994,** 93, 159-172.

5. Iyer, R. G.; Aitken, J. A.; Kanatzidis, M. G. *Solid State Sci.* **2004,** 6, 451-459.

6. Galdamez, A.; Manriquez, V.; Kasaneva, J.; Avila, R. E. *Mater. Res. Bull.* **2003,** 38, 1063-1072.

7. Maisonneuve, V.; Cajipe, V. B.; Simon, A.; VonDerMuhll, R.; Ravez, J. *Phys. Rev. B.* **1997,** 56, 10860-10868.

8. Maisonneuve, V.; Evain, M.; Payen, C.; Cajipe, V. B.; Molinie, P. *J. Alloys Compd.* **1995,** 218, 157-164.

9. Maisonneuve, V.; Reau, J. M.; Dong, M.; Cajipe, V. B.; Payen, C.; Ravez, J. *Ferroelectr.* **1997,** 196, 577-580.

10. Misuryaev, T. V.; Murzina, T. V.; Aktsipetrov, O. A.; Sherstyuk, N. E.; Cajipe, V. B.; Bourdon, X. *Solid State Commun.* **2000,** 115, 605-608.

11. Simon, A.; Ravez, J.; Maisonneuve, V.; Payen, C.; Cajipe, V. B. *Chem. Mat.* **1994,** 6, 1575-1580.

12. Bourdon, X.; Maisonneuve, V.; Cajipe, V. B.; Payen, C.; Fischer, J. E. *J. Alloys Compd.* **1999,** 283, 122-127.

13. Pfeiff, R.; Kniep, R. *J. Alloys Compd.* **1992,** 186, 111-133.

14. Vysochanskii, Y. M.; Molnar, A. A.; Gurzan, M. I.; Cajipe, V. B.; Bourdon, X. *Solid State Commun.* **2000,** 115, 13-17.

15. Burr, G.; Durand, E.; Evain, M.; Brec, R. *J. Solid State Chem.* **1993,** 103, 514-518.

16. Kroupa, J.; Tyagur, Y. I.; Grabar, A. A.; Vysochanskii, Y. M. *Ferroelectr.* **1999,** 223, 421-428.

17. Vysochanskii, Y. *Ferroelectr.* **1998,** 218, 629-636.

18. Odoulov, S. G.; Shumelyuk, A. N.; Brost, G. A.; Magde, K. M. *Appl. Phys. Lett.* **1996,** 69, 3665-3667.

19. Shumelyuk, A.; Hryhorashchuk, A.; Odoulov, S. *Phys. Rev. A* **2005,** 72, 6.

20. *SMART, SAINT, SHELXTL V-5 and SADABS*, Bruker Analytical X-ray Instruments, Inc.: Madison, 1998.

21. *X-AREA, X-SHAPE, and X-RED*, STOE & Cie GmbH: Darmstadt, 2004.

22. Wendlandt, W. W.; Hecht, H. G. Reflectance spectroscopy; Interscience Publishers: New York, NY, 1966.

23. Kortüm, G. Reflectance spectroscopy. Principles, methods, applications; Springer: Berlin, Germany, 1969.

24. Tandon, S. P.; Gupta, J. P. *Phys. Status Solidi* **1970,** 38, 363-&.

25. Singh, D. J.; Nordström, L. Planewaves, pseudopotentials, and the LAPW method; 2nd ed.; Springer: New York, NY, 2006.

26. Hohenberg, P.; Kohn, W. *Phys. Rev. B.* **1964,** 136, B864-B871.

27. Kohn, W.; Sham, L. J. *Phys. Rev.* **1965,** 140, A1133-A1138.

28. Perdew, J. P.; Burke, K.; Ernzerhof, M. *Phys. Rev. Lett.* **1996,** 77, 3865-3868.

29. Koelling, D. D.; Harmon, B. N. *J. Phys. C. Solid State* **1977,** 10, 3107-3114.

30. Blaha, P.; Schwarz, K.; Madsen, G.; Kvasnicka, D.; Luitz, J. *WIEN2K, An Augmented Plane Wave + Local Orbitals Program for Calculating Crystal Properties*, Karlheinz Schwarz Technical University: Wien: Vienna, 2001.

31. McCarthy, T. J.; Kanatzidis, M. G. *J. Chem. Soc. Chem. Commun.* **1994,** 1089-1090.

32. Becker, R.; Brockner, W.; Schafer, H. *Z. Naturforsch. A* **1984,** 39, 357-361.

33. Israel, R.; de Gelder, R.; Smits, J. M. M.; Beurskens, P. T.; Eijt, S. W. H.; Rasing, T.; van Kempen, H.; Maior, M. M.; Motrija, S. F. *Z. Kristall.* **1998,** 213, 34-41.

34. Burdett, J. K.; Eisenstein, O. *Inorg. Chem.* **1992,** 31, 1758-1762.

35. Pearson, R. G. *P. Natl. Acad. Sci. USA.* **1975,** 72, 2104-2106.

36. Pearson, R. G. *Theochem-Journal of Molecular Structure* **1983,** 12, 25-34.

37. Burdett, J. K. Chemical bonding in solids; Oxford University Press: New York, NY, 1995; pp 246.

38. Wei, S. H.; Zhang, S. B.; Zunger, A. *Phys. Rev. Lett.* **1993,** 70, 1639-1642.

39. Dronskowski, R.; Blochl, P. E. *J. Phys. Chem.* **1993,** 97, 8617-8624.

CHAPTER 3

WIDE COMPOSITIONAL AND STRUCTURAL DIVERSITY IN THE SYSTEM Tl/Bi/P/Q (Q = S, Se) AND OBSERVATION OF VICINAL P-Tl *J*-COUPLING IN THE SOLID STATE.

INTRODUCTION

Bismuth chalcogenide compounds have a great deal of structural diversity due in part to the flexibility of the coordination environment of Bi and the so-called inert lone pair effect.[1-7] In addition to the common octahedral coordination of Bi, examples of trigonal pyramidal,[8] square pyramidal,[9] and capped trigonal prismatic[10] coordination have been observed.[11-13] The bismuth chalcogenide building blocks can form various modules which are subsequently assembled into more complex crystalline arrangements. Examples of such assemblies can be seen in various homologous series,[14,15] as well as in the large class of minerals known as sulfosalts.[16-19] The chalcophosphate anions are a special class of chalcogenides with a broad reactivity and structural characteristics with general formula of $[P_xQ_y]^{z-}$ (Q=S, Se). They can be stabilized as alkali metal salts[20,21] or a coordinating ligands to a variety of metal centers.[22-29] Bismuth can bind to various chalcophosphate ligands, as for example in the compounds $KBiP_2S_7$,[30] $KBiP_2S_6$[31] and $K_3Bi(PS_4)_2$[32] which contain the $[P_2S_7]^{4-}$, $[P_2S_6]^{4-}$ and $[PS_4]^{3-}$ anions, respectively. Each anion can be selectively formed by slightly varying the reaction conditions, and a variety of phases can therefore be rationally synthesized.[33] In addition, chalcophosphate compounds generally are semiconductors with medium to wide energy gaps and can exhibit fascinating physical properties including pronounced photoconductivity, and photorefractive properties[34,35] pyroelectric and piezoelectric coefficients, and interesting electro-optic and nonlinear-properties.[36] Nevertheless, they are relatively little investigated compounds.

Thallium is often thought of as a pseudo-alkali metal due to its monovalency and similar ionic radius to potassium, however, with a lower electronegativity, the

substitution of the former is expected to yield products that are less ionic in nature, and therefore likely to feature stronger covalent bonding to the anionic framework. The effect of increased covalency results in a marked reduction in the size of the forbidden energy gap[37-39] and therefore, the study of this interaction could allow for the tuning of optical and electronic properties.

Because of the rich structural diversity of chalcophosphate phases and the possibility of optical and electronic tunability, we targeted the system Tl/Bi/P/Q (Q = S, Se) for investigation. Here, we report six new thallium bismuth chalcophosphate compounds which have 1-, 2- or 3- dimensional structures and span a range of optical band gaps. The range of bonding modes of the chalcophosphate $[P_xQ_y]^{z-}$ ligands combined with the coordinative flexibility of both the Tl^+ and Bi^{3+} cations allows for rich structural chemistry in this system.

In previous studies, ^{31}P solid state NMR has been shown to provide definitive structural information. Chemical shifts of selenophosphate compounds are strongly dependent on the type of anion present,[40] and ^{31}P-^{31}P dipolar coupling and ^{31}P chemical shift anisotropy are dependent on the type of chalcophosphate ion.[41] Although NMR spectroscopy provides information about the types of ions present in a compound, it is known that crystallographically inequivalent P atoms often have different chemical shifts even when only a single type of chalcophosphate ion is present. The present work provides evidence that different chemical shifts in compounds with the same anion do not arise from distortions within the $[P_xQ_y]^{z-}$ coordination geometry, but instead are correlated with differences in $[P_xQ_y]^{z-}$ ligand-to-metal ion coordination geometry. To our knowledge, this work also provides the first example of splittings due to P-Tl J-

coupling in the solid state and the first example of splitting from two-bond P-Tl J-coupling.

EXPERIMENTAL SECTION

Reagents

Chemicals were used as obtained unless otherwise noted: bismuth chunks (Tellurex Inc., Traverse City, MI, 99.999%), selenium shot (Tellurex Inc., Traverse City, MI, 99.999%), phosphorous (MCB Reagents, Gibbstown, NJ, amorphous red), thallium metal (ABCR, Karlsruhe, Germany, 99.999%), sublimed sulfur flowers (CCI, Vernon, CA). Selenium and bismuth were ground in an agate mortar and pestle to ~ 100 mesh. Phosphorous was freeze dried with benzene.

Synthesis

α-$TlBiP_2Se_6$ [I]: A mixture of Tl (0.431g, 2.1 mmol), Bi (0.4408g, 2.1 mmol), P (0.1309g, 4.2 mmol), Se (0.9989g, 12.6 mmol) was loaded into a fused silica ampoule and flame sealed under a reduced atmosphere of ~ 10^{-4} mbar. After shaking to increase homogeneity, the tube was loaded into a protective ceramic sheath and placed in a furnace. The mixture was heated to 700 °C over 24 h, held there for 24 h, and then cooled back to room temperature over a period of 96 h. A homogenous grey metallic crystalline ingot was isolated that fractured like graphite to give air-stable black plates. Energy dispersive spectroscopic (EDS) microprobe analysis of single crystals gave an average composition of $Tl_{1.2}Bi_{1.0}P_{1.9}Se_{6.1}$.

β-$TlBiP_2Se_6$ [II]: A sample portion of [I] was loaded into a fused silica ampoule and flame sealed under a reduced atmosphere of ~10^{-4} mbar. The ampoule was then heated to 400 °C over 4 h, and held there for 22 d, and then qunched in air. A homogenous grey metallic crystalline ingot was isolated that fractured like graphite to give air-stable black plates. EDS Microprobe analysis gave an average composition of $Tl_{1.0}Bi_{1.0}P_{2.0}Se_{5.6}$.

$TlBiP_2S_6$ [III]: A mixture of Tl (0.195g, 1.0 mmol), Bi (0.1990g, 1.0 mmol), P (0.1768g, 5.7mmol), and S (13.4 mmol) was loaded into a fused silica ampoule and flame sealed under a reduced atmosphere of ~10^{-4} mbar. After shaking to increase homogeneity, the tube was loaded into a protective ceramic sheath and placed in a furnace. The mixture was heated to 700 °C over 12 h, held there for 24 h, and then cooled to room temperature over 12 h. An ingot with a silvery surface was obtained that could be crushed to air stable red plates. EDS Microprobe analysis gave an average composition of $Tl_{1.0}Bi_{1.0}P_{2.2}S_{6.4}$.

$Tl_3Bi_3(PS_4)_4$ [IV]: A mixture of Tl (0.321g, 1.6 mmol), Bi (0.3288g, 1.6 mmol), P (0.0649g, 2.1 mmol), and S (0.2861g, 8.9 mmol) was loaded into a fused silica ampoule and treated as described above. The mixture was reacted with the same heating profile as in [I]. A deep red crystalline ingot was isolated was composed of air-stable red plates. Microprobe analysis gave an average composition of $Tl_{1.1}Bi_{1.0}P_{1.3}S_{5.0}$.

$TlBiP_2S_7$ [V]: A mixture of Tl (0.2921g, 1.4mmol), Bi (0.2980g, 1.4 mmol), P (0.0883g, 2.9mmol) and S (0.3201g, 9.7mmol) was loaded into a fused silica ampoule and treated as described above. The mixture was heated to 550 °C over 3 h, held there for 2 h, and then cooled to room temperature over 12 h. A silvery ingot was isolated was

composed of air-stable red plates. Microprobe analysis gave an average composition of $Tl_{1.0}Bi_{1.0}P_{1.9}S_{6.9}$.

$Tl_3Bi(PS_4)_2$ [VI]: A mixture of Tl (1.076g, 5.3mmol), Bi (0.3670g, 1.8mmol), P (0.1083g, 3.5mmol), and S (0.4504g, 14.0mmol) was loaded into a fused silica ampoule and and treated as described above. The mixture was then allowed to react with the same heating profile as in [I]. A silvery ingot was isolated that fractured into bright red plates. Microprobe analysis of several crystals gave an average composition of $Tl_{3.1}Bi_{1.0}P_{1.8}S_{8.4}$.

Single crystals of $Tl_3Bi(PS_4)_2$ with high enough quality to obtain a satisfactory refinement could not be obtained. Many crystals were screened, and all showed evidence of twinning in the form of a rotational smearing of higher angle spots perpendicular to (010), Figure 3-1. Presumably, each crystal that was mounted was a stack of plates with a slight rotation from one plate to the next.

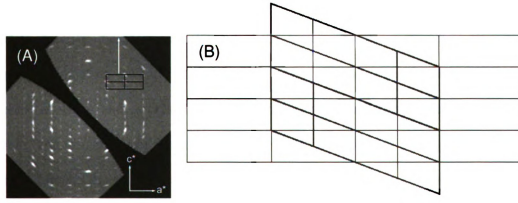

Figure 3-1 (A) The intensity weighted orthorhombic reciprocal lattice of $Tl_3Bi(PS_4)_3$ down **b*** indicating the satellite reflections that could not be indexed with integral *(hkl)*. (B) The view down the **b*** axis of the orthorhombic and monoclinic cells that were used to attempt to model $Tl_3Bi(PS_4)_3$.

It was possible to index the data with a monoclinic cell with a = 25.314(5) Å, b = 6.660(1) Å, c = 17.950(1) Å, β = 110.67(3)°, Z = 8, V = 2831.6(13) Å^3. A solution in the $P2_1/c$ space group was found that shows the same zig-zag $[Bi(PS_4)_2]_n^{3n-}$ chains as in $K_3Bi(PS_4)_4$.[32] The model did not converge as was evidenced by a relatively high reliability factor (~12%), negative thermal parameters, and high residual peaks of electron density. Furthermore, the model suggested a positional disorder of the Bi^{3+} ions down the chain axis that resulted in a 50% occupation of the Bi^{3+} ions in each of two different sites. The space group $P2_1$ was also tested to verify that the 50%/50% disorder was not a result of an artificial symmetry restriction. A significant improvement in reliability statistics was not obtained.

A view of an intensity weighted reciprocal lattice suggested that the monoclinic cell might not have been the most appropriate choice, as it was possible to index a smaller orthorhombic cell that was close to the cell of the potassium analog[32] with a superstructure or modulation vector to describe the remaining reflections. An orthorhombic unit cell with a = 8.973(2) Å, b = 6.653(1) Å, and c = 23.676(5) Å was used to describe the main reflections and the remaining reflections could be indexed using a modulation vector of (1/2, 0, 1/2). This cell becomes the initial cell when doubled in the a- and c- crystallographic directions and transformed to the monoclinic setting. The refinement of the structure in the space group *Pnma* converged to a final R value of about 8.8% but a suitable super-space group could not be found that modeled the satellite reflections. The K-analog has $P2_12_12_1$ symmetry, a space group which is a minimal non-isomorphic subgroup of *Pnma*. Although a convergent model was obtained using $P2_12_12_1$, it did not result in a significant decrease in reliability statistics and again,

it was not possible to find a suitable corresponding super spacegroup. The cell obtained by doubling the a- and c- axes removes the need for the modulation vector and is the orthorhombic translation of the above monoclinic cell, but no convergent model using this doubled cell was found.

$Tl_4Bi_2(PS_4)_2(P_2S_6)$ [VII]: Though the structure of [VII] was previously reported,[39] the authors made no attempt to optimize the synthesis. Crystals of [VII] were obtained from a mixture of Tl (0.874, 4.3mmol), Bi (0.3670g, 2.1mmol), P (0.1990g, 6.4mmol), and S (0.4795g, 15.0mmol) was loaded into a fused silica ampoule and flame-sealed under a reduced pressure of ~ 10^{-4} mbar. After shaking to increase homogeneity, the tube was loaded into a protective ceramic sheath and placed in a furnace. The mixture was then allowed to react with the same heating profile as in [I]. A homogenous looking silvery ingot was isolated that fractured into bright red plates. Presumably a minor amorphous P/S containing by product is present but could not be observed by X-ray diffraction. EDS Microprobe analysis of several crystals gave an average composition of $Tl_{2.3}Bi_{1.0}P_{2.8}S_{11.1}$.

Powder X-ray Diffraction

All samples were assessed for phase purity using powder X-ray diffraction. Powder patterns were obtained using an Inel CPS 120 powder X-ray diffractometer with monochromatized Cu Kα radiation (λ = 1.540598 Å) operating at 40 kV and 20 mA equipped with a position-sensitive detector with a 2θ range of 0 - 120° and calibrated with LaB_6.

Single Crystal X-ray Diffraction

Intensity data for single crystals of [I] – [VI] were collected on a Bruker SMART platform CCD diffractometer using Mo Kα radiation operating at 40 kV and 40 mA. A full sphere of data was collected and individual frames were acquired with a 10 s exposure time and a 0.3° omega rotation. The SMART software was used for data collection, and SAINT software was used for data extraction and reduction. An analytical absorption correction to the data was performed and direct methods were used to solve and refine the structures with the SHELXTL[42] software package.

Intensity data for several crystals of [VI] were also collected on a Stoe IPDS II diffractometer with Mo Kα radiation operating at 50 kV and 40 mA on with a 34 cm image plate. Individual frames were collected with a 60 s exposure time and a 0.5° omega rotation. The X-SHAPE and X-RED[43] software packages were used for data extraction and reduction and to apply an analytical absorption correction. The SHELXTL and JANA2000[44] software packages were used to solve and refine the structure. The parameters for data collection and the details of the structural refinement are given in Table 3-1. Atomic coordinates for [I]-[V] are displayed in Tables 3-2 through 3-6.

Table 3-1. Crystallographic data, experimental and refinement details for the Tl/Bi/P/Se and Tl/Bi/P/S compounds.

	[I] α-$TlBiP_2Se_6$	[I] β-$TlBiP_2Se_6$	[III] $TlBiP_2S_6$	[IV] $Tl_3Bi_3(PS_4)_4$	[V] $TlBiP_2S_7$
Crystal system	Monoclinic	Monoclinic	Monoclinic	Monoclinic	Monoclinic
Space group	$P2_1/c$	$P2_1/c$	$P2_1$	$P2_1/c$	$P2_1$
λ, Å (Mo Kα)	0.071073	0.071073	0.071073	0.071073	0.071073
a, Å	12.539(3)	12.250(2)	6.5967(12)	20.8189(7)	9.5028(17)
b, Å	7.4990(18)	7.5518(15)	7.3749(14)	13.2281(3)	12.290(2)
c, Å	12.248(3)	22.834(5)	9.7911(18)	22.2029(7)	9.0771(16)
α, °	90	90	90	90	90
β, °	113.731(4)	97.65(3)	91.270(3)	117.896(2)	90.561(3)
γ, °	90	90	90	90	90
Z	4	8	2	8	4
Crystal dimensions, mm	0.26 x 0.10 x 0.03	0.10 x 0.08 x 0.03	0.10 x 0.04 x 0.03	0.20 x 0.08 x 0.06	0.20 x 0.08 x 0.02
D_{calc} g/cm^3	5.979	6.022	4.656	4.614	4.384
μ, mm^{-1}	52.879	53.261	36.921	38.764	33.374
R_{int}, %	5.3	7	3.1	6.8	4.4
total reflections/ independent	6233/2495	16039/5255	3068/1367	44454/12396	8406/1522
final R/Rw, %[a]	4.0/9.8	4.1/7.1	2.3/5.1	4.6/9.9	1.9/4.0

[a] $R = \Sigma(|F_o| - |F_c|)/\Sigma|F_o|$. $R_w = [\Sigma w(|F_o| - |F_c|)^2/\Sigma w|F_o|^2]^{1/2}$

Table 3-2. Fractional atomic coordinates and U(eq) values for α-$TlBiP_2Se_6$ with standard deviations in parenthesis.

atom	x	y	z	U_{eq}[a]
Bi	0.1206(1)	0.1500(1)	0.3404(1)	14(1)
Tl	0.4226(1)	0.5757(1)	0.6549(1)	20(1)
Se(1)	0.4128(1)	0.7343(1)	0.4013(1)	13(1)
Se(2)	0.3113(1)	-0.0086(1)	0.5730(1)	14(1)
Se(3)	0.1683(1)	0.5097(1)	0.4384(1)	12(1)
Se(4)	0.3379(1)	0.1983(1)	0.3184(1)	13(1)
Se(5)	0.0568(1)	0.3126(1)	0.1124(1)	12(1)
Se(6)	0.1144(1)	-0.1790(1)	0.1911(1)	12(1)
P(1)	0.2382(3)	0.6313(3)	0.3154(3)	10(1)
P(2)	0.2395(3)	0.0902(3)	0.6948(3)	10(1)

[a] $U_{(eq)} = (\Sigma_i\Sigma_j U_{ij} a_i^* a_j^* a_i \cdot a_j)/3 \times 1000$

Table 3-3. Fractional atomic coordinates and U(eq) values for β-$TlBiP_2Se_6$ with standard deviations in parenthesis.

atom	x	y	z	U_{eq}[a]
Bi(1)	0.2013(1)	0.6539(1)	0.0796(1)	12(1)
Bi(2)	0.0618(1)	0.1509(1)	0.1714(1)	13(1)
Tl(3)	-0.3379(1)	-0.0827(1)	0.0784(1)	15(1)
Tl(4)	0.5826(1)	0.4076(1)	0.1744(1)	15(1)
Se(1)	-0.0233(1)	0.8216(1)	0.0961(1)	11(1)
Se(2)	0.0517(1)	0.5042(1)	0.2177(1)	10(1)
Se(3)	0.7851(1)	0.7170(1)	0.2023(1)	11(1)
Se(4)	0.0013(1)	0.3103(1)	0.0575(1)	11(1)
Se(5)	-0.1821(1)	0.2003(1)	0.1582(1)	11(1)
Se(6)	0.2782(1)	0.4943(2)	-0.0345(1)	12(1)
Se(7)	0.4333(1)	0.6952(1)	0.0899(1)	11(1)
Se(8)	0.4579(1)	0.4922(2)	0.2891(1)	13(1)
Se(9)	0.2560(1)	0.8117(1)	0.1926(1)	11(1)
Se(10)	0.1992(1)	1.0057(1)	0.0323(1)	11(1)
Se(11)	0.4689(1)	0.2285(1)	0.0499(1)	11(1)
Se(12)	0.2768(1)	0.3163(1)	0.1541(1)	11(1)
P(1)	-0.1448(3)	0.4039(4)	0.0967(2)	10(1)
P(2)	0.9177(3)	0.6268(4)	0.1559(2)	10(1)
P(3)	0.3359(3)	0.1245(4)	0.0927(2)	10(1)
P(4)	0.5979(3)	0.4038(4)	0.3468(2)	10(1)

[a] $U_{(eq)} = (\Sigma_i\Sigma_j U_{ij} a_i^* a_j^* a_i \cdot a_j)/3 \times 1000$

Table 3-4. Fractional atomic coordinates and U(eq) values for $TlBiP_2S_6$ with standard deviations in parenthesis.

atom	x	y	z	U_{eq}[a]
Tl	0.1955(1)	0.1512(1)	0.0002(1)	19(1)
Bi	-0.7058(1)	0.4030(1)	-0.5193(1)	13(1)
P(1)	-0.3002(4)	0.1370(5)	-0.1971(3)	10(1)
P(2)	-0.1918(5)	0.3652(4)	-0.3242(3)	8(1)
S(1)	-0.4433(4)	0.5538(4)	-0.6965(3)	12(1)
S(2)	0.3277(5)	-0.2817(4)	0.0071(3)	14(1)
S(3)	-0.8419(5)	0.7509(4)	-0.4855(3)	11(1)
S(4)	0.4177(4)	0.0532(4)	0.3228(3)	10(1)
S(5)	0.0843(5)	0.4454(4)	0.2305(3)	13(1)
S(6)	-0.9275(5)	0.4532(4)	-0.2443(3)	11(1)

[a] $U_{(eq)} = (\Sigma_i\Sigma_j U_{ij} a_i^* a_j^* a_i \cdot a_j)/3 \times 1000$

Table 3-5. Fractional atomic coordinates and U(eq) values for $Tl_3Bi_3(PS_4)_4$ with standard deviations in parenthesis.

atom	x	y	z	U_{eq}[a]
Bi(1)	0.6636(1)	0.2389(1)	0.3434(1)	28(1)
Bi(2)	0.8190(1)	0.7366(1)	0.6581(1)	26(1)
Bi(3)	0.8705(1)	0.3959(1)	0.0602(1)	25(1)
Bi(4)	0.7078(1)	0.1521(1)	0.0621(1)	27(1)
Bi(5)	0.6485(1)	0.6512(1)	0.9339(1)	28(1)

Table 3-5 continued

Bi(6)	0.8062(1)	0.6101(1)	0.4352(1)	26(1)
Tl(1)	0.5211(1)	0.0410(1)	0.1510(1)	54(1)
Tl(2)	0.4113(1)	0.2394(1)	0.3327(1)	82(1)
Tl(3)	0.6264(1)	0.4588(1)	0.1431(1)	61(1)
Tl(4)	0.1379(1)	0.4876(1)	0.1505(1)	55(1)
Tl(5)	0.8937(1)	0.1771(2)	0.8316(1)	154(1)
Tl(6)	0.9909(1)	0.0377(1)	0.1551(1)	53(1)
S(1)	0.8109(3)	0.6054(3)	0.0628(2)	28(1)
S(2)	0.9366(3)	0.5496(3)	0.0182(3)	35(1)
S(3)	0.9140(3)	0.7088(3)	0.5467(3)	43(1)
S(4)	0.7853(2)	0.6790(3)	0.9115(2)	24(1)
S(5)	0.9160(3)	0.4535(3)	0.4887(2)	31(1)
S(6)	0.8550(3)	0.2831(3)	0.9434(2)	39(1)
S(7)	0.7405(2)	0.0954(3)	0.9312(2)	29(1)
S(8)	0.8604(2)	0.3179(3)	0.5828(2)	24(1)
S(9)	0.5846(3)	0.4968(4)	0.9842(3)	40(1)
S(10)	0.7015(3)	0.0611(3)	0.4283(2)	31(1)
S(11)	0.6031(3)	0.2556(3)	0.9471(2)	30(1)
S(12)	0.7349(2)	0.1367(3)	0.5836(2)	24(1)
S(13)	0.5954(3)	0.5056(4)	0.5105(3)	38(1)
S(14)	0.6471(3)	0.6384(3)	0.4117(2)	25(1)
S(15)	0.7693(3)	0.9366(3)	0.0670(2)	34(1)
S(16)	0.6508(3)	0.7528(3)	0.0467(2)	31(1)
S(17)	0.9023(2)	0.5593(3)	0.7246(2)	30(1)
S(18)	0.9639(3)	0.7893(3)	0.7367(2)	41(1)
S(19)	0.0107(2)	0.3344(3)	0.1208(2)	28(1)
S(20)	0.0823(3)	0.5952(4)	0.8008(2)	35(1)
S(21)	0.6924(3)	0.0809(3)	0.2713(2)	29(1)
S(22)	0.8024(3)	0.1535(4)	0.2075(2)	38(1)
S(23)	0.6243(3)	0.1959(3)	0.1201(2)	29(1)
S(24)	0.7240(3)	0.3225(3)	0.2644(2)	38(1)
S(25)	0.6951(3)	0.8978(4)	0.7879(2)	36(1)
S(26)	0.7826(3)	0.9244(3)	0.6941(2)	37(1)
S(27)	0.7668(3)	0.8016(3)	0.2470(2)	32(1)
S(28)	0.8727(3)	0.6225(4)	0.3600(2)	45(1)
S(29)	0.6049(3)	0.8652(4)	0.2899(2)	35(1)
S(30)	0.5044(3)	0.8181(5)	0.3638(2)	43(1)
S(31)	0.5750(3)	0.0906(3)	0.7950(3)	43(1)
S(32)	0.5174(3)	0.3256(3)	0.7674(2)	33(1)
P(1)	0.8626(2)	0.6560(3)	0.0107(2)	22(1)
P(2)	0.8443(2)	0.3480(3)	0.4861(2)	22(1)
P(3)	0.6544(3)	0.1094(3)	0.4860(2)	23(1)
P(4)	0.6643(3)	0.6107(3)	0.5090(2)	23(1)
P(5)	0.0149(2)	0.3472(3)	0.2143(2)	25(1)
P(6)	0.7123(3)	0.1866(3)	0.2166(2)	25(1)
P(7)	0.7776(3)	0.8498(3)	0.7718(2)	25(1)
P(8)	0.5054(2)	0.8183(3)	0.2723(2)	27(1)

[a] $U_{(eq)} = (\Sigma_i \Sigma_j U_{ij} a_i^* a_j^* a_i \cdot a_j)/3 \times 1000$

Table 3-6. Fractional atomic coordinates and U(eq) values for $TlBiP_2S_7$ with standard deviations in parenthesis.

atom	x	y	z	U_{eq}[a]
Bi(1)	0.3411(1)	0.3622(1)	0.1199(1)	22(1)
Tl(2)	0.8813(1)	0.1896(1)	0.3771(1)	36(1)
P(1)	0.7782(2)	0.6028(1)	0.5192(2)	14(1)
P(2)	0.6808(2)	0.4630(1)	0.2006(2)	14(1)
S(1)	0.1160(2)	0.2059(1)	0.1128(2)	21(1)
S(2)	0.1211(2)	0.4454(2)	0.2938(2)	21(1)
S(3)	0.4084(2)	0.1718(1)	-0.0697(2)	19(1)
S(4)	0.7526(2)	0.4475(1)	0.4212(2)	19(1)
S(5)	0.5061(2)	0.5563(1)	0.1868(2)	20(1)
S(6)	0.1640(2)	0.4712(2)	-0.0755(2)	20(1)
S(7)	0.6514(2)	0.3058(1)	0.1486(2)	19(1)

[a] $U_{(eq)} = (\Sigma_i\Sigma_j U_{ij} a_i^* a_j^* a_i \cdot a_j)/3 \times 1000$

Energy Dispersive Spectroscopy

A JEOL JSM-35C scanning electron microscope equipped with a Tracor Northern energy dispersive spectroscopy detector was used for quantitative microprobe analysis. Data were collected using an accelerating voltage of 25 kV and a collection time of 60s and results were averaged over several sample areas.

Differential Thermal Analysis

Differential thermal analyses were performed with a Shimadzu DTA-50 thermal analyzer. A ground sample weighing ~25mg was sealed in a quartz ampoule under reduced pressure. An equivalent mass of alumina was sealed in an identical ampoule to serve as a reference. The samples were heated to 850 °C at a rate of 10 °C/min, cooled to 150 °C at a rate of 10 °C/min, reheated to 850 °C at a rate of 10 °C/min, and then cooled to room temperature at a rate of 10 °C/min.

UV/Vis Spectroscopy

Optical band gaps were determined using Kubelka-Munk theory[45-47] on data collected by diffuse reflectance UV/Vis spectroscopy on finely ground samples at room temperature. A background was collected before each scan using $BaSO_4$. A spectrum was collected for the region of 200-2500 nm with a Shimadzu UV-3101 PC double-beam, double-monochromator spectrophotometer.

NMR Spectroscopy

Room temperature solid-state NMR spectra were collected on a 9.4 T spectrometer (Varian Infinity Plus) using a double resonance magic angle spinning (MAS) probe. Samples were spun at frequencies ranging from 5 kHz to 15 kHz in zirconia rotors of 4 mm outer diameter and with a ~50 μL sample volume. Bloch decay spectra were taken with a 4 μs 90° pulse (calibrated using 85% H_3PO_4) and with relaxation delays ranging from 10 to 5000 s. Each spectrum was processed with ≤ 100 Hz line broadening and up to a 10^{th} order polynomial baseline correction. The spectra were referenced to 85% H_3PO_4 at 0 ppm.

Quantitative spectra were collected by ensuring that the pulse delay between scans was at least 2-5 times T_1. All of the compounds except [I] and [III] had T_1 relaxation times in the range of 1500-1750 sec, which is typical for the chalcophosphate compounds previously studied.[48]

Room temperature solid state NMR spectra of [VI] and [VII] were also collected on a Bruker DSX300 NMR spectrometer using a double resonance magic angle spinning

(MAS) probe with zirconia rotors of 4 mm outer diameter. Bloch decay spectra were collected with a 4.5 μs 90° pulse and a relaxation delay of 2500 s.

RESULTS AND DISCUSSION

Syntheses

It was possible to form α-$TlBiP_2Se_6$ [I] by direct combination of the elements. The compound β-$TlBiP_2Se_6$ [II], however, was not formed directly from the melt but was instead formed after annealing the α-phase for an extended time (~22 days) below the melting point. Presumably, the α-compound is the kinetically stable one, whereas the β-phase is thermodynamically stable. The rotation of the chain *(vide infra)* that accounts for the difference between the two compounds presumably has a high energy of activation, and a short (i.e. several hours to several days) anneal time is insufficient to affect such a conversion. Though the α-$MBiP_2Se_6$ (M = K, Tl) phases are isomorphous, it is interesting to note that β-$TlBiP_2Se_6$ and β-$KBiP_2Se_6$[49] are different structure types, with the latter being formed after annealing a glass formed by rapid quenching. As in the case of the K analog, it was possible to form a glass by quenching a stoichiometric melt of Tl/Bi/2P/6Se but after annealing the glass, the α-phase was again isolated. A Tl^+-containing compound that is isomorphous to β-$KBiP_2Se_6$[49] was not found.

Compounds [III] – [IV] have a 1:1 ratio of Tl to Bi. By slightly varying the reaction conditions, it was possible to prepare each as the dominant crystalline phase. Based on the experimental information we have gathered thus far, we can produce a schematic reactivity table that places these compounds in a greater context as shown in Figure 3-2.

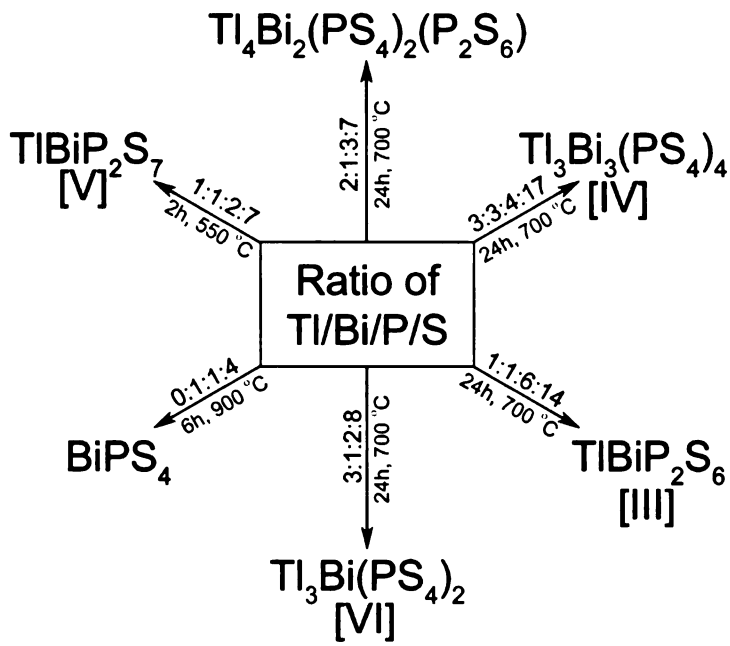

Figure 3-2. Schematic of the optimized reaction conditions required to produce the known Tl/Bi/P/S compounds as the dominant crystalline product. The stoichiometric ratio, soak time, and soak temperature are indicated.

It was initially a challenge to reproduce $TlBiP_2S_7$ as $Tl_3Bi_3(PS_4)_4$ often formed. $TlBiP_2S_7$ [IV] was originally discovered reaction conditions identical to those used for α-$TlBiP_2Se_6$ [I] but with S instead of Se. The intended $TlBiP_2S_6$ stoichiometry was not produced by this reaction, but rather $Tl_3Bi_3(PS_4)_4$ [IV] was produced as the dominant crystalline product. Although its presence could not be confirmed with powder X-ray diffraction, $Tl_3Bi_3(PS_4)_4$ must have been accompanied by a glassy phase composed of the two extra equivalents of both P and S. Upon further investigation, it was determined that the additional P is not necessary to produce compound [IV] in pure form, but that some additional S is essential. The optimized reaction conditions for producing compound [IV] were determined to be 3Tl/3Bi/4P/17S, that is, an extra equivalent of S.

It is possible that the extra equivalent of S in the form of S_x^{2-} chains reduced the acidity of the melt wherein compound [IV] could be formed. The metal to chalcogenide ratio is extremely important in the melt, and changes of as little as 0.2 stoichiometric equivalents were observed to have the marked effect of producing a completely different crystalline compound.[50] A stoichiometric combination of 3Tl/3Bi/4P/16S did not produce compound [IV] but gave a product that contained a significant amount of $TlBiP_2S_6$ [III] along with $BiPS_4$ as a minor phase. In terms of a 1:1 Tl:Bi ratio, this results in a deficiency of both P and S relative to the stoichiometry of the dominant crystalline compound, suggesting that the S was consumed by oxidizing the metals before P could be fully oxidized to the 5+ state. To produce compound [III] as the dominant crystalline product, it was therefore necessary to employ a flux with limited acidity to stabilize the $[P_2S_6]^{4-}$ unit. A reaction with the stoichiometric ratio of Tl/Bi/6P/14S was subsequently found to produce compound [III] as the sole crystalline product. Attempts to remove the glassy impurities by washing with ethylenediamine, methanol, and ether resulted in a product that was amorphous by powder X-ray diffraction suggesting that compound [III] decomposes under such conditions.

$TlBiP_2S_7$ [V] was formed from a stoichiometric mixture of the elements, but with a heating profile that was both lower in temperature and shorter in time than any of the other reactions. When slowly cooled, a mixture of Tl/Bi/2P/7S produced mainly compound [IV] but also some $BiPS_4$. Presumably, compound [V] is more kinetically stable and a more rapid cooling rate is necessary to avoid the more thermodynamically stable compounds.

It was also possible to prepare $Tl_4Bi_2(PS_4)_2(P_2S_6)$[39] [VII] in pure form by adding an additional equivalent of P (i.e. 2Tl/Bi/3P/7S). The overoxidation of P to 5+ was prevented by the extra phosphorous, and it was possible to stabilize both the P^{4+} and P^{5+} species in the compound.[51]

Structure Description

α-TlBiP$_2$Se$_6$ [I] and β-TlBiP$_2$Se$_6$ [II]: α-$TlBiP_2Se_6$ [I] is isomorphous with α-KMP_2Se_6[52,53] (M = Sb, Bi), Figure 3-3. The structure is built up of $[MP_2Se_6]^-$ layers that are separated by Tl^+ ions with a mean Tl-Se distance of 3.34 Å.

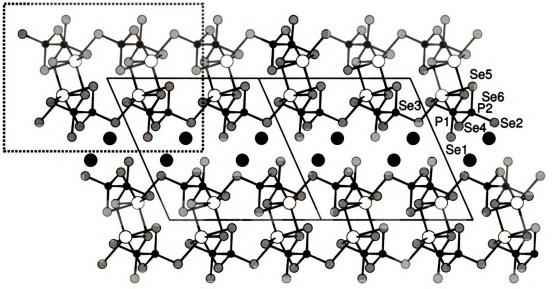

Figure 3-3. α-$TlBiP_2Se_6$ [I] down the [010] direction showing the lamellae separated by a layer of Tl^+ ions with the double-chain moiety common to [I] and [II] emphasized by the rectangular dotted outline. Small black spheres are P, large black spheres are Tl, large white spheres are Bi, and shaded spheres are Se.

Comparatively, the K^+ analog has K-Se bond distances averaging 3.36 Å. Each Tl^+ cation is 7-coordinate with a distorted monocapped octahedral geometry, Figure 3-4A,

and each bismuth is 6-coordinate with four different $[PS_4]^{3-}$ units, Figure 3-4B. One of the $[P_2Se_6]^{4-}$ anions is tris-chelated to Bi^{3+} (Se(3), Se(4), Se(5)) with Bi-Se bonds ranging from 2.8506(14) Å to 3.1253(14) Å in length. Neighboring BiS_6 are connected to form a chain along down (010) by bridging Bi-Se(6) bonds at a distance of 3.1253(14) Å.

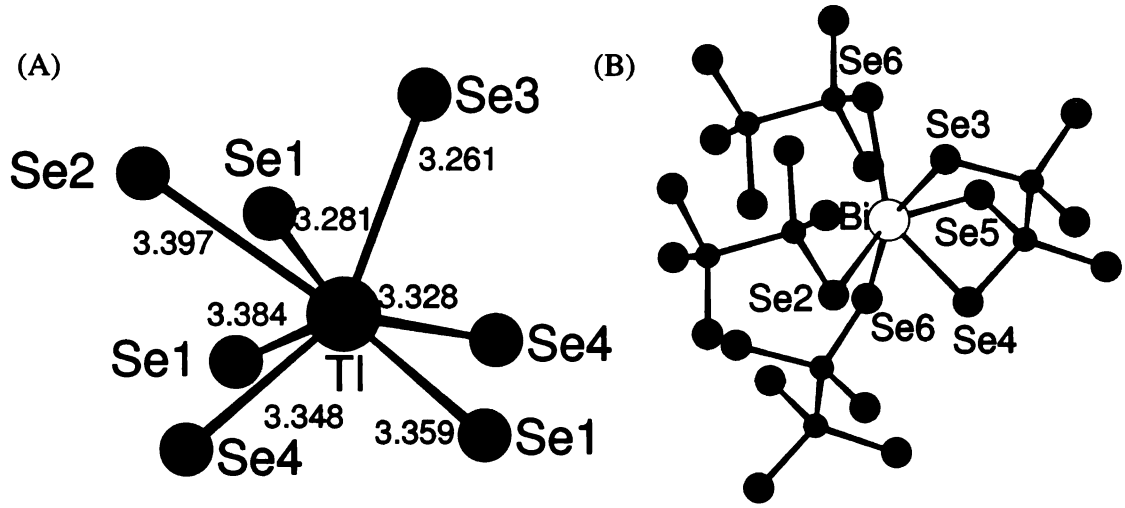

Figure 3-4. (A) The coordination of Tl^{+} in α-$TlBiP_2Se_6$ [I] and (B) the coordination of Bi^{3+} showing tris-chelation by one $[P_2Se_6]^{4-}$ and monodentate bonding by each of the other three $[P_2Se_6]^{4-}$ anions.

Finally, a double chain is assembled through the Bi-Se(2) bond where Se(2) is on a $[P_2Se_6]^{4-}$ ion in a neighboring chain along the (001) axis. Neighboring double chains are assembled by the same Bi-Se(2) bond. The layer assembled from the double chains is separated from an identical layer by Tl^{+} ions. The P-P bond distance in the $[P_2Se_6]^{4-}$ anion is 2.228(4) Å, and the P-Se bond distances range from 2.155(3) Å to 2.222(3) Å. There is one Se atom on the $[P_2Se_6]^{4-}$ anion that is terminal and interacts only with Tl^{+} ions. Table 3- 7 contains selected bond lengths and angles for compound [I].

Table 3-7. Selected bond lengths and angles for α-$TlBiP_2Se_6$ with bond lengths (Å) and angles (°) with standard uncertainties in parenthesis.

Bi—Se5	2.8506(14)	Se5—Bi—Se4	75.90(4)
Bi—Se4	2.8676(14)	Se5—Bi—Se3	86.42(4)
Bi—Se3	2.9148(12)	Se4—Bi—Se3	82.88(3)
Bi—Se6	3.0531(13)	Se5—Bi—Se6	80.18(4)
Bi—$Se6^{i}$	3.0919(13)	Se4—Bi—Se6	80.89(3)
Bi—Se2	3.1253(14)	Se3—Bi—Se6	161.03(4)
		Se5—Bi—$Se6^{i}$	79.78(3)
Tl—Se3	3.2615(14)	Se4—Bi—$Se6^{i}$	146.07(3)
Tl—Se1	3.2814(15)	Se3—Bi—$Se6^{i}$	72.25(3)
Tl—$Se4^{v}$	3.3277(14)	Se6—Bi—$Se6^{i}$	117.86(3)
Tl—$Se4^{iv}$	3.3476(14)	Se5—Bi—Se2	149.99(4)
Tl—$Se1^{iv}$	3.3590(13)	Se4—Bi—Se2	74.12(4)
Tl—$Se1^{vi}$	3.3843(14)	Se3—Bi—Se2	91.25(3)
Tl—$Se2^{vii}$	3.3974(14)	Se6—Bi—Se2	93.68(3)
Tl—$Se2^{viii}$	3.6999(15)	$Se6^{i}$—Bi—Se2	127.80(4)
Se1—P1	2.155(3)	Se1—P1—$Se6^{vii}$	113.62(12)
Se2—P2	2.160(3)	Se1—P1—Se3	114.65(14)
Se3—P1	2.220(3)	$Se6^{vii}$—P1—Se3	111.94(13)
Se4—$P2^{ii}$	2.197(3)	Se2—P2—$Se4^{v}$	116.69(14)
Se5—$P2^{ii}$	2.222(3)	Se2—P2—$Se5^{v}$	116.07(14)
Se6—$P1^{iii}$	2.203(3)	$Se4^{v}$—P2—$Se5^{v}$	105.46(12)
P1—$P2^{ii}$	2.228(4)	Se2—P2—$P1^{v}$	108.57(13)
		Se1—P1—$P2^{ii}$	108.30(15)
		$Se6^{vii}$—P1—$P2^{ii}$	102.37(15)
		Se3—P1—$P2^{ii}$	104.71(13)
		$Se4^{v}$—P2—$P1^{v}$	103.47(15)
		$Se5^{v}$—P2—$P1^{v}$	105.32(14)

(i) -x, 0.5+y, 0.5-z; (ii) x, 0.5-y, -0.5+z; (iii) x, -1+y, z; (iv) 1-x, 1-y, 1-z; (v) x, 0.5-y, 0.5+z; (vi) x, 1.5-y, 0.5+z; (vii) x, 1+y, z; (viii) 1-x, 0.5+y, 1.5-z; (ix) x, 1.5-y, -0.5+z; (x) 1-x, -0.5+y, 1.5-z; (xi) -x, -0.5+y, 0.5-z.

The compound β-$TlBiP_2Se_6$ [II] crystallizes in the monoclinic spacegroup $P2_1/c$. The structure is built up from the same chains described as those in α-$KBiP_2Se_6$ and α-$TlBiP_2Se_6$. The difference between the α- and β-$TlBiP_2Se_6$ compound is that in the latter, the layer is broken apart by a rotation about the (010) axis of $[BiP_2Se_6]_4^{4-}$ double chains such that 1-dimensionality is preserved, Figure 3-5.

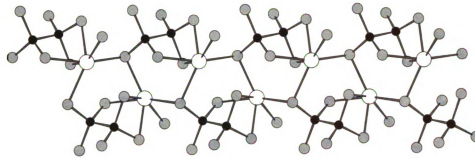

Figure 3-5. Assembly of the chain common to both [I] and [II] viewed down the (001) direction.

There are two such chains per unit cell with one centered at the origin, and the other centered at ½ along the c-axis. Each chain is separated along the (100) direction by Tl^+ ions, Figure 3-6. Tl(1) forms a distorted bicapped octahedron. Seven of the Tl-Se distances are relatively short with an average distance of 3.40Å. The remaining interaction between Tl(1) and Se(8) is weak with a bond length of 3.5813(17) Å. Tl(2) is also a distorted bicapped octahedron, again with seven short and one longer Tl-Se interaction. The average length of the shorter bonds is 3.34 Å, and the longer Tl(2)-Se(12) interaction is 3.7761(15) Å, Figure 3-7A.

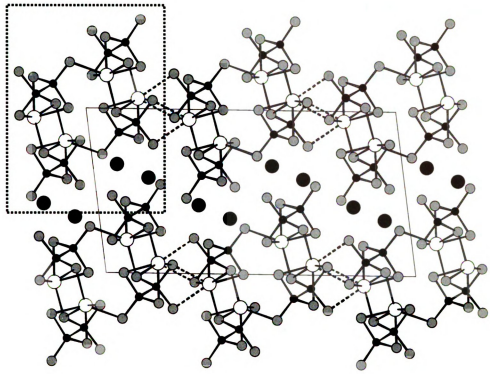

Figure 3-6. β-$TlBiP_2Se_6$ [II] down the (010) axis showing emphasizing the weak inter-chain interaction with a dashed line, and double-chain moiety common to [I] and [II] emphasized by rectangular outline.

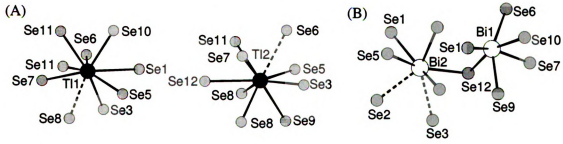

Figure 3-7 (A) The coordination of Tl^+ in β-$TlBiP_2Se_6$ and (B) the coordination of Bi^{3+} showing the weak inter-chain Bi-Se interaction with a dashed line.

Each Bi^{3+} center is tris-chelated by Se atoms with an average Bi-Se bond length of 2.88 Å, Figure 3-7B. Two chains are then connected together to form a double-chain with a Bi(1)-Se(6) bond length of 3.1259(16) Å, and the chains interact weakly with neighboring double chains with Bi(2)-Se(2) lengths of 3.2419(16) Å and Bi(2)-Se(3)

3.2627(18) Å, Figure 3-7B. Table 3-8 contains selected bond lengths and angles for compound [II].

Table 3-8. Selected bond lengths and angles for β- $TlBiP_2Se_6$ with bond lengths (Å) and angles (°) with standard uncertainties in parenthesis.

Bi1—Se7	2.8374(14)	Se7—Bi1—Se9	76.47(5)
Bi1—Se9	2.8406(16)	Se7—Bi1—Se10	83.56(4)
Bi1—Se10	2.8671(13)	Se9—Bi1—Se10	86.70(4)
Bi1—Se1	3.0974(14)	Se7—Bi1—Se1	147.24(3)
Bi1—Se6	3.1259(16)	Se9—Bi1—Se1	79.83(4)
Bi1—Se12	3.1352(14)	Se10—Bi1—Se1	72.73(4)
Bi2—Se4	2.8717(16)	Se7—Bi1—Se6	72.68(4)
Bi2—Se2	2.8786(13)	Se9—Bi1—Se6	149.08(4)
Bi2—Se5	2.9858(14)	Se10—Bi1—Se6	91.84(4)
Bi2—Se12	2.9885(14)	Se1—Bi1—Se6	129.04(4)
Bi2—$Se1^{ii}$	3.1226(13)	Se7—Bi1—Se12	79.90(4)
Bi2—$Se2^{iii}$	3.2419(16)	Se9—Bi1—Se12	80.29(4)
Bi2—$Se3^{iv}$	3.2627(18)	Se10—Bi1—Se12	160.93(4)
		Se1—Bi1—Se12	117.98(4)
Tl1—Se5	3.2565(15)	Se6—Bi1—Se12	92.23(4)
Tl1—$Se10^{i}$	3.2802(17)	Se4—Bi2—Se2	85.74(4)
Tl1—$Se7^{v}$	3.3065(13)	Se4—Bi2—Se5	73.89(4)
Tl1—$Se11^{vi}$	3.3356(17)	Se2—Bi2—Se5	80.19(4)
Tl1—$Se11^{vii}$	3.3377(14)	Se4—Bi2—Se12	80.26(4)
Tl1—$Se6^{vi}$	3.3764(14)	Se2—Bi2—Se12	75.12(4)
Tl1—$Se3^{v}$	3.3792(17)	Se5—Bi2—Se12	145.30(3)
Tl1—$Se8^{iii}$	3.5813(17)	Se4—Bi2—$Se1^{ii}$	78.94(4)
Tl2—Se8	3.2658(17)	Se2—Bi2—$Se1^{ii}$	155.90(4)
Tl2—Se11	3.2846(17)	Se5—Bi2—$Se1^{ii}$	77.76(4)
Tl2—Se7	3.2928(15)	Se12—Bi2—$Se1^{ii}$	119.71(4)
Tl2—$Se8^{iv}$	3.3008(14)	Se4—Bi2—$Se2^{iii}$	139.90(4)
Tl2—$Se5^{viii}$	3.3434(14)	Se2—Bi2—$Se2^{iii}$	89.19(3)
Tl2—Se3	3.4056(14)	Se5—Bi2—$Se2^{iii}$	66.05(4)
Tl2—$Se9^{iv}$	3.4733(18)	Se12—Bi2—$Se2^{iii}$	136.31(4)
Tl2—Se12	3.7761(15)	$Se1^{ii}$—Bi2—$Se2^{iii}$	90.66(4)
Tl2—$Se6^{ix}$	3.8876(18)	Se4—Bi2—$Se3^{iv}$	141.72(4)
		Se2—Bi2—$Se3^{iv}$	65.25(4)
Se1—$P2^{vii}$	2.194(3)	Se5—Bi2—$Se3^{iv}$	121.30(4)
Se2—$P2^{vii}$	2.219(4)	Se12—Bi2—$Se3^{iv}$	68.89(4)
Se3—P2	2.165(4)	$Se1^{ii}$—Bi2—$Se3^{iv}$	135.98(3)
Se4—P1	2.220(3)	$Se2^{iii}$—Bi2—$Se3^{iv}$	67.51(4)
Se5—P1	2.172(4)		
Se6—$P1^{i}$	2.159(4)	$Se6^{i}$—P1—Se5	118.15(15)
Se7—$P4^{xii}$	2.205(4)	$Se6^{i}$—P1—Se4	115.33(18)
Se8—P4	2.127(4)	Se5—P1—Se4	106.61(13)

Table 3-8 continued

Se9—P4^{xii}	2.220(3)	Se6^{i}—P1—P2^{vii}	107.38(14)
Se10—P3^{x}	2.213(4)	Se5—P1—P2^{vii}	103.14(17)
Se11—P3	2.156(3)	Se4—P1—P2^{vii}	104.76(15)
Se12—P3	2.204(3)	Se3—P2—Se1^{viii}	115.13(13)
		Se3—P2—Se2^{viii}	111.08(17)
P1—P2^{vii}	2.230(4)	Se1^{viii}—P2—Se2^{viii}	113.52(14)
P4—P3^{xii}	2.246(4)	Se3—P2—P1^{viii}	108.35(16)
		Se1^{viii}—P2—P1^{viii}	104.11(17)
		Se2^{viii}—P2—P1^{viii}	103.61(13)
		Se11—P3—Se12	112.38(13)
		Se11—P3—Se10^{ii}	114.84(18)
		Se12—P3—Se10^{ii}	112.18(14)
		Se11—P3—P4^{iv}	108.44(15)
		Se12—P3—P4^{iv}	102.62(16)
		Se10^{ii}—P3—P4^{iv}	105.29(14)
		Se8—P4—Se7^{iv}	115.78(15)
		Se8—P4—Se9^{iv}	118.31(18)
		Se7^{iv}—P4—Se9^{iv}	105.16(13)
		Se8—P4—P3^{xii}	110.08(14)
		Se7^{iv}—P4—P3^{xii}	101.93(17)
		Se9^{iv}—P4—P3^{xii}	103.73(15)

(i) -x, 1-y, -z; (ii) x, -1+y, z; (iii) -x, -0.5+y, 0.5-z; (iv) 1-x, -0.5+y, 0.5-z; (v) -1+x, -1+y, z; (vi) -x, -y, -z; (vii) -1+x, y, z; (viii) 1+x, y, z; (ix) 1-x, 1-y, -z; (x) x, 1+y, z; (xi) -x, 0.5+y, 0.5-z; (xii) 1-x, 0.5+y, 0.5-z; (xiii) 1+x, 1+y, z.

$TlBiP_2S_6$ [III]: $TlBiP_2S_6$ [III] crystallizes in the monoclinic spacegroup $P2_1$. The structure is closely related to that of $K(RE)P_2Se_6$ (RE = Y, Gd)[54] and isomorphous to β-KMP_2Se_6 (M = Sb, Bi)[49] and $KBiP_2S_6$.[31] The structure is composed of $[Bi(P_2S_6)]^{1-}$ layers separated by Tl^+ cations, Figure 3-8.

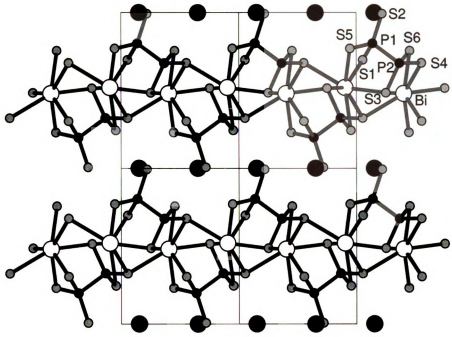

Figure 3-8. The structure of $TlBiP_2S_6$ [III] viewed down the (100) axis showing the lamellar stacking motif.

The Tl^+ ions are spherically coordinated by nine S atoms with an average Tl-S interaction of 3.35 Å, Figure 3-9A. The Bi^{3+} atoms are tris-chelated by a $[P_2S_6]^{4-}$ anion with Bi-Se distances ranging from 2.717(3) Å to 2.805(3) Å. A second $[P_2S_6]^{4-}$ anion is chelated to the Bi^{3+} cation with Bi-S bond distances of 2.741(3) Å and 3.114(3) Å. Two other $[P_2S_6]^{4-}$ anions are chelated to the Bi^{3+} cation with Bi-S distances of 3.125(3), Figure 3-8B. The P-P distance is 2.221(4) Å.

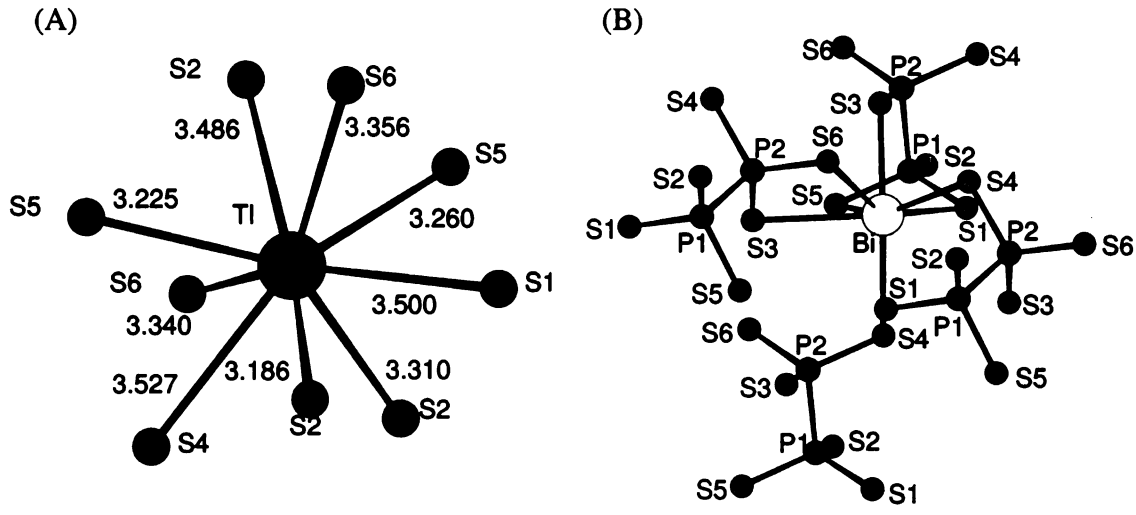

Figure 3-9. (A) the Tl^{+} coordination environment, and (B) the coordination environment of Bi^{3+} in $TlBiP_2Se_6$ [III].

Table 3-9 contains selected bond lengths and angles for compound [III]. The difference between the Se-containing compounds (i.e. [I] and [II]), and compound [III] is that in the former, the Bi^{3+} ions undulate in a direction perpendicular to the chain between two different positions down the length of the chain, so that when the chains assemble they form a slab that has the thickness of two $[P_2Se_6]^{4-}$ capped Bi^{3+} ions. In compound [III], the Bi^{3+} ions do not undulate, and therefore the resulting slab is only one Bi^{3+} coordination environment thick.

Table 3-9. Selected bond lengths and angles for $TlBiP_2S_6$ with bond lengths (Å) and angles (°) with standard uncertainties in parenthesis.

Tl—$S2^{i}$	3.186(3)	S1—Bi—S3	84.78(10)
Tl—S5	3.225(3)	S1—Bi—$S5^{vii}$	72.88(9)
Tl—$S5^{ii}$	3.261(3)	S3—Bi—$S5^{vii}$	81.06(9)
Tl—S2	3.310(3)	S1—Bi—$S4^{v}$	81.34(9)
Tl—$S6^{iii}$	3.340(3)	S3—Bi—$S4^{v}$	76.90(9)
Tl—$S6^{iv}$	3.356(3)	$S5^{vii}$—Bi—$S4^{v}$	147.35(9)
Tl—$S2^{v}$	3.486(3)	S1—Bi—S6	145.26(9)
Tl—$S1^{vi}$	3.499(3)	S3—Bi—S6	67.85(8)

Table 3-9 continued

Tl—S4	3.527(3)	$S5^{vii}$—Bi—S6	120.66(8)
		$S4^{v}$—Bi—S6	72.17(8)
Bi—S1	2.717(3)	S1—Bi—$S4^{vii}$	81.08(9)
Bi—S3	2.741(3)	S3—Bi—$S4^{vii}$	157.26(8)
Bi—$S5^{vii}$	2.805(3)	$S5^{vii}$—Bi—$S4^{vii}$	77.82(8)
Bi—$S4^{v}$	2.895(3)	$S4^{v}$—Bi—$S4^{vii}$	118.04(6)
Bi—S6	3.114(3)	S6—Bi—$S4^{vii}$	131.19(8)
Bi—$S4^{vii}$	3.125(3)		
		$S2^{v}$—P1—$S5^{ii}$	116.26(19)
P1—$S2^{v}$	1.967(4)	$S2^{v}$—P1—$S1^{x}$	118.5(2)
P1—$S5^{ii}$	2.038(4)	$S5^{ii}$—P1—$S1^{x}$	106.4(2)
P1—$S1^{x}$	2.060(4)	$S6^{iv}$—P2—$S4^{v}$	114.09(18)
P2—$S6^{iv}$	2.003(4)	$S6^{iv}$—P2—$S3^{x}$	112.0(2)
P2—$S4^{v}$	2.035(4)	$S4^{v}$—P2—$S3^{x}$	112.21(19)
P2—$S3^{x}$	2.062(4)		
		$S2^{v}$—P1—P2	109.6(2)
P1—P2	2.221(4)	$S5^{ii}$—P1—P2	101.59(18)
		$S1^{x}$—P1—P2	102.35(18)
		$S6^{iv}$—P2—P1	108.37(17)
		$S4^{v}$—P2—P1	105.52(19)
		$S3^{x}$—P2—P1	103.80(16)

(i) 1-x, 0.5+y, -z; (ii) -x, -0.5+y, -z; (iii) -1-x, -0.5+y, -z; (iv) 1+x, y, z; (v) -x, 0.5+y, -z; (vi) -x, -0.5+y, -1-z; (vii) -1+x, y, -1+z; (viii) -1+x, y, z; (ix) -1-x, 0.5+y, -1-z; (x) -1-x, -0.5+y, -1-z; (xi) -x, 0.5+y, -1-z; (xii) 1-x, -0.5+y, -z; (xiii) x, -1+y, z; (xiv) -1-x, 0.5+y, -z; (xv) 1+x, y, 1+z.

$Tl_3Bi_3(PS_4)_4$ [IV]: $Tl_3Bi_3(PS_4)_4$ [IV] crystallizes in the monoclinic space group $P2_1/c$. Crystal twinning in a merohedral fashion was a major difficulty in solving and refining the structure. Data sets on several crystals were collected but could not be successfully refined as large residual electron densities remained. Careful examination of the reciprocal lattice revealed a second twin domain rotated 180° along the a-axis. When the corresponding twin law of

$$\begin{bmatrix} a' \\ b' \\ c' \end{bmatrix} = \begin{bmatrix} 1 & 0 & 0 \\ 0 & -1 & 0 \\ -1 & 0 & -1 \end{bmatrix} \cdot \begin{bmatrix} a \\ b \\ c \end{bmatrix} \quad (1)$$

was applied, the R-value dropped from 28% to 5%. This led to small residuals in the electron density map and with a twin fraction of 43.2(1)%.

The 3-dimensional structure of the compound can be seen as an assembly of $[Bi_3(PS_4)_4]^{3-}$ slabs stacked along the b-axis, Figure 3-10A. The slabs are interconnected with Bi-S bonds and form channels in each direction which are occupied by Tl atoms.

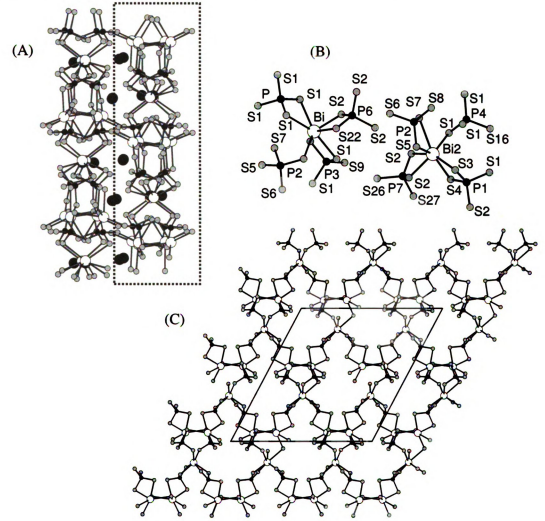

Figure 3-10. (A) $Tl_3Bi_3(PS_4)_4$ [IV] viewed down the *a*-axis showing the stacking of the $Tl_3Bi_3(PS_4)_4$ along the *b*-axis with a slab emphasized by rectangular outline, (B) an individual slab of $Tl_3Bi_3(PS_4)_4$ as viewed down the *c*-axis showing the empty channels for the Tl^+ ions and (C) the coordination environments of Bi(1) and Bi(2).

The $Tl_3Bi_3(PS_4)_4$ slabs consist of trigonal prismatic and square pyramidal Bi^{3+} atoms and $[PS_4]^{3-}$ anions, Figure 3-10C. Each trigonal prismatic Bi^{3+} atom (Bi(1) and Bi(2)) is surrounded by four $[PS_4]^{3-}$ anions forming a cross-shaped Bi-$(PS_4)_4$ unit. These units are connected with the trigonal prismatic Bi^{3+} atoms (Bi(3), Bi(4), Bi(5) and Bi(6)), to form the slab. Bi(1) and Bi(2) are coordinated by six S atoms to form a distorted trigonal prism Figure 3-10D. The geometry is distorted because of the stereochemically active $6s^2$ lone pair of Bi^{3+}. Two $[PS_4]^{3-}$ tetrahedra share one edge with the rectangular planes of the trigonal prism and the other two $[PS_4]^{3-}$ anions share a corner with the two remaining vertices of the prism. All four $[PS_4]^{3-}$ anions share one edge with the square pyramidal BiS_5 units Bi(3), Bi(4), Bi(5) and Bi(6). The remaining S atoms of the two corner shared $[PS_4]^{3-}$ units on the pyramid are attached on two BiS_5 units of a different slab.

The Bi-S distances in the trigonal prism vary from 2.709(5) Å to 2.922(4) Å for Bi(1) and 2.791(5) Å to 2.883(5) Å for Bi(2). The four equatorial bonds in the BiS_5 units range from 2.768(4) Å to 2.996(5) Å and the shorter axial distance from 2.627(5) Å to 2.706(4) Å. The P-S distances in all $[PS_4]^{3-}$ units range from 2.007(6) Å to 2.064(6) Å.

The coordination number of Tl^+ ions varies from six up to eight S atoms, Figure 3-10. In particular, Tl(1) is surrounded by eight S atoms forming a distorted dodecahedron with Tl-S distances from 3.159(5) Å to 3.698(5) Å, Figure 3-9A. The Tl(1) dodecahedron shares a corner through the bridging S(29) atom with the six coordinate Tl(2) center. The distances in this octahedron vary from 3.071(5) Å to 3.585(5) Å, Figure 3-10B. A corner of the distorted $Tl(2)S_6$ octahedron is shared with the seven-coordinate

Tl(3) which has Tl-S distances from 3.084(5) Å to 3.507(5) Å, Fig 11C. Tl(4), Tl(5) and Tl(6) are located in a different channel from the other Tl atoms. Tl(4) is surrounded by eight S atoms with distances from 3.153(6) Å to 3.772(6) Å, Fig 11D. Tl(5) and Tl(6) are six coordinated with one corner shared S(20) atom and Tl-S distances in the range of 3.085(4) Å to 3.717(5) Å, Figure 3-9E, and 3-9F, respectively. Selected bond lengths and angles for compound [IV] are given in Table 3-10.

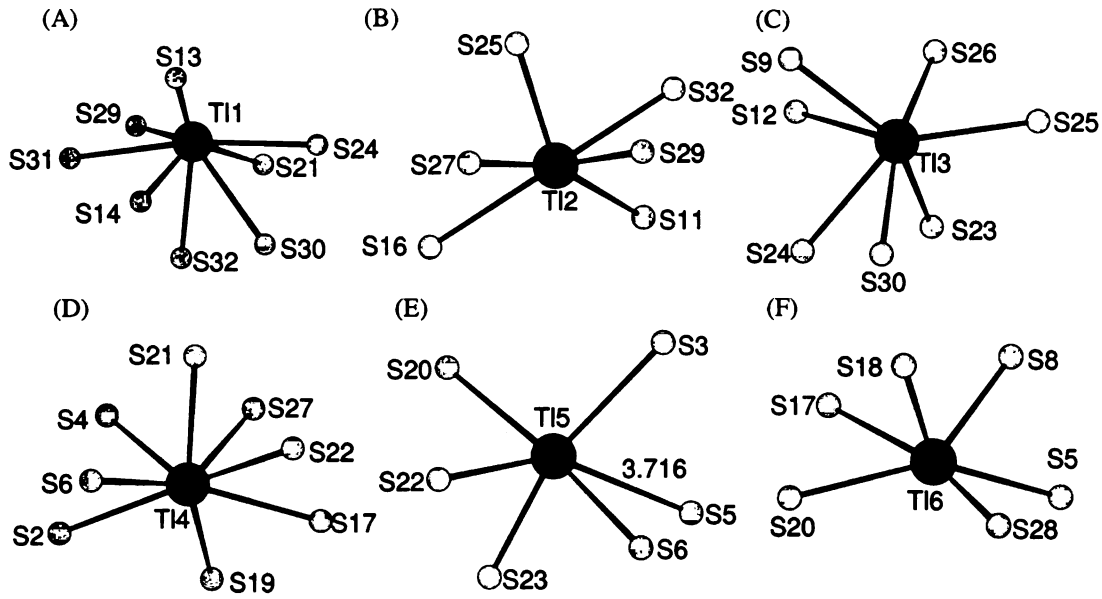

Figure 3-11. The coordination environments of the crystallographically unique Tl^+ ions in $Tl_3Bi_3(PS_4)_4$ [IV].

Table 3-10. Selected bond lengths and angles for $Tl_3Bi_3(PS_4)_4$ with bond lengths (Å) and angles (º) with standard uncertainties in parenthesis.

Bi1—S31^{i}	2.792(6)	S31^{i}—Bi1—S23	81.2(2)
Bi1—S23	2.816(6)	S31^{i}—Bi1—S32^{i}	71.59(16)
Bi1—S32^{i}	2.831(6)	S23—Bi1—S32^{i}	114.29(17)
Bi1—S21	2.855(5)	S31^{i}—Bi1—S21	130.47(17)
Bi1—S7^{i}	2.875(5)	S23—Bi1—S21	70.65(15)
Bi1—S10	2.887(5)	S32^{i}—Bi1—S21	83.77(17)
Bi1—S11^{i}	3.101(6)	S31^{i}—Bi1—S7^{i}	72.63(15)
Bi2—S27^{i}	2.711(6)	S23—Bi1—S7^{i}	81.47(16)
Bi2—S18	2.776(6)	S32^{i}—Bi1—S7^{i}	137.63(17)
Bi2—S26	2.817(5)	S21—Bi1—S7^{i}	137.76(17)
Bi2—S17	2.875(5)	S31^{i}—Bi1—S10	147.2(2)
Bi2—S15^{i}	2.911(5)	S23—Bi1—S10	131.56(18)
Bi2—S1^{iv}	2.918(5)	S32^{i}—Bi1—S10	91.88(16)
Bi3—S19^{viii}	2.703(5)	S21—Bi1—S10	72.84(14)
Bi3—S20^{v}	2.767(5)	S7^{i}—Bi1—S10	106.57(14)
Bi3—S2	2.845(5)	S31^{i}—Bi1—S11^{i}	80.84(19)
Bi3—S6	2.877(5)	S23—Bi1—S11^{i}	155.09(15)
Bi3—S8^{ii}	2.905(5)	S32^{i}—Bi1—S11^{i}	75.83(15)
Bi3—S1	3.050(5)	S21—Bi1—S11^{i}	134.22(14)
Bi3—S12^{ii}	3.130(5)	S7^{i}—Bi1—S11^{i}	76.77(15)
Bi4—S24^{ii}	2.667(5)	S10—Bi1—S11^{i}	67.46(15)
Bi4—S11	2.820(5)	S27^{i}—Bi2—S18	106.13(18)
Bi4—S12^{ii}	2.850(5)	S27^{i}—Bi2—S26	72.87(15)
Bi4—S22	2.894(5)	S18—Bi2—S26	87.6(2)
Bi4—S13^{ii}	2.943(6)	S27^{i}—Bi2—S17	79.90(17)
Bi4—S8^{ii}	3.007(5)	S18—Bi2—S17	70.37(16)
Bi4—S15	3.104(5)	S26—Bi2—S17	138.48(16)
Bi5—S30^{ii}	2.687(6)	S27^{i}—Bi2—S15^{i}	103.00(17)
Bi5—S14^{ii}	2.819(5)	S18—Bi2—S15^{i}	124.39(19)
Bi5—S16	2.820(5)	S26—Bi2—S15^{i}	146.60(18)
Bi5—S29^{ii}	2.891(6)	S17—Bi2—S15^{i}	69.55(14)
Bi5—S9^{xi}	2.921(6)	S27^{i}—Bi2—S1^{iv}	139.15(16)
Bi5—S10^{xii}	3.035(5)	S18—Bi2—S1^{iv}	87.17(16)
Bi6—S28^{xiv}	2.634(6)	S26—Bi2—S1^{iv}	69.23(14)
Bi6—S3	2.764(5)	S17—Bi2—S1^{iv}	140.20(16)
Bi6—S4^{i}	2.829(5)	S15^{i}—Bi2—S1^{iv}	100.24(14)
Bi6—S5	2.892(5)	S19^{viii}—Bi3—S20^{v}	73.92(16)
Bi6—S25^{i}	3.000(6)	S19^{viii}—Bi3—S2	78.81(16)
Bi6—S7^{i}	3.023(5)	S20^{v}—Bi3—S2	111.18(19)
Bi6—S14	3.123(6)	S19^{viii}—Bi3—S6	85.91(18)
		S20^{v}—Bi3—S6	149.20(17)
Tl1—S32^{i}	3.150(6)	S2—Bi3—S6	86.68(17)
Tl1—S24^{ii}	3.265(6)	S19^{viii}—Bi3—S8^{ii}	76.74(15)

Table 3-10 continued

Tl1—S31^{xiii}	3.273(7)	S20^{v}—Bi3—S8^{ii}	82.25(17)
Tl1—S13^{iii}	3.291(6)	S2—Bi3—S8^{ii}	147.39(15)
Tl1—S21	3.348(6)	S6—Bi3—S8^{ii}	70.42(14)
Tl1—S14^{iii}	3.364(6)	S19^{viii}—Bi3—S1	128.11(15)
Tl1—S29^{xi}	3.603(6)	S20^{v}—Bi3—S1	82.67(15)
Tl1—S30^{iii}	3.699(7)	S2—Bi3—S1	67.49(15)
Tl2—S29^{iii}	3.071(6)	S6—Bi3—S1	128.03(15)
Tl2—S25^{xiii}	3.132(6)	S8^{ii}—Bi3—S1	145.10(14)
Tl2—S32^{i}	3.284(6)	S19^{viii}—Bi3—S12^{ii}	136.28(14)
Tl2—S27^{xv}	3.380(7)	S20^{v}—Bi3—S12^{ii}	72.28(15)
Tl2—S16^{xv}	3.482(5)	S2—Bi3—S12^{ii}	139.72(14)
Tl2—S11^{i}	3.587(6)	S6—Bi3—S12^{ii}	110.65(16)
Tl2—Tl3^{iii}	3.883(2)	S8^{ii}—Bi3—S12^{ii}	71.97(13)
Tl2—Tl1^{xv}	4.192(2)	S1—Bi3—S12^{ii}	73.49(13)
Tl3—S23	3.081(6)	S30^{ii}—Bi5—S14^{ii}	80.53(19)
Tl3—S30^{iii}	3.239(7)	S30^{ii}—Bi5—S16	89.65(18)
Tl3—S9	3.257(6)	S14^{ii}—Bi5—S16	71.26(15)
Tl3—S26^{xvi}	3.287(7)	S30^{ii}—Bi5—S29^{ii}	71.70(16)
Tl3—S12^{ii}	3.350(5)	S14^{ii}—Bi5—S29^{ii}	84.85(16)
Tl3—S25^{i}	3.411(5)	S16—Bi5—S29^{ii}	151.97(16)
Tl3—S24^{ii}	3.508(6)	S30^{ii}—Bi5—S9^{xi}	75.09(18)
Tl4—S19	3.153(6)	S14^{ii}—Bi5—S9^{xi}	141.66(16)
Tl4—S27^{xv}	3.305(6)	S16—Bi5—S9^{xi}	79.38(17)
Tl4—S17^{v}	3.313(6)	S29^{ii}—Bi5—S9^{xi}	114.07(19)
Tl4—S2^{ix}	3.355(6)	S30^{ii}—Bi5—S10^{xii}	116.23(19)
Tl4—S21^{xv}	3.363(6)	S14^{ii}—Bi5—S10^{xii}	151.43(16)
Tl4—S4^{xiii}	3.372(5)	S16—Bi5—S10^{xii}	128.24(14)
Tl4—S22^{xv}	3.551(6)	S29^{ii}—Bi5—S10^{xii}	79.52(15)
Tl4—S6^{ix}	3.720(5)	S9^{xi}—Bi5—S10^{xii}	66.91(15)
Tl4—S2^{xvii}	3.918(6)	S24^{ii}—Bi4—S11	85.80(16)
Tl5—S23^{i}	3.130(8)	S24^{ii}—Bi4—S12^{ii}	80.10(16)
Tl5—S6^{xviii}	3.254(6)	S11—Bi4—S12^{ii}	71.53(14)
Tl5—S22^{i}	3.363(7)	S24^{ii}—Bi4—S22	73.39(16)
Tl5—S20^{xix}	3.384(6)	S11—Bi4—S22	147.37(17)
Tl5—Tl6^{xx}	3.646(2)	S12^{ii}—Bi4—S22	80.18(16)
Tl5—S3^{xxi}	3.667(6)	S24^{ii}—Bi4—S13^{ii}	76.10(17)
Tl5—S5^{i}	3.717(7)	S11—Bi4—S13^{ii}	81.60(16)
Tl5—P6^{i}	3.872(6)	S12^{ii}—Bi4—S13^{ii}	145.15(16)
Tl5—S28^{xxii}	4.072(8)	S22—Bi4—S13^{ii}	116.03(19)
Tl6—S8^{ii}	3.089(5)	S24^{ii}—Bi4—S8^{ii}	140.93(14)
Tl6—S18^{vi}	3.128(6)	S11—Bi4—S8^{ii}	112.93(15)
Tl6—S17^{ii}	3.178(6)	S12^{ii}—Bi4—S8^{ii}	74.59(14)
Tl6—S28^{x}	3.209(6)	S22—Bi4—S8^{ii}	73.33(15)

Table 3-10 continued

Tl6—S5^{ii}	3.280(6)	S13^{ii}—Bi4—S8^{ii}	138.07(15)
Tl6—S20^{xxiii}	3.382(5)	S24^{ii}—Bi4—S15	122.32(17)
Tl6—S3^{ii}	3.927(6)	S11—Bi4—S15	127.44(15)
		S12^{ii}—Bi4—S15	148.21(15)
S1—P1	2.019(7)	S22—Bi4—S15	85.17(16)
S2—P1	2.033(7)	S13^{ii}—Bi4—S15	66.55(15)
S3—P1^{iv}	2.044(7)	S8^{ii}—Bi4—S15	74.22(14)
S4—P1^{xi}	2.056(6)	S28^{xiv}—Bi6—S3	95.0(2)
S5—P2	2.024(7)	S28^{xiv}—Bi6—S4^{i}	84.23(19)
S6—P2^{ii}	2.044(7)	S3—Bi6—S4^{i}	72.01(15)
S7—P2^{ii}	2.056(8)	S28^{xiv}—Bi6—S5	75.78(17)
S8—P2	2.057(7)	S3—Bi6—S5	79.46(16)
S9—P3^{ii}	2.001(7)	S4^{i}—Bi6—S5	143.39(15)
S10—P3	2.046(8)	S28^{xiv}—Bi6—S25^{i}	70.90(18)
S11—P3^{ii}	2.051(7)	S3—Bi6—S25^{i}	151.65(17)
S12—P3	2.061(7)	S4^{i}—Bi6—S25^{i}	81.94(15)
S13—P4	2.020(8)	S5—Bi6—S25^{i}	118.48(16)
S14—P4	2.039(7)	S28^{xiv}—Bi6—S7^{i}	113.8(2)
S15—P4^{ii}	2.044(8)	S3—Bi6—S7^{i}	128.03(16)
S16—P4^{ii}	2.065(7)	S4^{i}—Bi6—S7^{i}	148.42(15)
S17—P5^{v}	2.037(7)	S5—Bi6—S7^{i}	68.14(14)
S18—P5^{v}	2.046(7)	S25^{i}—Bi6—S7^{i}	80.28(15)
S19—P5	2.045(7)	S28^{xiv}—Bi6—S14	136.21(16)
S20—P5^{xxv}	2.042(8)	S3—Bi6—S14	116.33(17)
S21—P6	2.012(7)	S4^{i}—Bi6—S14	78.03(14)
S22—P6	2.016(8)	S5—Bi6—S14	136.57(14)
S23—P6	2.047(7)	S25^{i}—Bi6—S14	67.19(14)
S24—P6^{i}	2.080(7)	S7^{i}—Bi6—S14	71.08(14)
S25—P7	1.998(8)		
S26—P7^{xxviii}	2.030(7)		
S27—P7^{xxii}	2.059(7)		
S28—P7^{xxii}	2.074(8)		
S29—P8	2.015(8)		
S30—P8	2.042(8)		
S31—P8^{ix}	2.047(7)		
S32—P8^{ix}	2.061(7)		

(i) x, -1.5-y, 0.5+z; (ii) x, -1.5-y, -0.5+z; (iii) 1-x, -0.5+y, 0.5-z; (iv) x, -0.5-y, 0.5+z; (v) 1-x, -1-y, 1-z; (vi) 2-x, -1-y, 1-z; (vii) 2-x, 0.5+y, 1.5-z; (viii) 1+x, y, z; (ix) 1-x, -1-y, -z; (x) 2-x, 0.5+y, 0.5-z; (xi) x, -1+y, z; (xii) x, -2.5-y, -0.5+z; (xiii) 1-x, -2-y, -z; (xiv) x, 1+y, z; (xv) 1-x, 0.5+y, 0.5-z; (xvi) x, -0.5-y, -0.5+z; (xvii) -1+x, y, z; (xviii) x, y, 1+z; (xix) 1-x, -0.5+y, 1.5-z; (xx) 2-x, -2-y, 1-z; (xxi) 2-x, -0.5+y, 1.5-z; (xxii) x, -2.5-y, 0.5+z; (xxiii) 1+x, -1.5-y, -0.5+z; (xxiv) x, y, -1+z; (xxv) -x, -1-y, 1-z; (xxvi) -1+x, -1.5-y, 0.5+z; (xxvii) 1-x, 0.5+y, 1.5-z; (xxviii) x, 1+y, 1+z; (xxix) 2-x, -0.5+y, 0.5-z; (xxx) -1+x, -1.5-y, -0.5+z; (xxxi) x, -1+y, -1+z; (xxxii) 2-x, -2-y, -z

$TlBiP_2S_7$ [V]: $TlBiP_2S_7$ crystallizes in the monoclinic spacegroup $P2_1/c$ and is isomorphous to $KBiP_2S_7$.[32] The structure is composed of corrugated $[BiP_2S_7]^{1-}$ layers, Figure 3-12, separated by 8-coordinate Tl^+ with an average Tl-S distance of 3.34 Å, Figure 3-13A. Each Bi^{3+} ion is bis-chelated to three $[P_2S_7]^{4-}$ anions (average Bi-Se bond lengths of 2.92 Å) and chelated by another $[P_2S_7]^{4-}$ anion (Bi-S bond length of 2.778(2) Å, Figure 3-12B. Table 3-11 contains selected bond lengths and angles for compound [V].

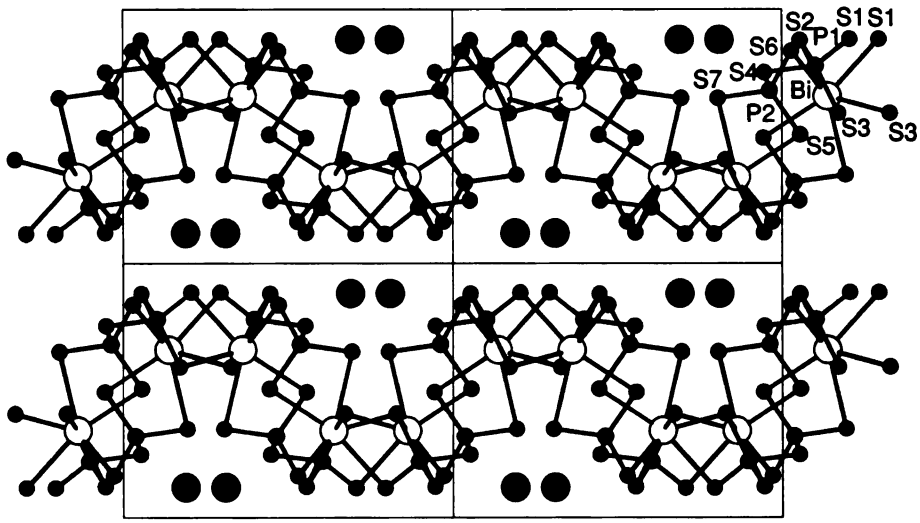

Figure 3-12. The structure of $TlBiP_2S_7$ [V] viewed down the (001) axis showing the corrugated lamellar packing.

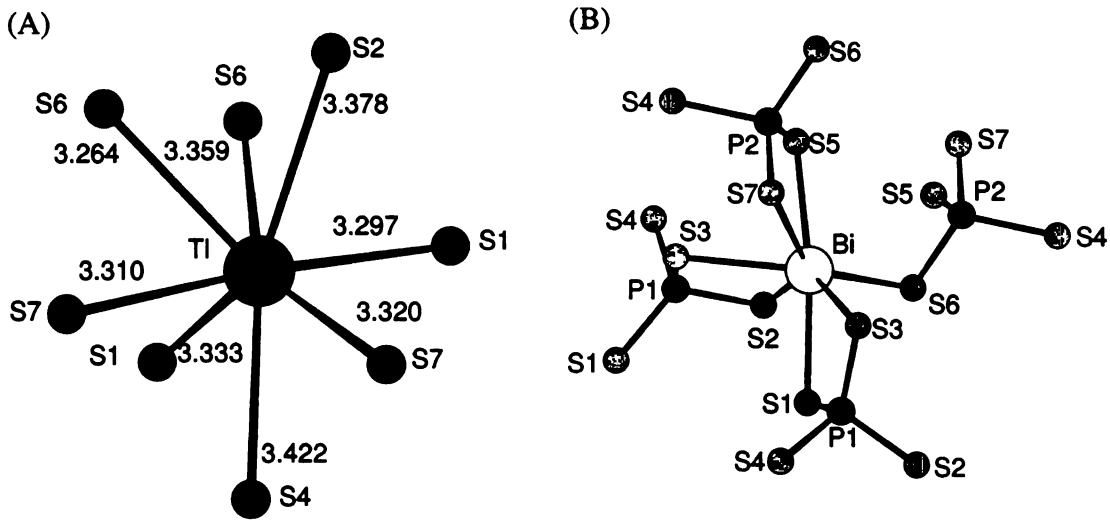

Figure 3-13. (A) The Tl^{+} coordination environment. Tl atom is green. (B) the coordination environment of Bi^{3+} in $TlBiP_2S_7$ [V].

Table 3-11. Selected bond lengths and angles for α-$TlBiP_2S_7$ with bond lengths (Å) and angles (°) with standard uncertainties in parenthesis.

Bi—S6	2.7780(18)	S6—Bi—S2	74.63(5)
Bi—S2	2.8238(18)	S6—Bi—S1	82.05(5)
Bi—S1	2.8752(19)	S2—Bi—S1	72.53(5)
Bi—$S3^{i}$	2.9124(18)	S6—Bi—$S3^{i}$	144.34(5)
Bi—S5	2.9156(18)	S2—Bi—$S3^{i}$	70.59(5)
Bi—S3	2.9778(18)	S1—Bi—$S3^{i}$	94.72(5)
Bi—S7	3.0376(19)	S6—Bi—S5	93.42(5)
		S2—Bi—S5	89.24(5)
Tl—$S6^{vi}$	3.2640(19)	S1—Bi—S5	161.77(5)
Tl—$S1^{vii}$	3.2973(18)	$S3^{i}$—Bi—S5	78.65(5)
Tl—$S7^{i}$	3.3099(18)	S6—Bi—S3	98.15(5)
Tl—S7	3.3202(19)	S2—Bi—S3	140.53(5)
Tl—$S1^{viii}$	3.3330(19)	S1—Bi—S3	68.03(5)
Tl—$S6^{viii}$	3.3589(19)	$S3^{i}$—Bi—S3	113.61(4)
Tl—$S2^{vi}$	3.3784(19)	S5—Bi—S3	130.19(5)
Tl—S4	3.4224(18)	S6—Bi—S7	138.27(5)
Tl—$S2^{vii}$	3.960(2)	S2—Bi—S7	139.31(5)
		S1—Bi—S7	124.82(5)
P1—$S1^{ii}$	2.019(2)	$S3^{i}$—Bi—S7	71.41(5)
P1—$S3^{ii}$	2.022(3)	S5—Bi—S7	69.47(5)
P1—$S2^{ix}$	2.028(2)	S3—Bi—S7	69.92(5)
P1—S4	2.118(2)		
P2—S7	2.009(2)	$S1^{ii}$—P1—$S3^{ii}$	108.31(11)
P2—S5	2.019(3)	$S1^{ii}$—P1—$S2^{ix}$	116.52(12)
P2—$S6^{xii}$	2.037(2)	$S3^{ii}$—P1—$S2^{ix}$	109.89(10)
P2—S4	2.118(2)	$S1^{ii}$—P1—S4	111.82(10)
		$S3^{ii}$—P1—S4	112.05(11)
		$S2^{ix}$—P1—S4	98.04(10)
		S7—P2—S5	114.80(11)
		S7—P2—$S6^{xii}$	110.52(11)
		S5—P2—$S6^{xii}$	109.84(11)
		S7—P2—S4	100.26(10)
		S5—P2—S4	111.5(1)
		$S6^{xii}$—P2—S4	109.53(11)

(i) x, 0.5-y, 0.5+z; (ii) 1-x, 0.5+y, 0.5-z; (iii) -1+x, 0.5-y, -0.5+z; (iv) -1+x, y, z; (v) x, 0.5-y, -0.5+z; (vi) 1-x, -0.5+y, 0.5-z; (vii) 1+x, y, z; (viii) 1+x, 0.5-y, 0.5+z; (ix) 1-x, 1-y, 1-z; (x) 2-x, 1-y, 1-z; (xi) 2-x, 0.5+y, 0.5-z; (xii) 1-x, 1-y, -z.

$Tl_3Bi(PS_4)_2$ [VI]: This compound is isotypic to $K_3Bi(PS_4)_2$. The structure solution revealed the same straight $[Bi(PS_4)_2]^{3-}$ chains as in the K-analog, Fig 3-14A.

Furthermore, comparison of the powder X-ray diffraction patterns with simulated ones from the known K^+ containing phase as well as the solutions discussed here suggested that the compounds were nearly identical. The chains, however, exhibited position disorder in the Bi^{3+} atoms, which were separated from each other along the chain axis by a distance of approximately 0.85 Å, Figure 3-14B.

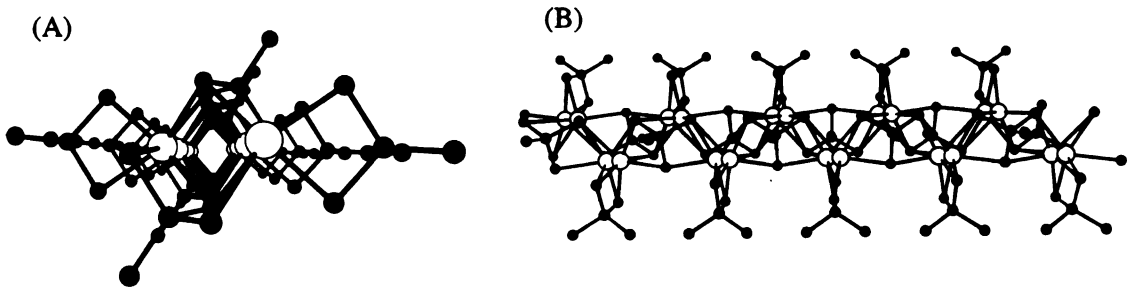

Figure 3-14. (A) The $[Bi(PS_4)_2]^{3-}$ chain that runs down the *b*-axis and (B) perpendicular to the *b*-axis showing the Bi^{3+} positional disorder. Bi atoms in white, phosphorous and sulfur atoms in black and shaded, respectively.

Optical Properties

Diffuse reflectance measurements suggest that the optical band gaps of the title compounds are smaller than those of the K^+ analogs. The spectrum of α-$TlBiP_2Se_6$ [I] indicated that the band gap was about 1.23 eV, Figure 3-15A, whereas α-$KBiP_2Se_6$ was reported to have a band gap of 1.61 eV.[52,53] The average Tl-Se distance in the former was 3.38 Å whereas the average K-Se distance in the latter was 3.36 Å. The similarities in bond lengths is expected given that Tl^+ and K^+ have similar ionic radii (1.5 Å for Tl^+ vs. 1.4 Å for K^+).[55] The reduction in band gap in the Tl^+ analogs is therefore likely due to the increased covalency of the interaction between the metal and Se.

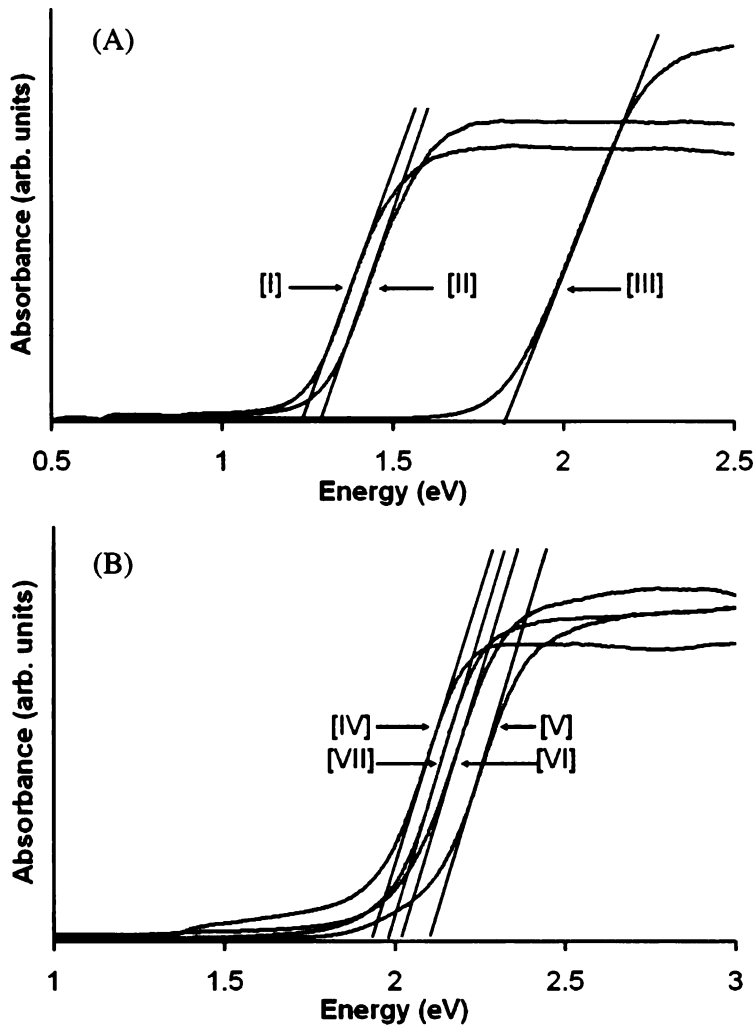

Figure 3-15. The optical absorption spectra showing energy band gaps of (A) α-$TlBiP_2Se_6$ [I]: 1.23 eV, β-$TlBiP_2Se_6$ [II]: 1.27 eV, and $TlBiP_2S_6$ [III]: 1.81 eV; and (B) $Tl_3Bi_3(PS_4)_4$ [IV]: 1.88 eV, $TlBiP_2S_7$ [V]: 1.87 eV, $Tl_3Bi(PS_4)_4$ [VI]: 1.87 eV, and $Tl_4Bi_2(P_2S_6)(PS_4)_2$ [VII]: 1.98 eV.

In most main group metal chalcogenides with semiconducting band gaps, the top of the valence band is dominated by chalcogen based filled p-orbitals, whereas the bottom of the conduction band is mainly based on empty p-orbitals of the main group metal.[37] The substitution of K for Tl in K/M/Q structures enhances the Tl-Q bonding through increased covalency which further broadens the bands near the energy gap causing it to shrink.[39]

It is not surprising that, given the similarity between the $[BiP_2Se_6]^{1-}$ frameworks in α-$TlBiP_2Se_6$ [I] and β-$TlBiP_2Se_6$ [II] and the similar Tl-Se bond lengths that the optical band gaps are also similar with showing an absorption edge at 1.27 eV. The band gap of $TlBiP_2S_6$ [III] is slightly larger at 1.81 eV as is expected upon the substitution of Se for S in structurally related compounds (i.e. containing a $[P_2Q_6]^{4-}$ anion), Figure 3-15A.

$TlBiP_2S_7$ [V] was determined to have an optical band gap of 1.87 eV, Figure 3-15B. The isomorphic analog of compound [V], $KBiP_2S_7$, was reported at 2.25 eV.[5] $Tl_3Bi_3(PS_4)_4$ [IV], $Tl_3Bi(PS_4)_2$ [VI] and $Tl_4Bi_2(PS_4)_2(P_2S_6)$ [VII] have optical band gaps of 1.88 eV, 1.98 eV and 1.97 eV.

Solid State NMR

Spectra are displayed in Figure 3-16, and Table 3-12 presents chemical shifts (CSs), line widths, integrated intensities, chemical shift anisotropies (CSAs), and longitudinal relaxation times (T_1s). The chemical shifts and chemical shift anisotropies of each of the reported thio- and selenophosphate materials are within the ranges expected for related materials.[48]

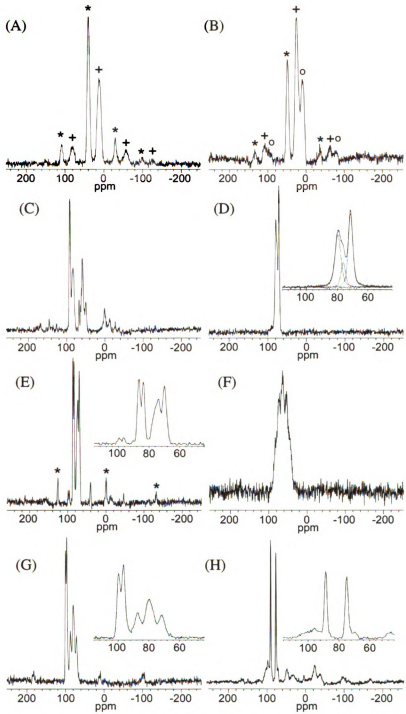

Figure 3-16. ^{31}P NMR spectra of (A) α-$TlBiP_2Se_6$ [I], (B) β-$TlBiP_2Se_6$ [II], (C) $TlBiP_2S_6$ [III], (D) $Tl_3Bi_3(PS_4)_4$ [IV], (E) $TlBiP_2S_7$ [V], (F) $Tl_3Bi(PS_4)_2$ [VI], (G) $Tl_4Bi_2(PS_4)_2(P_2S_6)$, and (H) $KBiP_2S_7$. Each spectrum was an average of four scans with a delay between pulses of 5000 s. Each spectrum was processed with ≤ 100 Hz line broadening. Peaks and their corresponding spinning sidebands are grouped with like symbols.

Table 3-12. ^{31}P chemical shift (CS), chemical shift anisotropy (CSA), and T_1 values of the Tl/Bi/P/Se and Tl/Bi/P/S compounds.

Compound	CS[a] (ppm)	Line Widths[a] (Hz)	Integrated Intensities [b]	CSA[c] (ppm)	T_1[d] (s)
α-$TlBiP_2Se_6$ [I]	40.0, 12.4	1060, 1640	100, 90	n.d.	n.d.
β-$TlBiP_2Se_6$ [II]	48.9, 24.7, 9.1	1000, 1390, 1650	53, 100, 68	n.d.	1500(150)
$Tl_3Bi_3(PS_4)_4$ [IV]	79.3, 75.8, 71.0	730, 500, 570	100, 30, 91	69	1500(100)
$TlBiP_2S_7$ [V]	85.2, 75.4	320, 860	67, 100	n.d.	1750(150)
$Tl_3Bi(PS_4)_2$ [VI]	79.9	1600	100	n.d.	1500(100)
$Tl_4Bi_2(PS_4)_2(P_2S_6)$ [VII]	98.2, 79.3	410, 800	91, 100	137, n.o.	1300(300)

n.d. = not determined, n.o. = not observable.

[a] Uncertainties in CS are approximately ± 0.5 ppm, and uncertainties in line widths are approximately ± 10 Hz. These parameters were determined by a mathematical deconvolution of the peak with equal contributions from Gaussian and Lorentzian line shapes.

[b] Intensities were normalized with the most intense peak set to 100. For compounds with splittings due to J-coupling, the integrated intensities of the constituent peaks were summed.

[c] Principal CSA values were determined using a Herzfeld-Berger analysis computer program (HBA 1.5, Eichele, K., Wasylishen, R.E., Dalhousie University and Universtät Tübingen, 2006). The reported CSA = $\delta_{11} - \delta_{33}$, i.e. the approximate overall width of the static CS powder pattern. Maximum CSA uncertainties are ± 20 ppm.

[d] Uncertainties are indicated in parenthesis.

Phosphorous-Thallium J-coupling: The spectrum of $TlBiP_2S_7$ [V] had two sets of peaks centered at 85.2 ppm and 72.4 ppm with splittings of 481 Hz and 783 Hz, respectively, Figure 3-16E. One possible cause of these splittings is two-bond P-Tl *J*-couplings and this hypothesis was tested using the isomorphic analog $KBiP_2S_7$.[5] The ^{31}P NMR spectrum of the analog contained two singlet peaks centered at 85.2 ppm and 75.4 ppm, Figure 3-16H, indicating that the splitting observed in the spectrum of [V] was due to P-Tl coupling. The ^{31}P atoms in the $[P_2S_7]^{4-}$ ion are crystallographically inequivalent and it is interesting that the P-Tl *J*-coupling is observed while the two-bond P-P *J*-coupling is not apparent. It was not possible to rationalize the spitting patterns based on numbers of equivalent and inequivalent Tl. ^{203}Tl (30% abundant) and ^{205}Tl (70% abundant) would resonate at 228.89 and 231.14 MHz in a 9.4 T magnet, respectively, and

distinct couplings to the different spin ½ Tl isotopes were not observed. In liquid state NMR studies of organophosphorous thallium compounds, distinct ^{31}P-^{203}Tl and ^{31}P-^{205}Tl couplings were also not observed.[56]

There was additional evidence for two-bond P-Tl *J*-coupling in the spectra of other title compounds. The 9.4 T NMR spectrum of $Tl_4Bi_2(PS_4)_2(P_2S_6)$ [VII] contained two peaks centered at 98.2 ppm with a 490 Hz splitting and three peaks centered at 79.3 ppm with neighboring peak splittings of 1390 Hz and 1180 Hz. At 7 T, the respective splittings were 510 Hz, 1390 Hz, and 1180 Hz. The constancy of the splitting magnitudes with respect to magnetic field is a marker of *J*-coupling. Similarly, at 9.4 T the NMR spectrum of $Tl_3Bi(PS_4)_2$ [VI] appeared to be a multiplet centered at 79.9 ppm with neighboring peak separations of ~1400 Hz, Figure 3-16F. At 7 T the same splitting magnitudes were observed.

The spectral line widths of the Tl-containing chalcophosphate materials are also relatively broad compared to the chalcophosphate materials that do not contain Tl.[40,57] For example, $KBiP_2S_7$ had a line width of 337 Hz, whereas some of the Tl-containing compounds had line widths greater than 1600 Hz. The increased line widths are likely due in part to unresolved P-Tl coupling.

To the best of our knowledge, this is the first example of P-Tl coupling observed in the solid state, although one bond P-Tl coupling in the liquid state has been observed. For example, coupling constants of 3203 and 3144 Hz were detected in spectra of $Ph_2P(Me_2Tl)_2PPh_2$.[56] To our knowledge, our work is also the first example of two-bond P-Tl *J*-coupling. Through-space *J*-coupling is also possible when there is significant overlap of the van der Waals radii of the coupled nuclei.[58] For the title compounds there

was not a good correlation between the magnitude of *J* and the distance between P and Tl which suggests that two-bond coupling is dominant. Comparison of these experimental *J*-couplings with *J*-couplings derived from electronic structure calculations may be one way to now validate the calculation method.

Splittings due to P-P *J*-coupling have been observed in compounds with directly bonded crystallographically inequivalent P-atoms.[40] Such splittings were a possibility in compounds [I] and [II], but they were not observed, likely because of the broad spectral line widths.

Peak Assignments: $Tl_4Bi_2(PS_4)_2(P_2S_6)$[39] [VII] provided an interesting example of a structure with both $[P_2S_6]^{4-}$ and $[PS_4]^{3-}$ anions. The chemical shift ranges of these two anions are known to be overlapped and differences in the CSA magnitudes for the two anions were used for chemical assignment. The NMR spectrum of [VII] showed two sets of peaks: a doublet centered at 98.2 ppm, and a triplet centered at 79.3 ppm, Figure 3-16G. The crystallographic structural solution contained two inequivalent P sites: one in the $[PS_4]^{3-}$ anion, and one in the $[P_2Se_6]^{4-}$ anion. Spinning sidebands were observed only for the doublet, and so the P atom corresponding to this site must have a larger magnitude CSA than the triplet. The magnitude of the CSA of $[PS_4]^{3-}$ has previously been shown to be significantly lower than that of $[P_2S_6]^{4-}$ anions,[40] so the triplet and doublet were therefore assigned to the $[PS_4]^{3-}$ and $[P_2S_6]^{4-}$ units, respectively.

Chemical shift assignment was also made for compounds with crystallographically inequivalent ^{31}P atoms that were in the same type of $[P_xQ_y]^{z-}$ anion. The spectrum of β-$TlBiP_2Se_6$ [II], showed three peaks with a ratio of integrated signal

intensity of about 1:2:1 with chemical shifts of 48.9, 24.7, and 9.1 ppm, Figure 3-16B. There were four crystallographically inequivalent P sites with some variation in the numbers of Bi^{3+} and Tl^{+} ions close to the $[P_2Se_6]^{4-}$ anions. These variations were correlated with the chemical shifts using the following scheme. For each P site, spheres of 4 Å diameter were considered around each of the bonded Se atoms and the total numbers of Bi^{3+} and Tl^{+} ions were counted within these spheres. The 4 Å diameter was a reasonable cutoff for defining proximate metal ions as the Se-metal ion distances formed two groups: one with 2.8 Å < $d_{Se\text{-}metal}$ < 4.0 Å and one with $d_{Se\text{-}metal}$ > 4.5 Å. Within these spheres P(1) and P(3) had three Bi^{3+} and three Tl^{+} ions, P(2) had four Bi^{3+} and two Tl^{+} ions, and P(4) had two Bi^{3+} and four Tl^{+} ions. The central NMR spectral peak can be attributed to P(1) and P(3) which have the same number of vicinal Bi^{3+} and Tl^{+} ions and the other distinct peaks can be attributed to P(2) and P(4). It is not possible using this method to determine the specific chemical shift that corresponds to each site. This model only groups ^{31}P sites by similarities in coordination and does not predict the magnitude or sign of the chemical shift differences.

$Tl_3Bi_3(PS_4)_4$ [IV] is another example of this approach to assignment. The NMR spectrum showed three peaks with the approximate intensity ratio of 4:1:3 and shifts of 79.3 ppm, 75.8 ppm, and 71.0 ppm, Figure 3-16D. A mathematical deconvolution of the spectrum was only successful when the feature furthest downfield was modeled by two closely spaced peaks.

There are eight inequivalent P sites and an assignment was made by grouping them into three distinct coordination environments using a scheme similar to that for compound [II]. However, only proximate Bi^{3+} ions were considered for compound [IV]

as the S-Tl distances had a more continuous distribution than was found for compound [II]. The P(1), P(3) and P(4) centered $[PS_4]^{3-}$ anions had four proximate Bi^{3+}ions, the P(2) centered $[PS_4]^{3-}$ ion had four proximate Bi^{3+} ions and the four remaining $[PS_4]^{3-}$ anions had two proximate Bi^{3+} ions. It is reasonable that the $[PS_4]^{3-}$ anions with similar coordination environments have the same chemical shifts and the ratio of the intensities can be explained on this basis.

The numbers of crystallographically inequivalent P atoms and the numbers of distinct shifts were equal for compounds [I] and [V], Figure 3-16A, E, respectively. Each peak in the NMR spectrum corresponds to one of these crystallographically inequivalent sites. Chemical shifts were not calculated and therefore specific peaks cannot at present be attributed to particular crystallographic sites. Impurity peaks and the lack of an accurate crystal structure precluded assignment in compounds [III] and [VI], respectively, Figure 3-16C, F.

CONCLUDING REMARKS

A broad family of compounds can be stabilized in the Tl/Bi/P/Q (Q=S,Se) system and contains examples of 1-, 2-, and 3-dimensional structural motifs. This high degree of structural diversity likely has its origins in the flexibility of the Bi^{3+} and Tl^{+} coordination environments, and also in the flexibility of the Tl-Q interaction with the covalent Bi/P/Q framework. The reaction chemistry of the Tl/Bi/P/S system proved to be more diverse and subtle than we originally expected, and small changes in stoichiometry resulted in different reaction paths and compounds. This explains why we often experience problems with reproducibility with some of the compounds we report here (e.g.

$Tl_3Bi_3(PS_4)_4$ vs. $TlBiP_2S_7$). One reason for this rich chemistry seems to be the ability of the thiophosphate anions to convert from one to another with small changes in P/S ratio. All three species $[PS_4]^{3-}$, $[P_2S_6]^{4-}$ and $[P_2S_7]^{4-}$ were observed as well as combinations thereof such as in $Tl_4Bi_2(PS_4)_2(P_2S_6)$.[39]

The corresponding selenium system was less diverse and $[PSe_4]^{3-}$ and $[P_2Se_7]^{4-}$ species were not observed. In selenophosphate chemistry, the most stable species under moderate Lewis basic conditions is the P^{4+} anion $[P_2Se_6]^{4-}$.[22] By slightly varying the stoichiometry of the reaction conditions, it is often possible to produce a given phase in pure form. Because of the increased ionicity, it may also be possible to tune the optical properties of these materials by making solid solutions with potassium. Such a study is also likely to yield new compounds. Similar richness and diversity might be observed in other Tl/M/P/Q systems perhaps with M = Sb, Au, In, Pd, Zn, Cd, Hg, and the Lanthanides.

^{31}P solid state NMR spectroscopy of the reported compounds demonstrates similar chemical shifts and chemical shift anisotropies to related materials.[40] It was possible to assign the peaks of inequivalent ^{31}P atoms from the same $[P_xQ_y]^{z-}$ anion type by considering differences in the metal ion coordination to the $[P_xQ_y]^{z-}$ unit and by considering CSA magnitudes. More specific assignment of peaks would require detailed calculations. Such calculations would be challenging because of the presence of numerous heavy atoms in the structures. Splittings due to P-Tl J-couplings were observed, and to the best of our knowledge, this is the first example of two bond P-Tl J-coupling and the first observation of P-Tl J-coupling in the solid state.

REFERENCES

1. Kanatzidis, M. G. *Chem. Mat.* **1990,** 2, 353-363.

2. Kanatzidis, M. G.; Park, Y. *J. Am. Chem. Soc.* **1989,** 111, 3767-3769.

3. Kanatzidis, M. G.; Park, Y. *Chem. Mat.* **1990,** 2, 99-101.

4. Park, Y. B.; Kanatzidis, M. G. *Angew. Chem. Int. Ed.* **1990,** 29, 914-915.

5. McCarthy, T. J.; Kanatzidis, M. G. *Inorg. Chem.* **1995,** 34, 1257-1267.

6. Chondroudis, K.; Kanatzidis, M. G. *J. Solid State Chem.* **1998,** 138, 321-328.

7. Iordanidis, L.; Bilc, D.; Mahanti, S. D.; Kanatzidis, M. G. *J. Am. Chem. Soc.* **2003,** 125, 13741-13752.

8. McCarthy, T. J.; Ngeyi, S. P.; Liao, J. H.; Degroot, D. C.; Hogan, T.; Kannewurf, C. R.; Kanatzidis, M. G. *Chem. Mat.* **1993,** 5, 331-340.

9. Iordanidis, L.; Brazis, P. W.; Kyratsi, T.; Ireland, J.; Lane, M.; Kannewurf, C. R.; Chen, W.; Dyck, J. S.; Uher, C.; Ghelani, N. A.; Hogan, T.; Kanatzidis, M. G. *Chem. Mat.* **2001,** 13, 622-633.

10. Iordanidis, L.; Schindler, J. L.; Kannewurf, C. R.; Kanatzidis, M. G. *J. Solid State Chem.* **1999,** 143, 151-162.

11. Kohatsu, I.; Wuensch, B. J. *Acta. Crystallogr. B* **1976,** 32, 2401-2409.

12. Cook, R.; Schafer, H. *Rev. Chim. Miner.* **1982,** 19, 19-27.

13. Wiegers, G. A.; Meetsma, A.; Vansmaalen, S.; Haange, R. J.; Wulff, J.; Zeinstra, T.; Deboer, J. L.; Kuypers, S.; Vantendeloo, G.; Vanlanduyt, J.; Amelinckx, S.; Meerschaut, A.; Rabu, P.; Rouxel, J. *Solid State Commun.* **1989,** 70, 409-413.

14. Mrotzek, A.; Kanatzidis, M. G. *Acc. Chem. Res* **2003,** 36, 111-119.

15. Kanatzidis, M. G. *Acc. Chem. Res* **2005,** 38, 359-368.

16. Makovicky, E. *Fortschr. Miner.* **1981,** 59, 137-190.

17. Makovicky, E. *Z. Kristall.* **1985,** 173, 1-23.

18. Makovicky, E. *Fortschr. Miner.* **1985,** 63, 45-89.

19. Makovicky, E. *Neues Jahrb. Mineral.-Abh.* **1989,** 160, 269-297.

20. Chung, I.; Do, J.; Canlas, C. G.; Weliky, D. P.; Kanatzidis, M. G. *Inorg. Chem.* **2004,** 43, 2762-2764.

21. Knaust, J. M.; Dorhout, P. K. *J. Chem. Crystallogr.* **2006,** 36, 217-223.

22. Kanatzidis, M. G. *Curr. Opin. Solid. St. M.* **1997,** 2, 139-149.

23. Coste, S.; Hanko, J.; Bujoli-Doeuff, M.; Louarn, G.; Evain, M.; Brec, R.; Alonso, B.; Jobic, S.; Kanatzidis, M. G. *J. Solid State Chem.* **2003,** 175, 133-145.

24. Manriquez, V.; Galdamez, A.; Ruiz-Leon, D. *Mater. Res. Bull.* **2006,** 41, 1337-1344.

25. Belkyal, I.; El Azhari, M.; Wu, Y. D.; Bensch, W.; Hesse, K. F.; Depmeier, W. *Solid State Sci.* **2006,** 8, 59-63.

26. Gieck, C.; Tremel, W. *Chem.-Eur. J.* **2002,** 8, 2980-2987.

27. Coste, S.; Kopnin, E.; Evain, M.; Jobic, S.; Brec, R.; Chondroudis, K.; Kanatzidis, M. G. *Solid State Sci.* **2002,** 4, 709-716.

28. Hess, R. F.; Gordon, P. L.; Tait, C. D.; Abney, K. D.; Dorhout, P. K. *J. Am. Chem. Soc.* **2002,** 124, 1327-1333.

29. Coste, S.; Kopnin, E.; Evain, M.; Jobic, S.; Payen, C.; Brec, R. *J. Solid State Chem.* **2001,** 162, 195-203.

30. McCarthy, T. J.; Kanatzidis, M. G. *Chem. Mat.* **1993,** 5, 1061-1063.

31. Manriquez, V.; Galdamez, A.; Leon, D. R.; Garland, M. T.; Jimenez, M. *Z. Krist. New Cryst. St.* **2003,** 218, 151-152.

32. McCarthy, T.; Kanatzidis, M. G. *J. Alloys Compd.* **1996,** 236, 70-85.

33. Chung, I.; Karst, A. L.; Weliky, D. P.; Kanatzidis, M. G. *Inorg. Chem.* **2006,** 45, 2785-2787.

34. Odoulov, S. G.; Shumelyuk, A. N.; Brost, G. A.; Magde, K. M. *Appl. Phys. Lett.* **1996,** 69, 3665-3667.

35. Shumelyuk, A.; Hryhorashchuk, A.; Odoulov, S. *Phys. Rev. A* **2005,** 72, 6.

36. Kroupa, J.; Tyagur, Y. I.; Grabar, A. A.; Vysochanskii, Y. M. *Ferroelectr.* **1999,** 223, 421-428.

37. Wachter, J. B.; Chrissafis, K.; Petkov, V.; Malliakas, C. D.; Bilc, D.; Kyratsi, T.; Paraskevopoulos, K. M.; Mahanti, S. D.; Torbrugge, T.; Eckert, H.; Kanatzidis, M. G. *J. Solid State Chem.* **2007,** 180, 420-431.

38. Iyer, R. G.; Aitken, J. A.; Kanatzidis, M. G. *Solid State Sci.* **2004,** 6, 451-459.

39. McGuire, M. A.; Reynolds, T. K.; DiSalvo, F. J. *Chem. Mat.* **2005,** 17, 2875-2884.

40. Canlas, C. G.; Kanatzidis, M. G.; Weliky, D. P. *Inorg. Chem.* **2003,** 42, 3399-3405.

41. Gunne, J.; Eckert, H. *Chem.-Eur. J.* **1998,** 4, 1762-1767.

42. *SMART, SAINT, SHELXTL V-5 and SADABS*, Bruker Analytical X-ray Instruments, Inc.: Madison, 1998.

43. *X-AREA, X-SHAPE, and X-RED*, STOE & Cie GmbH: Darmstadt, 2004.

44. Petricek, V.; Dusek, M.; Palatinus, L. *Jana2000. The Crystallographic Computing System*, Praha, Czech Republic, 2000.

45. Wendlandt, W. W.; Hecht, H. G. Reflectance spectroscopy; Interscience Publishers: New York, NY, 1966.

46. Kortüm, G. Reflectance spectroscopy. Principles, methods, applications; Springer: Berlin, Germany, 1969.

47. Tandon, S. P.; Gupta, J. P. *Phys. Status Solidi* **1970,** 38, 363-367.

48. Canlas, C. G.; Muthukumaran, R. B.; Kanatzidis, M. G.; Weliky, D. P. *Solid State Nucl. Magn. Reson.* **2003,** 24, 110-122.

49. Breshears, J. D.; Kanatzidis, M. G. *J. Am. Chem. Soc.* **2000,** 122, 7839-7840.

50. Kanatzidis, M. G.; Sutorik, A. C. *Progr. Inorg. Chem.* **1995,** 43, 151-265.

51. Gave, M.; Bilc, D.; Mahanti, S.; Breshears, J.; Kanatzidis, M. *Inorg. Chem.* **2005,** 5293-5303.

52. McCarthy, T. Ph.D. Thesis, Michigan State University, East Lansing, MI, 1994.

53. McCarthy, T. J.; Kanatzidis, M. G. *J. Chem. Soc. Chem. Commun.* **1994,** 1089-1090.

54. Chen, J. H.; Dorhout, P. K.; Ostenson, J. E. *Inorg. Chem.* **1996,** 35, 5627-5633.

55. Greenwood, N. N.; Earnshaw, A. Chemistry of the Elements; 2nd ed.; Butterworth-Heinemann: Boston, MA, 1997; pp 1176, 1205.

56. Walther, B.; Bauer, S. *J. Organomet. Chem.* **1977,** 142, 177-184.

57. Regelsky, G. Ph.D. Thesis, University of Munster, Munster, Germany, 2000.

58. Bryce, D. L.; Wasylishen, R. E. *J. Mol. Struct.* **2002,** 602, 463-472.

CHAPTER 4

IMPROVED RESOLUTION AND DETECTION OF ^{31}P-Tl *J*-COUPLINGS AT 21 T IN ^{31}P MAGIC ANGLE SPINNING NMR SPECTRA OF INORGANIC COMPOUNDS CONTAINING Tl/Bi/P/S.

INTRODUCTION

The first examples of phosphorous-thallium *J*-couplings in the solid state were recently reported for crystalline compounds containing Tl, Bi, P, and Q (Q = S or Se). The detection of these couplings was based on comparisons of ^{31}P magic angle spinning NMR spectra at 9.4 T and 7 T spectra and also on comparisons between ^{31}P NMR spectra of Tl- and non Tl-containing isomorphic analogues.[1] Figure 4-1 displays the structures of $Tl_4Bi_2(PS_4)_2(P_2S_6)$[2] and $TlBiP_2S_7$ which were two of the compounds in this class that exhibited these couplings.

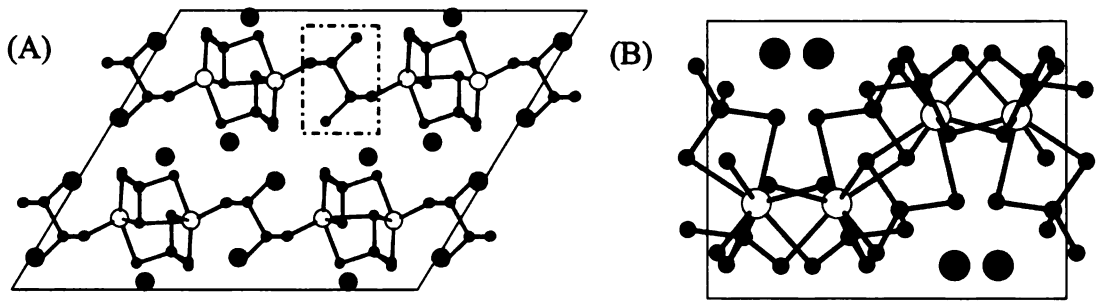

Figure 4-1. (A) The structure of $Tl_4Bi_2(PS_4)_2(P_2S_6)$ viewed down the *b*-axis. Large black spheres are Tl, large hollow spheres are Bi, small black spheres are P, and small shaded spheres are S. A $[P_2S_6]^{4-}$ anion is highlighted in a dashed box. Two Tl^+ ions have been removed so that the highlighted $[P_2S_6]^{4-}$ unit is more clearly displayed. Two of the Ss in this unit are not visible because they are directly behind displayed Ss. (B) The structure of $TlBiP_2S_7$ viewed down the *c*-axis. Large black spheres are Tl, large hollow spheres are Bi, small black spheres are P, and small shaded spheres are S. A single unit cell is shown for each structure.

The $Tl_4Bi_2(PS_4)_2(P_2S_6)$ compound contained $[P_2S_6]^{4-}$ and $[PS_4]^{3-}$ units linked together in layers by coordinating Bi^{3+} ions. These layers were separated by layers of Tl^+ ions. The $TlBiP_2S_7$ compound contained $[P_2S_7]^{4-}$ units linked together in two-dimensional layers by coordinating Bi^{3+} ions with Tl^+ ions between the layers. These structures demonstrated that the detected 500-1400 Hz splittings were due to two-bond P-

Tl couplings and such couplings were the first example of non-one-bond P-Tl couplings in either the liquid- or the solid-state.

Although there are seven known compounds containing Tl, Bi, P, and Q and eight known compounds containing K, Bi, P, and Q,[3-9] only β-$TlBiP_2Se_6$/β-$KBiP_2Se_6$ and $TlBiP_2S_7$/$KBiP_2S_7$ are structurally isomorphic. Although the crystal structure is not yet fully refined for $Tl_3Bi(PS_4)_2$,[9] this compound is likely structurally similar to $K_3Bi(PS_4)_2$.[4] It is somewhat surprising that there are only a few examples of structural isomorphism because Tl^+ and K^+ have similar ionic radii (i.e. 0.150 Å and 0.138 Å, respectively).[10] Electronic structure calculations might provide insight into why the simple replacement $K^+ \rightarrow Tl^+$ is infrequently observed in the absence of a significant geometric structural modification. Splittings due to P-Tl J-couplings may be useful experimental parameters to validate these calculations.

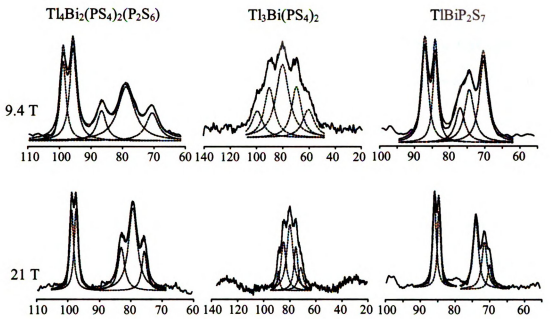

Figure 4-2. ^{31}P NMR spectra of $Tl_4Bi_2(PS_4)_2(P_2S_6)$, $Tl_3Bi(PS_4)_2$, and $TlBiP_2S_7$ obtained at 9.4 T and 21 T. The experimental spectra are represented by solid lines and the best-fit Lorentzian functions used to deconvolve the spectra are represented by dashed lines. The sums of the Lorentzians are also shown as dashed lines and fitted well to the corresponding experimental spectra.

Ultra-high field (21 T) NMR spectra of three thallium bismuth thiophosphates are reported, along with a comparison to the previously obtained 9.4 T spectra. Besides providing additional confirmation of the P-Tl J-couplings, the 21 T spectra offered a significant enhancement of chemical shift resolution over the spectra collected at lower field.

EXPERIMENTAL SECTION

The compounds $Tl_4Bi_2(PS_4)_2(P_2S_6)$, $Tl_3Bi(PS_4)_2$, and $TlBiP_2S_7$ were produced as described previously.[1] The ultra high field NMR spectra were collected on a Bruker AVANCE 21 T spectrometer operating at 362 Mhz. The 9.8 T NMR spectra were collected on a Varian Infinity Plus spectrometer operating at 162 Mhz. Each spectrum

was obtained at ambient temperature with magic angle spinning and was the sum of four Bloch decay scans. Pulse width calibration and chemical shift referencing were done with 85% H_3PO_4 (= 0 ppm). Each spectrum was processed identically with 50 Hz line broadening and baseline correction.

RESULTS AND DISCUSSION

Figure 4-2 displays the 9.4 and 21 T ^{31}P magic angle spinning spectra of three compounds: $Tl_4Bi_2(PS_4)_2(P_2S_6)$, $Tl_3Bi(PS_4)_2$, and $TlBiP_2S_7$. Each of the spectra could be fitted well to a sum of Lorentizian functions. In Figure 4- 2, the experimental spectra are displayed as solid lines, the individual Lorentzian functions are displayed as dotted lines, and the sums of the Lorentzian functions are also displayed as dotted lines. The spectra of $Tl_4Bi_2(PS_4)_2(P_2S_6)$ and $TlBiP_2S_7$ were separated into two clusters of Lorentzian peaks and the spectrum of $Tl_3Bi(PS_4)_2$ was a single cluster of Lorentzian peaks. Table 4-1 lists the peak shifts, linewidths, and integrated intensities of the fitted Lorentzians and Table 4- 2 lists the average shift of each cluster of Lorentzian peaks as well as the splittings between adjacent Lorentzian peaks in the same cluster. For each compound, the consistency between the average shifts and the peak splittings at different fields confirmed that the splittings were likely due to ^{31}P-Tl J-couplings. Tl has two abundant isotopes with similar gyromagnetic ratios and splittings due to individual Tl isotopes were not resolved. The upfield clusters of the $TlBiP_2S_7$ spectra were not included in Table 4-2 because it was not possible to make an assignment with a consistent average shift and peak splitting at the two fields. This difficulty may have been

due to overlapping peaks from unidentified impurities in the sample. Minor impurities were also apparent as additional peaks in the powder diffraction pattern.

Table 4-1. Chemical shifts, linewidths, and integrated intensities of the fitted Lorentzian components of the spectra. [a]

Compound	9.4 T			21 T		
	Peak (ppm)	Linewidth (Hz) [b]	Integrated intensity [c]	Peak (ppm)	Linewidth (Hz) [b]	Integrated intensity [c]
$Tl_4Bi_2(PS_4)(P_2S_6)$	99.8	350	51	98.8	520	42
	96.6	420	71	97.4	540	44
	87.6	570	31	83	910	40
	79.8	1040	100	79.3	1200	100
	71.5	760	38	75.7	700	27
$Tl_3Bi(PS_4)_2$	99.2	1600	31	88.7	750	11
	90	1490	54	84.7	1630	59
	80	1890	100	79.8	2060	100
	69.4	1410	52	75.3	1300	42
	60.3	1710	35	71.6	1610	27
$TlBiP_2S_7$	87	360	93	85.9	430	82
	84.1	290	66	84.6	390	67
	77	510	47	77	650	100
	74.4	530	74	71.5	640	67
	70.3	460	100	70	430	24

[a] Fitting of the Lorentzian functions was done with the OriginPro 7.5 program.

[b] The linewidth is the fitting parameter from a Lorentzian peak function.

[c] The Lorentzian component with maximum integrated intensity was assigned a value of 100.

Table 4- 2. Average chemical shifts and splittings of the spectral clusters.

Compound	Cluster identity	9.4 T		21 T	
		Shift (ppm)	Splitting (Hz)	Shift (ppm)	Splitting (Hz)
$Tl_4Bi_2(PS_4)(P_2S_6)$	Downfield doublet	98.2	520	98.1	510
	Upfield triplet	79.6	1270, 1350	79.3	1350, 1310
$Tl_3Bi(PS_4)_2$	Quintet	79.8	~1580	80.0	~1560
$TlBiP_2S_7$	Downfield doublet	85.6	470	85.3	470
	Upfield doublet [a]	72.4	670	74.3	2000

[a] This doublet was the two components of the cluster with the greatest integrated intensity.

There were two crystallographically inequivalent P in $Tl_4Bi_2(PS_4)_2(P_2S_6)$ and one P was associated with the $[PS_4]^{3-}$ unit and one P was associated with the $[P_2S_6]^{4-}$ unit. The downfield "doublet" exhibited much larger chemical shift anisotropy than did the upfield "triplet" and the doublet and triplet were respectively assigned to the $[P_2S_6]^{4-}$ and $[PS_4]^{3-}$ units, respectively.[1,11] The ^{31}P in the $[P_2S_6]^{4-}$ and $[PS_4]^{3-}$ units had respectively five and six Tl separated by two bonds and the reason for the simple experimental splitting patterns was therefore not obvious. The ratio of relative integrated intensities of the double and triplet was 0.72 at 9.4 T and 0.51 at 21 T. The 9.4 T result was closer to the 1.0 ratio expected from the crystal structure. The lower ratio observed at 21 T may be a result of a shorter recycle delay and the consequent effect of differential longitudinal relaxation for the doublet and triplet.

The spectra of $Tl_3Bi(PS_4)_2$ could be fitted as a quintet at both fields. The structure of this compound has not been fully refined. The compound $K_3Bi(PS_4)_2$ is isotypic and has a well-refined structure[1] so using the refined structural model for comparative purposes is reasonable. There are two crystallographically inequivalent P atoms in $K_3Bi(PS_4)_2$ and one ^{31}P has 10 K^+ separated by two bonds while the other ^{31}P has 6 K^+ ions separated by two bonds. The $Tl_3Bi(PS_4)_2$ quintet cannot be not trivially understood by the replacement of K^+ ions with Tl^+ ions in this structure.

The spectra of $TlBiP_2S_7$ contained two clusters of peaks. At both fields, the downfield cluster was fitted as a doublet and the upfield cluster was fitted as a triplet. There was some variation in the appearance and the fitting of the upfield regions at the two different fields. These variations were likely due to: (1) as-yet unidentified impurities

in the samples; and (2) the shorter recycle delay used at 21 T and the consequent possible effects of differential longitudinal relaxation. There were two crystallographically inequivalent P in $TlBiP_2S_7$ and the most reasonable assignment was the downfield doublet as one ^{31}P and some part of the upfield triplet as the other ^{31}P.

Table 4-1 shows that the linewidths in Hz of the individual Lorentzian components were not strongly dependent on field strength. The splittings due to J-couplings in Hz were also independent of field and there was therefore similar appearance of individual clusters at the two fields. However, in ppm units, the total linewidth of a cluster was approximately inversely proportional to field, and this led to greatly improved resolution between clusters at 21 T, i.e. better chemical shift resolution. This enhanced resolution was particularly noteworthy for the compound $Tl_4Bi_2(PS_4)_2(P_2S_6)$ for which the doublet and triplet were completely resolved at 21 T.

Good spectral deconvolution with Lorentzian functions suggested that the line widths were dominated by the transverse relaxation rate. Such dominance may hold for crystalline compounds that have small chemical shielding inhomogeneity at each site. In addition, T_2 may not vary strongly as a function of applied field strength if $T_2 << T_1$.[12] This inequality was likely valid for these compounds. It has also been observed that the ^{31}P longitudinal relaxation rates of metal selenophosphates were linearly correlated with the squares of dipolar couplings to the ^{31}P.[13] These couplings are independent of magnetic field strength and could also contribute to the transverse relaxation rates of metal thiophosphates.

CONCLUDING REMARKS

Motivations for ultra-high field magic angle spinning spectroscopy of solids have included improved resolution in spectra of biological macromolecules due to attenuation of broadening from ^{13}C-^{13}C J-couplings,[14] reduction of second-order quadrupolar broadening,[15] and improved sensitivity.[16] The present study provides an example of greatly improved chemical shift resolution at 21 T for spin ½ nuclei in crystalline inorganic solids. This improvement correlated with field-independent line widths and splittings due to ^{31}P-Tl J-couplings. These splittings may be useful parameters for understanding the electronic structure of these compounds.

REFERENCES

1. Gave, M.; Malliakas, C. D.; Weliky, D. P.; Kanatzidis, M. G. *Inorg. Chem.* **2007,** 46, 3632-3644.

2. McGuire, M. A.; Reynolds, T. K.; DiSalvo, F. J. *Chem. Mat.* **2005,** 17, 2875-2884.

3. McCarthy, T. Ph.D. Thesis, Michigan State University, East Lansing, MI, 1994.

4. McCarthy, T.; Kanatzidis, M. G. *J. Alloys Compd.* **1996,** 236, 70-85.

5. McCarthy, T. J.; Kanatzidis, M. G. *Chem. Mat.* **1993,** 5, 1061-1063.

6. McCarthy, T. J.; Kanatzidis, M. G. *J. Chem. Soc. Chem. Commun.* **1994,** 1089-1090.

7. Breshears, J. D.; Kanatzidis, M. G. *J. Am. Chem. Soc.* **2000,** 122, 7839-7840.

8. Manriquez, V.; Galdamez, A.; Leon, D. R.; Garland, M. T.; Jimenez, M. *Z. Krist. New Cryst. St.* **2003,** 218, 151-152.

9. Gave, M.; Weliky, D. P.; Kanatzidis, M. G. *Inorg. Chem.* **2007,** Accepted. DOI 10.1021/ic701211a

10. Greenwood, N. N.; Earnshaw, A. Chemistry of the Elements; 2nd ed.; Butterworth-Heinemann: Boston, MA, 1997; pp 75, 222.

11. Canlas, C. G.; Kanatzidis, M. G.; Weliky, D. P. *Inorg. Chem.* **2003,** 42, 3399-3405.

12. Harris, R. K. Nuclear Magnetic Resonance Spectroscopy; Longman Scientific and Technical: New York, NY, 1983; p 87.

13. Canlas, C. G.; Muthukumaran, R. B.; Kanatzidis, M. G.; Weliky, D. P. *Solid State Nucl. Magn. Reson.* **2003,** 24, 110-122.

14. Straus, S. K.; Bremi, T.; Ernst, R. R. *Chem. Phys. Lett.* **1996,** 262, 709-715.

15. Hoatson, G. L.; Zhou, D. H. H.; Fayon, F.; Massiot, D.; Vold, R. L. *Phys. Rev. B.* **2002,** 66, 224103-1.

16. Marulanda, D.; Tasayco, M. L.; Cataldi, M.; Arriaran, V.; Polenova, T. *J. Phys. Chem. B* **2005,** 109, 18135-18145.

CHAPTER 5

NEW POTASSIUM BISMUTH THIOPHOSPHATES INCLUDING THE MODULATED $K_{1.5}Bi_{2.5}(PS_4)_3$.

INTRODUCTION

Chalcophosphate compounds generally are semiconductors with medium to wide energy gaps and can exhibit fascinating physical properties including pronounced photoconductivity,[1] photorefractive gain,[2,3] ferroelectricity,[4-6] electro-optic[7] and second harmonic generation[8] properties. The chalcophosphate anions are a special class of polyanions with broad reactivity and structural characteristics with general formula of $[P_xQ_y]^{z-}$ (Q=S, Se). They can be stabilized as alkali metal salts[9,10] or coordinating ligands to a variety of metal centers.[11-18] The chemistry of these materials has been substantially developed in the past decade thanks to the application of the flux synthesis technique which served as a medium for reaction chemistry and tool for discovery. Bismuth chalcogenide compounds have a great deal of structural diversity due in part to the so-called inert lone pair effect[19-25] and the flexibility in the coordination environment including trigonal pyramidal,[26] square pyramidal,[27] and capped trigonal prismatic.[28,29] Bismuth can bind to various chalcophosphate ligands, as for example in the compounds $KBiP_2S_7$[26,30], $KBiP_2S_6$[31] and $K_3Bi(PS_4)_2$,[30] which contain the $[P_2S_7]^{4-}$, $[P_2S_6]^{4-}$ and $[PS_4]^{3-}$ anions, respectively. Each anion can be selectively formed by slightly varying the reaction conditions, and a variety of phases can therefore be rationally synthesized.[32]

The K/Bi/P/S chemistry was investigated further to search for K^+ analogs of the recently reported Tl/Bi/P/S compounds.[33] Due to their monovalency and similar ionic radii, K^+ and Tl^+ are often considered to have similar chemical reactivity and form structurally related compounds. Additionally, related A/M/P/Q (A= K, Rb, Cs, M = Bi, Pb, Q = S, Se) compounds exhibit a reduction in structural dimensionality as the proportion of alkali metal is increased.[31,34-36] Low-dimensional materials are of interest

because they may have accessible networks suitable for ion exchange reactions which can either produce metastable isomorphic analogs, or following structural rearrangement, new compounds.[37] We describe here the compounds $K_3Bi_3(PS_4)_4$ [I], $K_{1.5}Bi_{2.5}(PS_4)_3$ [II] and $K_9Bi(PS_4)_4$ [III]. The first two feature unique extended Bi/P/S arrangements with [II] exhibiting an incommensurate superstructure arising from a modulation of the occupation of the Bi and Tl atoms. The third compound [III] is a molecular salt with an eight coordinate mononuclear $[Bi(PS_4)_4]^{9-}$ complex.

EXPERIMENTAL SECTION

Reagents

Chemicals were used as obtained unless otherwise noted: bismuth chunks (Tellurex Inc., Traverse City, MI, 99.999%), phosphorous (MCB Reagents, Gibbstown, NJ, amorphous red), sublimed sulfur flowers (CCI, Vernon, CA), potassium metal, (Aldrich Chemical Co., Inc., St. Louis, MO) Bismuth was ground in an agate mortar and pestle to ca. 100 mesh. Phosphorous was freeze-dried and K_2S was prepared by a modified literature preparation.[23,38]

Synthesis

Manipulations of Bi, P, and S were carried out in ambient conditions and then transferred into a Vacuum Atmospheres Dri-Lab glovebox filled with N_2 where the appropriate amount of K_2S was added.

$K_3Bi_3(PS_4)_4$ [I]: A mixture of K_2S (0.174g, 1.6 mmol), Bi (0.3941 1.9 mmol), P (0.0781g, 2.5 mmol), and S (0.3533g, 11.0 mmol) was loaded into a fused silica ampoule and flame sealed under a reduced atmosphere of $\sim 10^{-4}$ mbar. After shaking to

increase homogeneity, the tube was inserted into a protective ceramic sheath and placed in a furnace. The mixture was heated to 600 °C over 12h, held there for 12h, and then cooled back to room temperature over a period of 6h. An inhomogenous red crystalline ingot was isolated that was a mixture of $K_3Bi_3(PS_4)_4$ [I] (~70%), $K_{1.5}Bi_{2.5}(PS_4)_3$ [II] (~20%), $K_3Bi(PS_4)$ (5%) and Bi_2S_3 (~5%). Microprobe analysis averaged over several sample areas of the single crystal used for the diffraction experiments gave an average composition of $K_{1.0}Bi_{1.0}P_{1.4}S_{5.8}$.

$K_{1.5}Bi_{2.5}(PS_4)_3$ [II]: An ampoule containing a mixture of K_2S (0.039g, 0.35 mmol), Bi (0.2461g, 1.2 mmol), P (0.0435g, 1.4 mmol), and S (0.1709g, 5.4 mmol) was allowed to react under the same conditions as were used to produce compound [I]. A homogenous red crystalline ingot was isolated that was composed of air-stable red plates of $K_{1.5}Bi_{2.5}(PS_4)_3$ in quantitative yield. Microprobe analysis averaged over several sample areas of the single crystal used for diffraction experiments gave an average composition of $K_{1.5}Bi_{2.4}P_{3.2}S_{11.9}$.

$K_9Bi(PS_4)_4$ [III]: An ampoule containing a mixture of K_2S (0.414g, 3.8 mmol), Bi (0.1749g, 0.84 mmol), P (0.1040, 3.4 mmol), and S (0.3078g, 9.6 mmol) that was prepared in the same manner as [I] was heated to 600 °C over 18h, held there for 2h, and then cooled back to room temperature over a period of 8h. A homogenous red crystalline ingot was isolated that was composed of very moisture-sensitive red plates (~90%) and greenish gelatinous decomposition products (~10%). The relative amount of the decomposition products increased quickly and under a light microscope, it was possible to observe regions of the sample decomposing. Microprobe analysis averaged over several sample areas of the single crystal used for diffraction experiments gave an average composition of $K_{9.0}Bi_{0.8}P_{4.3}S_{16.7}$.

Ion Exchange

Because of the large thermal parameters and channel diameters, various sample portions containing [I] were subjected to conditions wherein ion exchange might occur. For solid state topotactic ion exchange,[39] a ~0.05 mmol sample portion of compound [I] was ground in an agate mortar and pestle with ~1.9 mmol AI (A = Rb, Cs) and placed into a 1 cm die. The sample was then pressed into a pellet with ~4500 kg of force. The pellets were loaded into glass sample vials and placed into an 80°C oven for 7d. The products were then washed twice with deionized water, twice with acetone, and once with ether to isolate a black powder.

Solution phase ion exchange was attempted by combining a ~0.09 mmol sample portion of compound [I], ~3.3 mmol ACl (A = Rb, Cs) and ~10 mL deionized water in a glass vial that was stirred overnight. The resulting black powder was washed twice with deionized water, twice with acetone, and once with ether.

Microprobe analysis of the products from both the solid state and solution phase ion-exchange experiments suggested that some exchange had occurred although the stoichiometric ratio of the elements changed from crystal to crystal. The salt counterion (Cl^- or I^-) was not found in significant amounts suggesting that the Rb or Cs was in fact the compound rather than left over from incomplete washing. Powder X-ray diffraction of the powders after solution-based ion exchange matched well with the calculated patterns for [I] while those from the solid state ion exchange showed a similar pattern of peaks but with a slight shift towards higher 2θ angles.

Powder X-ray Diffraction

All samples were assessed for phase purity using powder X-ray diffraction. Powder patterns were obtained using an INEL CPS 120 powder X-ray diffractometer with monochromatized Cu Kα radiation (λ = 1.540598 Å) operating at 40 kV and 20 mA equipped with a position-sensitive detector with a 2θ range of 0 - 120° and calibrated with a LaB_6 standard.

Single Crystal X-ray Diffraction

Intensity data for single crystals of [I] and [III] were collected on a Bruker SMART platform CCD diffractometer using Mo Kα radiation operating at 40 kV and 40 mA. A full sphere of data was collected and individual frames were acquired with a 10 s exposure time and a 0.3° omega rotation. The SMART software was used for data collection, and SAINT software was used for data extraction and reduction. An analytical absorption correction to the data was performed and direct methods were used to solve and refine the structures with the SHELXTL[40] software package. The details of data collection and refinement are summarized in Table 5-1. Fractional atomic coordinates for [I] through [III] are displayed in Tables 5-2 through 5-4.

Table 5-1. Crystallographic Data, Experimental and Refinement Details for the Reported Phases.

	$K_3Bi_3(PS_4)_4$ [I]	$K_{1.5}Bi_{2.5}(PS_4)_3$ [II]	$K_9Bi(PS_4)_4$[III]
Temperature, K	298	298	298
Crystal system	Tetragonal	Monoclinic	Orthorhombic
Space group	*P4/ncc*	*P2/c(α½γ)00*	$P2_12_12$
λ, Å (Mo Kα)	0.071073	0.071073	0.071073
a, Å	21.0116(8)	21.7939(13)	18.306(4)
b, Å	21.0116(8)	8.805(8)	8.926(2)
c, Å	13.3454(10)	10.0301(6)	9.710(2)
α, °	90	90	90
β, °	90	90.013(5)	90
γ, °	90	90	90
q	n/a	0.5**a***+0.16**b***+0.25**c***	n/a
Z	8	4	2
Crystal dimensions, mm	0.40 x 0.03 x 0.03	0.10=8 x 0.08 x 0.04	0.20 x 0.15 x 0.08
D_{calc} g/cm^3	3.114	3.583	2.507
μ, mm^{-1}	19.648	24.187	7.992
R_{int}, %	14.2	7.98	10.6
totalreflections/ independent	61112/3575	11921/6107	16260/3640
final R/Rw, %[a]	6.7/17.7	6.6/13.3 5.2/12.7 (main) 13.0/24.6 (sat)	5.8/8.9
Residual electron density, A^{-3}	4.29 (0.80 Å from Bi(1))	5.27	1.45 (0.45 Å from Bi(2))

[a] $R = \Sigma(|F_o| - |F_c|)/\Sigma|F_o|$. $R_w = [\Sigma w(|F_o| - |F_c|)^2/\Sigma w|F_o|^2]^{1/2}$

Table 5-2. Fractional atomic coordinates and U(eq) values for $K_3Bi_3(PS_4)_4$ [I] with standard deviations in parenthesis.

atom	x	y	z	U_{eq}[a]
Bi(1)	0.4904(1)	0.1003(1)	0.3629(1)	26(1)
Bi(2)	0.3987(1)	-0.1013(1)	0.2500	26(1)
K(1)	0.4569(3)	0.2426(2)	0.0814(4)	45(1)
K(2)	0.2500	-0.2500	0.7500	710(80)
K(3)	0.2500	0.2500	0.5340(110)	600(80)
P(1)	0.4260(2)	0.0615(2)	0.1261(3)	19(1)
P(2)	0.5636(2)	0.2467(2)	0.3319(3)	24(1)
S(1)	0.3777(2)	0.0583(3)	0.2579(3)	36(1)
S(2)	0.5127(2)	0.1040(2)	0.1568(3)	18(1)
S(3)	0.3887(2)	0.1195(2)	0.5183(3)	27(1)
S(4)	0.4419(3)	-0.0291(2)	0.0762(3)	32(1)
S(5)	0.4673(2)	0.2260(2)	0.3371(4)	28(1)
S(6)	0.2728(2)	-0.0926(2)	0.1900(3)	28(1)
S(7)	0.3197(2)	-0.852(3)	0.4236(3)	35(1)
S(8)	0.6082(3)	0.1663(2)	0.3767(4)	38(1)

[a] $U_{(eq)} = (\Sigma_i\Sigma_j U_{ij} a_i^* a_j^* a_i \cdot a_j)/3 \times 1000$

Table 5-3. Fractional atomic coordinates and U(eq) values for the average structure of $K_{1.5}Bi_{2.5}(PS_4)_3$ [II] with standard deviations in parenthesis.

atom	x	y	z	U_{eq}[a]	Occupancy
Bi1	0.390114(14)	0.11713(4)	0.85565(3)	0.02332(9)	
Bi2	0.890097(14)	0.38299(4)	-0.35563(3)	0.02747(9)	
Bi3	0.54423(13)	0.5	0.75	0.0225(3)	0.481(3)
K3	0.544226	0.5	0.75	0.0225(3)	0.519(3)
Bi4	-0.04215(9)	0	0.75	0.0238(3)	0.507(3)
K4	-0.042152	0	0.75	0.0238(3)	0.411(3)
K1	0.24992(11)	0.2501(3)	0.4944(2)	0.0376(6)	
P1a	0.24995(7)	0.25205(15)	0.90660(13)	0.0212(3)	
P1b	0.43553(7)	0.23598(15)	0.54091(14)	0.0212(3)	
P1c	0.93547(7)	0.26391(15)	-0.04082(14)	0.0212(3)	
S1a	0.27121(11)	0.0661(3)	0.7905(2)	0.0217(3)	
S2a	0.22915(13)	0.4333(3)	0.7892(2)	0.0320(4)	
S3a	0.32424(11)	0.2963(3)	0.0230(2)	0.0249(3)	
S4a	0.17576(11)	0.2008(3)	0.0228(2)	0.0268(3)	
S1b	0.38524(11)	0.3602(3)	0.6767(2)	0.0217(3)	
S2b	0.39548(12)	0.2456(3)	0.3579(2)	0.0320(4)	
S3b	0.43918(11)	0.0186(3)	0.6091(2)	0.0249(4)	
S4b	0.52195(11)	0.3251(3)	0.5291(2)	0.0268(4)	
S1c	0.88525(11)	0.1396(3)	-0.1766(2)	0.0217(3)	
S2c	0.89543(12)	0.2540(3)	0.1422(2)	0.0320(4)	
S3c	0.93900(11)	0.4813(3)	-0.1089(2)	0.0249(4)	
S4c	0.02194(11)	0.1751(3)	-0.0290(2)	0.0268(4)	

[a] $U_{(eq)} = (\Sigma_i\Sigma_j U_{ij} a_i^* a_j^* a_i \cdot a_j)/3 \times 1000$

Table 5-4. Fractional atomic coordinates and U(eq) values for $K_9Bi(PS_4)_4$ [III] with standard deviations in parenthesis.

atom	x	y	z	U_{eq}[a]
Bi	0.0000	0.0000	0.7262(1)	39(1)
K(1)	0.2500(1)	-0.4982(3)	1.2486(2)	37(1)
K(2)	0.2308(1)	0.182(3)	0.2405(2)	42(1)
K(3)	-0.0766(1)	-0.3551(3)	0.9985(3)	34(1)
K(4)	0.0000	0.0000	0.2338(3)	31(1)
K(5)	0.0877(2)	-0.3721(3)	0.4841(3)	38(1)
S(1)	0.2456(2)	-0.2327(3)	0.9996(5)	29(1)
S(2)	0.1041(1)	-0.0053(4)	0.9481(2)	30(1)
S(3)	0.0873(2)	-0.3070(3)	1.1525(3)	30(1)
S(4)	0.1013(2)	-0.3462(4)	0.8159(3)	46(1)
S(5)	0.1084(1)	-0.0209(3)	0.5175(3)	27(1)
S(6)	0.2294(2)	0.2609(3)	0.5246(3)	39(1)
S(7)	0.0827(2)	0.2962(3)	0.3320(3)	31(1)
S(8)	0.0603(2)	0.2893(4)	0.6672(3)	50(1)
P(1)	0.1359(1)	-0.2264(3)	0.9796(3)	18(1)
P(2)	0.1231(1)	0.2086(3)	0.5085(3)	19(1)

[a] $U_{(eq)} = (\Sigma_i\Sigma_j U_{ij} a_i^* a_j^* a_i \cdot a_j)/3 \times 1000$

The crystal structure of compound [I] indicated that the K^+ ion sites within the channels (*vide infra)* had large thermal parameters, particularly along the channel axis. An attempt was made to model this behavior as a series of sequential cation sites with partial site occupancy, but a significant decrease in reliability statistics was not obtained. Intensity data for a single crystal of [II] was collected on a Stoe IPDS II diffractometer with Mo Kα radiation operating at 50 kV and 40 mA on with a 34 cm image plate. Individual frames were collected with a 0.5° omega rotation using the X-AREA software.[41] The X-SHAPE and X-RED software packages were used for data extraction and reduction and to apply an analytical absorption correction. The SHELXTL and JANA2000[42] software packages were used to solve and refine the structure.

The single crystal XRD measurement of [II] was first measured with an exposure time of 2 minutes and showed reflections belonging to an orthorhombic cell. Analysis of the systematic absences indicated the space group *Pnna*. Direct methods performed with the SHELX program package gave a partial solution and the structure was then refined to yield a satisfying description in terms of interatomic distances and residual electron density values, but with high thermal parameters and residual electron density. The crystal was then remeasured with a 6 min exposure time. The intention was to check for extra reflections in the diffraction pattern that would reveal additional order in the structure in the form of a structural modulation. Modulated structures have a periodic deviation of atomic positions, site occupancies, or thermal displacement parameters. Therefore in the structure, translational symmetry of the unit cell is lost and is described in the crystallographic solution as a perturbation to the unit cell. The modulation is manifested in the diffraction pattern because main reflections that correspond to unit cell periodicity are observed along with weaker satellite reflections that correspond to the

period of the modulation. These satellite reflections are found in the diffraction pattern along the modulation vector **q** in the reciprocal lattice.[43,44] The reciprocal lattice showed weak first order satellite reflections, incommensurate with the orthorhombic cell that could be indexed with the one-dimensional vector $\mathbf{q} = [^1/_4, ^1/_2, 0.16]$.

This modulation vector can not be combined with orthorhombic symmetry,[45] so the crystal class was lowered and the 3D space group changed to the highest isomorphic subgroup *P*2/*n*. This space group contains two (3+1)-dimensional superspace groups, $P2/c(\alpha ½ \gamma)00$ and $P2/c(\alpha ½ \gamma)0s$, of which only the first gave a useful result after subsequent refinement. Atomic positions were transferred from the *Pnna* model, yielding 22 positions, and the main reflections quickly refined to low residual values (R_{obs}/R_{all}=0.034/0.068) for the average structure. Then, modulation waves were applied to the structure to account for satellite reflections. Occupational modulation waves were applied to the mixed K/Bi sites and positional modulation waves were applied to all atoms in the structure.

The $[PS_4]^{3-}$ tetrahedra were modeled as being internally rigid to decrease the number of crystallographic parameters in the refinement. One $[PS_4]^{3-}$ anion was chosen as the molecular model and the atomic parameters were first refined individually. The molecular positions and parameters common for the entire molecule were then refined in a rigid body approximation. The final overall reliability statistics converged to R/Rw = 6.6/13.3% (R/Rw = 5.2/12.7% for main reflections and R/Rw = 13.0/24.6% for satellite reflections) for 11921 reflections ($I/\sigma(I)>3$) and 158 parameters.

In an alternative attempt, it was possible to divide the **q** vector into a rational part, $\mathbf{q}^r = [0, ½, 0]$, and an irrational part, $\mathbf{q}^i = [0.25, 0, 0.16]$. The rational part could then be excluded by applying a centering condition. This resulted in the super space

group $X2/c(\alpha 0 \gamma)00$, where X corresponded to the (3+1)-dimensional centering [0, ½, 0, ½]. However, this required that the *b*-axis was doubled and so the overall gain in such a description for an already large unit cell was limited and was therefore not considered. Only 35% of the satellite reflections met the observation criteria of $I>3\sigma$ and the absence of higher orders made the modulation difficult to model precisely. The final residual values are about 13% for the satellites but the low overall R value (6.61%) reflects the minor effect of the modulation on the structure. The exchange of Bi for K in two different sites can apparently be made smoothly, with no drastic effects on the rest of the structure and thus the weak intensity of the satellite reflections.

Electron Microscopy

A JEOL JSM-35C scanning electron microscope equipped with a Tracor Northern energy dispersive spectroscopy detector was used for quantitative microprobe analysis. Data were collected using an accelerating voltage of 25 kV and a collection time of 60 s and results were averaged over several sample areas.

Differential Thermal Analysis

Differential thermal analyses were performed with a Shimadzu DTA-50 thermal analyzer. A ground sample weighing ~25 mg was sealed in a quartz ampoule under reduced pressure. An equivalent mass of alumina was sealed in an identical ampoule to serve as a reference. The samples were heated to 850 °C at a rate of 10 °C/min, cooled to 150 °C at a rate of 10 °C/min, reheated to 850 °C at a rate of 10 °C/min, and then cooled to room temperature at a rate of 10 °C/min.

Raman Spectroscopy

Raman (750-100 cm^{-1}) spectra were collected using a BIO-RAD FT spectrometer equipped with a Spectra-Physics Topaz T10-106c 1.064 nm YAG laser and a Ge detector. Samples were ground into a fine powder and loaded into fused silica tubes and 64 scans were averaged.

Solid State NMR

Room-temperature ^{31}P solid-state NMR spectra were collected on a 9.4 T spectrometer (Varian Infinity Plus) using a double resonance magic angle spinning (MAS) probe. Samples were spun at frequencies ranging from 5 kHz to 15 kHz in 4 mm outer diameter zirconia rotors and a ~50 μL sample volume. Bloch decay spectra were taken with a 4 μs 90° pulse (calibrated and referenced to 85% H_3PO_4 at 0 ppm) and relaxation delays ranging from 10 to 5000 s. Each spectrum was processed with 10 Hz line broadening and up to a 10^{th} order polynomial baseline correction.

The longitudinal relaxation time (T_1) of each compound was estimated by fitting to the equation:

$$S(t) = S_0(1 - e^{-\tau / T_1}) \quad (1)$$

where τ is the experimental delay time, $S(\tau)$ is the experimental signal intensity, and S_0 is a fitting parameter representing the signal intensity at $\tau = \infty$.[46]

RESULTS AND DISCUSSION

Synthetic Reactions

The compounds $K_{1.5}Bi_{2.5}(PS_4)_3$ [II] and $K_9Bi(PS_4)_4$ [III] were produced by direct stoichiometric reaction of K_2S, Bi, P, and S, however, we were not able to prepare

$K_3Bi_3(PS_4)_4$ [I] as the dominant compound without additional K_2S_x in the reaction. Presumably, the K_2S_x acted as a flux in which [I] could grow. If K_xS_y was not added, [II] was produced in high yields. When the value of x in K_2S_x was decreased, $K_3Bi(PS_4)_2$[30] was produced along with a significant amount of Bi_2S_3. The synthesis of $K_9Bi(PS_4)_4$ required even more basic K_2S_x compositions. In syntheses of compound [I] we always observed compound [II] and $K_3Bi(PS_4)_2$ present in detectable quantities.

Compounds [I] and [II] were stable in ambient conditions, but [III] was highly moisture sensitive and decomposed rapidly when exposed to air. This reactivity can be attributed to the presence of the highly charged $[Bi(PS_4)_4]^{9-}$ molecular anion in the structure.[47]

In an attempt to prepare pure $K_3Bi_3(PS_4)_4$, a melt of the same composition was quenched in ice water. The intention was to kinetically trap a solid with the correct stoichiometry which could then be annealed at a given temperature to produce crystalline $K_3Bi_3(PS_4)_4$. The resultant solid was an amorphous glass as confirmed with powder X-ray diffraction. Differential thermal analysis of the glass indicated the onset of crystallization at about 320 °C. The sample was then carefully annealed at 320 °C but the resulting product was found to be $K_{1.5}Bi_{2.5}(PS_4)_3$ with no evidence for compound [I]. It is likely that compound [I] is stabilized by the presence of a K_2S_x flux and is not just kinetically stable.

Structure Description

$K_3Bi_3(PS_4)_4$ [I]:

This compound has a complex 3-dimensional $[Bi_3(PS_4)_4]^{3-}$ anionic framework with infinite parallel tunnels running through it, Figure 5-1A. The tunnels are parallel to the c-axis and are filled with charge balancing K^+ ions. There are two types of tunnels in the structure. Type-I tunnels are located at (¾, ¼) in the ab-plane and have K2 atoms in their center. Type-II tunnels are located at (¼, ¾) and accommodate the K1 and K3 atoms. Each tunnel type is surrounded by four other tunnels of the other type.

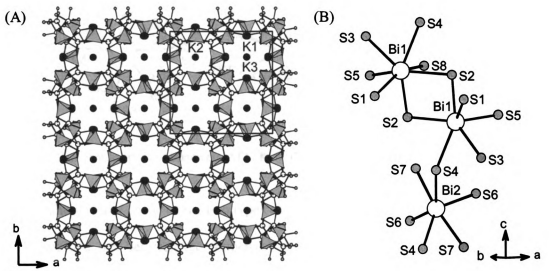

Figure 5-1. (A) $K_3Bi_3(PS_4)_4$ viewed down the [001] axis showing the large channels that are occupied by K^+ ions. (B) An undulating Bi_3S_{12} chain that forms the walls of the tunnels.

The K(1) atoms are located at the tunnel edge interacting with S atoms with an average K-S bond length of 3.33 Å, Figure 5-2A. The K(3) central axes are located at the tunnel center with K-S distances of ~4 Å, Figure 5-2C. The K(3) atoms are located in the same tunnel as the K(1) atoms but instead of being placed on the edge, they are situated along the walls of the tunnel. The K(2) site is distorted square planar with K(2)-S interactions of 3.436(5) Å, Figure 5-2B. The K2 and K3 ion sites had large thermal

parameters and the possibility of this being due to long range order was considered. Zone photos obtained with X-ray diffraction using relatively long exposure times did not reveal any evidence for weak satellite reflections and therefore significant contributions from a modulation are unlikely. Therefore the large thermal parameters are probably due to static positional disorder of the K^+ atoms in the oversized tunnels. The greatest displacement in each case was along the (001) axis which suggests the possibility of high ion mobility within the tunnels.

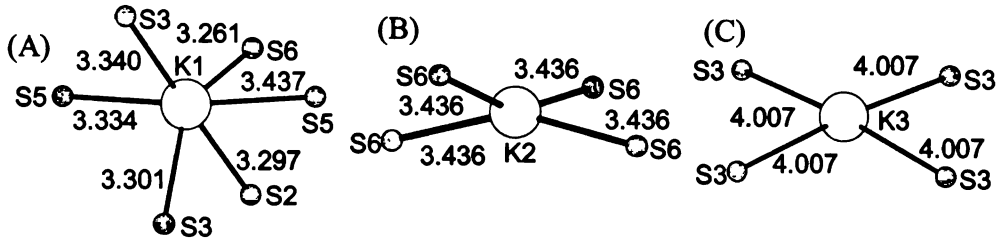

Figure 5-2. The coordination environments of (A) K(1), (B) K(2), and (C) K(3) ions in $K_3Bi_3(PS_4)_4$.

The size and shape of the two types of tunnels were approximated by plotting the isosurface that lies between the framework atoms, Figure 5-3.[48] The smaller tunnel (type-I) has a maximum diameter of ~3.1 Å, and the larger one (type-II) has a maximum diameter of ~4.4 Å. The two types of tunnels do not seem to be connected by holes of significant girth.

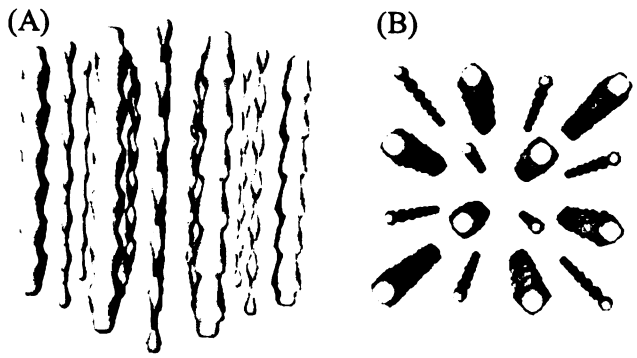

Figure 5-3. Void space representation of $K_3Bi_3(PS_4)_4$ showing the relative sizes and contours of each of the channels viewed (A) perpendicular to [001] and (B) parallel to [001].

The $[Bi_3(PS_4)_4]^{3-}$ framework itself is built from undulating chains of Bi-S polyhedra. If the P-atoms are ignored, the structure is made of pairs of parallel Bi_3S_{12} chains, Figure 5-1B. In each chain, the distorted Bi polyhedra share corners or edges. Bi(1) is pseudo 8-coordinate and is chelated by three $[PS_4]^{3-}$ anions. Seven of the Bi-S distances are relatively short with an average bond length of 2.91 Å. The remaining interaction is between Bi(1) and S(4) distance at 3.451(6) Å and is likely elongated due to the stereochemically active so-called $6s^2$ lone pair of electrons on Bi. The stereochemical activity presumably arises from an interaction between the Bi 6s valence electrons and the chalcogen valence p-orbitals that results in an asymmetric distribution of the former.[49] Two Bi(1) atoms are bridged by S atoms with Bi(1)-S(2) distances of 2.791(4) and 3.026(4) Å. Bi(1) is also connected to Bi(2) by a bridging S atom. Bi(2) is pseudo 8-coordinate and is chelated by three $[PS_4]^{3-}$ anions and forms the inner wall of the tunnel. Six of the Bi-S distances are relatively short with an average bond length of 2.85 Å. The putative lone pair of electrons on Bi is suggested by the elongated Bi(2)-S(1) of distance of 3.384(6) Å. The action of the 4-fold axis on the chain of

$[Bi_3(PS_4)_4]^{3-}$ forms into the tunnel. Selected bond lengths and angles are displayed in Table 5-5.

Table 5-5. Selected bond lengths and angles for $K_3Bi_3(PS_4)_4$ with bond lengths (Å) and angles (°), with standard uncertainties in parenthesis

Bi1—S5	2.707(5)	S5—Bi1—S2	82.99(13)	$S3^{viii}$—K1—$S1^{vii}$	139.5(2)
Bi1—S2	2.791(4)	S5—Bi1—S8	71.86(15)	$S5^{ix}$—K1—$S1^{vii}$	118.42(16)
Bi1—S8	2.844(5)	S2—Bi1—S8	84.50(14)	$S3^{ix}$—K1—$S1^{vii}$	57.21(13)
Bi1—S1	2.888(5)	S5—Bi1—S1	95.13(16)	S5—K1—$S1^{vii}$	56.77(13)
Bi1—S3	3.006(5)	S2—Bi1—S1	70.64(12)	$S7^{viii}$—K1—$S1^{vii}$	134.72(19)
Bi1—$S2^{i}$	3.026(4)	S8—Bi1—S1	153.38(15)	$S6^{x}$—K2—$S6^{xi}$	153.05(15)
Bi1—$S4^{ii}$	3.091(5)	S5—Bi1—S3	80.15(13)	$S6^{x}$—K2—$S6^{iv}$	77.62(15)
Bi2—S6	2.770(4)	S2—Bi1—S3	142.73(12)	$S6^{xi}$—K2—$S6^{iv}$	108.84(15)
Bi2—$S6^{i}$	2.770(4)	S8—Bi1—S3	120.58(15)	$S6^{x}$—K2—$S6^{xii}$	108.84(15)
Bi2—S7	2.870(4)	S1—Bi1—S3	78.04(13)	$S6^{xi}$—K2—$S6^{xii}$	77.62(15)
Bi2—$S7^{i}$	2.870(4)	S5—Bi1—$S2^{i}$	136.37(13)	$S6^{iv}$—K2—$S6^{xii}$	153.04(15)
Bi2—S4	2.916(5)	S2—Bi1—$S2^{i}$	78.40(12)	$S6^{x}$—K2—$S8^{xiii}$	64.29(11)
Bi2—$S4^{i}$	2.916(5)	S8—Bi1—$S2^{i}$	67.38(13)	$S6^{xi}$—K2—$S8^{xiii}$	103.24(11)
		S1—Bi1—$S2^{i}$	114.76(14)	$S6^{iv}$—K2—$S8^{xiii}$	141.55(11)
K1—$S6^{vii}$	3.259(7)	S3—Bi1—$S2^{i}$	134.64(11)	$S6^{xii}$—K2—$S8^{xiii}$	54.66(11)
K1—S2	3.296(6)	S5—Bi1—$S4^{ii}$	116.36(15)	$S6^{x}$—K2—$S8^{xiv}$	103.24(11)
K1—$S3^{viii}$	3.302(7)	S2—Bi1—$S4^{ii}$	150.64(13)	$S6^{xi}$—K2—$S8^{xiv}$	64.29(11)
K1—$S5^{ix}$	3.334(7)	S8—Bi1—$S4^{ii}$	81.44(14)	$S6^{iv}$—K2—$S8^{xiv}$	54.66(11)
K1—$S3^{ix}$	3.340(7)	S1—Bi1—$S4^{ii}$	125.06(14)	$S6^{xii}$—K2—$S8^{xiv}$	141.55(11)
K1—S5	3.437(7)	S3—Bi1—$S4^{ii}$	65.78(12)	$S8^{xiii}$—K2—$S8^{xiv}$	127.89(16)
K1—$S7^{viii}$	3.663(8)	$S2^{i}$—Bi1—$S4^{ii}$	72.42(12)	$S6^{x}$—K2—$S8^{ii}$	141.55(11)
K1—$S1^{vii}$	3.703(7)	S6—Bi2—$S6^{i}$	102.1(2)	$S6^{xi}$—K2—$S8^{ii}$	54.66(11)
K2—$S6^{x}$	3.437(5)	S6—Bi2—S7	70.95(13)	$S6^{iv}$—K2—$S8^{ii}$	64.29(11)
K2—$S6^{xi}$	3.437(5)	$S6^{i}$—Bi2—S7	85.25(15)	$S6^{xii}$—K2—$S8^{ii}$	103.24(11)
K2—$S6^{iv}$	3.437(5)	S6—Bi2—$S7^{i}$	85.25(15)	$S8^{xiii}$—K2—$S8^{ii}$	154.09(15)
K2—$S6^{xii}$	3.437(5)	$S6^{i}$—Bi2—$S7^{i}$	70.95(13)	$S8^{xiv}$—K2—$S8^{ii}$	59.10(16)
K2—$S8^{xiii}$	3.850(6)	S7—Bi2—$S7^{i}$	142.0(2)	$S6^{x}$—K2—$S8^{xv}$	54.66(11)
K2—$S8^{xiv}$	3.850(6)	S6—Bi2—S4	91.87(15)	$S6^{xi}$—K2—$S8^{xv}$	141.55(11)
K2—$S8^{ii}$	3.850(6)	$S6^{i}$—Bi2—S4	134.95(13)	$S6^{iv}$—K2—$S8^{xv}$	103.24(11)
K2—$S8^{xv}$	3.850(6)	S7—Bi2—S4	139.52(15)	$S6^{xii}$—K2—$S8^{xv}$	64.29(11)
K3—S3	4.006(9)	$S7^{i}$—Bi2—S4	67.81(13)	$S8^{xiii}$—K2—$S8^{xv}$	59.10(16)
K3—$S3^{v}$	4.006(9)	S6—Bi2—$S4^{i}$	134.94(13)	$S8^{xiv}$—K2—$S8^{xv}$	154.09(15)
K3—$S3^{vii}$	4.006(9)	$S6^{i}$—Bi2—$S4^{i}$	91.87(15)	$S8^{ii}$—K2—$S8^{xv}$	127.89(16)
K3—$S3^{xvi}$	4.006(9)	S7—Bi2—$S4^{i}$	67.81(13)	S3—K3—$S3^{v}$	89.8(2)
K3—$K1^{xvii}$	4.40(2)	$S7^{i}$—Bi2—$S4^{i}$	139.52(15)	S3—K3—$S3^{vii}$	89.8(2)
K3—$K1^{iii}$	4.40(2)	S4—Bi2—$S4^{i}$	107.97(19)	$S3^{v}$—K3—$S3^{vii}$	174.(4)
K3—$K1^{ii}$	4.40(2)			S3—K3—$S3^{xvi}$	174.(4)
K3—$K1^{xi}$	4.40(2)	$S6^{vii}$—K1—S2	74.07(15)	$S3^{v}$—K3—$S3^{xvi}$	89.8(2)
K3—$S5^{v}$	5.29(7)	$S6^{vii}$—K1—$S3^{viii}$	134.57(19)	$S3^{vii}$—K3—$S3^{xvi}$	89.8(2)
		S2—K1—$S3^{viii}$	60.85(13)	S3—K3—$S5^{v}$	56.8(8)

Table 5-5 continued

P1—S3^{viii}	2.020(6)	S6^{vii}—K1—S5^{ix}	109.81(19)	S3^{v}—K3—S5^{v}	44.1(7)
P1—S1	2.031(6)	S2—K1—S5^{ix}	116.74(19)	S3^{vii}—K3—S5^{v}	132.(2)
P1—S4	2.044(6)	S3^{viii}—K1—S5^{ix}	86.98(16)	S3^{xvi}—K3—S5^{v}	119.7(18)
P1—S2	2.071(6)	S6^{vii}—K1—S3^{ix}	108.58(18)	K1^{xvii}—K3—S5^{v}	157.(3)
P2—S7^{vii}	2.015(6)	S2—K1—S3^{ix}	174.7(2)	K1^{iii}—K3—S5^{v}	101.3(9)
P2—S8	2.022(7)	S3^{viii}—K1—S3^{ix}	116.8(2)	K1^{ii}—K3—S5^{v}	38.9(5)
P2—S6^{vii}	2.063(6)	S5^{ix}—K1—S3^{ix}	67.02(14)	K1^{xi}—K3—S5^{v}	87.0(7)
P2—S5	2.071(7)	S6^{vii}—K1—S5	61.52(14)		
		S2—K1—S5	65.47(13)	S3^{viii}—P1—S1	113.4(3)
		S3^{viii}—K1—S5	101.51(17)	S3^{viii}—P1—S4	109.2(3)
		S5^{ix}—K1—S5	170.7(2)	S1—P1—S4	109.4(3)
		S3^{ix}—K1—S5	111.46(18)	S3^{viii}—P1—S2	109.5(3)
		S6^{vii}—K1—S7^{viii}	71.44(16)	S1—P1—S2	106.4(3)
		S2—K1—S7^{viii}	66.27(14)	S4—P1—S2	108.8(3)
		S3^{viii}—K1—S7^{viii}	84.98(17)	S7^{vii}—P2—S8	110.6(3)
		S5^{ix}—K1—S7^{viii}	57.34(14)	S7^{vii}—P2—S6^{vii}	106.8(3)
		S3^{ix}—K1—S7^{viii}	118.75(18)	S8—P2—S6^{vii}	110.9(3)
		S5—K1—S7^{viii}	119.20(18)	S7^{vii}—P2—S5	111.1(3)
		S6^{vii}—K1—S1^{vii}	69.13(15)	S8—P2—S5	105.5(3)
		S2—K1—S1^{vii}	120.95(17)	S6^{vii}—P2—S5	112.0(3)

(i) 0.5+y, -0.5+x, 0.5-z; (ii) 0.5-y, 0.5-x, 0.5+z; (iii) x, 0.5-y, 0.5+z; (iv) 0.5+y, -x, 1-z; (v) y, 0.5-x, z; (vi) 1-x, -0.5+y, 0.5-z; (vii) 0.5-y, x, z; (viii) 0.5-y, 0.5-x, -0.5+z; (ix) x, 0.5-y, -0.5+z; (x) x, -0.5-y, 0.5+z; (xi) 0.5-x, y, 0.5+z; (xii) -y, -0.5+x, 1-z; (xiii) -0.5+x, -0.5+y, 1-z; (xiv) 1-x, -y, 1-z; (xv) y, -1+x, 0.5+z; (xvi) 0.5-x, 0.5-y, z; (xvii) y, x, 0.5+z; (xviii) 1-x, -y, -z.

$K_{1.5}Bi_{2.5}(PS_4)_3$ [II]:

The structure of this compound is incommensurately modulated, and has a 3D framework structure, Figure 5- 4A. $K_{1.5}Bi_{2.5}(PS_4)_3$ [II] adopts the monoclinic super spacegroup $P2/c(\alpha\frac{1}{2}\gamma)$ with the modulation vector having a*, b* and c* components. The related compound $K_3Ce_2(PS_4)_3$.[50] was also found to be modulated and has the super spacegroup $C2/c(\alpha 0 \gamma)$.

In the orthorhombic model before the modulation was introduced, there was one Bi^{3+} site (Bi(1)), one K^+ site (K(2)), and one site that could only be described as being mixed between K^+ and Bi^{3+} (K(3)/Bi(3)) with a 50% occupancy, Figure 5-5. The

framework is built of interconnected "$Bi_2(PS_4)_4$" double chains, Figure 5-4B. Bi(2) atoms are bridged by S(11) along the a-axis in a zigzag pattern to form a single chain. Two chains are connected by a P(2) centered $[PS_4]^{3-}$ ion to form the double chains. Neighboring double chains are then interconnected by bridging P(1) centered $[PS_4]^{3-}$ ions and by K(3) ions that undulate down the a-axis. The K(3)/Bi(3) and K(4)/Bi(4) mixed sites are located in the channels between the chains. Selected bond lengths and angles are given in Table 5-6.

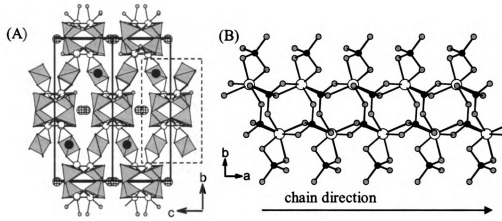

Figure 5-4. (A) The 3D approximant structure of $K_{1.5}Bi_{2.5}(PS_4)_3$ as viewed down [100] showing the assembly of the chains centered at ½ the [010] and [001] axes, and (B) the assembly of "$Bi_2(PS_4)_4$" chains, emphasized in a rectangular outline. (B) An individual "$Bi_2(PS_4)_4$" chain as viewed down the [001] axis.

In the case of compounds [I], [III], $KBiP_2S_7$,[26,30] $KBiP_2S_6$[31] and $K_3Bi(PS_4)_2$[30] no cation site disorder was observed, and therefore the possibility of a structural modulation rather than random disorder was considered. X-ray diffraction data with a longer exposure time was subsequently collected to look for satellite reflections indicating long range order. The data revealed first order reflections that could be

indexed with the modulation vector $\mathbf{q} = 0.25\mathbf{a}^*+0.5\mathbf{b}^*+0.16\mathbf{c}^*$. Higher order satellite reflections were not observed.

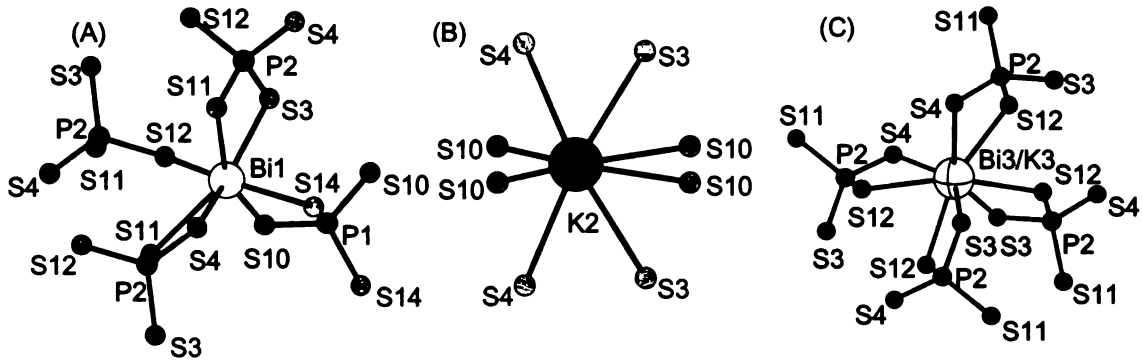

Figure 5-5. The coordination environment of (A) Bi(1), (B) K(2), and (C) the K(3)/Bi(3) mixed site in $K_{1.5}Bi_{2.5}(PS_4)_3$.

Table 5-6. Selected bond lengths for $K_{1.5}Bi_{2.5}(PS_4)_3$ with bond lengths (Å), with standard uncertainties in parenthesis.

	average	min	max				
Bi1-S1a	2.712(5)	2.704(6)	2.719(6)		S1a-P1a-S2a		110.2(2)
Bi1-S1b	2.797(5)	2.740(5)	2.852(5)		S1a-P1a-S3a		107.3(2)
Bi1-S3a	2.715(5)	2.689(5)	2.740(5)		S1a-P1a-S4a		108.9(2)
Bi1-S2b	3.193(5)	3.020(5)	3.371(5)		S2a-P1a-S3a		111.1(2)
Bi1-S3b	2.829(5)	2.796(5)	2.866(5)		S2a-P1a-S4a		109.1(2)
Bi1-S3b	3.006(5)	2.970(5)	3.046(5)		S3a-P1a-S4a		110.2(2)
Bi1-S4b	2.895(5)	2.876(5)	2.919(5)				
Bi2-S2a	2.720(6)	2.717(5)	2.724(5)	K4-S1c	3.063(5)	3.012(5)	3.107(5)
Bi2-S4a	2.729(5)	2.724(5)	2.735(5)	K4-S1c	3.064(5)	3.011(5)	3.108(5)
Bi2-S1c	2.797(5)	2.763(5)	2.833(5)	K4-S2c	3.141(5)	3.106(5)	3.169(5)
Bi2-S2c	3.200(5)	3.155(5)	3.241(5)	K4-S2c	3.140(5)	3.106(5)	3.170(5)
Bi2-S3c	2.831(5)	2.821(5)	2.839(5)	K4-S4c	2.967(5)	2.952(5)	2.981(5)
Bi2-S3c	3.004(5)	2.992(5)	3.015(5)	K4-S4c	3.072(5)	3.056(5)	3.087(5)
Bi2-S4c	2.892(5)	2.878(5)	2.907(5)	K4-S4c	2.968(5)	2.951(5)	2.982(5)
				K4-S4c	3.073(5)	3.056(5)	3.087(5)
Bi3-S1b	3.069(5)	3.043(5)	3.099(5)				
Bi3-S1b	3.073(5)	3.043(5)	3.098(5)	K1-S1a	3.419(7)	3.382(7)	3.450(7)
Bi3-S2b	3.132(5)	3.036(5)	3.223(5)	K1-S1a	3.487(7)	3.465(7)	3.506(7)
Bi3-S2b	3.126(5)	3.036(5)	3.223(5)	K1-S2a	3.400(7)	3.377(7)	3.421(7)
Bi3-S4b	2.974(5)	2.899(5)	3.055(5)	K1-S2a	3.499(7)	3.452(7)	3.542(7)
Bi3-S4b	3.063(5)	3.007(5)	3.124(5)	K1-S1b	3.604(8)	3.597(8)	3.612(8)
Bi3-S4b	2.980(5)	2.899(5)	3.056(5)	K1-S2b	3.452(8)	3.385(8)	3.531(8)
Bi3-S4b	3.067(5)	3.006(5)	3.124(5)	K1-S1c	3.600(8)	3.554(8)	3.649(8)
				K1-S2c	3.451(9)	3.428(9)	3.476(9)
K3-S1b	3.069(5)	3.043(5)	3.099(5)				
K3-S1b	3.073(5)	3.043(5)	3.098(5)	P1a-S1a	2.062(5)	2.062(5)	2.062(5)
K3-S2b	3.132(5)	3.036(5)	3.223(5)	P1a-S2a	2.035(5)	2.035(5)	2.035(5)
K3-S2b	3.126(5)	3.036(5)	3.223(5)	P1a-S3a	2.034(6)	2.034(6)	2.035(5)
K3-S4b	2.974(5)	2.899(5)	3.055(5)	P1a-S4a	2.045(6)	2.044(6)	2.045(5)

Table 5-6 continued

K3-S4b	3.063(5)	3.007(5)	3.124(5)
K3-S4b	2.980(5)	2.899(5)	3.056(5)
K3-S4b	3.067(5)	3.006(5)	3.124(5)
Bi4-S1c	3.063(5)	3.012(5)	3.107(5)
Bi4-S1c	3.064(5)	3.011(5)	3.108(5)
Bi4-S2c	3.141(5)	3.106(5)	3.169(5)
Bi4-S2c	3.140(5)	3.106(5)	3.170(5)
Bi4-S4c	2.967(5)	2.952(5)	2.981(5)
Bi4-S4c	3.072(5)	3.056(5)	3.087(5)
Bi4-S4c	2.968(5)	2.951(5)	2.982(5)
Bi4-S4c	3.073(5)	3.056(5)	3.087(5)

Upon transformation to $P2/c(\alpha\frac{1}{2}\gamma)00$, the mixed K/Bi position from the orthorhombic model was split into two positions (K(3)/Bi(3)) and K(4)/Bi(4)), and all thermal displacement parameters were reasonable. The application of an occupational modulation indicated that the modulation between K(4) and Bi(4) had a small amplitude whereas the modulation between K(3) and B(3) had a larger amplitude, Figure 5-6. A summary of the applied modulation waves is displayed in Table 5-7. After taking into account this occupational modulation, the stoichiometry refined to $K_{1.47}Bi_{2.49}P_3S_{12}$, in close agreement with the microprobe analysis. A positional modulation was then applied to all atoms in the structure as well as to the rigid $[PS_4]^{3-}$ units. The largest positional deviations (~ 0.1 Å) were observed in Bi(1) and the $[PS_4]^{3-}$ tetrahedron closest to it. The modulation over several unit cells is displayed in Figure 5-7.

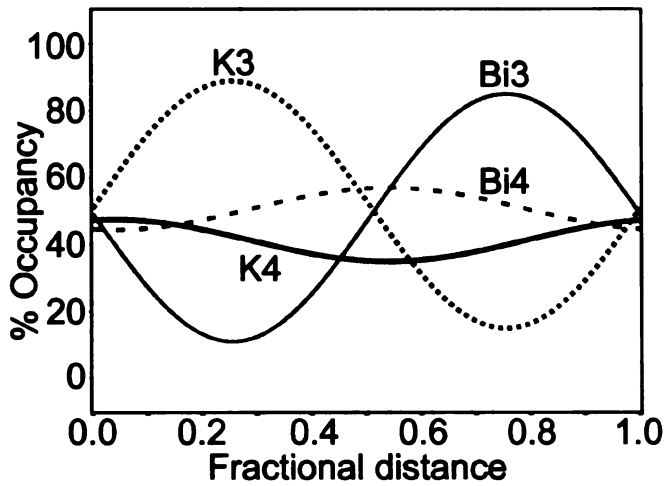

Figure 5-6. Percent occupancies of the complementary modulated sites K(3)/Bi(3) and K(4)/Bi(4) in $K_{1.5}Bi_{2.5}(PS_4)_3$ with the ordinate representing the fractional distance along the modulation axis.

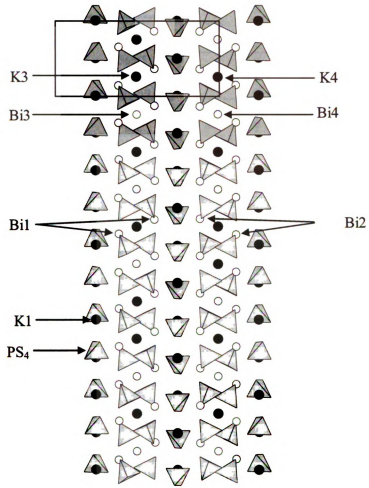

Figure 5-7. View of $K_{1.5}Bi_{2.5}(PS_4)_3$ down the *b* axis, showing how the K and Bi atoms interchange differently along the *c* axis for the K3/Bi3 and K4/Bi4 pairs. The subcell is displayed in black lines.

Table 5-7. Modulation parameters for $K_{1.5}Bi_{2.5}(PS_4)_3$

Occupation waves			
		U_{cos}	U_{sin}
Bi3		-0.0512(7)	0.366(5)
K3		0.0512(7)	-0.366(5)
Bi4		-0.062(4)	0.0083(6)
K4		0.062(4)	-0.0083(6)
Displacement waves			
		U_{cos}	U_{sin}
Bi1	x	-0.00111(5)	-0.00083(5)
	y	-0.01021(9)	-0.00568(10)
	z	0.00604(9)	0.00927(8)
Bi2	x	0.00004(5)	0.00002(5)
	y	0.00013(11)	-0.00115(11)
	z	-0.00096(10)	-0.00114(10)
Bi3	x	0.00107(11)	0.000150(15)
	y	0.00108(4)	-0.0077(3)
	z	0.00160(19)	0.00022(3)
K3	x	0.00107(11)	0.000150(15)
	y	0.00108(4)	-0.0077(3)
	z	0.00160(19)	0.00022(3)
Bi4	x	0.000081(16)	0.00061(12)
	y	-0.0025(2)	0.00033(3)
	z	-0.00025(3)	-0.00191(19)
K4	x	0.000081(16)	0.00061(12)
	y	-0.0025(2)	0.00033(3)
	z	-0.00025(3)	-0.00191(19)
K1	x	-0.0009(3)	-0.0001(3)
	y	0.0003(7)	0.0060(7)
	z	0.0035(6)	0.0030(6)
P1a	x	-0.00034(15)	-0.00102(14)
	y	-0.0005(3)	-0.0026(3)
	z	0.0027(2)	0.0071(2)
P1b	x	-0.00158(13)	-0.00158(12)
	y	-0.0037(3)	-0.0042(3)
	z	0.0045(3)	0.0096(2)
P1c	x	-0.00072(13)	-0.00073(13)
	y	0.0026(3)	0.0023(3)
	z	-0.0011(2)	-0.0013(2)
S1a	x	-0.0009(2)	-0.0008(2)
	y	-0.0007(4)	-0.0009(3)
	z	0.0025(4)	0.0051(3)
S2a	x	0.0003(2)	0.0010(2)
	y	0.0001(4)	0.0004(3)
	z	0.0030(4)	0.0090(3)
S3a	x	-0.00019(18)	-0.00188(17)
	y	-0.0022(5)	-0.0072(5)
	z	0.0028(4)	0.0110(4)
S4a	x	-0.00051(18)	-0.00234(17)
	y	0.0008(5)	-0.0028(5)
	z	0.0026(4)	0.0030(4)
S1b	x	-0.0015(2)	-0.00105(19)
	y	-0.0030(5)	-0.0028(4)
	z	0.0043(4)	0.0095(3)
S2b	x	-0.00153(19)	-0.00260(18)
	y	-0.0039(5)	-0.0072(4)
	z	0.0045(4)	0.0105(3)
S3b	x	-0.00183(18)	-0.00083(18)
	y	-0.0035(4)	-0.0032(4)
	z	0.0050(4)	0.0119(4)
S4b	x	-0.00148(18)	-0.00180(18)
	y	-0.0043(5)	-0.0034(4)
	z	0.0045(4)	0.0063(4)
S1c	x	-0.00089(19)	-0.0008(2)
	y	0.0028(5)	0.0030(5)
	z	-0.0009(4)	-0.0016(4)
S2c	x	-0.00073(19)	-0.00082(19)
	y	0.0033(5)	0.0021(5)
	z	-0.0011(4)	-0.0014(4)
S3c	x	-0.00043(18)	-0.00042(18)
	y	0.0025(4)	0.0024(4)
	z	-0.0014(4)	-0.0008(4)
S4c	x	-0.00084(18)	-0.00085(18)
	y	0.0019(4)	0.0016(4)
	z	-0.0010(4)	-0.0013(4)

$K_9Bi(PS_4)_4$ [III]:

Compound [III] has discreet molecules of $[Bi(PS_4)_4]^{9-}$ and is structurally related to $Rb_9Ce(PS_4)_4$[47] and $K_9Ce(PS_4)_4$,[51] Figure 5-8A. The $[Bi(PS_4)_4]^{9-}$ molecules are arranged in layers parallel to the bc-plane with the K^+ atoms in between. The molecular complex $[Bi(PS_4)_4]^{9-}$ anion features two chelating $[PS_4]^{3-}$ ligands and two monodentate

$[PS_4]^{3-}$ anions, Figure 5- 8B. The average Bi-S distance is 2.86 Å. The next-nearest S atoms on the monodentate $[PS_4]^{3-}$ are 3.708(4) Å away from Bi. K^+ is in a distorted bicapped octahedral site with K-S distances averaging 3.38 Å, Figure 5-9. The P-S distances average 2.04 Å. Selected bond lengths and angles are displayed in Table 5-8.

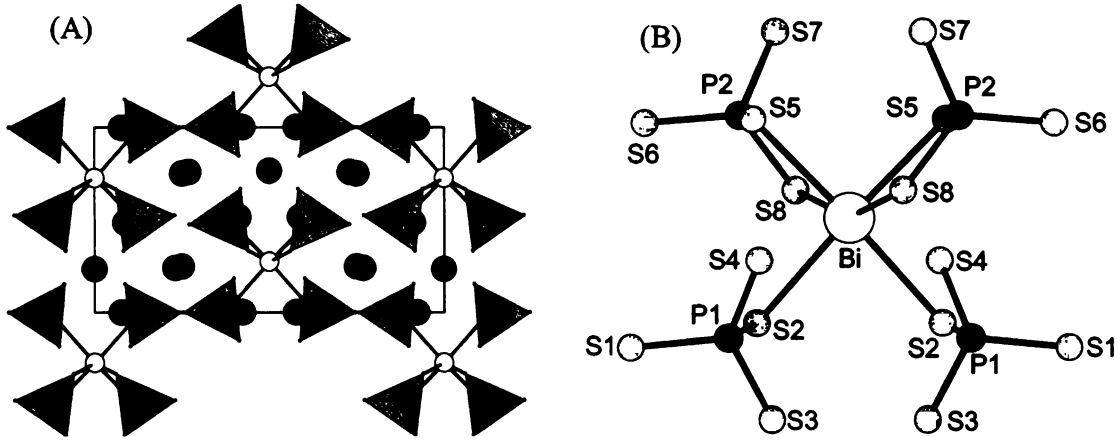

Figure 5-8. (A) View down [010] of $K_9Bi(PS_4)_4$ and (B) a view of an individual molecule of $[Bi(PS_4)]^{9-}$.

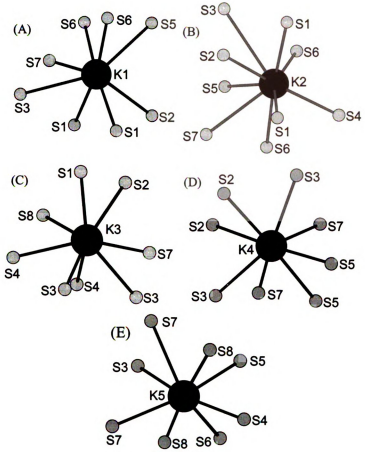

Figure 5-9. The coordination environment of (A) K(1), (B) K(2), (C) K(3), (D) K(4), and (E) K(5) ions in $K_9Bi(PS_4)_4$.

Table 5-8. Selected bond lengths and angles for $K_9Bi(PS_4)_4$ with bond lengths (Å) and angles (°), with standard uncertainties in parenthesis.

Bi—S5^{i}	2.842(3)	S5^{i}—Bi—S5	89.05(11)	S8^{i}—K3—S3^{v}	126.85(10)
Bi—S5	2.842(3)	S5^{i}—Bi—S8	93.86(8)	S2^{i}—K3—S3^{v}	158.60(11)
Bi—S8	2.866(4)	S5—Bi—S8	69.38(8)	S1^{xi}—K3—S3^{v}	98.69(9)
Bi—S8^{i}	2.866(4)	S5^{i}—Bi—S8^{i}	69.38(8)	S4^{v}—K3—S3	118.13(11)
Bi—S2	2.877(3)	S5—Bi—S8^{i}	93.86(8)	S7^{x}—K3—S3	64.73(8)
Bi—S2^{i}	2.877(3)	S8—Bi—S8^{i}	156.95(12)	S8^{i}—K3—S3	109.25(11)
		S5^{i}—Bi—S2	175.95(8)	S2^{i}—K3—S3	94.43(8)
K1—S1^{ii}	3.194(5)	S5—Bi—S2	94.04(7)	S1^{xi}—K3—S3	146.18(12)
K1—S6^{ii}	3.215(4)	S8—Bi—S2	84.79(9)	S3^{v}—K3—S3	88.21(9)
K1—S2^{ii}	3.284(3)	S8^{i}—Bi—S2	112.95(9)	S4^{v}—K3—S4	83.0(1)
K1—S1	3.386(5)	S5^{i}—Bi—S2^{i}	94.04(7)	S7^{x}—K3—S4	119.86(10)
K1—S5^{ii}	3.453(3)	S5—Bi—S2^{i}	175.95(8)	S8^{i}—K3—S4	56.48(9)
K1—S6^{iii}	3.457(4)	S8—Bi—S2^{i}	112.95(9)	S2^{i}—K3—S4	92.41(9)
K1—S3	3.558(4)	S8^{i}—Bi—S2^{i}	84.79(9)	S1^{xi}—K3—S4	148.34(12)
K1—S7^{iii}	3.661(4)	S2—Bi—S2^{i}	83.0(1)	S3^{v}—K3—S4	106.37(9)
K1—P1^{ii}	3.664(3)	S1^{ii}—K1—S6^{ii}	170.20(11)	S3—K3—S4	55.20(8)
K1—P2^{ii}	3.790(3)	S1^{ii}—K1—S2^{ii}	61.85(8)	S7—K4—S7^{i}	145.23(13)
K2—S1^{vi}	3.250(5)	S6^{ii}—K1—S2^{ii}	108.47(10)	S7—K4—S3^{vi}	122.32(8)
K2—S1^{vii}	3.251(5)	S1^{ii}—K1—S1	85.44(5)	S7^{i}—K4—S3^{vi}	67.03(7)
K2—S6^{viii}	3.317(4)	S6^{ii}—K1—S1	89.34(11)	S7—K4—S3^{xii}	67.03(7)
K2—S4^{vii}	3.348(4)	S2^{ii}—K1—S1	67.51(9)	S7^{i}—K4—S3^{xii}	122.32(8)
K2—S6	3.508(4)	S1^{ii}—K1—S5^{ii}	116.05(11)	S3^{vi}—K4—S3^{xii}	152.05(13)
K2—S5	3.518(3)	S6^{ii}—K1—S5^{ii}	60.25(8)	S7—K4—S2^{vi}	89.39(8)
K2—S2^{vi}	3.673(3)	S2^{ii}—K1—S5^{ii}	76.74(7)	S7^{i}—K4—S2^{vi}	120.21(9)
K2—P2	3.680(3)	S1—K1—S5^{ii}	121.91(10)	S3^{vi}—K4—S2^{vi}	60.83(8)
K2—P1^{vi}	3.769(3)	S1^{ii}—K1—S6^{iii}	100.37(11)	S3^{xii}—K4—S2^{vi}	95.12(9)
K2—S7	3.781(4)	S6^{ii}—K1—S6^{iii}	85.94(5)	S7—K4—S2^{xii}	120.21(9)
K3—S4^{v}	3.234(4)	S2^{ii}—K1—S6^{iii}	121.83(11)	S7^{i}—K4—S2^{xii}	89.39(8)
K3—S7^{x}	3.283(4)	S1—K1—S6^{iii}	170.52(11)	S3^{vi}—K4—S2^{xii}	95.12(9)
K3—S8^{i}	3.284(4)	S5^{ii}—K1—S6^{iii}	62.30(7)	S3^{xii}—K4—S2^{xii}	60.83(8)
K3—S2^{i}	3.292(4)	S1^{ii}—K1—S3	97.90(9)	S2^{vi}—K4—S2^{xii}	68.98(10)
K3—S1^{xi}	3.347(4)	S6^{ii}—K1—S3	86.14(9)	S7—K4—S5	61.75(7)
K3—S3^{v}	3.372(4)	S2^{ii}—K1—S3	122.53(9)	S7^{i}—K4—S5	89.39(9)
K3—S3	3.380(4)	S1—K1—S3	57.13(8)	S3^{vi}—K4—S5	82.21(7)
K3—S4	3.710(4)	S5^{ii}—K1—S3	146.04(10)	S3^{xii}—K4—S5	121.80(8)
K4—S7	3.192(3)	S6^{iii}—K1—S3	114.24(9)	S2^{vi}—K4—S5	109.67(6)
K4—S7^{i}	3.192(3)	S1^{ii}—K1—S7^{iii}	81.91(9)	S2^{xii}—K4—S5	177.32(8)
K4—S3^{vi}	3.268(3)	S6^{ii}—K1—S7^{iii}	107.89(9)	S7—K4—S5^{i}	89.38(9)
K4—S3^{xii}	3.268(3)	S2^{ii}—K1—S7^{iii}	143.06(11)	S7^{i}—K4—S5^{i}	61.74(7)
K4—S2^{vi}	3.366(3)	S1—K1—S7^{iii}	119.28(9)	S3^{vi}—K4—S5^{i}	121.80(8)
K4—S2^{xii}	3.366(3)	S5^{ii}—K1—S7^{iii}	116.94(8)	S3^{xii}—K4—S5^{i}	82.21(7)
K4—S5	3.400(3)	S6^{iii}—K1—S7^{iii}	54.93(7)	S2^{vi}—K4—S5^{i}	177.32(8)
K4—S5^{i}	3.400(3)	S3—K1—S7^{iii}	66.31(8)	S2^{xii}—K4—S5^{i}	109.67(6)
K5—S5	3.174(4)	S1^{vi}—K2—S1^{vii}	86.79(5)	S5—K4—S5^{i}	71.78(10)

Table 5-8 continued

K5—S4	3.239(4)	$S1^{vi}$—K2—$S6^{viii}$	89.96(11)	S5—K5—S4	79.56(10)
K5—$S3^{vi}$	3.272(4)	$S1^{vii}$—K2—$S6^{viii}$	159.63(11)	S5—K5—$S3^{vi}$	85.70(9)
K5—$S7^{xiii}$	3.310(4)	$S1^{vi}$—K2—$S4^{vii}$	93.14(10)	S4—K5—$S3^{vi}$	165.05(12)
K5—$S8^{i}$	3.324(4)	$S1^{vii}$—K2—$S4^{vii}$	60.90(8)	S5—K5—$S7^{xiii}$	158.79(11)
K5—$S7^{i}$	3.518(4)	$S6^{viii}$—K2—$S4^{vii}$	99.27(10)	S4—K5—$S7^{xiii}$	120.65(11)
K5—$S8^{xiii}$	3.542(4)	$S1^{vi}$—K2—S6	172.88(13)	$S3^{vi}$—K5—$S7^{xiii}$	73.73(8)
K5—$S6^{viii}$	3.552(4)	$S1^{vii}$—K2—S6	98.21(11)	S5—K5—$S8^{i}$	79.79(10)
K5—$P2^{xiii}$	3.805(4)	$S6^{viii}$—K2—S6	83.60(5)	S4—K5—$S8^{i}$	60.97(10)
		$S4^{vii}$—K2—S6	84.94(9)	$S3^{vi}$—K5—$S8^{i}$	118.98(11)
P1—S1	2.020(4)	$S1^{vi}$—K2—S5	122.35(11)	$S7^{xiii}$—K5—$S8^{i}$	114.51(11)
P1—S2	2.080(4)	$S1^{vii}$—K2—S5	134.49(11)	S5—K5—$S7^{i}$	87.60(9)
P1—S3	2.032(4)	$S6^{viii}$—K2—S5	62.98(8)	S4—K5—$S7^{i}$	118.15(11)
P1—S4	2.018(4)	$S4^{vii}$—K2—S5	138.2(1)	$S3^{vi}$—K5—$S7^{i}$	63.27(8)
P2—S5	2.068(4)	S6—K2—S5	57.01(7)	$S7^{xiii}$—K5—$S7^{i}$	87.73(9)
P2—S6	2.007(4)	$S1^{vi}$—K2—$S2^{vi}$	57.11(9)	$S8^{i}$—K5—$S7^{i}$	57.23(8)
P2—S7	2.023(4)	$S1^{vii}$—K2—$S2^{vi}$	64.41(9)	S5—K5—$S8^{xiii}$	143.94(10)
P2—S8	2.054(4)	$S6^{viii}$—K2—$S2^{vi}$	129.10(11)	S4—K5—$S8^{xiii}$	64.71(9)
		$S4^{vii}$—K2—$S2^{vi}$	118.29(8)	$S3^{vi}$—K5—$S8^{xiii}$	130.18(10)
		S6—K2—$S2^{vi}$	129.70(11)	$S7^{xiii}$—K5—$S8^{xiii}$	57.10(8)
		S5—K2—$S2^{vi}$	100.55(8)	$S8^{i}$—K5—$S8^{xiii}$	78.8(1)
		$S1^{vi}$—K2—S7	132.95(11)	$S7^{i}$—K5—$S8^{xiii}$	104.44(10)
		$S1^{vii}$—K2—S7	79.33(9)	S5—K5—$S6^{viii}$	63.90(8)
		$S6^{viii}$—K2—S7	116.76(9)	S4—K5—$S6^{viii}$	85.86(10)
		$S4^{vii}$—K2—S7	117.35(10)	$S3^{vi}$—K5—$S6^{viii}$	85.38(10)
		S6—K2—S7	53.47(8)	$S7^{xiii}$—K5—$S6^{viii}$	108.34(10)
		S5—K2—S7	55.16(7)	$S8^{i}$—K5—$S6^{viii}$	134.95(11)
		$S2^{vi}$—K2—S7	76.48(8)	$S7^{i}$—K5—$S6^{viii}$	139.56(10)
		P2—K2—S7	31.43(6)	$S8^{xiii}$—K5—$S6^{viii}$	115.53(10)
		$P1^{vi}$—K2—S7	101.97(8)	S4—P1—S1	111.9(2)
		$S4^{v}$—K3—$S7^{x}$	131.94(10)	S4—P1—S3	109.04(16)
		$S4^{v}$—K3—$S8^{i}$	67.85(9)	S1—P1—S3	110.24(19)
		$S7^{x}$—K3—$S8^{i}$	160.19(11)	S4—P1—S2	107.42(16)
		$S4^{v}$—K3—$S2^{i}$	134.64(11)	S1—P1—S2	108.60(16)
		$S7^{x}$—K3—$S2^{i}$	89.14(9)	S3—P1—S2	109.56(15)
		$S8^{i}$—K3—$S2^{i}$	72.14(9)	S6—P2—S7	109.34(17)
		$S4^{v}$—K3—$S1^{xi}$	93.46(11)	S6—P2—S8	113.76(18)
		$S7^{x}$—K3—$S1^{xi}$	85.65(12)	S7—P2—S8	107.16(17)
		$S8^{i}$—K3—$S1^{xi}$	92.98(12)	S6—P2—S5	110.70(16)
		$S2^{i}$—K3—$S1^{xi}$	67.88(8)	S7—P2—S5	111.75(16)
		$S4^{v}$—K3—$S3^{v}$	59.84(8)	S8—P2—S5	104.03(17)
		$S7^{x}$—K3—$S3^{v}$	72.78(8)		

(i) -x, -y, z; (ii) 0.5-x, -0.5+y, 2-z; (iii) x, -1+y, 1+z; (iv) x, y, 1+z; (v) -x, -1-y, z; (vi) x, y, -1+z; (vii) 0.5-x, 0.5+y, 1-z; (viii) 0.5-x, -0.5+y, 1-z; (ix) x, 1+y, -1+z; (x) -x, -y, 1+z; (xi) -0.5+x, -0.5-y, 2-z; (xii) -x, -y, -1+z; (xiii) x, -1+y, z; (xiv) 0.5-x, 0.5+y, 2-z; (xv) 0.5+x, -0.5-y, 2-z; (xvi) x, 1+y, z.

Structural Dimensionality

To place the stoichiometry and the dimensionality of the compounds in a greater context, it is useful to consider each of the known $[PS_4]^{3-}$ containing compounds as a member of the homologous series $(K_3PS_4)_n(BiPS_4)_m$, Scheme 1.[31,34-36] In this formalism, the compound $BiPS_4$ is a member of the series with an n:m ratio of 0. $BiPS_4$ has a dense three-dimensional framework. As the n:m ratio increases the dimensionality of the framework is reduced. Thus, the Bi/P/S framework in $K_{1.5}Bi_{2.5}(PS_4)_3$ [II] at an n:m ratio of 0.20 is also three-dimensional but the framework architecture is relatively open with tunnels accommodating K ions. When the n:m ratio is increased to 0.33, an even more open three-dimensional framework compound $K_3Bi_3(PS_4)_3$ [I] is stabilized. A further increase of the n:m ratio to 1 gives the one-dimensional chains of $K_3Bi(PS_4)_2$, and the largest n:m ratio of 3 gives the molecular $K_9Bi(PS_4)_4$ [III]. As the n:m ratio is increased, the three-dimensional covalent $BiPS_4$ framework is dismantled by dilution with ionic K_3PS_4 that lowers dimensionality of the resultant compound. Dimensional reduction of a covalent framework can be a practical formalism in studying structural evolution in solids and has been discussed earlier as a means to controlling the structures and properties of materials.[52,53] For example, in the incorporation of K_2S into HgS amounts to the introduction of S^{2-} atoms in the diamond lattice of HgS and the generation of anionic low-dimensional $[Hg_xS_y]^{n-}$ frameworks. In essence, the dense packed lattice of the parent compound is "diluted" with S^{2-} atoms which progressively dismantle it. The K^+ acts as a "non-interfering" counterion. A chemical homology created in this way is of the type $(K_2S)_m(HgS)_n$.[54] Other such examples in chalcogenides include $(A_2Q)_m(CdQ)_n$[55] and $(A_2Q)_m(Bi_2Q_3)_n$[26,56] systems.

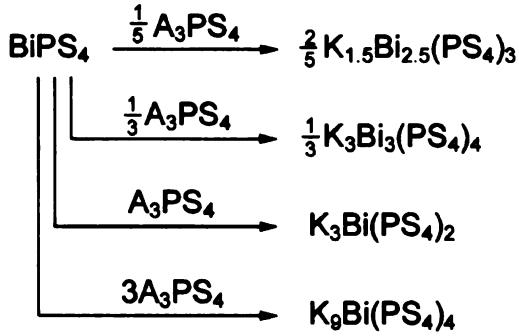

Scheme 1

Raman Spectroscopy

Raman spectra were collected for each of the title compounds, Figure 5-10. In each case, a peak at ~410 cm^{-1} was observed, which is attributed to the $[PS_4]^{3-}$ symmetrical stretch.[57] Also, each spectrum showed a band of overlapping peaks from ~150 cm^{-1} to ~300 cm^{-1} that showed similarities to the Raman spectrum of Bi_2S_3 suggesting that those peaks can be attributed to various Bi-S vibrational modes. A small amount highly crystalline material Bi_2S_3 may dominate the Raman spectrum even though it is present in small quantities.

Compound [II] also showed a third intense region of features with peaks centered at 519, 538, and 562 cm^{-1}, Figure 5-10B. Despite the presence of some of compound [II] in the sample used to collect a Raman spectrum of compound [I], this region of features was not evident for the NMR spectrum of $K_3Bi_3(PS_4)_4$, Figure 5-10A. At present, the exact assignment of these modes that appear to be unique to compound [II] is not complete, but it is possible that the metal-sulfur bonds would give rise to features in this region. Perhaps the distortion of the site to accommodate either K or Bi gives rise to the proper coordination geometry to yield Raman active modes. This region would be much weaker in the compounds that do not experience modulation, as supported by the

Raman spectra of compounds [I] and [III], Figure 5-10. Given that the intensity ratios of these peaks are dependent on the composition of the sample, it is unlikely that the higher energy peaks are overtones of those at lower energy.

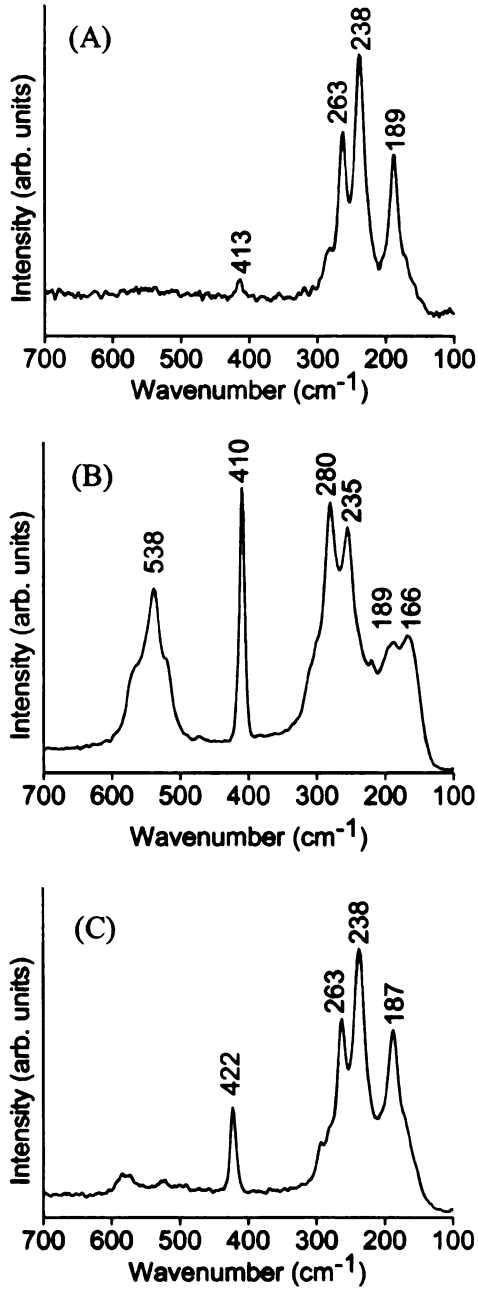

Figure 5-10. The Raman spectra of (A) $K_3Bi_3(PS_4)_4$, (B) $K_{1.5}Bi_{2.5}(PS_4)_3$ and (C) $K_9Bi(PS_4)_4$. The $K_3Bi_3(PS_4)_4$ sample used to collect the spectrum also contained several crystalline impurities (see text).

Solid State NMR

NMR spectroscopy has been a useful tool in studying modulated compounds and provides structural information that is complementary with the crystallographic data. The NMR line shapes and spin-lattice relaxation times of modulated compounds are known to be strongly dependent on the nature of the modulation vector **q**.[58] The spectral line-widths of modulated compounds tend to be broader than those of related compounds without modulation because the loss of translational periodicity gives rise to an essentially infinite number of different chemical environments. Therefore, the shielding parameter has a wide range of values, and the spectral line is broadened. Because of enhanced phonon scattering processes, spin-lattice relaxation in incommensurately modulated compounds is more efficient and longitudinal relaxation times tend to be shorter in such compounds.[58]

A summary of the chemical shifts, peak widths, intensities, and T_1 relaxation times for compounds [II] and [III] are found in Table 5-9 and the spectra of [II] and [III] are displayed in Figure 5-11. The NMR spectra of $K_{1.5}Bi_{2.5}(PS_4)_3$ [II] indicated two isotropic peaks centered at 88.4 ppm and 71.8 ppm with peak widths of 1150 and 890 Hz, respectively, and a longitudinal relaxation time T_1 of 600(100) s, Figure 5-11A. It is expected that compounds with significant contributions from incommensurate structural modulations have NMR line widths that are broadened and longitudinal relaxation times that are shortened relative to phases that are not modulated.[58] The NMR data on compound [II] indicated only a slight increase in line width but no significant decrease in the longitudinal relaxation time relative to the isoelemental compound [III]. This is consistent with the crystallographic evidence that suggests the effect of the modulation on compound [II] is relatively small.

Table 5-9. ^{31}P chemical shift (CS), chemical shift anisotropy (CSA), and T_1 values.

Compound	CS[a] (ppm)	Peak Widths (Hz)[a]	Integrated Intensities [b]	T_1[c] (s)
$K_{1.5}Bi_{2.5}(PS_4)_3$[II]	88.4, 71.8	1150, 890	45.5, 100.0	690(30), 510(60)
$K_9Bi(PS_4)_4$ [III]	79.7	640	100	640(120)

[a] Uncertainties in CS are approximately ± 0.5 ppm, and uncertainties in line widths are approximately ± 10 Hz. The chemical shift was determined by a mathematical deconvolution of the peaks after fitting with a Lorentzian lineshape, and peak widths were determined by calculating the full width at half maximum (FWHM).

[b] Intensities were normalized with the most intense peak set to 100.

[c] Uncertainties are indicated in parenthesis.

For compound [II], the upfield peak at 71.8 ppm had roughly double the integrated intensity of the downfield peak at 88.4 ppm. The crystallographic analysis suggested three unique P atoms, and the NMR intensity data could be explained by an overlap of the peaks arising from two of the P atoms. P(1b) and P(1c) are located within the double chain and have six metal ion neighbors two bonds away. P(1a) bridges neighboring double chains and has five metal ion neighbors two bonds away. The upfield peak can be attributed to P(1b) and P(1c) which are related by symmetry, and the downfield peak can be attributed to P(1a).

The NMR spectrum of $K_9Bi(PS_4)_4$ [III] contained two isotropic peaks centered at 86.1 ppm and 79.7 ppm, with 2:5 ratio of signal intensity, line widths of 300 and 640 Hz, and longitudinal relaxation times of 1350±125 s and 640±120 s, respectively, Figure 5-11B. There were two crystallographically inequivalent P sites in [III] that could have been assigned to the two peaks observed in the NMR. However, deviations from a 1:1 intensity ratio and different line widths and relaxation times for the two peaks do not support this assignment. A more plausible explanation is that the 64.3 ppm line is due to an impurity that may have been formed by the partial decomposition of compound [III]

by moisture. The narrower line width is consistent with a new mobile species formed by a reaction of [III] with atmospheric water. Signals from the two crystallographically inequivalent P sites in compound [III] were not resolved and were instead overlapped.

The presence of impurity phases in batches of compound $K_3Bi_3(PS_4)_4$ [I] was evident in the X-ray powder diffraction diagrams. These phases are thiophosphate species as indicated by the large number of peaks in the ^{31}P NMR spectrum. These peaks were not assigned.

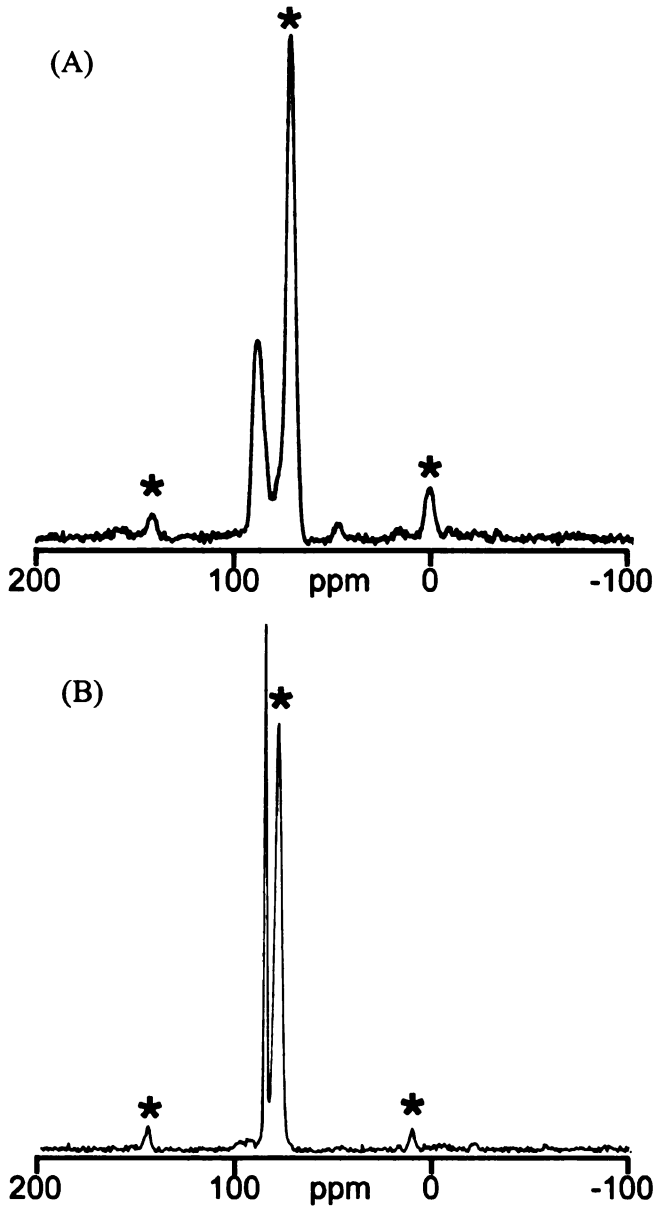

Figure 5-11. ^{31}P NMR spectra of (A) $K_{1.5}Bi_{2.5}(PS_4)_3$ and (B) $K_9Bi(PS_4)_4$ with isotropic peaks and their spinning sidebands grouped under like symbols.

CONCLUDING REMARKS

It is evident from this work that the group 15 alkali chalcophosphate class of compounds contains a rich and diverse collection of species with wide variability in bonding motifs.[19-25] The present report adds three new compounds to this class, including an example of a phase with an incommensurate structural modulation.

Decreased framework dimensionality is favored in compounds with a larger proportion of K_3PS_4. It is interesting to note that there are only several isomorphic compounds in common between the K/Bi/P/S and the previously reported Tl/Bi/P/S classes, namely $MBiP_2S_7$, and $M_3Bi(PS_4)_2$ (M = K, Tl). None of the new compounds described here have a known Tl^+ analog, and even though the $K_3Bi_3(PS_4)_4$ and $Tl_3Bi_3(PS_4)_4$ have the same stoichiometry, the structures are quite different.[33] Attempts to form mixed K/Tl solid solutions containing K/Tl/Bi/P/S may produce novel pseudo-quaternary materials with different structures. Finally, flexibility in the Bi coordination in this system is notable, as well as the chemical conditions required to stabilize each compound. The flux conditions previously studied[30] did not identify the title compounds. Thus, the diversity in the group 15 alkali metal chalcophosphates is even greater than was previously considered, and now even includes an example of a modulated compound.

REFERENCES

1. Galdamez, A.; Manriquez, V.; Kasaneva, J.; Avila, R. E. *Mater. Res. Bull.* **2003,** 38, 1063-1072.

2. Odoulov, S. G.; Shumelyuk, A. N.; Brost, G. A.; Magde, K. M. *Appl. Phys. Lett.* **1996,** 69, 3665-3667.

3. Shumelyuk, A.; Hryhorashchuk, A.; Odoulov, S. *Phys. Rev. A* **2005,** 72, 6.

4. Bourdon, X.; Maisonneuve, V.; Cajipe, V. B.; Payen, C.; Fischer, J. E. *J. Alloys Compd.* **1999,** 283, 122-127.

5. Carpentier, C. D.; Nitsche, R. *Mater. Res. Bull.* **1974,** 9, 1097-1100.

6. Rogach, E. D.; Sviridov, E. V.; Arnautova, E. A.; Savchenko, E. A.; Protsenko, N. P. *Zh. Tekh. Fiz.* **1991,** 61, 201-204.

7. Kroupa, J.; Tyagur, Y. I.; Grabar, A. A.; Vysochanskii, Y. M. *Ferroelectr.* **1999,** 223, 421-428.

8. Misuryaev, T. V.; Murzina, T. V.; Aktsipetrov, O. A.; Sherstyuk, N. E.; Cajipe, V. B.; Bourdon, X. *Solid State Commun.* **2000,** 115, 605-608.

9. Knaust, J. M.; Dorhout, P. K. *J. Chem. Crystallogr.* **2006,** 36, 217-223.

10. Chung, I.; Do, J.; Canlas, C. G.; Weliky, D. P.; Kanatzidis, M. G. *Inorg. Chem.* **2004,** 43, 2762-2764.

11. Kanatzidis, M. G. *Curr. Opin. Solid. St. M.* **1997,** 2, 139-149.

12. Coste, S.; Hanko, J.; Bujoli-Doeuff, M.; Louarn, G.; Evain, M.; Brec, R.; Alonso, B.; Jobic, S.; Kanatzidis, M. G. *J. Solid State Chem.* **2003,** 175, 133-145.

13. Manriquez, V.; Galdamez, A.; Ruiz-Leon, D. *Mater. Res. Bull.* **2006,** 41, 1337-1344.

14. Belkyal, I.; El Azhari, M.; Wu, Y. D.; Bensch, W.; Hesse, K. F.; Depmeier, W. *Solid State Sci.* **2006,** 8, 59-63.

15. Gieck, C.; Tremel, W. *Chem.-Eur. J.* **2002,** 8, 2980-2987.

16. Coste, S.; Kopnin, E.; Evain, M.; Jobic, S.; Brec, R.; Chondroudis, K.; Kanatzidis, M. G. *Solid State Sci.* **2002,** 4, 709-716.

17. Hess, R. F.; Gordon, P. L.; Tait, C. D.; Abney, K. D.; Dorhout, P. K. *J. Am. Chem. Soc.* **2002,** 124, 1327-1333.

18. Coste, S.; Kopnin, E.; Evain, M.; Jobic, S.; Payen, C.; Brec, R. *J. Solid State Chem.* **2001,** 162, 195-203.

19. Kanatzidis, M. G. *Chem. Mat.* **1990,** 2, 353-363.

20. Kanatzidis, M. G.; Park, Y. *J. Am. Chem. Soc.* **1989,** 111, 3767-3769.

21. Kanatzidis, M. G.; Park, Y. *Chem. Mat.* **1990,** 2, 99-101.

22. Park, Y. B.; Kanatzidis, M. G. *Angew. Chem. Int. Ed.* **1990,** 29, 914-915.

23. McCarthy, T. J.; Kanatzidis, M. G. *Inorg. Chem.* **1995,** 34, 1257-1267.

24. Chondroudis, K.; Kanatzidis, M. G. *J. Solid State Chem.* **1998,** 138, 321-328.

25. Iordanidis, L.; Bilc, D.; Mahanti, S. D.; Kanatzidis, M. G. *Journal of the American Chemical Society* **2003,** 125, 13741-13752.

26. McCarthy, T. J.; Ngeyi, S. P.; Liao, J. H.; Degroot, D. C.; Hogan, T.; Kannewurf, C. R.; Kanatzidis, M. G. *Chem. Mat.* **1993,** 5, 331-340.

27. Iordanidis, L.; Brazis, P. W.; Kyratsi, T.; Ireland, J.; Lane, M.; Kannewurf, C. R.; Chen, W.; Dyck, J. S.; Uher, C.; Ghelani, N. A.; Hogan, T.; Kanatzidis, M. G. *Chem. Mat.* **2001,** 13, 622-633.

28. Iordanidis, L.; Schindler, J. L.; Kannewurf, C. R.; Kanatzidis, M. G. *J. Solid State Chem.* **1999,** 143, 151-162.

29. Kohatsu, I.; Wuensch, B. J. *Acta. Crystallogr. B* **1976,** 32, 2401-2409.

30. McCarthy, T.; Kanatzidis, M. G. *J. Alloys Compd.* **1996,** 236, 70-85.

31. Manriquez, V.; Galdamez, A.; Leon, D. R.; Garland, M. T.; Jimenez, M. *Z. Krist. New Cryst. St.* **2003,** 218, 151-152.

32. Chung, I.; Karst, A. L.; Weliky, D. P.; Kanatzidis, M. G. *Inorg. Chem.* **2006,** 45, 2785-2787.

33. Gave, M.; Malliakas, C. D.; Weliky, D. P.; Kanatzidis, M. G. *Inorg. Chem.* **2007,** 46, 3632-3644.

34. Zimmermann, H.; Carpentier, C. D.; Nitsche, R. *Acta. Crystallogr. B* **1975,** 31, 2003-2006.

35. Chondroudis, K.; McCarthy, T. J.; Kanatzidis, M. G. *Inorg. Chem.* **1996,** 35, 840-844.

36. Chondroudis, K.; Kanatzidis, M. G.; Sayettat, J.; Jobic, S.; Brec, R. *Inorg. Chem.* **1997,** 36, 5859-5868.

37. Sayettat, J.; Bull, L. M.; Jobic, S.; Gabriel, J. C. P.; Fourmigue, M.; Batail, P.; Brec, R.; Inglebert, R. L.; Sourisseau, C. *J. Mater. Chem.* **1999,** 9, 143-153.

38. Fehér, F. Handbuch der Präparativen Anorganischen Chemie; Ferdinand Enke Verlag: Stuttgart, Germany, 1954; Vol. 1, pp 280-281.

39. Chondroudis, K.; Kanatzidis, M. G. *J. Solid State Chem.* **1998,** 136, 328-332.

40. *SMART, SAINT, SHELXTL V-5 and SADABS*, Bruker Analytical X-ray Instruments, Inc.: Madison, 1998.

41. *X-AREA, X-SHAPE, and X-RED*, STOE & Cie GmbH: Darmstadt, 2004.

42. Petricek, V.; Dusek, M.; Palatinus, L. *Jana2000. The Crystallographic Computing System*, Praha, Czech Republic, 2000.

43. Evain, M.; Boucher, F.; Gourdon, O.; Petricek, V.; Dusek, M.; Bezdicka, P. *Chem. Mat.* **1998,** 10, 3068-3076.

44. Gourdon, O.; Hanko, J.; Boucher, F.; Petricek, V.; Whangbo, M. H.; Kanatzidis, M. G.; Evain, M. *Inorg. Chem.* **2000,** 39, 1398-1409.

45. International Tables of Crystallography Vol. C; Kluwer Academic Publishers: Dordrecht, Netherlands, 2004.

46. Canlas, C. G.; Muthukumaran, R. B.; Kanatzidis, M. G.; Weliky, D. P. *Solid State Nucl. Magn. Reson.* **2003,** 24, 110-122.

47. Chondroudis, K.; Kanatzidis, M. G. *Inorg. Chem. Commun.* **1998,** 1, 55-57.

48. Nagy, T. F.; Mahanti, S. D.; Dye, J. L. *Zeolites* **1997,** 19, 57-64.

49. Stoltzfus, M. W.; Woodward, P. M.; Seshadri, R.; Klepeis, J. H.; Bursten, B. *Inorg. Chem.* **2007,** 46, 3839-3850.

50. Gauthier, G.; Evain, M.; Jobic, S.; Brec, R. *Solid State Sci.* **2002,** 4, 1361-1366.

51. Gauthier, G.; Jobic, S.; Danaire, V.; Brec, R.; Evain, M. *Acta Crystallogr. C* **2000,** 56, 117.

52. Tulsky, E. G.; Long, J. R. *Chem. Mat.* **2001,** 13, 1149-1166.

53. Long, J. R.; McCarty, L. S.; Holm, R. H. *J. Am. Chem. Soc.* **1996,** 118, 4603-4616.

54. Axtell, E. A.; Park, Y.; Chondroudis, K.; Kanatzidis, M. G. *J. Am. Chem. Soc.* **1998,** 120, 124-136.

55. Axtell, E. A.; Liao, J. H.; Pikramenou, Z.; Kanatzidis, M. G. *Chem.-Eur. J.* **1996,** 2, 656-666.

56. Kanatzidis, M. G.; McCarthy, T. J.; Tanzer, T. A.; Chen, L. H.; Iordanidis, L.; Hogan, T.; Kannewurf, C. R.; Uher, C.; Chen, B. X. *Chem. Mat.* **1996,** 8, 1465-1474.

57. Evenson, C. R.; Dorhout, P. K. *Inorg. Chem.* **2001,** 40, 2884-2891.

58. Blinc, R. *Phys. Rep.* **1981,** 79, 331-398.

CHAPTER 6

MIXED METAL ARGYRODITES: PHASE TRANSITIONS BY CHEMICAL COMPOSITION.

INTRODUCTION

The class of compounds known as the argyrodites are tetrahedrally close-packed structures with the formula $A^{m+}_{(12-n-x)/m}B^{n+}X^{2-}_{6-x}Y^{-}_{x}$ (A = Cu, Ag, Cd, Hg; B = Ga, Si, Ge, Sn, P, As; X = S, Se; Y = Cl, Br, I and $0 \leq x \leq 1$).[1] The mineral argyrodite, Ag_8GeS_6, is a naturally occurring representative of this class of compounds, and for historical reasons, the name also refers to the entire class. Most examples of argyrodites have a crystalline structure at higher temperatures with the spacegroup *F*-43*m* and significantly disordered cation sites. At reduced temperatures, various lower symmetry structures have been reported wherein the cations become more ordered.

All of the argyrodite structures can be considered as modifications to the *F*-43*m* structure of Cu_6PS_5Br.[1] In this structure, the Cu^+ ions are distributed randomly over a number of sites with local tetrahedral symmetry, Figure 6-1A. The *F*-43*m* symmetry is therefore somewhat misleading and only results because of the positional averaging that is inherent to X-ray crystallography. An anionic framework is formed by corner shared $[PS_4]^{3-}$ tetrahedra, Figure 6-1B. The remaining S^{2-} and Br^- ions are randomly mixed in an icosahedral site surrounded by $[PS_4]^{3-}$ tetrahedra, Figure 6-1C.

The parent Cu_6PS_5Br structure is modified in a number of different ways to form each of the other members of the argyrodite class of compounds. For example, the structure of γ-Ag_7PSe_6 was determined at 473 K,[2] and also contains $[PSe_4]^{3-}$ tetrahedra, but only half as many per unit cell as Cu_6PS_5Br. The other half of the sites are occupied by Se^{2-} ions. The metal cations, as in the case of Cu_6PS_5Br are disordered over a number of tetrahedral sites, but there is no atom in the icosahedral site. At lower temperature

(293 K), F-43m structure is modified, and the resultant compound β-Ag_7PSe_6 is formed. This compound has the $P2_13$ space group, and differs from the $F\text{-}43m$ structure in the arrangement of the Ag^+ ions. Rather than being disordered over a large number of tetrahedral sites, the Ag^+ ions preferentially occupy a smaller number of sites with slightly distorted linear, triangular, and tetrahedral metal-selenium coordination.[2-4] The decrease in symmetry as the temperature is lowered is perhaps misleading and is actually the result of the averaging of atomic positions that occurs on the relatively long timescales that diffraction data are collected.

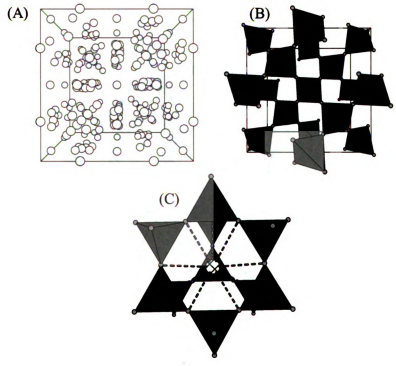

Figure 6-1. The room temperature structure of Cu_6PS_5Br in the $F\text{-}43m$ spacegroup showing (A) the disordered sites containing Cu^+ ions, (B) The anionic framework of corner shared $[PS_4]^{3-}$ tetrahedra, and (C) the icosahedral coordination of the mixed S/Br site. Hollow spheres are Cu, light grey spheres are S, and the central atom in (C) is the mixed S/Br site.

Another modification to the parent *F*-43*m* structure occurs in the compound Cd_4GeS_6, Figure 6-2.[5] This compound differs principally due to lowering of symmetry from cubic to monoclinic. This change in symmetry accommodates a distortion in the packing of the GeS_4 tetrahedra which occupy half of the tetrahedral sites, as is the case with the $P2_13$ structure, Figure 6-2. The packing of the S^{2-} ions in the other half of the sites is also distorted due to the monoclinic symmetry. Another significant difference is that the Cd^{2-} sites are ordered, rather than the disorder or partial disorder that is present in the cubic argyrodite modifications.

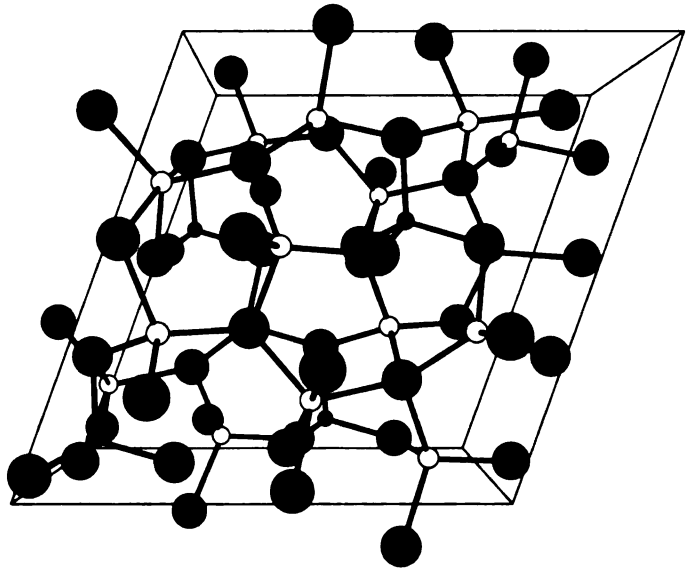

Figure 6-2. The structure of Cd_4GeS_6 down the *b*-axis showing the monoclinic cell. Hollow spheres are Cd, shaded spheres are S, and black spheres are P.

The elucidation of argyrodite structures are notoriously difficult because of significant twinning that occurs during the phase transition. For example, the structure of Cu_8GeS_6 was solved using a crystallographic model containing a 12-fold twin.[6] For the compound Ag_7TaS_6, a cubic *F*-43*m* structure was observed at 1123 K, and a monoclinic

structure was observed at 873 K. These structures were solved using the same crystal for data collection but the high temperature structure was refined as a single crystal, and the lower temperature structure was refined as a 24-fold twin.[7] The twinning might reasonably occur during the synthesis of these materials since the transition temperatures are near the temperatures used for the reaction. Significant twinning is therefore a frequent obstacle in the solution of argyrodite structures.

The novel argyrodite compounds presented herein were initially serendipitously discovered in attempts to synthesize analogs to the previously reported compounds $CuBiP_2Se_6$ and $AgBiP_2Se_6$[8] except with Hg in place of Bi. The motivation for this substitution was to look for novel optical or structural properties that would result from having vacancies in the framework as a result of the substitution for Bi^{3+}/Hg^{2+} i.e. that 1/3 of these metal sites would be vacant in the latter. Isotypic compounds with site vacancies were not produced, and instead compounds with argyrodite structures were formed.

This class of compounds has potential commercial relevance. Argyrodite compounds like Ag_7PSe_6 have been shown to have significant ionic conductivity[2] and therefore may be useful in production of selectively permeable coatings, and in next-generation metal ion batteries. Additionally, the robustness of the argyrodie framework allows for a wide range of chemical compositions with closely related structures, and therefore tuning physical properties by adjusting the identities and stoichiometric ratios of the constituent elements may be possible.

The new argyrodite compounds with the possible stoichiometries of Ag_5HgPSe_6, $Ag_3Hg_2PSe_6$, $Ag_3Hg_2PSe_6$, $AgHg_3PSe_6$, and $CuHg_3PSe_6$ are presented here as well as

the as-yet unidentified novel crystalline compound produced in a reaction targeting $Hg_{3.5}PSe_6$.

EXPERIMENTAL SECTION

Reagents

Chemicals were used as obtained unless otherwise noted: mercury (triple distilled, Bethlehem Apparatus Co. Inc., Hellertown, PA), selenium shot (99.999%, Tellurex, Inc, Traverse City, MI), phosphorus (amorphous red, MCB Reagents, Gibbstown, NJ), copper (electrolytic dust, Fisher Scientific, Pittsburgh, PA) and silver powder, prepared as below. Selenium was ground in an agate mortar and pestle to ~100 mesh.

Synthesis

Preparation of Silver Powder: Silver powder was prepared by cutting a silver coin (31g) into centimeter sized pieces, which were subsequently dissolved in 200 mL of concentrated nitric acid by stirring overnight. The solution was then neutralized by addition of ammonium hydroxide. Finely divided silver particles were obtained after addition of ~10g of sodium borohydride to the solution which were isolated by filtration, washed with water, and dried in a 100 °C oven.

$Ag_{7-x}Hg_{x/2}PSe_6$: Mixtures of Ag, Bi, P, and Se were combined in the appropriate stoichiometric ratios to form the nominal compositions of Ag_7PSe_6 Ag_5HgPSe_6, $Ag_3Hg_2PSe_6$, $AgHg_3PSe_6$, and $Hg_{3.5}PSe_6$ with a total reactant mass of ~2g. The resultant mixtures were loaded into fused silica tubes and flame sealed at a reduced pressure of ~10^{-4} mbar. The tubes were shaken to increase homogeneity, and then loaded

into a protective ceramic sheath. The mixtures were heated to 800 °C over 24h, held there for 24h, and then cooled back to room temperature over 48h. Shiny black polyhedral crystals were obtained, some as large as 0.5 mm, Figure 6-3A.

$CuHg_3PSe_6$: A mixture of Cu (0.0816 g, 1.28 mmol), Hg (0.2923 g, 1.45 mmol), P (0.0756 g, 2.44 mmol), and Se (0.5925 g, 7.50 mmol) was loaded into a fused silica ampoule and prepared for the furnace identically as the $Ag_{7-x}Hg_{x/2}PSe_6$ samples. The mixture was then heated to 700 °C over 24 h, held there for 24 h and then cooled over 96 h. Shiny black polyhedral crystals were obtained and EDS analysis on the crystal used for X-ray diffraction had the stoichiometry $Cu_{1.3}Hg_{2.8}P_{1.0}Se_{4.8}$. A scanning electron micrograph of some of the crystals isolated from the reaction is displayed in Figure 6-3A. One interesting but presently unexplained feature was the ~1μm surface detail, Figure 6-3B.

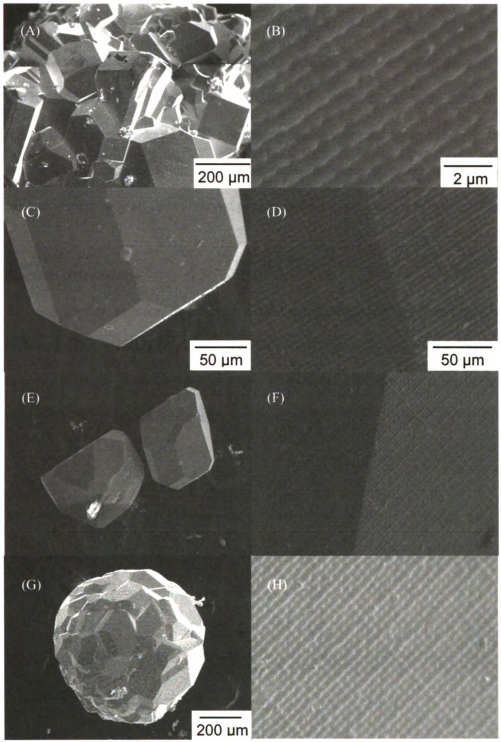

Figure 6-3. Scanning electron micrographs of the crystals formed in the reaction that produced $CuHg_3PSe_6$ with views of the ~2 µm surface detail observed on one of the of the crystals.

Powder X-ray Diffraction

Powder X-ray diffraction was performed with a Rigaku-Denki RW400F2 (Rotaflex) diffractometer equipped with a Cu *Kα* rotating anode operating at 45 kV and 100 mA with a 2°/min scan rate. The resultant powder patterns were indexed using the Jade 6.0 software package.[9] The indexing was performed by overlaying the powder pattern of the compound that was known to be an isomorphic analog, then refining the cell parameters to graft the overlayed peaks onto the experimental powder pattern.

Electron Microscopy

Scanning electron micrographs and energy dispersive spectroscopy (EDS) were collected using a JEOL JSM-35C electron microscope equipped with a Tracor Northern energy dispersive spectroscopy detector. EDS data were collected using an accelerating voltage of 25 kV and an accumulation time of 60 s.

Differential Thermal Analysis

Differential thermal analyses were performed with a Shimadzu DTA-50 thermal analyzer. A portion of the ingot obtained from the synthetic reaction weighing ~25 mg was finely ground and sealed in a fused silica ampoule under a reduced pressure of 10^{-4} mbar. An equivalent mass of alumina was sealed in an identical ampoule to serve as a reference. The samples were heated to 900 °C at a rate of 10 °C/min, cooled to 150 °C at a rate of 10 °C/min. The cycle was then repeated, except then cooled to room temperature.

Single Crystal X-ray Diffraction of $CuHg_3PSe_6$

A single crystal of $CuHg_3PSe_6$ with no obvious twinning was selected and X-ray diffraction data was subsequently collected on a Bruker SMART platform CCD diffractometer using Mo Kα radiation and operating at 40 kV and 40 mA. Individual frames were collected with a 10 sec exposure time and a 0.3° omega rotation. The SMART software was used for data collection and the SAINT software was used for data extraction and reduction. An analytical absorption correction to the data was performed using the SADABS software and direct methods were used to solve and refine the structure with the SHELXTL software package.[10]

The details of the refinement are displayed in Table 6-1. The unit cell of the crystal was monoclinic with a = 12.515(3) Å, b = 7.2328(14) Å, c = 12.446(3) Å and β = 109.36(3)°, and the structure was refined with the *Cc* space group. The structure closely resembles Cd_4GeS_6 with an isomorphic replacement with Cu and Hg for Cd, P for Ge, and Se for S.

The refinement suggested that the atoms Cu(1) and Hg(1) had complementary occupancy but were not located exactly on the same site. Each of the other Cu/Hg mixed sites, however, were reasonably constrained to occupy the same crystallographic site. In each case, the site occupancy refined to ~75% Hg and 25% Cu.

One potentially significant problem was with the relatively high residual electron density of 7.185 $e^-/Å^3$ that was located 1 Å away from the Cu(1) atom, Table 6-2. This residual electron density may be attributable to a third site in addition to the Cu(1) and Hg(1) atoms that were already accounted for, but this possibility was not explored. The isotropic thermal displacement parameter U(eq) for several atoms, namely P(1), Se(1), Se(2), Se(3) and Se(4) were unreasonably small. Another potential problem was observed in the anisotropic refinement of the thermal parameters wherein several of the tensors were zero, Table 6-3. This may be evidence for an unaccounted twin fragment.

Table 6-1. Crystallographic data and refinement details for Cu_3HgPSe_6.

Empirical formula	Cu Hg_3 P Se_6	
Formula weight	1170.04	
Temperature	293(2) K	
Wavelength	0.71073 Å	
Crystal system	Monoclinic	
Space group	*Cc*	
Unit cell dimensions	a = 12.515(3) Å	α= 90°
	b = 7.2328(14) Å	β= 109.36(3)°
	c = 12.446(3) Å	γ = 90°
Volume	1062.9(4) $Å^3$	
Z	4	
Density (calculated)	7.311 g/cm^3	
Absorption coefficient	65.799 mm^{-1}	
F(000)	1952	
Theta range for data collection	3.30 to 29.31°	
Index ranges	-17<=h<=16, -9<=k<=9, -17<=l<=16	
Reflections collected	6003	
Independent reflections	2564 [$R_{(int)}$ = 0.0706]	
Completeness to theta = 29.31°	98.6 %	
Refinement method	Full-matrix least-squares on F^2	
Data / restraints / parameters	2564 / 2 / 105	
Goodness-of-fit on F2	1.049	
Final R indices [I>σ(I)]	R1 = 0.0693, wR2 = 0.1552	
R indices (all data)	R1 = 0.0883, wR2 = 0.1622	
Extinction coefficient	0.00043(10)	
Largest diff. peak and hole	7.185 and -5.136 $e.Å^{-3}$	

Table 6-2. Fractional atomic coordinates and U(eq) values for $CuHg_3PSe_6$ with standard uncertainties in parenthesis.

atom	x	y	z	U(eq)[a]	Occupancy
Hg(1)	0.0163(2)	0.0828(3)	0.1250(2)	17(1)	75%
Cu(1)	-0.0153(17)	0.0350(30)	0.1625(16)	17(1)	25%
Hg(2)|Cu(2)	0.0354(1)	0.06471(3)	-0.0665(1)	22(1)	75%|25%
Hg(3)|Cu(3)	-0.2777(1)	0.1886(3)	0.2582(2)	24(1)	75%|25%
Hg(4)|Cu(4)	0.3635(3)	0.9430(4)	0.6306(2)	49(1)	75%|25%
P(1)	-0.2046(6)	0.2623(11)	-0.1304(6)	3(1)	100%
Se(1)	0.2261(2)	0.9924(5)	0.4260(2)	4(1)	100%
Se(2)	-0.0213(2)	0.2442(4)	-0.0805(2)	4(1)	100%
Se(3)	0.2218(2)	0.2639(4)	0.1836(2)	3(1)	100%
Se(4)	-0.2588(2)	0.0144(4)	-0.0537(2)	3(1)	100%
Se(5)	-0.0894(3)	0.2738(6)	0.2364(3)	20(1)	100%
Se(6)	0.0250(4)	-0.2665(6)	0.1228(4)	28(1)	100%

[a] $U_{(eq)} = (\Sigma_i\Sigma_j U_{ij} a_i^* a_j^* a_i \cdot a_j)/3 \times 1000$

Table 6-3. Anisotropic thermal displacement parameters for $CuHg_3PSe_6$ with standard uncertainties in parenthesis.

atom	U11	U22	U33	U23	U13	U12
Hg(1)	18(1)	11(1)	15(1)	-4(1)	-6(1)	11(1)
Cu(1)	18(1)	11(1)	15(1)	-4(1)	-6(1)	11(1)
Hg(2)	9(1)	50(1)	6(1)	1(1)	2(1)	-6(1)
Cu(2)	9(1)	50(1)	6(1)	1(1)	2(1)	-6(1)
Hg(3)	7(1)	19(1)	43(1)	24(1)	2(1)	2(1)
Cu(3)	7(1)	19(1)	43(1)	24(1)	2(1)	2(1)
Hg(4)	78(2)	37(2)	39(1)	-1(1)	30(1)	-4(1)
Cu(4)	78(2)	37(2)	39(1)	-1(1)	30(1)	-4(1)
P(1)	7(3)	2(4)	2(3)	0(2)	5(2)	1(3)
Se(1)	5(1)	2(2)	5(1)	0(1)	2(1)	-3(1)
Se(2)	0(1)	4(1)	6(1)	1(1)	0(1)	0(1)
Se(3)	4(1)	5(2)	0(1)	-2(1)	-1(1)	-1(1)
Se(4)	5(1)	3(2)	0(1)	2(1)	1(1)	0(1)
Se(5)	13(1)	30(2)	17(2)	-8(2)	5(1)	-3(2)
Se(6)	29(2)	23(2)	31(2)	-7(2)	7(2)	-2(2)

RESULTS AND DISCUSSION

Powder X-ray Diffraction

Ag_7PSe_6

The reported unit cell parameter for the solved crystal structure of β-Ag_7PSe_6 is 10.772(2) Å[11] which is outside of the error of the value for the indexed powder pattern of the present work of 10.783(2), Table 6-4. Indexing of all peaks was successful assuming the $P2_13$ space group that was determined previously. Presumably, this error is caused by a miscalibration of the diffractometer and the actual uncertainties in unit cell parameters are at least 0.007 Å. There was no evidence for other crystalline phases in the powder diffraction pattern, Figure 6-4.

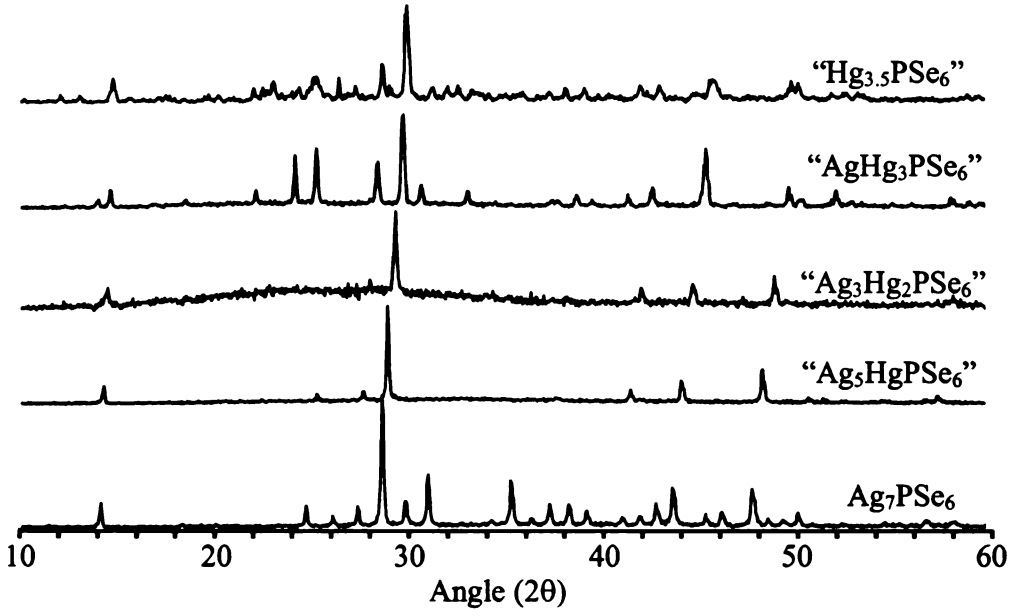

Figure 6-4. Powder X-ray diffraction of the Argyrodite materials. The Ag_7PSe_6 sample has been previously described. The quotation marks indicate the nominal stoichiometry of the product because a stoichiometric ratio that was refined from a crystallographic solution was unavailable.

Table 6-4. Unit cell parameters determined from the indexed powder X-ray diffraction patterns.

Compound	a (Å)	b (Å)	c (Å)	α (deg)	β (deg)	γ (deg)	Space Group
Ag_7PSe_6	10.783(2)	10.783(2)	10.783(2)	90	90	90	$P2_13$
Ag_5HgPSe_6	10.674(12)	10.674(12)	10.674(12)	90	90	90	*F*-43*m*
$Ag_3Hg_2PSe_6$	10.541(17)	10.541(17)	10.541(17)	90	90	90	*F*-43*m*
$AgHg_3PSe_6$	12.731(22)	7.354(10)	12.732(9)	90	109.45(5)	90	*Cc*
$Hg_{3.5}PSe_6$	12.643(30)	7.232(20)	12.593(27)	90	110.11(20)	90	*Cc*

"Ag_5HgPSe_6" and "$Ag_3Hg_2PSe_6$"

The sample with the nominal stoichiometry "Ag_5HgPSe_6" displayed a powder pattern that was closely related to γ-Ag_7PSe_6. The reported cell parameter of γ-Ag_7PSe_6 is 10.838(3) Å,[2] and the cell parameter of "Ag_5HgPSe_6" was determined to be 10.674(12). In the former, presumably the change in cell parameter is the result of a positive thermal expansion as the crystallographic data were collected at elevated

temperature to affect the phase transition. In the Hg-containing compound, however, the change in cell parameter is likely the result of the addition of Hg to the structure. The effective ionic radii of the Ag^{+} and Hg^{2+} are 0.115 and 0.102 Å, respectively,[12] which consistent with the decrease in cell parameter with increased substitution of the latter.

The powder X-ray diffraction pattern of the sample with the nominal stoichiometry "$Ag_3Hg_2PSe_6$" was also successfully indexed assuming a cubic unit cell and an *F*-43*m* space group. The unit cell was smaller than both the "Ag_5HgPSe_6" and Ag_7PSe_6 cells at 10.541(17) Å, which is consistent with further substitution of the smaller Hg^{2+} ions, Table 6-4.

"$AgHg_3PSe_6$"

The powder pattern for "$AgHg_3PSe_6$" did was not consistent with the cubic unit cells of the other argyrodite materials, but instead was indexed using a monoclinic cell with a = 12.731(22) Å, b = 7.354(10) Å, c = 12.732(9) Å, β = 109.45(5)°, and using the *Cc* space group, Table 6-4. The known argyrodite compound Cd_4GeS_6 also adopts the *Cc* space group with a similarly sized unit cell, namely a = 12.326(3) Å, b = 7.088(2) Å, c = 12.365(3) Å and β 110.08(2)°. This suggests that perhaps there is an isomorphic replacement of S for Se, P for Ge, and the Ag and Hg for Cd to produce the novel argyrodite material.

"$Hg_{3.5}PSe_6$"

The X-ray powder pattern for the sample with the nominal stoichiometry of "$Hg_{3.5}PSe_6$" did not have a powder pattern that matched any known structure. Though

the reaction stoichiometry might reasonably have produced some $Hg_2P_2Se_6$, diffraction peaks corresponding to this crystalline compound were not observed. One possible interpretation of the powder pattern is that a number of the peaks correspond to a structure that is similar to the *Cc* symmetry argyrodites but with a smaller unit cell, and the remaining peaks correspond to a second phase. This interpretation yielded a unit cell with a = 12.643(30) Å, b = 7.232(20) Å, c = 12.593(27) Å and β = 110.11(20)°. No successful index of the remaining peaks was obtained, perhaps because the peaks from the second phase overlap with those of the indexed phase.

$CuHg_3PSe_6$ Structural Information by Single Crystal X-ray Diffraction

In Cd_4GeS_6, all of the Cd sites are tetrahedral but in the structurally related $CuHg_3PSe_6$ compound where the Cd atoms are replaced by both Cu and Hg, there are some significant deviations from the parent structure. The structural refinement provided some insight about this deviation.

The single crystal X-ray refinement of $CuHg_3PSe_6$ contained a Cu(1) and Hg(1) mixed site where the Cu^+ and Hg^{2+} ions were not overlapped but the occupancies of the sites appeared to be complementary. The positions of the atoms were refined to be 0.78(2) Å apart, Table 6-5. This observation may provide some evidence for the Cu^+ and Hg^{2+} ions to preferentially adopt different coordination environments, and support the observation that Cu-Se and Hg-Se bond lengths tend to be different. Previously, Cu-Se distances of 2.392 Å were reported in the compound $CuBiP_2Se_6$,[8] and Hg-Se distances of 2.634 Å were reported in the compound HgSe.[13] The average bond lengths of the Cu(1)-Se atoms in $CuHg_3PSe_6$ in this bent coordination environment were 2.310 Å, Table 6-5.

The Hg(1) ion is coordinated in a tetrahedral geometry with an average Hg(1)-Se bond length of 2.650 Å, Figure 6-5, Table 6-5. None of the other mixed metal sites displayed any evidence for separation of the crystallographic sites.

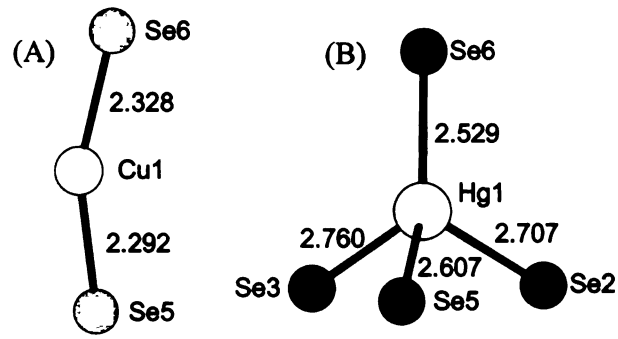

Figure 6-5. The coordination environments of (A) the Cu(1) in a bent coordination geometry and (B) Hg(1) in a distorted tetrahedral geometry in the structure of $CuHg_3PSe_6$. The positions of the Hg(1) and Cu(1) atoms were refined to be 0.78(2) Å apart.

The mixed Cu(2)/Hg(2) site was trigonal planar with an average metal-Se bond length of 2.562 Å, the Cu(3)/Hg(3) site was also trigonal planar with an average metal-Se bond length of 2.583 Å, and the average metal-se bond length was 2.493 Å, Figure 6-6, Table 6-5. Each of these average bond lengths is intermediate to the typical Cu-Se and Hg-Se bond lengths, but only slightly shorter than the Hg-Se bond lengths. This correlates with the greater Hg content (i.e. each site contains 75% Hg, and only 25% Cu).

Table 6-5. Selected bond lengths and angles for $CuHg_3PSe_6$ with bond lengths (Å) and angles (°), with standard uncertainties in parenthesis.

Hg1—Cu1	0.79(2)	Se6—Hg1—Se5	124.47(18)
Hg1—Se6	2.530(5)	Se6—Hg1—Se2	114.52(15)
Hg1—Se5	2.608(4)	Se5—Hg1—Se2	108.30(13)
Hg1—Se2	2.708(4)	Se6—Hg1—Se3	115.96(14)
Hg1—Se3	2.759(4)	Se5—Hg1—Se3	101.58(12)
Cu1—Se5	2.30(2)	Se2—Hg1—Se3	84.27(11)
Cu1—Se6	2.33(2)	Se5—Cu1—Se6	159.4(12)
Hg2|Cu2—$Se6^{i}$	2.482(5)	$Se6^{i}$—Hg2|Cu2—$Se5^{ii}$	131.42(16)
Hg2|Cu2—$Se5^{ii}$	2.499(4)	$Se6^{i}$—Hg2|Cu2—$Se4^{iii}$	112.48(13)
Hg2|Cu2—$Se4^{iii}$	2.704(3)	$Se5^{ii}$—Hg2|Cu2—$Se4^{iii}$	114.36(12)
Hg2|Cu2—Se2	2.991(4)	$Se6^{i}$—Hg2|Cu2—Se2	102.39(14)
Hg3|Cu3—$Se6^{iv}$	2.507(5)	$Se5^{ii}$—Hg2|Cu2—Se2	96.12(13)
Hg3|Cu3—Se5	2.535(4)	$Se4^{iii}$—Hg2|Cu2—Se2	81.99(10)
Hg3|Cu3—$Se4^{v}$	2.707(3)		
Hg3|Cu3—$Se1^{vi}$	3.021(4)	$Se6^{iv}$—Hg3|Cu3—Se5	129.81(17)
Hg4|Cu4—$Se5^{vii}$	2.401(5)	$Se6^{iv}$—Hg3|Cu3—$Se4^{v}$	115.85(14)
Hg4|Cu4—$Se6^{viii}$	2.419(6)	Se5—Hg3|Cu3—$Se4^{v}$	113.95(12)
Hg4|Cu4—$Se3^{ix}$	2.568(4)	$Se6^{iv}$—Hg3|Cu3—$Se1^{vi}$	99.03(13)
Hg4|Cu4—Se1	2.582(4)	Se5—Hg3|Cu3—$Se1^{vi}$	95.45(12)
		$Se4^{v}$—Hg3|Cu3—$Se1^{vi}$	79.61(11)
P1—Se2	2.172(7)		
P1—$Se1^{x}$	2.190(8)	$Se5^{vii}$—Hg4|Cu4—$Se6^{viii}$	114.6(2)
P1—$Se3^{xi}$	2.198(7)	$Se5^{vii}$—Hg4|Cu4—$Se3^{ix}$	114.88(15)
P1—Se4	2.239(8)	$Se6^{viii}$—Hg4|Cu4—$Se3^{ix}$	111.12(17)
		$Se5^{vii}$—Hg4|Cu4—Se1	112.65(16)
		$Se6^{viii}$—Hg4|Cu4—Se1	109.00(16)
		$Se3^{ix}$—Hg4|Cu4—Se1	92.48(15)
		Se2—P1—$Se1^{x}$	116.8(4)
		Se2—P1—$Se3^{xi}$	109.3(3)
		$Se1^{x}$—P1—$Se3^{xi}$	109.6(3)
		Se2—P1—Se4	105.7(3)
		$Se1^{x}$—P1—Se4	107.7(3)
		$Se3^{xi}$—P1—Se4	107.4(3)

(i) x, 1+y, z; (ii) x, 1-y, -0.5+z; (iii) 0.5+x, 0.5+y, z; (iv) -0.5+x, 0.5+y, z; (v) x, -y, 0.5+z; (vi) -0.5+x, -0.5+y, z; (vii) 0.5+x, 1.5-y, 0.5+z; (viii) 0.5+x, 0.5-y, 0.5+z; (ix) x, 1-y, 0.5+z; (x) -0.5+x, 1.5-y, -0.5+z; (xi) -0.5+x, 0.5-y, -0.5+z; (xii) x, -1+y, z; (xiii) 0.5+x, -0.5+y, z; (xiv) x, -y, -0.5+z.

In the isomorphic Cd_4GeS_6 compound, all of the Cd sites are tetrahedrally coordinated by S atoms, but in $CuHg_3PSe_6$, three of the sites have a coordination number of less than four. This may indicate that some longer range ordering of the Cu and Hg

atoms was present but was missed by the refinement. One possible explanation is that the ~2.6 Å metal-Se distance is dominated by the large Hg:Cu ratio. Since the Cu-Se bond length is typically shorter (i.e. ~2.4 Å) the Cu atom moves off center in the tetrahedral cage and adopts a coordination environment with a lower coordination number. For this model to be correct, presumably each metal site would have to be a mixture of two crystallographic sites that do not spatially overlap.

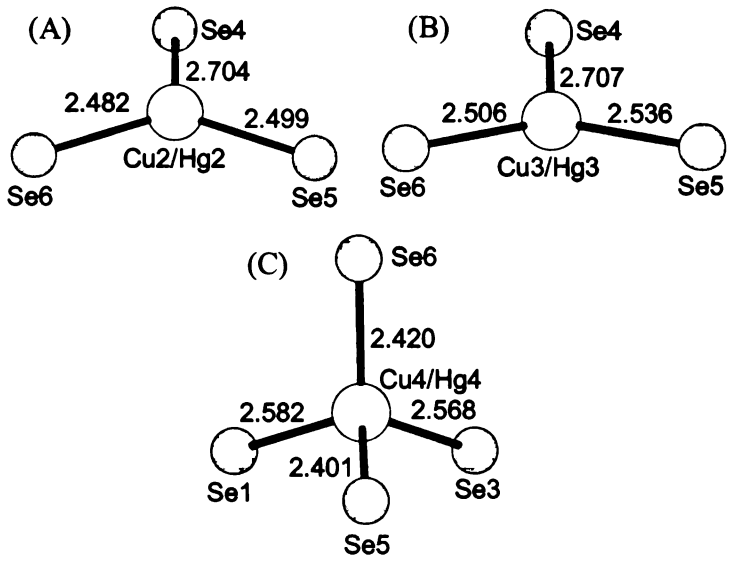

Figure 6-6. The coordination environments of (A) the trigonal planar Cu(2)/Hg(2) site, (B) the trigonal planar Cu(3)/Hg(3) site (C) the distorted tetrahedral Cu(4)/Hg(4) site in the compound $CuHg_3PSe_6$.

It is likely that a similar study aimed at producing the other members of the class of compounds $Cu_{7-x}Hg_{x/2}PSe_6$ would have the opposite trend in size with an increase in Hg content that was observed for the $Ag_{7-x}Hg_{x/2}PSe_6$ compounds. A typical Ag-Se bond length is ~2.8 Å as was observed in the compound $AgBiP_2Se_6$,[8] which is longer than the typical Hg-Se bond lengths of ~2.6 Å.[13] Conversely, the Cu-Se bond lengths are approximately 2.4 Å, so an increase in Cu content should produce a smaller unit cell.

Differential Thermal Analysis and Optical Absorption of $CuHg_3PSe_6$

The differential thermal analysis of $CuHg_3PSe_6$ displayed an endothermic feature indicative of the onset of melting upon heating at 740 °C. On the first cooling cycle a sharp exothermic event was observed at 645 °C but on the second cycle, an exothermic event was observed at 675 °C. Presumably, these features correspond to crystallization of the melt. Interestingly, the line shape represented a physical situation that is impossible, inset of Figure 6-7A. One interpretation is that crystallization is sufficiently exothermic that it raises the ambient temperature of the furnace. This provides evidence for the ready formation of argyrodite materials since crystallization presumably allows a thermodynamically very stable product to be formed, and therefore competing crystalline compounds can be avoided. Powder X-ray diffraction patterns collected before thermal treatment, after a single heating cycle, and after subsequent heating cycles did not have significant differences, and the shift in the crystallization temperature has not been successfully rationalized.

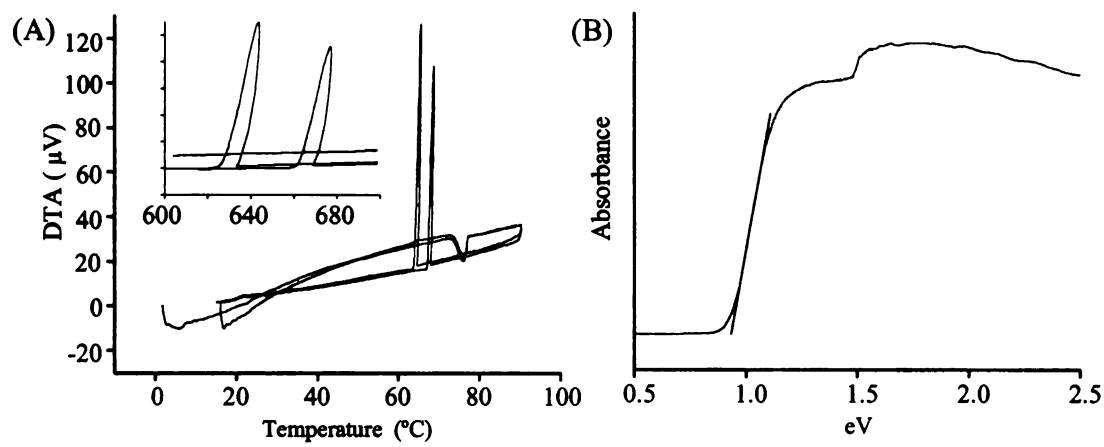

Figure 6-7. (A) The differential thermal analysis and (B) optical absorption spectrum of $CuHg_3PSe_6$.

The optical absorption spectrum of $CuHg_3PSe_6$ contained a strong absorption edge at 0.9 eV, which correlates with the black color of the polyhedral crystals, Figure 6-7B. There was also a minor feature that could be an absorption edge at ~1.3 eV which could presumably be assigned to an as yet unidentified crystalline phase.

CONCLUDING REMARKS

The new argyrodite materials presented herein are in interesting case where the cationic site has been populated with multiple metals. There is some preliminary evidence from the single crystal refinement of $CuHg_3PSe_6$ that some site preference for the monovalent cation (i.e. Cu^+) versus the trivalent cation (i.e. Hg^{3+}) is present, but problems with the crystallographic refinement make this observation questionable. The refinement of each of the cationic positions in the unit cell of the $Ag_{7-x}Hg_{x/2}PSe_6$ compounds was unsuccessful using the available powder diffraction data, and no satisfying refinement could be obtained perhaps due to limitations in the accuracy of the diffractometer. One additional possibility that could not be explored with the presently available data is that atoms with different sizes and formal charges do not randomly substitute but instead demonstrate longer range order.[14] In the future, studies using synchrotron radiation or neutron diffraction may be more suited to such a powder refinement, and the behavior of the cation sites may be further elucidated. More intense sources such as these may make the elucidation of longer range order possible. Additionally, some of the known argyrodite materials have temperature-dependant phase transitions, and variable-temperature diffraction experiments may indicate that the novel materials presented here have similar phase transitions.

REFERENCES

1. Kuhs, W. F.; Nitsche, R.; Scheunemann, K. *Mater. Res. Bull.* **1979,** 14, 241-248.

2. Evain, M.; Gaudin, E.; Boucher, F.; Petricek, V.; Taulelle, F. *Acta. Crystallogr. B* **1998,** 54, 376-383.

3. Gaudin, E.; Boucher, F.; Petricek, V.; Taullele, F.; Evain, M. *Acta. Crystallogr. B* **2000,** 56, 402-408.

4. Gaudin, E.; Petricek, V.; Boucher, F.; Taulelle, F.; Evain, M. *Acta. Crystallogr. B* **2000,** 56, 972-979.

5. Julienpouzol, M.; Jaulmes, S. *Acta Crystallogr. C* **1995,** 51, 1966-1968.

6. Onoda, M.; Chen, X. A.; Ishii, M.; Wada, H. *Solid State Ionics* **2000,** 136, 415-418.

7. Onoda, M.; Wada, H.; Sato, A.; Ishii, M. *J. Alloys Compd.* **2004,** 383, 113-117.

8. Gave, M.; Bilc, D.; Mahanti, S.; Breshears, J.; Kanatzidis, M. *Inorg. Chem.* **2005,** 5293-5303.

9. *Jade 6.0*, Materials Data, Inc. Livermore, CA.: 2003.

10. *SMART, SAINT, SHELXTL V-5 and SADABS*, Bruker Analytical X-ray Instruments, Inc.: Madison, 1998.

11. Evain, M.; Boucher, F.; Gourdon, O.; Petricek, V.; Dusek, M.; Bezdicka, P. *Chem. Mat.* **1998,** 10, 3068-3076.

12. Greenwood, N. N.; Earnshaw, A. Chemistry of the Elements; 2nd ed.; Butterworth-Heinemann: Boston, MA, 1997; pp 1176, 1205.

13. Earley, J. W. *Am. Mineral.* **1950,** 35, 337-364.

14. Gave, M.; Weliky, D. P.; Kanatzidis, M. G. *Inorg. Chem.* **2007,** 46, 11063-11074.

CHAPTER 7

$Cs_4P_2Se_{10}$: A NEW COMPOUND DISCOVERED WITH THE APPLICATION OF SOLID STATE AND HIGH TEMPERATURE NMR.

INTRODUCTION

Chalcophosphates are compounds with oxidized phosphorus and at least one P-Q bond, where Q = S, Se, or Te. These compounds exhibit an impressively rich structural diversity because of the large number of stable $[P_xQ_y]^{z-}$ building blocks that can be stabilized and the variety of binding modes in which they can engage.[1] They are important in the areas of catalysis, ceramics, glasses, and molecular sieves.[2-4] Previously, solid state nuclear magnetic resonance (NMR) has been useful in providing structural information about chalcophosphate materials.[5-10] Most notably, in selenophosphate materials there is a general correlation between the chemical shifts (CSs) of anions and the presence or absence of a P-P bond. Compounds containing a P-P bond resonate between 25 and 95 ppm whereas those that do not contain a P-P bond resonate between -115 and 5 ppm.[11] Additionally, the spectral intensity of a peak in a NMR spectrum is proportional to the number of nuclei that have the corresponding chemical environment.[12] Therefore, NMR spectroscopy is a useful tool to evaluate phase purity in cases where competing compounds have the same NMR-active nucleus.

There is little experimental data about the species that exist at high temperature although it has been proposed that different $[P_xQ_y]^{z-}$ anions exist in the melt in various equilibria.[1] Since there is ^{31}P chemical shift discrimination between P-P and non P-P bonded selenophosphate species in room temperature solids, *in-situ* ^{31}P NMR studies of high temperature syntheses can potentially provide information about the identity of ^{31}P-containing species that exist at high temperature. The known compound $Cs_4P_2Se_9$[13] was initially chosen for a high temperature NMR study because: (1) the synthesis temperature could be reached by our NMR probe; (2) the compound contained the interesting Se-

bridged $[P_2Se_9]^{4-}$ anion; and (3) the compound melts congruently which suggests that spectra of subsequent high temperature remelts should be similar to one another and that some correlation can be made between the remelt spectra and the spectrum of the solid compound.

The new compound $Cs_4P_2Se_{10}$ which was discovered following high temperature *in-situ* NMR synthesis intended to produce $Cs_4P_2Se_9$ is reported here. Room temperature solid state ^{31}P NMR spectra of the synthetic products clearly showed that $Cs_4P_2Se_9$ was not the dominant crystalline product and the structure of $Cs_4P_2Se_{10}$ was subsequently solved with X-ray diffraction of single crystals obtained from the NMR synthesis. Synthetic conditions were varied to ascertain the important factors leading to dominant $Cs_4P_2Se_9$ or $Cs_4P_2Se_{10}$ products and high temperature ^{31}P NMR spectra of synthetic melts were obtained and analyzed.

EXPERIMENTAL SECTION

Reagents

Chemicals were used as obtained unless otherwise noted: phosphorous (MCB Reagents, Gibbstown, NJ, amorphous red), selenium shot (Tellurex Inc., Traverse City, MI, 99.999%) cesium metal, (Aldrich Chemical Co., Inc., St. Louis, MO). Phosphorous was freeze dried and Cs_2Se was prepared by a modified literature preparation.[14,15] P_2Se_5 was prepared by combining a stoichiometric amount of the elements in a pyrex ampoule, flame-sealing at a reduced pressure of 100 mTorr, then heating to 300 °C over 6 h, holding there for 6 h, and then quenching in air. Manipulations of all starting materials were performed under a nitrogen atmosphere in a dry box (Vacuum Atmospheres).

Synthesis

The synthesis that produced $Cs_4P_2Se_{10}$ as the dominant P-containing product was performed by combining Cs_2Se (0.186 g, 0.53 mmol), P_2Se_5 (0.124 g, 0.27 mmol), and Se (0.192 g, 2.4 mmol) which were subsequently ground together in an agate mortar and pestle to increase homogeneity. This resulted in a reaction stoichiometry with the nominal composition "$Cs_4P_2Se_{16}$" or an excess of six equivalents of Se relative to the $Cs_4P_2Se_{10}$ stoichiometry. The extra Se in the reaction stoichiometry was added to favor the production of $Cs_4P_2Se_{10}$ rather than $Cs_4P_2Se_9$.[13] Approximately 75 mg of this mixture was loaded into a fused silica ampoule, sealed at ~100 mTorr, and placed in the high temperature NMR probe. The sample was then heated at a rate of 10 °C/min, with pauses in the temperature ramp to collect isothermal NMR spectra. After reaching the maximum temperature of 600 °C and collecting an NMR spectrum, the sample was cooled back to room temperature at a rate of 10 °C/min, again pausing for spectral collection. The total time spent above room temperature was ~6 h. A room temperature ^{31}P NMR spectrum following the *in situ* synthesis contained a dominant isotropic peak at –52.8 ppm and integration of all the spectral peaks indicated that $Cs_4P_2Se_{10}$ was >99% of the total P-containing compounds, Figure 7-1A. Powder X-ray diffraction indicated that elemental Se also remained in the final products. It was also possible to prepare $Cs_4P_2Se_{10}$ with a conventional high temperature furnace using the same stoichiometry and a heating/cooling profile of a similar length. Crystals of $Cs_4P_2Se_{10}$ were air and moisture stable over a period of at least several hours.

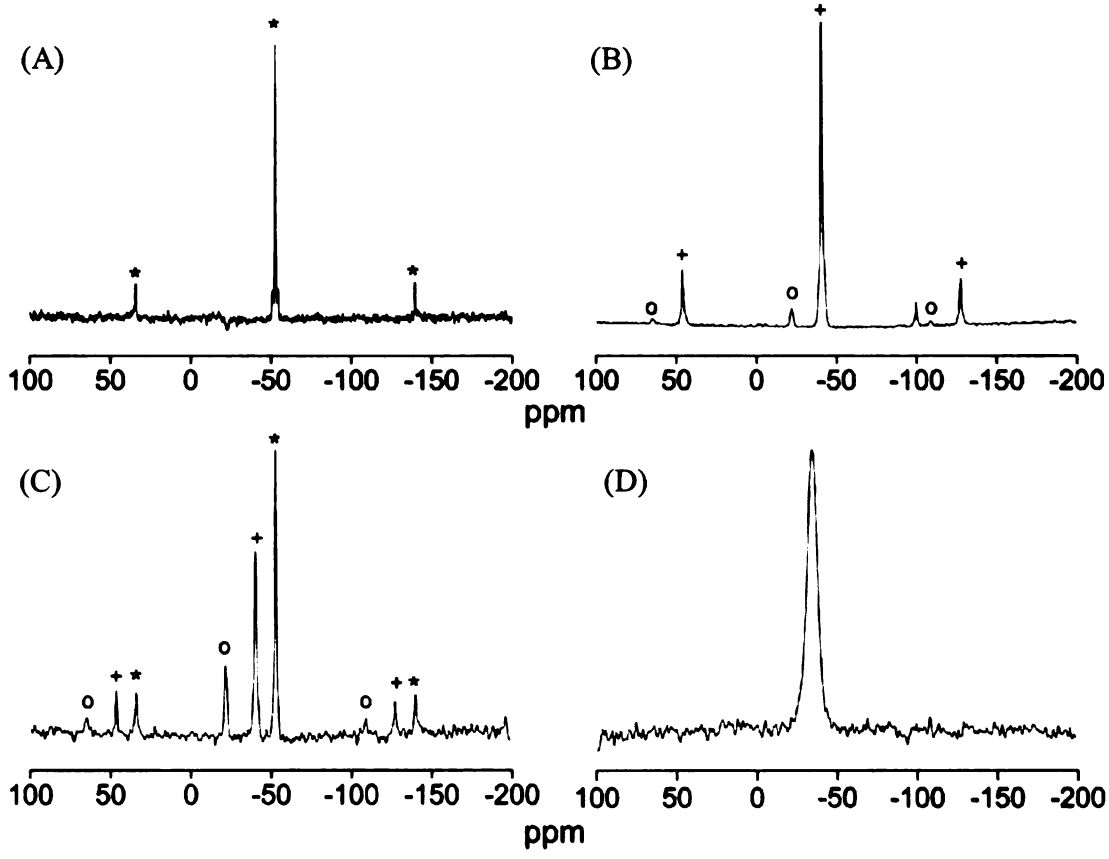

Figure 7-1. Ambient temperature ^{31}P magic angle spinning NMR spectra of the final products of: (A) a "$Cs_4P_2Se_{16}$" reaction stoichiometry indicating $Cs_4P_2Se_{10}$ as the dominant ^{31}P-containing species at -52.8 ppm; (B) a "$Cs_4P_2Se_8$" reaction stoichiometry indicating $Cs_4P_2Se_9$ as the dominant ^{31}P-containing species at -39.9 ppm; and (C) a "$Cs_4P_2Se_{12}$" reaction stoichiometry that produced $Cs_4P_2Se_9$ and $Cs_4P_2Se_{10}$ in a ~3:5 ratio. Panel D displays the static ^{31}P NMR spectrum of a 350 ^{o}C melt of the products in C. The peak with a chemical shift of -22.0 ppm in panels B and C was not assigned and the peak at -99.8 ppm in panel B was not assigned. For spectra A-C, the spinning frequency was 14 kHz and spinning sidebands are grouped with the corresponding isotropic peak using like symbols with * ≡ $Cs_4P_2Se_{10}$, + ≡ $Cs_4P_2Se_9$, and o ≡ unassigned peak with -22.0 ppm isotropic shift.

$Cs_4P_2Se_9$ was produced in high purity by combining Cs_2Se (0.281g, 0.82 mmol), P_2Se_5 (0.186 g, 0.41 mmol), and Se (0.032 g, 0.41 mmol) in a fused silica ampoule. This resulted in a "$Cs_4P_2Se_8$" reaction stoichiometry and under these Se starved conditions, $Cs_4P_2Se_9$ is favored. The ampoule was subsequently sealed under a reduced pressure of

~100 mTorr and allowed to react in a furnace. The sample was heated to 700 °C over 12 h, held at 700 °C for 12 h, and then cooled to room temperature over 12 h. The room temperature ^{31}P NMR spectrum had a dominant isotropic peak at -39.9 ppm and integration of all the spectral peaks indicated that $Cs_4P_2Se_9$ was >90% of the ^{31}P-containing compounds, Figure 7-1B. There were also peaks at -22.0 ppm and -99.8 ppm that accounted for the remainder of the spectral intensity but were not assigned. The powder X-ray diffraction pattern contained only peaks that corresponded to $Cs_4P_2Se_9$.

Vitrification of the mixture with "$Cs_4P_2Se_{16}$" stoichiometry was accomplished by sealing a sample portion in a fused silica ampoule under a reduced pressure of ~100 mTorr, flame heating until molten, and then rapidly quenching in ice water. Complete vitrification was confirmed by powder X-ray diffraction.

Single Crystal X-ray Diffraction

Intensity data for single crystals of $Cs_4P_2Se_{10}$ were collected on a Bruker SMART platform CCD diffractometer using Mo Kα radiation operating at 40 kV and 40 mA, Table 7-1. Fractional atomic coordinates are displayed in Table 7-2 and selected bond lengths and angles are displayed in Table 7-3. A full sphere of data was collected and individual frames were acquired with a 10 s exposure time and a 0.3° Ω rotation. The SMART software was used for data collection, and SAINT software was used for data extraction and reduction. An analytical absorption correction to the data was performed and direct methods were used to solve and refine the structures with the SHELXTL[16] software package.

Powder X-ray Diffraction

Powder X-ray diffraction was performed with a Rigaku-Denki RW400F2 (Rotaflex) diffractometer equipped with a Cu Kα rotating anode operating at 45 kV and 100 mA with a 2°/min scan rate.

Table 7-1. Crystallographic data for $Cs_4P_2Se_{10}$

Formula	Cs4P2Se10	d_{calc} (g/cm^3)	4.153
FW	1383.18	μ (mm^{-1})	23.113
Space group	P-1	λ (Å)	0.71073
a (Å)	7.3587(11)	Temp (K)	298
b (Å)	7.4546(11)	2θ max (°)	28.30
c (Å)	10.1420(15)	R[a] (I>2σ(I))	R1 = 0.0395
α (°)	85.938(2)		wR2 = 0.0716
β (°)	88.055(2)	R[a] (all)	R1 = 0.0687
γ (°)	85.609(2)		wR2 = 0.0789
V (Å^3)	553.10(14)		
Z	1		

[a] $R = \Sigma(|F_o| - |F_c|)/\Sigma|F_o|$. $R_w = [\Sigma w(|F_o| - |F_c|)^2/\Sigma w|F_o|^2]^{1/2}$

Table 7-2. Fractional atomic corrdinates for $Cs_4P_2Se_{10}$ with standard deviations in parenthesis.

atom	x	y	z
Cs1	0.2210(1)	0.2754(1)	0.9686(1)
Cs2	0.1943(1)	-0.1431(1)	1.3603(1)
Se1	0.2682(1)	0.7719(1)	0.9946(1)
Se2	0.3081(1)	0.0372(1)	0.6737(1)
Se3	0.0229(1)	0.6635(1)	0.7046(1)
Se4	0.5116(1)	0.5897(1)	0.7599(1)
Se5	0.4017(1)	-0.6057(1)	1.4616(1)
P	0.2533(3)	0.7841(3)	0.7789(2)

Table 7-3. Selected bond lengths Å and angles (°) for $Cs_4P_2Se_6$ with standard uncertainties in parenthesis.

Cs1—Se2	3.5999(12)	Se2—Cs1—Se1^{i}	98.40(2)	Se5—Cs2—Se1^{iii}	91.31(2)
Cs1—Se1^{i}	3.6487(12)	Se2—Cs1—Se4^{ii}	136.97(3)	Se2^{vi}—Cs2—Se1^{iii}	82.20(2)
Cs1—Se4^{ii}	3.6769(11)	Se1^{i}—Cs1—Se4^{ii}	121.94(3)	Se2^{iv}—Cs2—Se5^{vii}	64.72(2)
Cs1—Se1^{iii}	3.7348(12)	Se2—Cs1—Se1^{iii}	60.58(2)	Se2^{v}—Cs2—Se5^{vii}	150.79(3)
Cs1—Se3^{i}	3.7543(12)	Se1^{i}—Cs1—Se1^{iii}	85.52(2)	Se5—Cs2—Se5^{vii}	36.99(3)
Cs1—Se1	3.7718(12)	Se4^{ii}—Cs1—Se1^{iii}	105.05(2)	Se2^{vi}—Cs2—Se5^{vii}	52.92(2)
Cs1—Se1^{ii}	3.7762(12)	Se2—Cs1—Se3^{i}	151.36(3)	Se1^{iii}—Cs2—Se5^{vii}	106.06(2)
Cs1—Se4	3.7815(11)	Se1^{i}—Cs1—Se3^{i}	59.45(2)	Se2^{iv}—Cs2—Se3^{i}	81.89(2)
Cs1—Se3	4.0230(12)	Se4^{ii}—Cs1—Se3^{i}	62.58(2)	Se2^{v}—Cs2—Se3^{i}	56.86(2)

Table 7-3 continued

		$Se1^{iii}$—Cs1—$Se3^{i}$	97.29(2)	Se5—Cs2—$Se3^{i}$	174.05(3)
Cs2—$Se2^{iv}$	3.6835(12)	Se2—Cs1—Se1	125.33(3)	$Se2^{vi}$—Cs2—$Se3^{i}$	98.24(3)
Cs2—$Se2^{v}$	3.7433(12)	$Se1^{i}$—Cs1—Se1	104.42(2)	$Se1^{iii}$—Cs2—$Se3^{i}$	94.65(2)
Cs2—Se5	3.7522(12)	$Se4^{ii}$—Cs1—Se1	62.04(2)	$Se5^{vii}$—Cs2—$Se3^{i}$	140.01(3)
Cs2—$Se2^{vi}$	3.8038(13)	$Se1^{iii}$—Cs1—Se1	166.51(3)	$Se2^{iv}$—Cs2—$Se3^{viii}$	56.76(2)
Cs2—$Se1^{iii}$	3.8210(12)	$Se3^{i}$—Cs1—Se1	80.51(2)	$Se2^{v}$—Cs2—$Se3^{viii}$	80.29(2)
Cs2—$Se5^{vii}$	3.8251(12)	Se2—Cs1—$Se1^{ii}$	85.58(2)	Se5—Cs2—$Se3^{viii}$	65.82(2)
Cs2—$Se3^{i}$	3.8256(12)	$Se1^{i}$—Cs1—$Se1^{ii}$	164.68(3)	$Se2^{vi}$—Cs2—$Se3^{viii}$	117.21(2)
Cs2—$Se3^{viii}$	3.8891(12)	$Se4^{ii}$—Cs1—$Se1^{ii}$	51.56(2)	$Se1^{iii}$—Cs2—$Se3^{viii}$	145.71(3)
Cs2—$Se4^{vi}$	4.0678(12)	$Se1^{iii}$—Cs1—$Se1^{ii}$	83.59(2)	$Se5^{vii}$—Cs2—$Se3^{viii}$	71.46(2)
		$Se3^{i}$—Cs1—$Se1^{ii}$	111.37(2)	$Se3^{i}$—Cs2—$Se3^{viii}$	108.89(2)
Se1—P	2.190(2)	Se1—Cs1—$Se1^{ii}$	84.84(2)	$Se2^{iv}$—Cs2—$Se4^{vi}$	118.71(3)
Se2—P^{iii}	2.159(2)	Se2—Cs1—Se4	77.82(2)	$Se2^{v}$—Cs2—$Se4^{vi}$	126.19(3)
Se3—P	2.160(2)	$Se1^{i}$—Cs1—Se4	134.20(3)	Se5—Cs2—$Se4^{vi}$	34.10(2)
Se4—P	2.312(2)	$Se4^{ii}$—Cs1—Se4	83.33(2)	$Se2^{vi}$—Cs2—$Se4^{vi}$	72.12(2)
		$Se1^{iii}$—Cs1—Se4	127.31(2)	$Se1^{iii}$—Cs2—$Se4^{vi}$	58.15(2)
Se4—$Se5^{vi}$	2.3125(13)	$Se3^{i}$—Cs1—Se4	130.32(3)	$Se5^{vii}$—Cs2—$Se4^{vi}$	54.02(2)
Se5—$Se5^{vii}$	2.4045(19)	Se1—Cs1—Se4	50.85(2)	$Se3^{i}$—Cs2—$Se4^{vi}$	151.64(3)
		$Se1^{ii}$—Cs1—Se4	61.07(2)	$Se3^{viii}$—Cs2—$Se4^{vi}$	99.08(2)
		Se2—Cs1—Se3	81.70(3)	$Se4^{vi}$—Se5—$Se5^{vii}$	99.15(6)
		$Se1^{i}$—Cs1—Se3	78.51(2)	$Se2^{x}$—P—Se3	113.11(10)
		$Se4^{ii}$—Cs1—Se3	118.03(3)	$Se2^{x}$—P—Se1	116.67(10)
		$Se1^{iii}$—Cs1—Se3	136.25(3)	Se3—P—Se1	115.17(10)
		$Se3^{i}$—Cs1—Se3	108.52(2)	$Se2^{x}$—P—Se4	107.73(10)
		Se1—Cs1—Se3	56.10(2)	Se3—P—Se4	109.49(10)
		$Se1^{ii}$—Cs1—Se3	116.77(2)	Se1—P—Se4	92.14(9)
		Se4—Cs1—Se3	55.71(2)		
		$Se2^{iv}$—Cs2—$Se2^{v}$	105.69(2)	Se3—P—Cs1	71.49(6)
		$Se2^{iv}$—Cs2—Se5	92.66(3)	Se1—P—Cs1	64.65(6)
		$Se2^{v}$—Cs2—Se5	123.04(3)	Se4—P—Cs1	64.51(6)
		$Se2^{iv}$—Cs2—$Se2^{vi}$	73.48(3)	$Se2^{x}$—P—$Cs1^{x}$	57.99(6)
		$Se2^{v}$—Cs2—$Se2^{vi}$	154.34(3)	Se3—P—$Cs1^{x}$	124.72(8)
		Se5—Cs2—$Se2^{vi}$	82.40(2)	Se1—P—$Cs1^{x}$	61.53(6)
		$Se2^{iv}$—Cs2—$Se1^{iii}$	154.59(3)	Se4—P—$Cs1^{x}$	125.46(8)
		$Se2^{v}$—Cs2—$Se1^{iii}$	93.00(2)	Cs1—P—$Cs1^{x}$	125.30(6)

(i) -x, 1-y, 2-z; (ii) 1-x, 1-y, 2-z; (iii) x, -1+y, z; (iv) x, y, 1+z; (v) -x, -y, 2-z; (vi) 1-x, -y, 2-z; (vii) 1-x, -1-y, 3-z; (viii) x, -1+y, 1+z; (ix) -x, -y, 3-z; (x) x, 1+y, z; (xi) x, y, -1+z; (xii) x, 1+y, -1+z.

NMR Spectroscopy

Room temperature ^{31}P NMR spectra were collected on a 9.4 T spectrometer (Varian Infinity Plus) using a magic angle spinning (MAS) probe (Varian Chemagnetics)

and served as an analytical tool to assess the phase purity of P-containing compounds. Samples were spun at 7 to 14 kHz in zirconia rotors of 4 mm outer diameter and a ~50 μL sample volume. Bloch decay spectra were taken with a 4.6 μs $\pi/2$ pulse calibrated using H_3PO_4 which also served as a chemical shift reference at 0 ppm. Four scans were summed with a 5000 s recycle delay. The longitudinal relaxation time of $Cs_4P_2Se_{10}$ at ambient temperature was determined by fitting the signal intensity as a function of relaxation delay to an exponential buildup function.[5]

High temperature ^{31}P NMR spectra were collected on a 9.4 T spectrometer (Varian Infinity Plus) using a static probe (Doty Scientific) with a 5.5 μs $\pi/2$ pulse calibrated at room temperature using H_3PO_4 which also served as a chemical shift reference at 0 ppm. Several hundred to several thousand scans were averaged with recycle delays ranging from 0.1 s to 10 s. Sample temperatures ranging from 250 °C to 600 °C were reached at a rate of 10 °C/min and were allowed to equilibrate for ~5 min before data collection.

All NMR spectra were processed with line broadening and baseline correction.

Differential Thermal Analysis (DTA)

Differential thermal analysis (DTA) was performed on a Shimadzu DTA-50 thermal analyzer. Sample portions (~30 mg) were sealed under a reduced pressure of ~80 mTorr in fused silica, and an equivalent mass of Al_2O_3 in a similarly prepared ampoule served as a reference. The sample was heated to 600 °C at a rate of 10 °C/minute and then cooled at a rate of 10 °C /minute back to room temperature. The residues after DTA were analyzed by powder X-ray diffraction.

RESULTS AND DISCUSSION

Identification and Structure Description of $Cs_4P_2Se_{10}$

The initial goal of synthesizing $Cs_4P_2Se_9$ in a sealed tube in the NMR spectrometer was to obtain high temperature ^{31}P NMR spectra and to identify species present in the synthetic melt. After one of the syntheses was complete, the room temperature ^{31}P NMR spectrum contained a dominant peak at -52.8 ppm in addition to the -39.9 ppm shift of $Cs_4P_2Se_9$.[11] The -52.8 ppm peak could not be assigned to any known compound. Single deep reddish brown crystals were isolated, screened using X-ray diffraction, and the structure of $Cs_4P_2Se_{10}$ was subsequently solved. A summary of the details of the refinement are displayed in Table 7-1. All of the peaks in the powder X-ray diffraction pattern of the sample prepared using the optimized synthetic method corresponded either to the calculated $Cs_4P_2Se_{10}$ pattern or to elemental Se. The ^{31}P NMR peak at -52.8 ppm was therefore assigned to $Cs_4P_2Se_{10}$.

$Cs_4P_2Se_{10}$ has the molecular anion $[P_2Se_{10}]^{4-}$ which is composed of two PSe_4 tetrahedra that are connected by two central selenium atoms thus forming a tetraselenide fragment, Figure 7-2A. The PSe_4 tetrahedron is distorted with the Se-P-Se angles ranging from 92.14(9)° to 116.67(10)°. The lengths of the P-Se bonds are typical and range from 2.159(2) to 2.312(2) Å. Tables 7-2 and 7-3 contain the atomic and thermal parameters, and selected bond lengths and angles, respectively.

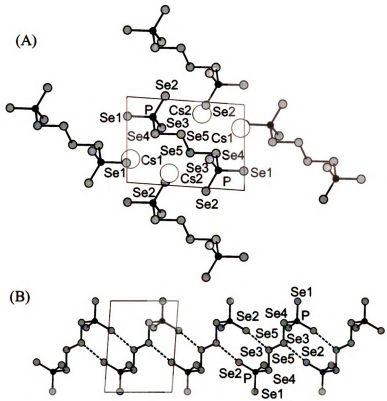

Figure 7-2. Structure of $Cs_4P_2Se_{10}$ (A) down the *a*-axis showing the $[P_2Se_{10}]^{4-}$ chains and (B) along the *b*-axis with the weak interaction between the $[P_2Se_{10}]^{4-}$ chains emphasized with a dashed line.

The Se-Se contacts range from 2.3125(13) to 2.4045(19) Å, a large range of bond lengths. This unusual behavior could be explained by the dihedral angles[17] around the bonds Se(4)-Se(5) and Se(5)-Se(5) of -83.78(1)° and 180.00(1)°, respectively. It is noteworthy that the Se(5)-Se(5) bond is shared by two planar structural moities namely Se(4)-Se(5)-Se(5)-Se(4) and Se(2)···Se(5)-Se(5)···Se(2) to give maximized lone pair repulsion in Se atoms and one of the longest Se-Se distances reported for a selenophosphate ligand. Comparable or even longer Se-Se distances have been found in the Se_n^{2-} (n = 2, 3) subunits in the K_2Se_2, Rb_2Se_2,[18] $Sr_4Sn_2Se_9$, $Sr_4Sn_2Se_{10}$[19] and

$Eu_8(Sn_4Se_{14})(Se_3)_2$.[20] A bond distance alteration in Q_4^{2-} (Q = S, Se) has been reported in $Cs_4P_2S_{10}$,[21] $APSe_6$ (A = K, Rb, Cs),[22] and unligated Se_4^{2-} ions.[23]

For $Cs_4P_2Se_{10}$, unusually short intra- and intermolecular Se···Se nonbonding interactions are observed at 3.243(4) and 3.399(4) Å. Intermolecular nonbonding interactions generate a pseudo-one dimensional infinite chain including eight-membered rings composed of P and Se atoms along the *b*-axis, Figure 7-2B.

The structure of $Cs_4P_2Se_{10}$ is related to the structure of $Cs_4P_2S_{10}$[21] and both contain the $[P_2Q_{10}]^{4-}$ anion. In $Cs_4P_2S_{10}$, there are two different conformations of the $[P_2S_{10}]^{4-}$ anion with dihedral angles about the central disulfide bonds of 89.6° and 0°. In $Cs_4P_2Se_{10}$, only one anionic conformation is present with a dihedral angle about the central diselenide bond of 180° *(vide supra)*. Additionally, there is positional disorder of the S atoms in $Cs_4P_2S_{10}$, and this is not evident for the Se atoms in $Cs_4P_2Se_{10}$.

Differential Thermal Analysis (DTA)

For the glass with "$Cs_4P_2Se_{16}$" stoichiometry, the first DTA heating cycle indicated an exothermic crystallization event centered at ~160 °C and broad endothermic melting features centered at 315 °C, Figure 7-3. The subsequent cooling cycle contained exothermic crystallization features that were centered near 275 °C. Subsequent DTA cycles were similar to the first cycle except that they did not contain the initial crystallization peak near 160 °C. Possible assignments of the DTA features are: (1) 160 °C exothermic feature, glass to crystal phase transition of $Cs_4P_2Se_{10}$ and Se; (2) 315 °C

endothermic feature/275 °C exothermic features, melting/crystallization of $Cs_4P_2Se_{10}$ and Se.

The assignment of the 160 °C feature is supported by several arguments. First, the feature is exothermic and is only observed during the first heating cycle as would be expected for a transition from a metastable glass to a thermodynamically stable crystal. Second, annealing the glass near the putative glass to crystal transition temperature resulted in formation of a mixture of crystalline materials that were predominately $Cs_4P_2Se_{10}$ and Se. ^{31}P solid state NMR and powder X-ray diffraction were the methods used to analyze the annealed material. The glass to crystal transition temperature of the $Cs_4P_2Se_{16}$ glass is lower than the corresponding temperatures that have been observed for glasses that form related metal selenophosphate compounds.[22,24,25] Materials with a reversible glass to crystal phase transition have potential use in data storage applications,[22,26-30] and further characterization of the phase change properties of $Cs_4P_2Se_{10}$ may be of technological relevance.

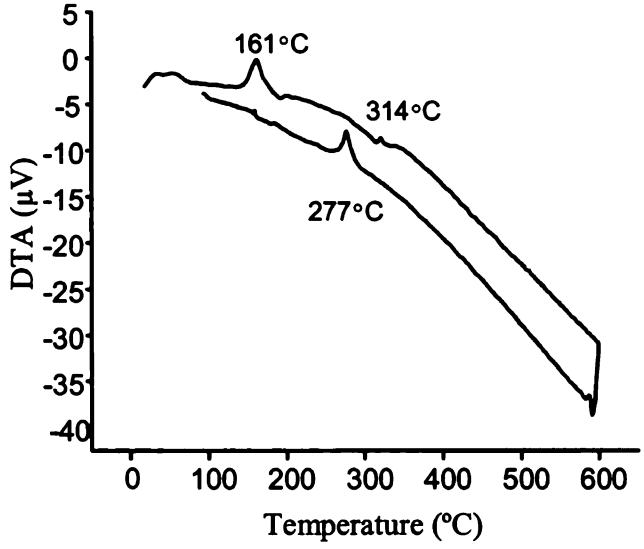

Figure 7- 3. Differential thermal analysis (DTA) of a mixture with "$Cs_4P_2Se_{16}$" stoichiometry that was quenched rapidly from the melt. The displayed plot is for the first heating/cooling cycle of this mixture. The interpretation of this plot relied on the powder X-ray diffraction pattern obtained following several heating/cooling cycles. This pattern indicated that $Cs_4P_2Se_{10}$ and elemental Se were the major crystalline products. In the displayed plot, the peak centered at ~160 °C is assigned to the glass to crystalline transition of $Cs_4P_2Se_{10}$ and Se, the peak centered at at ~315 °C is assigned to the melting of this mixture, and the peak centered at 277 °C is assigned to the subsequent recrystallization. The exothermic peak centered at ~160 °C was not observed for the second and subsequent heating/cooling cycles likely because the cooling rate was slow enough that crystalline rather than glassy material was formed. Thermal events due to pure Se were not observed perhaps because of insufficient Se or because of comelting/cocrystallization of Se with $Cs_4P_2Se_{10}$.

Competition between $Cs_4P_2Se_9$ and $Cs_4P_2Se_{10}$

Analysis of the products of furnace reactions done with different stoichiometries showed that reaction stoichiometry had a significant effect on the $Cs_4P_2Se_{10}$:$Cs_4P_2Se_9$ final product ratio. Reduction by one equivalent of Se relative to $Cs_4P_2Se_9$, i.e. "$Cs_4P_2Se_8$" reaction stoichiometry, produced $Cs_4P_2Se_9$ as the dominant ^{31}P-containing product with no $Cs_4P_2Se_{10}$, Figure 7-1B. Syntheses with increased Se relative to $Cs_4P_2Se_{10}$, i.e. "$Cs_4P_2Se_{10+x}$" with $1 < x < 5$ reaction stoichiometries, resulted in mixtures of $Cs_4P_2Se_9$ and $Cs_4P_2Se_{10}$. A representative spectrum of the products of the reaction where $x = 2$ is displayed in Figure 7-1C. For the "$Cs_4P_2Se_{16}$" reaction stoichiometry, $Cs_4P_2Se_{10}$ was the only P-containing compound, Figure 7-1A. The Figure 7- 1B,C spectra also had small peaks at -22.0 and -99.8 ppm that accounted for <10% of the total ^{31}P signal intensity. To our knowledge, these shifts do not correspond to the measured ^{31}P shifts of any known cesium selenophosphate compound. The related compound $Cs_4P_2S_{10}$ was synthesized with the "$Cs_4P_2S_{10.5}$" reaction stoichiometry and although there was excess S, the as-yet unknown compound $Cs_4P_2S_9$ was not produced.[21]

The literature preparation of $Cs_4P_2Se_9$ was done with the "$Cs_{5.4}P_2Se_{13.4}$" reaction stoichiometry that contained an excess of both Cs and Se relative to $Cs_4P_2Se_9$.[13] Although an excess of elemental Se in the present study was found to favor the production of $Cs_4P_2Se_{10}$, this effect appeared to be counteracted in the literature preparation by an increased Se^{2-}/Se ratio that was a result of the excess Cs_2Se. The

Se^{2-}/Se ratio correlates with the negative charge/Se atom ratio in the melt and increasing these ratios might reasonably favor selenophosphate anions with shorter Se chains.[31]

Experiments were also done to understand the effect of the length of the heating/cooling profile on the $Cs_4P_2Se_{10}$/$Cs_4P_2Se_9$ crystalline product ratio. The 600 °C furnace syntheses were done with a "$Cs_4P_2Se_{12}$" reaction stoichiometry and the heating/cooling profile length was varied between 18 h and 54 h. For all profile lengths, the final product distribution showed that $Cs_4P_2Se_{10}$ was more abundant than $Cs_4P_2Se_9$ but there was a general trend towards smaller $Cs_4P_2Se_{10}$:$Cs_4P_2Se_9$ ratios with longer heating/cooling profiles. This effect may provide some explanation for the discovery of $Cs_4P_2Se_{10}$ under the relatively short 6 h heating/cooling profile of the initial NMR syntheses.

^{31}P Room Temperature and High Temperature NMR Spectroscopy

A Herzfeld-Berger analysis[32] of a room temperature ^{31}P NMR spectrum of $Cs_4P_2Se_{10}$ taken at 7 kHz spinning frequency indicated δ_{11}, δ_{22}, δ_{33} chemical shift anisotropy (CSA) principal values of 50, -41, and -167 ppm, respectively,[33] and similar values were obtained at 12 kHz spinning frequency, Figure 7-4. The $\delta_{11} - \delta_{33}$ CSA principal value difference of ~215 ppm was comparable to that of $Cs_4P_2Se_9$ (~180 ppm) and other compounds with $[P_xSe_y]^{z-}$ anions containing $(Se\text{-}Se)_n$ linkages.[11] The longitudinal relaxation time T_1 of $Cs_4P_2Se_{10}$ was 2100 ± 600 s and was comparable to the T_1 values of other metal selenophosphate compounds.[5] For both $Cs_4P_2Se_9$ and

$Cs_4P_2Se_{10}$ peaks, splittings were observed corresponding to P-Se spin-spin coupling with coupling constant of ~270 Hz.

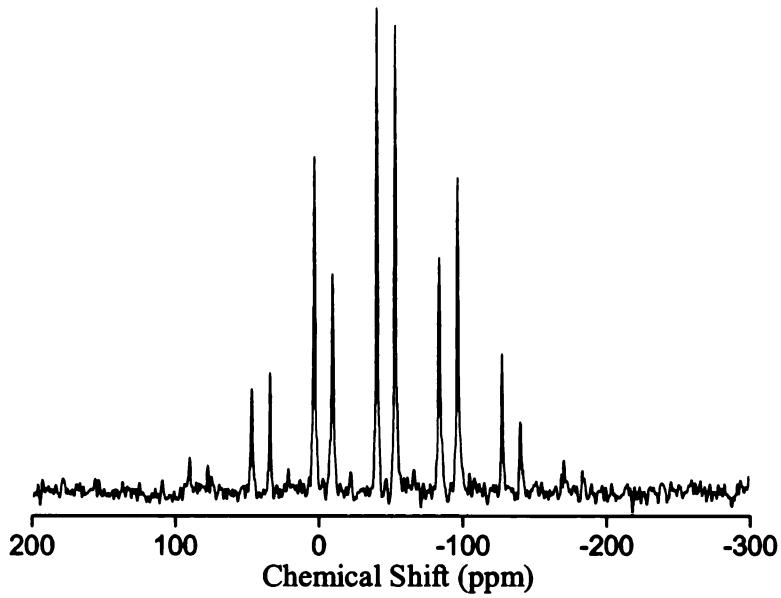

Figure 7-4. The room temperature ^{31}P NMR spectrum of a mixture with "$Cs_4P_2Se_{16}$" stoichiometry that was cooled over 24 h to produce crystalline $Cs_4P_2Se_{10}$ and $Cs_4P_2Se_9$. The MAS frequency was 7 kHz. The intensities of peaks corresponding to $Cs_4P_2Se_{10}$ were used for the determination of CSA principal values of this compound.

The high temperature ^{31}P NMR spectra of the melts of syntheses that produced $Cs_4P_2Se_{10}$ or $Cs_4P_2Se_{10}/Cs_4P_2Se_9$ mixtures contained one peak. Figure 7-1D displays a representative spectrum of a 350 °C melt formed from $Cs_4P_2Se_9$:$Cs_4P_2Se_{10}$ products in a 3:5 ratio, Figure 7-1C. Spectra obtained at a given temperature were independent of both the direction of the temperature ramp and the thermal history of the sample.

The -35 ppm shift at 350 °C was consistent with room temperature chemical shifts of compounds with non-P-P bonded selenophosphate anions and suggested that the P-containing high temperature species did not contain P-P bonds.[11] The high temperature shift was more positive than the crystalline $Cs_4P_2Se_9$ or $Cs_4P_2Se_{10}$ shifts observed at room temperature perhaps because of the loss of defined Cs^+ ion coordination. An

alternate interpretation is that the ^{31}P-containing species at high temperature were neither the $[P_2Se_9]^{4-}$ nor the $[P_2Se_{10}]^{4-}$ anions. At room temperature, the shifts of $Cs_4P_2Se_9$ and $Cs_4P_2Se_{10}$ differ by 13 ppm and it might be expected that if both $[P_2Se_9]^{4-}$ and $[P_2Se_{10}]^{4-}$ anions existed in high concentrations at high temperature, two peaks would be observed in the high temperature spectrum. However, only one peak was observed in all of the melts. The presence of two peaks in the room temperature spectrum but only one peak in the high temperature spectrum (Figure 7-1C,D) shows that there is not a clear NMR correlation between speciation in the crystalline products and speciation in the high temperature melt. It is possible that fast chemical exchange at high temperature prevented observation of discrete chemical shifts for the different species; however, such chemical exchange was not obvious. The final product spectra indicated an increase in the $Cs_4P_2Se_{10}$:$Cs_4P_2Se_9$ ratio with increasing Se but there was no clear trend of the ^{31}P chemical shift in the high temperature melts as a function of Se stoichioimetry. For a single temperature, the overall chemical shift variation in the melts as a function of stoichiometry was less than 10 ppm. In the future, spectra could be obtained at lower temperatures and broader line widths at these temperatures would provide evidence for chemical exchange.

The peak widths of the ^{31}P NMR spectra at 350 °C were typically ~7 ppm or ~1 kHz which was less than the CSA magnitudes of $Cs_4P_2Se_{10}$ (~215 ppm, 35 kHz) and $Cs_4P_2Se_9$ (~180 ppm, 30 kHz).[11] The relative sharpness of the line at high temperature indicated that most of the anisotropy had been averaged out by random tumbling. Therefore, the frequency of motion must be >30 KHz, or have a rotational correlation time of <5 μs/radian.[34] In the context of the Stokes-Einstein-Debye equation for a sphere

tumbling in a liquid, this correlation time τ is proportional to the viscosity η and is inversely proportional to the sphere volume V:

$$\tau = \eta / k_B T V \quad (1)$$

where k_B is the Boltzmann constant and T is temperature in K units.[35] Using a known T and estimated τ, Eq. 1 could be used to calculate either η or V given a value for the complementary property. Although neither η nor V in selenophosphate melts is known with certainty, there is some information to assess these quantities: (1) flame-heated melts readily flow when the sample tube is inverted; and (2) the P-containing species are likely small molecular rather than large polymeric species because the final crystalline products contain discrete $[P_2Se_9]^{4-}$ or $[P_2Se_{10}]^{4-}$ anions. In the next paragraph, (1) V is estimated from the dimensions of the $[P_2Se_{10}]^{4-}$ anion; (2) η is calculated using this value of V; and (3) comparison is made between this calculated η and visual assessment of the melt viscosity. This approach tests whether a viscosity calculated with the assumption of small P-containing anions is close to the viscosity estimated from visual observation of the melts.

The radius of the $[P_2Se_{10}]^{4-}$ anion was estimated to be $r \approx 8$ Å from the longest Se-Se distance within a single $[P_2Se_{10}]^{4-}$ anion and the Se^{2-} ionic radius. Using $V = 4\pi r^3/3$, $T = 1000$ K (estimated temperature of flame-heated melt), and $\tau = 5$ μs, Eq. 1 yielded $\eta \sim 15$ Pa·s which is comparable to the viscosity of honey at room temperature[36] or glycerol at 0 °C.[37] This calculated η is likely an upper limit because $\tau = 5$ μs is an upper limit and because the P-containing anions might be smaller than $[P_2Se_{10}]^{4-}$, e.g. $[PSe_4]^{3-}$ with corresponding smaller V. Despite these caveats, there is general consistency

between the calculated η and visual observation of the melt viscosity. The approach therefore yields qualitative support for the existence of small P-containing species.[22]

CONCLUDING REMARKS

The *in situ* NMR synthesis targeting $Cs_4P_2Se_9$ led to the discovery of $Cs_4P_2Se_{10}$ which can be formed with excess Se and a rapid heating/cooling profile. The $Cs_4P_2Se_{10}$ structure contained the novel discrete molecular anion $[P_2Se_{10}]^{4-}$. The chemically related compound $Cs_4P_2S_{10}$ is non-isomorphic, and it is possible that there are multiple polymorphs of both the thio- and seleno- compounds. The optimum $Cs_4P_2Se_{10}$ synthesis was performed in the high temperature NMR probe with an excess of Se relative to $Cs_4P_2Se_{10}$ and with a ~6 h heating/cooling profile. The $Cs_4P_2Se_{10}$:$Cs_4P_2Se_9$ final product ratio from furnace syntheses was dependent on stoichiometry and on the length of the heating/cooling profile. $Cs_4P_2Se_9$ and $Cs_4P_2Se_{10}$ were favored with Se-starved and Se-rich stoichiometries and with long and short heating/cooling profiles respectively.

Room temperature ^{31}P NMR spectra provided a facile means of evaluating the relative amounts of the P containing compounds made in furnace and NMR syntheses. In addition, some of these spectra presented in the paper have peaks that have not yet been assigned to known crystalline compounds. Careful screening of crystals from these reactions may therefore result in new compound identification.

The high temperature static ^{31}P NMR spectra of the synthetic melts contained one relatively narrow peak that may be the result of a rapidly tumbling selenophosphate anion that does not contain P-P bonds, i.e. a P^{5+} species. Future time-dependent studies of high temperature spectra may provide information about reaction rates. As illustrated by the

discovery of $Cs_4P_2Se_{10}$, future high temperature NMR syntheses may also aid discovery of new compounds.

REFERENCES

1. Kanatzidis, M. G. *Curr. Opin. Solid. St. M.* **1997,** 2, 139-149.

2. Bridenbaugh, P. *Mater. Res. Bull.* **1973,** 8, 1055-1060.

3. Rogach, E. D.; Sviridov, E. V.; Arnautova, E. A.; Savchenko, E. A.; Protsenko, N. P. *Zh. Tekh. Fiz.* **1991,** 61, 201-204.

4. Carpentier, C. D.; Nitsche, R. *Mater. Res. Bull.* **1974,** 9, 1097-1100.

5. Canlas, C. G.; Muthukumaran, R. B.; Kanatzidis, M. G.; Weliky, D. P. *Solid State Nucl. Magn. Reson.* **2003,** 24, 110-122.

6. Maxwell, R.; Eckert, H. *J. Am. Chem. Soc.* **1993,** 115, 4747-4753.

7. Maxwell, R.; Eckert, H. *J. Am. Chem. Soc.* **1994,** 116, 682-689.

8. Maxwell, R.; Eckert, H. *J. Phys. Chem.* **1995,** 99, 4768-4778.

9. Mutolo, P. F.; Witschas, M.; Regelsky, G.; Guenne, J. S. A. D.; Eckert, H. *J. Non-Cryst. Solids* **1999,** 257, 63-72.

10. Schmedt, A. J.; Meise-Gresch, K.; Eckert, H.; Holand, W.; Rheinberger, V. *Glass. Sci. Technol.* **2000,** 73, 90-97.

11. Canlas, C. G.; Kanatzidis, M. G.; Weliky, D. P. *Inorg. Chem.* **2003,** 42, 3399-3405.

12. Harris, R. K. Nuclear Magnetic Resonance Spectroscopy; Longman Scientific and Technical: New York, NY, 1983; pp 87.

13. Chondroudis, K.; Kanatzidis, M. G. *Inorg. Chem.* **1995,** 34, 5401-5402.

14. Fehér, F. Handbuch der Präparativen Anorganischen Chemie; Ferdinand Enke Verlag: Stuttgart, Germany, 1954; Vol. 1, pp 280-281.

15. McCarthy, T. J.; Kanatzidis, M. G. *Inorg. Chem.* **1995,** 34, 1257-1267.

16. *SMART, SAINT, SHELXTL V-5 and SADABS*, Bruker Analytical X-ray Instruments, Inc.: Madison, 1998.

17. Hordvik, A. *Acta. Chem. Scand.* **1966,** 20, 1885-1891.

18. Bottcher, P.; Getzschmann, J.; Keller, R. *Z. Anorg. Allg. Chem.* **1993,** 619, 476-488.

19. Pocha, R.; Johrendt, D. *Inorg. Chem.* **2004,** 43, 6830-6837.

20. Evenson, C. R.; Dorhout, P. K. *Z. Anorg. Allg. Chem.* **2001,** 627, 2178-2182.

21. Aitken, J. A.; Canlas, C.; Weliky, D. P.; Kanatzidis, M. G. *Inorg. Chem.* **2001,** 40, 6496-6498.

22. Chung, I.; Do, J.; Canlas, C. G.; Weliky, D. P.; Kanatzidis, M. G. *Inorg. Chem.* **2004,** 43, 2762-2764.

23. Brese, N. E.; Randall, C. R.; Ibers, J. A. *Inorg. Chem.* **1988,** 27, 940-943.

24. Wachter, J. B.; Chrissafis, K.; Petkov, V.; Malliakas, C. D.; Bilc, D.; Kyratsi, T.; Paraskevopoulos, K. M.; Mahanti, S. D.; Torbrugge, T.; Eckert, H.; Kanatzidis, M. G. *J. Solid State Chem.* **2007,** 180, 420-431.

25. Chrissafis, K.; Kyratsi, T.; Paraskevopoulos, K. M.; Kanatzidis, M. G. *Chem. Mater.* **2004,** 16, 1932-1937.

26. In *Advanced Data Storage Materials and Characterization Techniques*, MRS Proceedings, 2003; Hesselink, L.; Mijiritskii, A., Eds. 2003; p 803.

27. Edwards, A. H.; Pineda, A. C.; Schultz, P. A.; Martin, M. G.; Thompson, A. P.; Hjalmarson, H. P. *J. Phys.: Condens. Matter* **2005,** 17, L329-L335.

28. Ahn, D. H.; Kang, D. H.; Cheong, B. K.; Kwon, H. S.; Kwon, M. H.; Lee, T. Y.; Jeong, J. H.; Lee, T. S.; Kim, I. H.; Kim, K. B. *IEEE Electr. Device L.* **2005,** 26, 286-288.

29. Gidon, S.; Lemonnier, O.; Rolland, B.; Bichet, O.; Dressler, C.; Samson, Y. *Appl. Phys. Lett.* **2004,** 85, 6392-6394.

30. Ohta, T. *J. Optoelectron Adv. Mater.* **2001,** 3, 609-626.

31. Kanatzidis, M. G.; Sutorik, A. C. *Progr. Inorg. Chem.* **1995,** 43, 151-265.

32. Herzfeld, J.; Berger, A. E. *J. Chem. Phys.* **1980,** 73, 6021-6030.

33. Eichele, K.; Wasylishen, R. E. *HBA 1.5*, Dalhousie University and Universität Tübingen: 2006.

34. Harris, R. K. Nuclear Magnetic Resonance Spectroscopy; Longman Scientific and Technical: New York, 1983; pp 86.

35. Cavanagh, J.; Fairbrother, W.; Palmer III, A.; Skelton, N. Protein NMR Spectroscopy : Principles and Practice; Academic Press: San Diego, 1996; pp 17-19.

36. Juszczak, L.; Fortuna, T. *J. Food Eng.* **2006,** 75, 43-49.

37. Weast, R. C.; Astle, M. J., *CRC Handbook of Chemistry and Physics.* 60th ed.; CRC Press, Inc.: Boca Raton, 1980; p F-55.

CHAPTER 8

NUCLEAR MAGNETIC RESONANCE AND ELECTRON PARAMAGENTIC RESONANCE EVIDENCE FOR FREE RADICALS IN CHALCOGENIDE MELTS AND SYNTHESES.

INTRODUCTION

There has been much recent interest in various chalcophosphate compounds because of potentially useful physical properties such as ferroelectric ordering,[1-6] reversible glass-to-crystalline phase changes,[7-11] and magnetic phenomena.[12-14] The structures of these compounds contain an assortment of $[P_xQ_y]^{z-}$ (Q = S, Se, Te) anions, and some ability to choose the type of anion present in the final compound has been demonstrated by varying the reaction stoichiometry.[7,15,16] It was proposed that the products formed in these reactions may be affected by the equilibrium between $[P_xQ_y]^{z-}$ anions.[15]

The different $[P_xQ_y]^{z-}$ anions in the final crystalline products have different phosphorous bonding environments, and it has been shown that NMR spectroscopy provides useful structural information on these compounds. For example, the ^{31}P chemical shift is strongly dependent on the presence or absence of a P-P bond in metal selenophosphates, and ^{31}P-^{31}P dipolar coupling strength has been used to determine thiophosphate anion identity.[17,18] Therefore, if the hypothesis that the anions remain intact at high temperature is true, it is possible that species in high temperature metal chalcophosphate reactions could be characterized using ^{31}P NMR spectroscopy. There are also technical reasons for the choice of ^{31}P NMR and the metal chalcophosphate system. First, ^{31}P NMR spectroscopy has high sensitivity because the ^{31}P isotope has 100% abundance, spin ½, and a large gyromagnetic ratio. Second, many metal chalcophosphates have been prepared using temperatures within the range available to a commercially available high temperature NMR probe (200 °C – 600 °C). Third, the physical state of the metal chalcophosphate mixture at high temperature is often a melt, i.e. a viscous liquid in

which small species will tumble fairly rapidly. This tumbling will provide significant spatial averaging of the anisotropic chemical shift and dipolar couplings experienced by the ^{31}P nucleus and should result in sharper ^{31}P signals than would be observed in the solid state. Although magic angle spinning (MAS) of the sample can also average these anisotropic interactions, MAS at kHz frequencies is technically challenging for the sealed glass reaction ampoules used to contain the reaction mixtures. Flame sealing typically produces an ampoule shape with some non-cylindrical character and the consequent wobbling motion during MAS impedes spinning at high frequencies.

In this study, a combination of NMR and EPR spectroscopies was used to detect a significant population of free radicals in chalcophosphate and chalcostannate melts. The presence of free radicals can have a pronounced effect on many types of chemical reactions including those related to polymerization,[19] organic synthesis,[20-22] atmospheric chemistry,[23,24] and biology and medicine.[25,26] Free radicals in pure S and Se melts were first identified in the 1950s,[27-33] but to our knowledge, the presence of free radicals in chalcogenide-containing solid state reactions has not been previously considered. EPR signals have previously been observed in solid chalcophosphate materials, and it was proposed that the rapid longitudinal relaxation (20 – 80 s) of some room temperature crystalline compounds could be explained by the presence of some residual free radicals.[34] The identification of significant radical concentrations in such melts indicates that radical based reaction mechanisms merit serious consideration.

EXPERIMENTAL SECTION

Synthesis

Samples of a particular nominal stoichiometric composition were prepared by combining the appropriate ratio of the starting materials in fused silica ampoules, sealing *in vacuo* and then heating in computer controlled furnace. The reactants were either the elements or, in the case of the alkali metal-containing samples, A_2Q (A = Na, K, Rb, Cs; Q = S, Se).[35] This mixture was typically heated to 400 °C over 4h, held there for 12h, and then the furnace was turned off. Sample portions of the resultant ingot were resealed in fused silica ampoules and then either used for NMR or EPR spectroscopy. The compounds $K_2Cu_2P_4Se_{10}$[36] and $K_{1.5}Bi_{2.5}(PS_4)_3$[37] were synthesized according to their respective literature preparations. Samples denoted in quotation marks such as "PS_5" refer to an initial mixture of non-crystalline starting materials with the given stoichiometry and samples denoted without quotation marks such as $K_2Cu_2P_4Se_{10}$ refer to a single crystalline compound starting material.

Nuclear Magnetic Resonance (NMR)

The high temperature ^{31}P NMR spectra were collected on a 9.4 T spectrometer (Varian Infinity Plus) using a single resonance static probe (Doty Scientific). Sample portions of the previously described ingots weighing ~75 mg were sealed in fused silica ampoules *in vacuo* and placed in a protective fused silica sheath at the center of the coil in the probe. The samples were heated to the desired temperature at a rate of 10 °C / min and allowed to equilibrate for 5 min before data collection. The π pulse width was typically 12-16 μs and was calibrated to within 0.2 μs at each temperature where a spectrum was

spectrum was collected with the transmitter set at the resonant frequency of the observed spectral peak. The $\pi/2$ pulse duration was calculated as half of the π pulse width Longitudinal relaxation times were measured using an inversion recovery pulse sequence (π-τ-$\pi/2$-acquisition) and the data were fit to the equation[34]

$$I = (2I_0) - I_1 \cdot \left(1 - e^{(-T_1/\tau)}\right) \quad (1)$$

where I was the observed spectral intensity at pulse delay time τ, T_1 was the fitted longitudinal relaxation time, and I_0 and I_1 were fitting parameters that represented the signal intensity at $\tau = 0$ and $\tau = \infty$. The spectra were processed with minimal line broadening and baseline correction and referenced to 85% H_3PO_4 at 0 ppm. The total time spent above room temperature was ~4 h.

Room temperature ^{31}P NMR spectra were collected on the same spectrometer but using a Varian Chemagnetics double resonance magic angle spinning (MAS) probe. The sample volume in the 4 mm diameter zirconia rotors was ~50 μL and the MAS frequency was in the 8 – 14 KHz range. Each sample was ground to a fine powder before being packed in the rotor. The $\pi/2$ pulse width was ~4-6 μs and was calibrated using H_3PO_4, and spectra were processed identically to those at high temperature.

Electron Paramagnetic Resonance (EPR)

EPR spectra were collected on an X-band Bruker ESP300e instrument with a Bruker perpendicular mode 4102ST cavity. The microwave frequency was monitored by an EIP Microwave model 25B frequency counter. The samples were prepared by sealing *in vacuo* a known mass (~45 mg) of the desired starting material in a 3 mm outside diameter fused silica ampoule. The samples were then placed in a ceramic holder and

inserted in a furnace. The furnace was heated over 4 h to reach either 550 or 1000 °C and held there for 12 h. The samples were then removed from the furnace and holder and immediately quenched in ice water and placed into the EPR cavity. Single spectra were collected with ~200 mW X-band microwave radiation.

Approximate concentrations of radicals were determined using a calibration curve generated using known masses of 2,2-diphenyl-1-picrylhydrazyl (DPPH). After achieving critical cavity coupling, the iris of the resonator was fixed, and retuning for each subsequent reference and chalcophosphate or chalcostannate sample was performed without changing the iris setting. Spectra used for quantitation were collected using identical parameters, i.e. modulation amplitude, modulation frequency, time constant, sweep width, and temperature. Signal intensity was determined by fitting the background with up to a cubic polynomial fit and then performing a double integration. Quantitation of radicals in the 1000 °C quenched PS_5 sample was also performed using a $CuSO_4$ standard of known concentration. The samples used for calibration were prepared by standard dilution of $CuSO_4$ in a 1:1 mixture of glycerol and water, and then adding a known volume of the resultant solution to an EPR tube. The standard samples were quenched in liquid nitrogen before inserting into the EPR cavity which was maintained at 5 K during the measurement. The chalcophosphate samples were also maintained at 5 K during data collection which was otherwise performed identically to the procedure described above. For each sample, the radical concentration was converted to one unpaired electron spin per some number of atoms by dividing the experimentally derived radical concentration by the approximate number of atoms in the sample determined using the sample mass and composition.

Powder X-ray diffraction

Powder X-ray diffraction patterns of the crystalline compounds were collected before and after high temperature NMR measurements using a Rigaku-Denki RW400F2 (Rotaflex) powder diffractometer. The data were collected using a copper rotating anode operating at 45 kV and 100 mA.

RESULTS AND DISCUSSION

The original motivation for this study was to test the hypothesis that an equilibrium between the various $[P_xQ_y]^{z-}$ anions exists at high temperature, as was previously proposed.[15] During setup of the NMR spectrometer to study a prototypical chalcophosphate sample, it was serendipitously discovered that a cumulative Bloch decay signal could be obtained with pulsing with only ~100 ms delay between acquisitions. This result was initially surprising because of the typical ~1000 s T_1 value of ^{31}P in room temperature solid metal chalcophosphates, Table 8-1.[34] Although fast relaxation had been previously observed in high temperature NMR measurements of related materials,[38-42] we are not aware of a systematic study to understand this phenomenon or assign its cause.

NMR evidence for free radicals in chalcophosphate melts

Figure 8-1 displays representative spectra at different temperatures for a melt with "PS_5" stoichiometry and Figure 8-2 graphically displays the temperature dependences of the peak chemical shifts line widths, and longitudinal $1/T_1$ relaxation rates. Table 8-1 summarizes the high temperature NMR parameters for this and other melts and for some

of the NMR spectra before and after heating and cooling. Figure 8-3 displays two other representative high temperature NMR spectra of $K_2Cu_2P_4Se_{10}$ and "$KPSe_7$". The crystalline compounds $K_2Cu_2P_4Se_{10}$, $K_{1.5}Bi_{2.5}(PS_4)_3$, and KH_2PO_4 melted congruently so the initial and final compounds were the same as determined by comparisons of the powder X-ray diffraction patterns and the ^{31}P NMR spectra before and after thermal treatment.

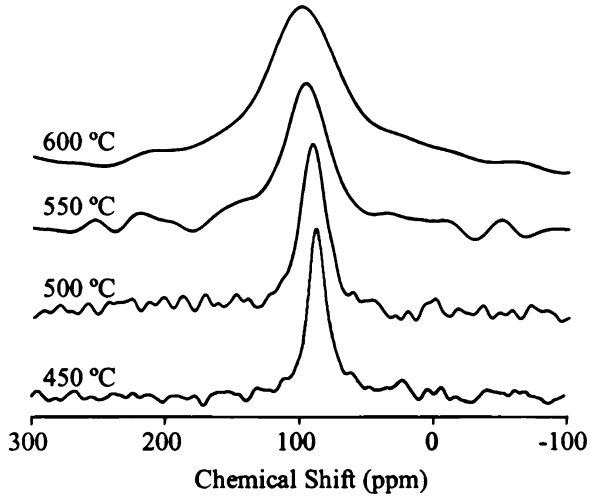

Figure 8-1. NMR spectra of a melt mixture with the nominal ratio "PS_5" showing the increase in chemical shift and peak width as a function of temperature. Spectra at 450, 500, 550, and 600 °C were acquired with acquisition delays of 2 s and represent the sums of 16 scans.

Table 8-1. NMR parameters in high temperature melts and room temperature solids. Samples in quotation marks represent nominal compositions, and those without quotation marks were pure crystalline compounds at room temperature. The 22 °C data listed above and below the high temperature data were collected before and after the high temperature data, respectively.

Sample	Temp. (°C)[a]	Peak Chemical Shift (ppm)[b]	Peak Width (KHz)[c]	Longitudinal Relaxation Time (ms)[d]
$KPSe_7$	350	-13.2	1.7	11.7
	450	3.4	2.2	2.5
	550	30.6	2.7	0.47
$Cs_4P_2Se_{16}$	22	35.0, -21.8	1.0, 4.8	n.d.
	350	-34.8	1	n.d.
	450	-21.4	1.5	n.d.
	550	7.06	2.3	n.d.
$K_4P_6Te_{25}$	550	355.8	2.5	0.7
$K_4P_6Se_{25}$	550	77.2	4	0.3
PS_5	350	80.4	4.1	115
	450	86.9	2.5	37
	550	98	5.7	9
$K_2Cu_2P_4Se_{10}$[e]	22	55.7	0.1	$1.0x10^6$
	400	93.3	3	4.8
	500	109.9	3.7	2.5
	600	130.9	5.1	1.5
$K_{1.5}Bi_{2.5}(PS_4)_3$[f]	22	55.7	1	$1.4x10^5$
	550	76	0.9	15.7
	22	88.8, 72.4	1.0, 0.8	$5.7x10^5$
KH_2PO_4	22	4.2	0.5	$1.3x10^6$
	350	-7.2, -14.7	0.6, 0.5	$6.7x10^3$
	22	4.5	0.7	$7.0x10^5$
KH_2PO_4S	350	-7.2, -13.2	1.0, 1.5	343

[a] The uncertainty in temperature is estimated to be ± 5 °C.

[b] Chemical shifts were determined by fitting the spectral peaks to a 50% Gaussian 50% Lorentzian line function and the reported chemical shift was the peak center fitting parameter. The uncertainty is estimated to be ± 0.5 ppm.

[c] Peak widths were determined by fitting the spectral peaks to a 50% Gaussian 50% Lorentzian line function and the reported line width measurement was the full width at half maximum (FWHM). A 50% Gaussian 50% Lorentzian line was chosen because it was in closer agreement with the experimental spectrum than a Gaussian or a Lorentzian line alone. Room temperature linewidths were measured under MAS conditions and high temperature linewidths were measured under static conditions. The estimated uncertainty in the line width is ± 5%.

[d] The method of measuring the longitudinal relaxation time is described in the text. The uncertainty is estimated to be ± 12 %.

[e] Chondroudis, K.; Kanatzidis, M. G. *Inorg. Chem.* **1998**, *37*, 2098-2099.

[f] Gave, M.; Weliky, D. P.; Kanatzidis, M. G. *Inorg. Chem.* **2007**, 46, 11063-11074.

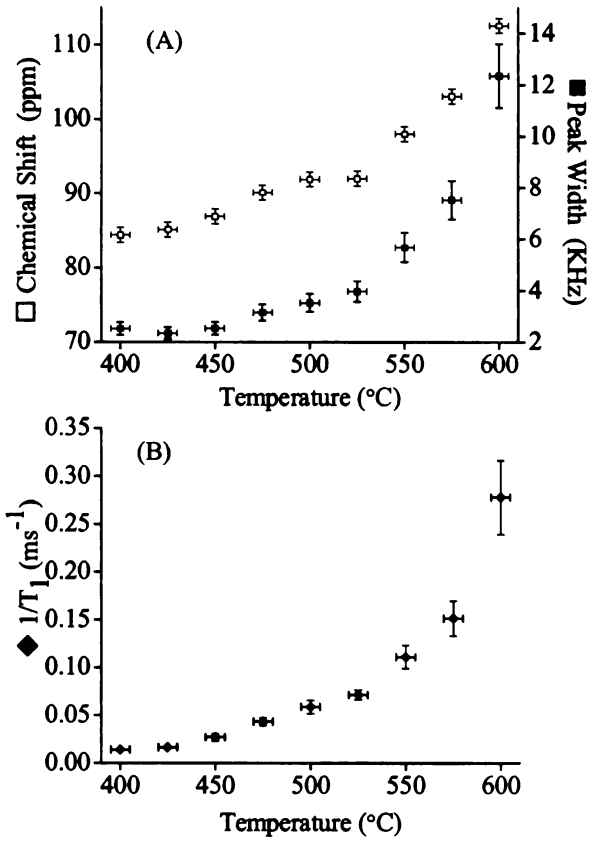

Figure 8-2. (A) Peak ^{31}P chemical shifts and peak widths as a function of temperature in a melt with the nominal composition "PS_5". Chemical shifts and peak widths were determined by fitting the spectral peak to a 50%/50% Gaussian and Lorentzian line function. The chemical shifts and peak widths are represented by open and closed squares, respectively. (B) ^{31}P longitudinal NMR relaxation rates for "PS_5" as a function of temperature.

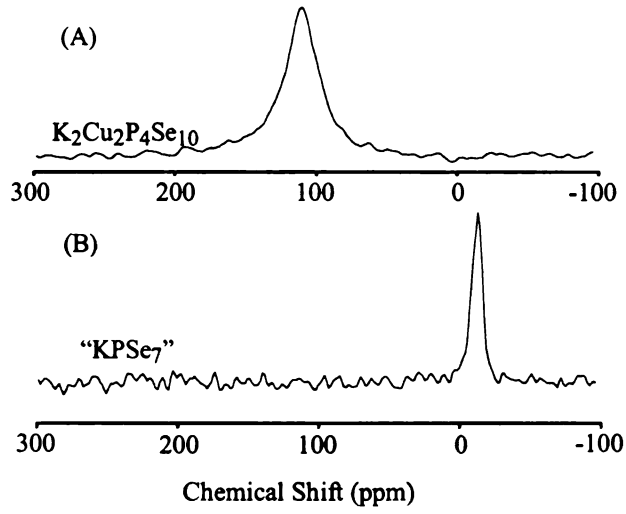

Figure 8-3. High temperature ^{31}P NMR spectra of (A) $K_2Cu_2P_4Se_{10}$ at 550 °C and (B) a sample with the nominal composition "$KPSe_7$" at 350 °C. The spectra were acquired with acquisition delays of 10 ms and 200 ms, respectively and represent the sums of 50 scans.

In all samples, a single ^{31}P NMR peak was observed in the melt, Figures 8-1 and 8-3. In samples for which spectra were obtained at multiple temperatures, the peak chemical shift moved downfield with increasing temperature and the line width and longitudinal relaxation rates increased with increasing temperature. In a single sample, the peak shifts, line widths, and longitudinal relaxation rates had non-linear dependence on temperature. Determination of the transverse relaxation time T_2 was attempted using a Carr-Purcell-Meiboom-Gill echo pulse sequence[43,44] but accurate determination of T_2 when $T_2 < 100$ μs is impossible because it is not possible to have pulses separated by less than 100 μs. The typical decay of the echoes occurred in <100 μs and this suggests an upper limit of ~100 μs on ^{31}P T_2 values in the melt.

For samples containing S, Se, or Te, the typical ^{31}P T_1 in the high temperature melt was ~10 ms and was ~10^5 times shorter than the typical room temperature T_1 of crystalline metal chalcophosphates. The effect was much less pronounced in the KH_2PO_4

melt and the T_1 for this melt at 350 °C was ~150 times shorter than the T_1 of the crystalline compound. The T_1 = 340 ms in the "KH_2PO_4S" melt at 350 °C can be compared to the T_1 = 6700 ms in the KH_2PO_4 melt and shows that the presence of chalcogen in the melt has a substantial effect on T_1. There does not appear to be different chemistry with addition of S because the X-ray powder pattern of the final ambient temperature "KH_2PO_4S" sample was a superposition of the KH_2PO_4 crystalline powder pattern and an amorphous background, presumably from elemental S.

The rapid longitudinal relaxation rates ($1/T_1$s) in the melts and the increases in $1/T_1$s, line widths and chemical shifts with increasing temperature are all potentially attributable to the presence of unpaired electron spins. The presence of radicals in melts of the pure S and Se has been well documented[28,30,31,45] so it is reasonable to consider that there are also radicals in chalcophosphate melts. Unpaired electrons typically increase nuclear spin relaxation rates because the electron spin has a large dipole moment and electron spin transitions can occur near the NMR frequency of the detected nucleus. Stable free radicals such as $[Cr(H_2O)_6]ClO_4$[46] and $Gd(dpm)_3$ (dpm = bis(2,2,6,6-tetramethyl-3,5-heptadionate))[47] have been intentionally added to solutions to decrease the nuclear spin T_1[48] and to allow more rapid collection of the NMR data. At sufficiently high concentrations (i.e. $>10^{-2}$ M), the unpaired electron spins will also increase the nuclear spin transverse relaxation rate and deshield the nucleus.[46,47] These effects are consistent with the relatively short T_2s and broad line widths of the ^{31}P NMR melt spectra and the downfield ^{31}P chemical shifts. Because free radicals are high energy species, it is reasonable that their concentration would increase with increasing temperature. This

hypothesis correlates with the larger ^{31}P longitudinal relaxation rates, line widths and peak chemical shifts at higher temperatures.

The dependence of the chemical shift and peak width is correlated with a non-linear increase of radical concentration as a function of temperature. This nonlinear dependence of the chemical shift, and peak width is modeled in more detail in Chapter 9. The paramagnetic contribution to the magnetic shielding depends linearly on the radical concentration.[28] Therefore, a non-linear change in chemical shift and peak width results from a non-linear increase in free radical concentration. A similar temperature dependence was also observed for pure elemental Se.[28]

Comparison of chalcophosphate melts to pure Se by high temperature NMR

The ^{77}Se T_1s of Se melts were 2 ms at 400 °C and ~0.2 ms at 600 °C[28] and were comparable to the high temperature chalcophosphate relaxation times summarized in Table 8-1. Over this same temperature range (400 – 600 °C) the transverse relaxation time, T_2 of the ^{77}Se melts changed from ~0.1 ms at 600 °C to ~0.8 ms at 400 °C, or linewidths in the T_2 broadened limit of ~3.2 KHz and ~0.4 KHz, respectively. These are comparable to the linewidths of the chalcophospate linewidths summarized in Table 8-1. The similarity of the ^{31}P NMR parameters in chalcophosphate melts and ^{77}Se NMR parameters in selenium melts as well as similarity of the parameter variations with temperature suggest that the parameters are governed by the same underlying phenomenon. For the pure Se melts, this phenomenon has clearly been shown to be a significant concentration of unpaired electron spins.

The change in the ^{77}Se chemical shift that was observed in a melt of pure Se[28] is similar to the change in the ^{31}P chemical shift in chalcophosphate melts in frequency units. Comparison of the ^{77}Se spectra at 400 and 600 °C showed a chemical shift difference $\delta_{600} - \delta_{400} \approx 85$ ppm, or 6.5 KHz assuming a 76.3 MHz ^{77}Se resonant frequency.[28] For the melts of $K_2Cu_2P_2Se_{10}$, the ^{31}P NMR spectra had $\delta_{600} - \delta_{400} \approx 37.6$ ppm, Table 8-1, or 6.1 KHz. The average hyperfine coupling strength between the electron and nucleus is independent of applied field, and is proportional to the number of unpaired spins that are present and proximate.[49] The similarity of the contact shifts in frequency units is evidence that the concentrations of free radicals in pure Se melts is comparable to that in the chalcophosphate melts. At 600 °C, pure elemental Se was reported to contain 1 unpaired electron per ~350 atoms.[28] For this comparison to be made, however, the assumption must be made that the hyperfine coupling between the electron and the ^{77}Se nuclei in the pure chalcogen melts is equivalent to the electron to phosphorous hyperfine coupling in the chalcophosphate melts.

High temperature NMR of a tellurophosphate-containing melt

The ^{31}P NMR spectrum of "$K_4P_6Te_{25}$" was similar to the other chalcophosphate melts studied in that there was a single resonance with a rapid relaxation rate, but the chemical shift was significantly further downfield than any of the other melts studied, Table 8-1. This indicated that the ^{31}P local environment in this melt was fundamentally different than those in the other O, S, or Se-containing melts. To date, there are only several known tellurophosphates with P-Te bonds, whereas there are thousands of members with P-O, P-S, or P-Se bonds. The chemical shifts of crystalline compound

$K_4P_8Te_4$ were -4.3, -16.9, and -34.6 ppm. These chemical shifts are similar to those observed in various oxo-, thio- and selenophosphate compounds. The combination of the NMR and synthetic results suggests that the species that exist in P/Te containing melts may be very different than those in P/O, P/S, and P/Se containing melts. The electronegativity of Te (2.1 Pauling units) is only slightly less than the electronegativites of Se (2.4 Pauling units) and S (2.5 Pauling units),[50] so the difference in the high temperature chemical shifts is unlikely to be explained solely by these electronegativities.

Room temperature electron paramagnetic resonance

Room temperature EPR spectra of rapidly quenched chalcophosphate melts were collected to test for the presence of radicals that were present at high temperature and did not recombine during the quenching process. This approach had previously been used to study radical concentration in quenched Se and S melts and it was estimated that there was ~100-fold loss in radical concentration during the quenching process presumably due to radical recombination.[51]

Figure 8-4 displays EPR spectra of "PS_5" samples quenched from 550 and 1000 °C and Figure 8-5 displays EPR spectra of "SnS_5", "PSe_5", and $K_{1.5}Bi_{2.5}(PS_4)_3$. The spectral lineshapes and intensities of the S-containing samples at a given temperature were approximately independent of the chemical stoichiometry. The 550 °C samples contained a symmetric line centered near $g \approx 2.00$ and with an ~ 5 G peak width, Figures 8-4B and 8-5A. The S-containing samples quenched from 1000 °C were also similar, and contained an asymmetric line centered at $g = 2.02$ with an ~230 G peak with, Figures 4A, 5C. Possible reasons for the broad line width and complex line shape of the 1000 °C samples

include: (1) the dominant radical species had a large hyperfine coupling between the unpaired electron spin and the ^{31}P nucleus, (2) the dominant radical species had a large g-anisotropy (3) there was a superposition of signals from chemically different radical species or (4) the dominant species was a biradical.[28] The "PSe_5" sample contained at least two different resonances centered at g = 2.007 and g ≈ 1.933 with line widths of 11 G and 75 G, respectively, Figure 8-5B.

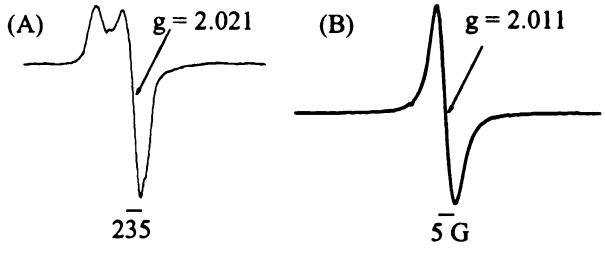

Figure 8-4. EPR spectra at room temperature of rapidly quenched "PS_5" samples. Prior to quenching, the sample temperature in the furnace was (A) 1000 °C or (B) 550 °C. Acquisition parameters were: (A) 10 G modulation amplitude, 2000 G sweep width and (B) 0.1 G modulation amplitude, 50 G sweep width.

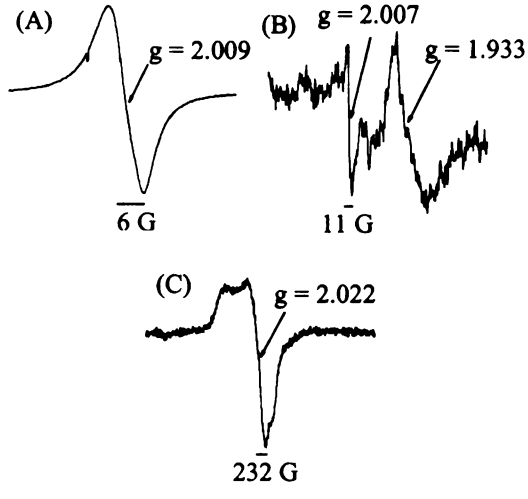

Figure 8-5. Room temperature EPR of (A) "SnS_5" quenched from 550 °C (B) "PSe_5" quenched from 550 °C and (C) $K_{1.5}Bi_{2.5}(PS_4)_3$ quenched from 1000 °C. Acquisition parameters were: (A) 1 G modulation amplitude, 40 G sweep width; (B) 1 G modulation amplitude, 500 G sweep width; and (C) 10 G modulation amplitude, 3000 G sweep width. Each spectrum was a single acquisition.

Comparison of integrated spectral intensities with those of DPPH and $CuSO_4$ standards yielded one unpaired electron per ~10^5 atoms in the 550 °C sample of Figure 8-4B and 1 unpaired electron per ~10^4 atoms in the 1000 °C sample of Figure 8-4A. The 550 °C quenched "SnS_5" sample of Figure 8-5A also contained 1 unpaired electron per ~10^4 atoms. Samples quenched from 1000 °C melts formed from the pure crystalline compound $K_{1.5}Bi_{2.5}(PS_4)_3$ had comparable line shapes, line widths, and radical concentrations to that of "PS_5" quenched from the same temperature, Figure 8-5C . Radical quantitation of the "PSe_5" sample was unreliable because of significant nonlinearity in the baseline and a partial overlap of the signals.

These data suggest that significant radical concentrations are a general feature of chalcogen-containing melts. The measured concentrations of 1 unpaired electron per 10^4-10^5 atoms in the quenched melts likely represents a lower limit on the radical concentrations in the high temperature melts because of loss of radicals during the quenching process presumably from radical recombination. A loss of at least 100-fold was reported in an earlier study on quenched Se and S melts.[51]

It was previously reported that pure Se at 600 °C and 100 bars contained 1 unpaired electron per ~350 atoms and pure Se at 1000 °C and 100 bars contained 1 unpaired electron per ~20 atoms.[28] If there is a 100-fold loss in radical concentration during the quenching process, the EPR results on the quenched melts correlate with radical concentrations in the thiophosphate and thiostannate melts of one unpaired electron per 10^3 atoms at 550 °C and one unpaired electron per 10^2 atoms at 1000 °C. These concentrations are comparable to the reported radical concentrations in the pure Se melts near these temperatures. To our knowledge, there is no similar literature on the

quantitation of elemental S, but our quantitation of a 550 °C quenched pure S melt was found to contain 1 unpaired electron per ~10^4 atoms. These concentrations are again comparable to the thiophosphate samples studied here, and also the concentration of radicals in pure Se, assuming the 100-fold loss of radicals upon quenching.

Most EPR spectra were obtained within minutes of quenching but for the "PS_5" sample quenched from 1000 °C, an additional spectrum was obtained four hours after quenching. The *g* values, line shape, and line width did not change with time but there was a ~10% loss in signal intensity after four hours that was evident as a change in the absolute intensity of the signal. This change can likely be ascribed to radical recombination that occurs at room temperature following the quench.

Chemical implications of free radicals

Free radical polymerizations of organic monomers occurs in the presence of ≤ 10^{-6} M radical concentration, or, assuming a dilute monomer concentration, about one radical per 10^8 atoms.[29,52] The radical concentration in chalcophosphate and chalcostannate melts appears to be 10^3-10^6 times greater and it is reasonable to consider that the radicals play some role in the melt chemistry and the eventual formation of ambient temperature crystalline products. One specific hypothesis is that the S-S or Se-Se bonds in complex anions[53] such as $[P_2S_{10}]^{4-}$ or $[P_2Se_{10}]^{4-}$ in crystalline compounds could be formed by radical recombination. The NMR T_1 data suggest that the concentrations of radicals are much higher in chalcophosphate melts than in oxyphosphate melts and this difference could be correlated with the larger variety of bonding motifs of chalcophosphate anions in crystalline compounds. For example, compounds with anions such as $[P_2S_{10}]^{4-}$ and

$[P_4Se_{10}]^{4-}$ have been observed but there are no reports to-date of compounds with the corresponding $[P_2O_{10}]^{4-}$ and $[P_4O_{10}]^{4-}$ anions even though thousands oxyphosphate compounds are known. One further possibility is that the differences that are observed between reactions performed at intermediate temperatures (i.e. 200 – 600 °C) and those at higher temperatures (i.e. > 600 °C)[54] may be correlated with the increase in radical concentration that occurs over those temperatures.

CONCLUDING REMARKS

^{31}P NMR and EPR studies provide compelling evidence for a radical concentration in chalcophosphate and chalcostannate melts of one unpaired spin per $10^2 - 10^5$ atoms and the radicals may play a significant role in the melt chemistry and formation of the final crystalline compounds. The radicals also have a significant impact on the application of ^{31}P NMR to these systems: the short relaxation times allow for spectra to be acquired rapidly, but also give rise to broad spectral lines. Future EPR studies will perhaps be useful for determining the structure of the radical-containing species.

REFERENCES

1. Bourdon, X.; Maisonneuve, V.; Cajipe, V. B.; Payen, C.; Fischer, J. E. *J. Alloys Compd.* **1999,** 283, 122-127.

2. Carpentier, C. D.; Nitsche, R. *Mater. Res. Bull.* **1974,** 9, 1097-1100.

3. Gave, M.; Bilc, D.; Mahanti, S.; Breshears, J.; Kanatzidis, M. *Inorg. Chem.* **2005,** 5293-5303.

4. Maisonneuve, V.; Cajipe, V. B.; Simon, A.; VonDerMuhll, R.; Ravez, J. *Phys. Rev. B.* **1997,** 56, 10860-10868.

5. Simon, A.; Ravez, J.; Maisonneuve, V.; Payen, C.; Cajipe, V. B. *Chem. Mat.* **1994,** 6, 1575-1580.

6. Vysochanskii, Y. *Ferroelectr.* **1998,** 218, 629-636.

7. Chung, I.; Do, J.; Canlas, C. G.; Weliky, D. P.; Kanatzidis, M. G. *Inorg. Chem.* **2004,** 43, 2762-2764.

8. Chrissafis, K.; Kyratsi, T.; Paraskevopoulos, K. M.; Kanatzidis, M. G. *Chem. Mat.* **2004,** 16, 1932-1937.

9. Gidon, S.; Lemonnier, O.; Rolland, B.; Bichet, O.; Dressler, C.; Samson, Y. *Appl. Phys. Lett.* **2004,** 85, 6392-6394.

10. Ohta, T. *J. Optoelectron. Adv. M.* **2001,** 3, 609-626.

11. Wachter, J. B.; Chrissafis, K.; Petkov, V.; Malliakas, C. D.; Bilc, D.; Kyratsi, T.; Paraskevopoulos, K. M.; Mahanti, S. D.; Torbrugge, T.; Eckert, H.; Kanatzidis, M. G. *J. Solid State Chem.* **2007,** 180, 420-431.

12. Chondroudis, K.; Kanatzidis, M. G. *Inorg. Chem. Commun.* **1998,** 1, 55-57.

13. Odile, J. P.; Steger, J. J.; Wold, A. *Inorg. Chem.* **1975,** 14, 2400-2402.

14. Taylor, B.; Steger, J.; Wold, A.; Kostiner, E. *Inorg. Chem.* **1974,** 13, 2719-2721.

15. Kanatzidis, M. G. *Curr. Opin. Solid. St. M.* **1997,** 2, 139-149.

16. Chung, I.; Karst, A. L.; Weliky, D. P.; Kanatzidis, M. G. *Inorg. Chem.* **2006,** 45, 2785-2787.

17. Canlas, C. G.; Kanatzidis, M. G.; Weliky, D. P. *Inorg. Chem.* **2003,** 42, 3399-3405.

18. Gunne, J.; Eckert, H. *Chem.-Eur. J.* **1998,** 4, 1762-1767.

19. Hutchinson, R. Handbook of Polymer Reaction Engineering; Wiley-VCH Verlag GmbH & Co. KGaA: Weinheim, Germany, 2005; Vol. 1, pp 153-212.

20. Wille, U. *Chem.-Eur. J.* **2002,** 8, 341-347.

21. Zhuikov, V. V. *Russ. J. Gen. Chem.* **1999,** 69, 1796-1800.

22. Kaim, W. *Z. Naturforsch. B* **1985,** 40, 61-66.

23. Monks, P. S. *Chem. Soc. Rev.* **2005,** 34, 376-395.

24. Mellouki, A.; Le Bras, G. *Mater. Sci. Forum.* **1999,** 301, 47-67.

25. Aruoma, O. I.; Halliwell, B. Molecular biology of free radicals in human diseases; OICA International: Sant Lucia, London, 1998.

26. Halliwell, B.; Gutteridge, J. M. C. Free radicals in biology and medicine; 4th ed.; Oxford University Press: New York, NY, 2007.

27. Sampath, P. I. *J. Chem. Phys.* **1966,** 45, 3519-3525.

28. Warren, W. W.; Dupree, R. *Phys. Rev. B.* **1980,** 22, 2257-2275.

29. Carswell, T. G.; Hill, D. J. T.; Hunter, D. S.; Pomery, P. J.; Odonnell, J. H.; Winzor, C. L. *Eur. Polym. J.* **1990,** 26, 541-544.

30. Koningsberger, D.; Van Wolput, J.; Rieter, P. *Chem. Phys. Lett.* **1971,** 8, 145-147.

31. Gardner, D. M.; Fraenkel, G. K. *J. Am. Chem. Soc.* **1956,** 78, 3279-3288.

32. Gardner, D. M.; Fraenkel, G. K. *J. Am. Chem. Soc.* **1954,** 76, 5891-5892.

33. Massen, C. H.; Weijts, A. G. L.; Poulis, J. A. *T. Faraday Soc.* **1964,** 60, 317-&.

34. Canlas, C. G.; Muthukumaran, R. B.; Kanatzidis, M. G.; Weliky, D. P. *Solid State Nucl. Magn. Reson.* **2003,** 24, 110-122.

35. Fehér, F. Handbuch der Präparativen Anorganischen Chemie; Ferdinand Enke Verlag: Stuttgart, Germany, 1954; Vol. 1, pp 280-281.

36. Chondroudis, K.; Kanatzidis, M. G. *Inorg. Chem.* **1998,** 37, 2098-2099.

37. Gave, M.; Weliky, D. P.; Kanatzidis, M. G. *Inorg. Chem.* **2007,** 46, 11063-11074.

38. Maxwell, R.; Eckert, H. *J. Phys. Chem.* **1995,** 99, 4768-4778.

39. Maxwell, R.; Eckert, H. *J. Am. Chem. Soc.* **1993,** 115, 4747-4753.

40. Maxwell, R.; Eckert, H. *J. Am. Chem. Soc.* **1994,** 116, 682-689.

41. Maxwell, R.; Erickson, H.; Eckert, H. *Z. Naturforsch. A* **1995,** 50, 395-404.

42. Schmedt, A. J.; Meise-Gresch, K.; Eckert, H.; Holand, W.; Rheinberger, V. *Glass. Sci. Technol.* **2000,** 73, 90-97.

43. Carr, H. Y.; Purcell, E. M. *Phys. Rev.* **1954,** 94, 630-638.

44. Meiboom, S.; Gill, D. *Rev Sci Instrum* **1958,** 29, 688-691.

45. Tveryanovich, Y. S.; Borisova, Z. U. *Inorg. Mater.* **1979,** 15, 1664-1667.

46. Freeman, R.; Pachler, K. G. R.; Lamar, G. N. *J. Chem. Phys.* **1971,** 55, 4586-4593.

47. Dechter, J. J.; Levy, G. C. *J. Magn. Reson.* **1980,** 39, 207-215.

48. Sharp, R.; Lohr, L.; Miller, J. *Prog. Nucl. Mag. Res. Sp.* **2001,** 38, 115-158.

49. Wertz, J. E.; Bolton, J. R. Electron spin resonance; elementary theory and practical applications; McGraw-Hill: New York,, 1972; pp 38-48.

50. Greenwood, N. N.; Earnshaw, A. Chemistry of the Elements; 2nd ed.; Butterworth-Heinemann: Boston, MA, 1997; pp 662, 754.

51. Bagley, B. G.; Waszczak, J. V.; Disalvo, F. J. *Solid State Commun.* **1972,** 11, 89-92.

52. Shen, J. C.; Tian, Y.; Zeng, Y. G.; Qiu, Z. W. *Makromol. Chem.-Rapid* **1987,** 8, 615-620.

53. Aitken, J. A.; Canlas, C.; Weliky, D. P.; Kanatzidis, M. G. *Inorg. Chem.* **2001,** 40, 6496-6498.

54. Kanatzidis, M. G.; Sutorik, A. C. *Progr. Inorg. Chem.* **1995,** 43, 151-265.

CHAPTER 9

ON THE SPECIATION OF CHALCOPHOSPHATE-CONTAINING MELTS.

INTRODUCTION

The presence of a significant concentration of free radicals in chalcogen-containing melts has recently been demonstrated.[1] The existence of the radicals was inferred from the ^{31}P high temperature NMR spectra that had chemical shifts, peak widths, and relaxation times that were strongly temperature dependent and these effects can be readily interpreted on the basis of the presence of free radicals.[2-4] The presence of the free radicals was confirmed by the presence of strong EPR signals on chalcogen-containing samples that had been rapidly quenched from the melt.[1,5]

Previously, it was shown that solid state NMR provides useful structural information of diamagnetic crystalline selenophosphate compounds. Most notably, the ^{31}P chemical shift of selenophosphate-containing crystalline compounds is correlated with the presence or absence of a P-P bond. Compounds that contain a selenophosphate anion with a P-P bond typically have positive chemical shifts, and compounds with a selenophosphate anion without a P-P bond typically have negative chemical shifts. For example, the compounds $Rb_2CdP_2Se_6$ and $Pb_2P_2Se_6$ which contain the molecular $[P_2Se_6]^{4-}$ anion have chemical shifts of 62.0 ppm and 29.1 ppm, respectively.[6] Conversely, compounds without a P-P bond typically have a negative chemical shift. Examples include $Cs_4P_2Se_9$ and Cu_3PSe_4 which contain the molecular $[P_2Se_9]^{4-}$ and $[PSe_4]^{3-}$ anions, respectively, and resonate at -39.9 ppm and -83.3 ppm.[6] The high temperature ^{31}P NMR spectra are not trivially interpreted in a similar fashion because: (1) crystal structures are available for the solid compounds but not for the liquid melts and therefore the ^{31}P chemical environments have not been previously determined; (2) the paramagnetic contact shift that occurs with increasing radical concentration is capable

of moving the ^{31}P spectral feature from a region that could be attributed to a non P-P bonded species to a region ascribed to P-P bonded species.

The chemical shift and peak width have a non-linear temperature dependence, and this dependence is correlated with the effects of the paramagnetic radical species. In this study, the effects of the free radicals on the chemical shift and peak width were modeled, and this effect was removed so that the chemical shift and peak width of the diamagnetic species could be determined. Some correlation existed between the modeled chemical shift and the chemical shift that would be expected based off of the ^{31}P chemical environment in the known solids. This provides some evidence that the phosphorous coordination in the crystalline solid may be closely related to the chemical environment in the liquid melt. In each case, the extrapolated peak width was significantly larger than is observed for typical crystalline compounds but smaller than what is observed in a typical amorphous glass.

EXPERIMENTAL SECTION

Reagents

Chemicals were used as obtained unless otherwise noted: phosphorous (MCB Reagents, Gibbstown, NJ, amorphous red), selenium shot (Tellurex Inc., Traverse City, MI, 99.999%), sulfur (Alfa Aesar, Ward Hill, MA, sublimed flowers), copper (Fisher Scientific, Hampton, NH, electrolytic dust), silver powder,[7] bismuth (Tellurex Inc., Traverse City, MI, 99.999%), potassium (Aldrich Chemical Co. Inc., St. Louis, MO), and thallium (ABCR, Karlsruhe, Germany, 99.999%). Selenium and bismuth were ground to

~100 mesh in an agate mortar and pestle. K_2Se[8,9] and P_2Se_5[10] were produced as described elsewhere.

Synthesis

The crystalline compounds $K_{1.5}Bi_{2.5}(PS_4)_3$,[11] $K_2Cu_2P_4Se_{10}$,[12] $TlBiP_2Se_6$,[13] and $RbPSe_6$[14,15] were prepared according to their respective literature preparations. $Hg_2P_2Se_6$ was produced by combining Hg (0.9356 g, 4.7 mmol), P (0.0627 g, 2.0 mmol), and Se (0.4728 g, 6.0 mmol) in a fused silica ampoule, then flame sealing under a reduced pressure of ~100 mTorr. This ampoule was loaded into a protective ceramic sheath, and then allowed to react by heating to 450 °C over 12h and holding there for 24h, then cooling over 6h back to room temperature.

A ~1:1 mole ratio of $Hg_2P_2Se_6$ and $RbPSe_6$ was formed by combining 17.7 mg and 26.6 mg, respectively. This sample was heated in the NMR spectrometer as described below. The Samples in quotation marks (i.e. "PS_5") represented mixtures that were not intended to produce a compound with a given stoichiometry. These mixtures were formed by combining the appropriate stoichiometric ratio of the reactants, sealing them in a fused silica ampoule, and then placing them into the high-temperature probe of the NMR spectrometer. Typical heating profiles for these samples are described below.

^{31}P High Temperature NMR Spectroscopy

The high temperature ^{31}P NMR spectra were collected on a 9.4 T spectrometer (Varian Infinity Plus) using a single resonance static probe (Doty Scientific). Sample portions weighing ~75 mg were sealed in fused silica ampoules *in vacuo* and placed in a

protective fused silica sheath at the center of the coil in the probe. The samples were heated to the desired temperature at a rate of 10 °C / min and allowed to equilibrate for 5 min before data collection. The π pulse width was typically 12-16 μs and was calibrated for each sample to within 0.2 μs at each temperature where a spectrum was collected with the transmitter set at the resonant frequency of the observed spectral peak. The $\pi/2$ pulse duration was calculated as half of the π pulse width. Longitudinal relaxation times were measured using an inversion recovery pulse sequence (π-τ-$\pi/2$-acquisition) and the data were fit to the equation[16]

$$I = (2I_0) - I_1 \cdot \left(1 - e^{(-T_1/\tau)}\right) \qquad (1)$$

where I was the observed spectral intensity at pulse delay time τ, T_1 was the fitted longitudinal relaxation time, and I_0 and I_1 were fitting parameters that represented the signal intensity at $\tau = 0$ and $\tau = \infty$. The spectra were processed with minimal line broadening and baseline correction and referenced to 85% H_3PO_4 at 0 ppm. The total time spent above room temperature was ~4 h. The spectra that were obtained upon the first heat/cool profile were indistinguishable from those obtained in subsequent heat/cool cycles.

The transverse relaxation time (T_2) was measured using a Carr-Purcell, Meiboom-Gill pulse sequence[17,18] ($\pi/2$ ($\tau/2$, π, $\tau/2)_n$ $\tau/2$). The intensity of the resulting echoes, I, was fit to the equation

$$I = I_0 e^{-\tau n/T_2} \qquad (2)$$

where τn is the time, and T_2 and I_0 are fitting parameters representing the transverse relaxation time and echo intensity at $\tau = 0$, respectively.

Chemical Shift and Peak Width Extrapolation

The change in chemical shift and peak width were fit to a standard exponential growth equation:

$$y = y_0 + Be^{T/t} \quad (3)$$

where the T was the absolute temperature, and y was either the chemical shift or the peak width. The variables y_0, B, and t were fitting parameters. This empirical equation was chosen because it provided a reasonable fit and because it provides a means to extrapolate the observed chemical shift to other temperatures. The chemical shifts and peak widths in the absence of significant contributions from the paramagnetic free radicals were estimated by calculating the value of y at T = 298 K, which is approximately room temperature. The room temperature NMR spectra of crystalline chalcophosphate materials typically did not demonstrate significant contributions from a radical species, and the intention of choosing 298 K was to provide a means to compare the NMR spectra of the crystalline materials to the high temperature NMR spectra. This fitting can be considered a "correction" to the chemical shift and peak width in the absence of significant effects of the free radical species. This model assumes that the chemical shift and peak width vary continuously as a function of temperature and that there is no discontinuity at the crystallization temperature. A discontinuity may result from the species in the melt being fundamentally different from those present in the crystalline solid. An interesting test of this assumption would be to collect high temperature NMR spectra under magic angle spinning conditions slightly above and below the melting point

and to then compare the experimental chemical shifts to the values predicted by this model.

Empirically, it was noticed that the parameter t in the fits of the chemical shifts of "$KP_{1.5}PSe_{6.3}$" (150.7) and "$Cs_4P_2Se_{16}$" (127.4) differed by about 20%. The average value of t for these two samples (139.1) was used for subsequent fits of the data from the remaining samples in which sufficient data was not available to justify fitting to a non-linear equation with three fitting parameters. In those cases, the value of t was fixed to 139.1, and the parameters y_0 and B were fit. There is presently no physical justification for fixing this parameter and more data would be required to determine if the fixing of the t parameter is physically valid. One criticism of this approach is that the parameter t was not constant in the fits of the peak widths for samples with a larger number of data points. For this reason, the peak widths of the samples with fewer data points were not fit to an exponential equation and therefore extrapolated peak widths for these samples were not determined.

Previously, the change in the chemical shift for molten Se was described by:[2]

where $\frac{\Delta H}{H}$ is the change in chemical shift in ppm units, c_s is the number of radicals per atom of Se, $\langle A \rangle$ is the average hyperfine coupling between the unpaired electron and the NMR active nucleus, γ_e and γ_n are the gyromagnetic ratios of the electron and nucleus, respectively, S is the spin quantum number, k_B is Boltzmann's constant, T is the temperature in Kelvin, and σ_{chem} is the chemical shift without the effects of the radicals. It was not possible to interpret the chalcophosphate data of the present work similarly

because magnetic susceptibility data were not available. These data are necessary to determine $\langle A \rangle$.

Estimation of the Thermodynamics of Radical Formation

Assuming that the paramagnetic radical species $[P]$ is in equilibrium with a diamagnetic species $[D]$:

$$[D] \leftrightarrow [P] \tag{5}$$

The equilibrium constant has the form:

$$K = [P]/[D] \tag{6}$$

Assuming a dilute concentration of the radical species, the concentration of the diamagnetic species is approximately constant and therefore,

$$K = [P] \tag{7}$$

The equilibrium constant K and the free energy change ΔG are related by:

$$K = e^{-\Delta G/RT} \tag{8}$$

where R is the ideal gas constant, and T is the absolute temperature. The free energy change can be expressed as:

$$\Delta G = \Delta H - T\Delta S \tag{9}$$

where ΔH and ΔS are the change in enthalpy and the change in entropy, respectively. By combining (8) and (9), it is evident that:

$$\ln K = \frac{-\Delta G}{RT} = \frac{-\Delta H}{RT} + \frac{\Delta S}{R} \tag{10}$$

The observed chemical shift in the NMR spectra is temperature dependent and it is proposed that this change occurs because of a change in the concentration of the radical species. The change in chemical shift, $\Delta\sigma$, is proportional to the equilibrium constant K.

$$K = n(\Delta\sigma) \tag{11}$$

where n is an unknown constant. The change in chemical shift at a given temperature is defined as the difference between the observed chemical shift, and the chemical shift extrapolated to T = 0 K. The radical species presumably collides with the NMR-active nucleus. This changes the local field at the nucleus and gives rise to the measured increase in chemical shift.[19] An increase in the number of radicals present increases the statistical probability that collisions will occur and therefore with an increased radical concentration, the enhancement to the chemical shift is increased. By combining (10) and (11),

$$\ln[n(\Delta\sigma)] = \frac{-\Delta G}{RT} = \frac{-\Delta H}{RT} + \frac{\Delta S}{R} \tag{12}$$

and a plot of the natural logarithm of the change in chemical shift versus the reciprocal of the absolute temperature will have a y-intercept of $\left(\frac{\Delta S}{R} - \ln(n)\right)$ and a slope of $\frac{-\Delta H}{R}$. Though ΔS cannot be calculated because n is unknown, it is possible to estimate ΔH in this manner.

RESULTS AND DISCUSSION

A summary of the ^{31}P high temperature NMR data is displayed in Table 9-1. All of the Se-containing melts displayed a strong dependence of chemical shift on

temperature. Over a ~200 °C temperature range, these compounds had an average of a 41.9 ppm chemical shift difference. It was not possible to properly phase the spectrum of $TlBiP_2Se_6$ at each temperature point, and therefore the peak positions could not be compared as a function of temperature for that compound.

The S-containing samples had a smaller dependence of chemical shift on temperature, for example, the chemical shift of the sample with "PS_5" stoichiometry changed 17.6 ppm over the same 200 °C temperature range. The chemical shift of the compound $K_{1.5}Bi_{2.5}(PS_4)_3$ changed by 1.5 ppm over a 50 °C temperature range.

Table 9-1. The ^{31}P chemical shifts, longitudinal relaxation times (T_1), and line widths of various chalcophosphate-containing materials as well as the final product determined from powder X-ray diffraction.

Stoichiometry	Temp. (°C)[a]	^{31}P Shift (ppm)[b]	T_1 (ms)[c]	Line Width (Hz)[d]	Final Product
"$KPSe_7$"	350	-13.2	11.6	1680	n/a
	450	3.4	2.54	2220	
	550	30.6	0.47	2730	
"$K_2PSe_{7.5}$"	350	-46.5	8.45	2110	n/a
	450	-35.9	2.16	2540	
	550	-14.7	0.8	2740	
"$KP_{1.3}Se_{5.2}$"	350	8.9	7.63	1880	n/a
	450	35.3	1.92	4080	
	550	60.7	0.48	5616	
"$KP_{1.5}Se_{6.3}$"	350	32.6	9.2	1920	n/a
	450	47.9	1.5	2620	
	550	77.2	0.28	4040	
"$Cs_4P_2Se_{16}$"	350	-34.8	n.d	950	$Cs_4P_2Se_{10}$
	450	-22.7	n.d	1320	
	550	8.3	n.d	2361	
"PS_5"	350	80.4	114.5	4130	n/a
	450	86.9	36.71	2530	
	550	98.0	9.08	5780	
$K_{1.5}Bi_{2.5}(PS_4)_3$	550	76	15.7	933	$K_{1.5}Bi_{2.5}(PS_4)_3$
	575	77.5	11	926	
	600	77.5	7.94	929	
$K_2Cu_2P_4Se_{10}$	500	93.3	4.84	2990	$K_2Cu_2P_4Se_{10}$
	550	109.9	2.47	3660	
	600	130.9	1.47	5130	
$TlBiP_2Se_6$	525	n.d.	12.4	n.d.	$TlBiP_2Se_6$
	550	n.d	10.2	n.d.	
	600	n.d	8.76	n.d.	
KH_2PO_4	350	-7.2	6.98	600	KH_2PO_4
"KH_2PO_4S"	350	-11.4	0.34	1200	KH_2PO_4

[a] The uncertainty in temperature is estimated to be ± 5 °C

[b] Chemical shifts were determined by fitting the spectral peaks to a 50% Gaussian 50% Lorentzian line function and the reported chemical shift was the peak center fitting parameter. The uncertainty in the chemical shift is estimated to be ± 0.5 ppm.

[c] The method of measuring the longitudinal relaxation time is described in the text. The uncertainty is estimated to be ± 12 %.

[d] Peak widths were determined by fitting the spectral peaks to a 50% Gaussian 50% Lorentzian line function and the reported line width measurement was the full width at half maximum (FWHM). A 50% Gaussian 50% Lorentzian line was chosen because it was in closer agreement with the experimental spectrum than a Gaussian or a Lorentzian line alone. Room temperature linewidths were measured under MAS conditions and high temperature linewidths were measured under static conditions. The estimated uncertainty in the line width is ± 5%.

Although there was some difference in the change in chemical shifts of the S and Se-containing samples as a function of temperature, both types of sample had a strong dependence of the longitudinal relaxation time T_1. At 550 – 600 °C, all of the S and Se-containing samples had 0.28 – 15.7 ms longitudinal relaxation times. T_1 times of about 500 – 3000 s are commonly observed in crystalline chalcophosphate materials at room temperature.[6,16,20]

Similarly, the ^{31}P spectral line widths are temperature dependent. The Se-containing samples had peak widths that increased by an average of ~12 Hz per °C. The peak width in the "PS_5" sample increased by ~8 Hz per °C, but the $K_{1.5}Bi_{2.5}(PS_4)_3$ sample had no appreciable dependence of the line width on temperature.

Chemical Shift Extrapolation

The contribution of the free radicals to the chemical shift and peak width for the sample with "$KP_{1.5}Se_{6.3}$" stoichiometry was modeled by fitting the chemical shift and peak width at each temperature to an exponential growth equation. A fit of the chemical shift and peak width of the "$KP_{1.5}Se_{6.3}$" sample is displayed in Figure 9-1, and the raw data are displayed in Table 9-2.

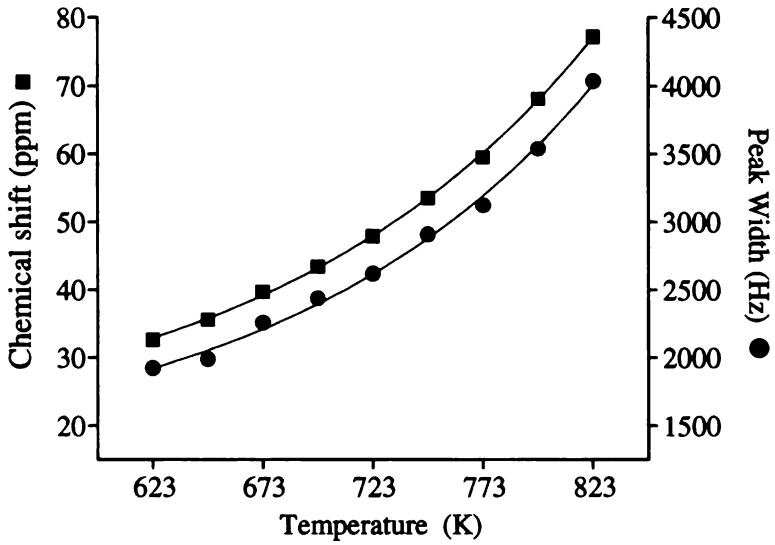

Figure 9-1. Fit of the experimental ^{31}P NMR chemical shift and peak width for the sample "$KP_{1.5}Se_{6.3}$". The fit values of y_0, B and t were 16.9, 0.26, and 150.7 for the chemical shift, and 1238, 8.89, and 143.4 for the peak width. The respective R^2 values for these fits were 99.953% and 99.625%. The chemical shift and peak width at T = 298 K were 18.7 ppm and ~1300 Hz. The temperature of 298 K was chosen to provide a means of comparison between the room temperature and high temperature NMR data.

The fit suggested that at 298 K, the chemical shift and peak width would be 18.7 ppm, and ~1300 Hz, respectively. This chemical shift is within the range of what would be expected for a P-P bonded species.[6]

Table 9-2. The ^{31}P chemical shift and peak width of the "$KP_{1.5}Se_{6.3}$" sample over the 623 - 823 K temperature range.

Temp. (°C)[a]	^{31}P Shift (ppm)[b]	T_1 (ms)[c]	Line Width (Hz)[d]
623	32.6	9.20	1924
648	35.6	6.00	1989
673	39.7	3.77	2259
698	43.4	2.80	2437
723	47.9	1.50	2619
748	53.5	1.06	2907
773	59.5	0.76	3124
798	68.1	0.51	3540
823	77.2	0.28	4037

[a] The uncertainty in temperature is estimated to be ± 5 °C

[b] Chemical shifts were determined by fitting the spectral peaks to a 50% Gaussian 50% Lorentzian line function and the reported chemical shift was the peak center fitting parameter. The uncertainty in the chemical shift is estimated to be ± 0.5 ppm.

[c] The method of measuring the longitudinal relaxation time is described in the text. The uncertainty is estimated to be ± 12 %.

[d] Peak widths were determined by fitting the spectral peaks to a 50% Gaussian 50% Lorentzian line function and the reported line width measurement was the full width at half maximum (FWHM). A 50% Gaussian 50% Lorentzian line was chosen because it was in closer agreement with the experimental spectrum than a Gaussian or a Lorentzian line alone. Room temperature linewidths were measured under MAS conditions and high temperature linewidths were measured under static conditions. The estimated uncertainty in the line width is ± 5%.

A fit of the chemical shift and peak width of the "$Cs_4P_2Se_{16}$" sample indicated a -44.2 ppm extrapolated chemical shift and a ~900 Hz extrapolated peak width, Figure 9-2. This stoichiometry is known to produce the crystalline compound $Cs_4P_2Se_{10}$ upon cooling, which has a -52.8 ppm chemical shift.[10] The closeness of the extrapolated chemical shift to the experimentally determined chemical shift of the crystalline compound suggested that the ^{31}P chemical environment of the solid and the melt are very similar, and it is plausible that $[P_4Se_{10}]^{4-}$ anions or some other species without P-P bonding exists in the molten liquid.

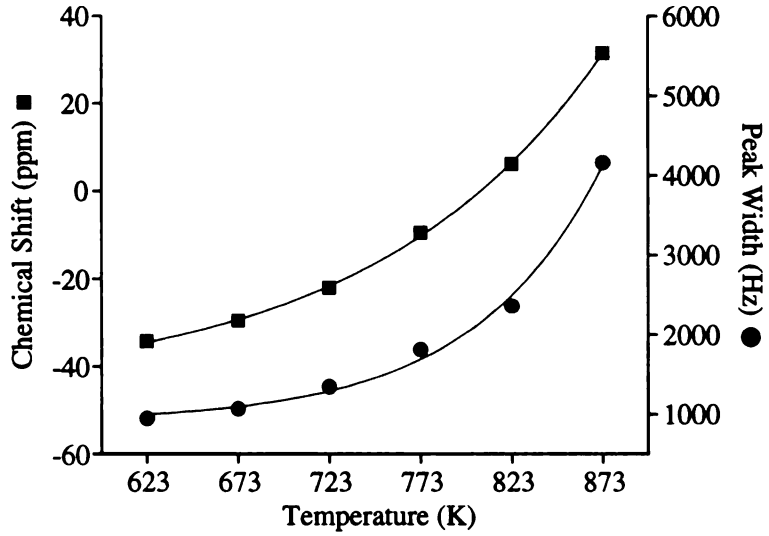

Figure 9-2. Fit of the experimental ^{31}P NMR chemical shift and peak width for the sample "$Cs_4P_2Se_{16}$". The fit values of y_0, B and t were -45.2, 0.08, and 127.4 for the chemical shift, and 907, 0.014, and 70.7 for the peak width. The respective R^2 values for these fits were 99.971% and 99.432%. The chemical shift and peak width at T = 298 K were -44.4 ppm and ~900 Hz.

Table 9-3. The ^{31}P chemical shift and peak width of the "$Cs_4P_2Se_{16}$" sample over the 623 – 873 K temperature range.

Temp. (K)[a]	^{31}P Shift (ppm)[b]	Line Width (Hz)[c]
623	-34.2	950
673	-29.5	1070
723	-22	1350
773	-9.5	1810
823	6.3	2360
873	31.6	4160

[a] The uncertainty in temperature is estimated to be ± 5 °C

[b] Chemical shifts were determined by fitting the spectral peaks to a 50% Gaussian 50% Lorentzian line function and the reported chemical shift was the peak center fitting parameter. The uncertainty in the chemical shift is estimated to be ± 0.5 ppm.

[c] Peak widths were determined by fitting the spectral peaks to a 50% Gaussian 50% Lorentzian line function and the reported line width measurement was the full width at half maximum (FWHM). A 50% Gaussian 50% Lorentzian line was chosen because it was in closer agreement with the experimental spectrum than a Gaussian or a Lorentzian line alone. Room temperature linewidths were measured under MAS conditions and high temperature linewidths were measured under static conditions. The estimated uncertainty in the line width is ± 5%.

The best fits of the ^{31}P chemical shifts of the "$Cs_4P_2Se_{16}$" and "$KP_{1.5}Se_{6.3}$" samples had similar fitting parameters for *t*. These were the only two Se-containing samples for which more than three ^{31}P NMR spectra at different temperature points was available. Because three parameters are simultaneously fit for the exponential buildup to correct for the presence of radicals, it was not reasonable to fit the data from the samples where only three different temperatures were used for NMR spectral collection. It was therefore assumed that the parameter *t* could be fixed for these samples. The value of *t* that was chosen for subsequent fits was 139.1 which was the average value obtained from the fits of the "$Cs_4P_2Se_{16}$" and "$KP_{1.5}Se_{6.3}$" samples. The parameters y_0 and *B* were subsequently fit to the available data.

One justification for fixing this parameter is that the right side of equation (4) may be approximately constant for each of the selenophosphate samples at a given temperature. The identity of the radical species may be the same in each case at a given temperature, and there is some evidence that the enthalpy of radical formation is similar for these compounds (*vide infra*). An additional empirical justification is that using this method produces an extrapolated chemical shift that is close to the experimentally determined one for the compound $K_2Cu_2P_4Se_{10}$. The extrapolated chemical shift at T = 298 K was 59.3 ppm and the experimental chemical shift for this compound is 55.7 ppm.[6] This lends further support to the possibility that the species that is present in the crystalline solid (i.e. the $[P_4Se_{10}]^{4-}$ anion) is also present in the liquid melt.

Table 9-4. Summary of the fitting parameters for each of the samples studied and the extrapolated chemical shift and peak width extrapolated to 298 K determined using those parameters. The standard uncertainties are given in parenthesis.

	Chemical Shift Fitting			Peak Width Fitting[a]			Extrapolated ^{31}P Shift (ppm)	Extrapolated Peak Width (Hz)
Stoichiometry	y_0	B	t	y_0	B	t		
"$KP_{1.5}Se_{6.3}$"	16.9(1.6)	0.26(0.07)	150.7(7.5)	1238(200)	8.9(7.4)	143.4(19.3)	18.7(1.6)	1300(200)
"$Cs_4P_2Se_{16}$"	-45.2(1.3)	0.08(0.02)	127.4(5.0)	907(120)	0.013(0.022)	70.7(8.9)	-44.4(1.3)	900(120)
"$KPSe_7$"	-25.7(2.1)	0.15(0.01)	139.1	n.d.	n.d.	n.d.	-24.4(2.1)	n.d.
"$K_2PSe_{7.5}$"	-56.3(0.2)	0.11(0.01)	139.1	n.d.	n.d.	n.d.	-55.3(0.2)	n.d.
"$KP_{1.3}Se_{5.2}$"	-2.5(1.9)	0.18(0.03)	139.1	n.d.	n.d.	n.d.	-1.0(1.9)	n.d.
$K_2Cu_2P_4Se_{10}$	58.1(1.9)	0.14(0.01)	139.1	n.d.	n.d.	n.d	59.3(1.9)	n.d.
"PS_5"	80.5(1.6)	$2.1(1.0)\times10^{-3}$	90.1(13)	2387(200)	$1.0(1.0)\times10^{-5}$	42.5(3.3)	80.5(1.6)	2400(200)

[a] n.d. indicates that the parameters were not determined because only one or two temperature points were available, therefore a fit to a non-linear equation was not reasonable.

It has been shown previously that an increased amount of P relative to the metal and chalcogen tends to produce compounds with lower valency P centers, i.e. P^{3+} and P^{4+}.[7,15] The anions $[P_2Se_6]^{4-}$ and $[P_6Se_{12}]^{4-}$ both contain phosphorus in the 4+ oxidation state and have been produced with stoichiometries rich in P. Therefore, it would be expected that the samples with the stoichiometry "$KP_{1.5}Se_{6.3}$" (18.7 ppm extrapolated chemical shift) and "$KP_{1.3}Se_{5.2}$" (-1.0 ppm extrapolated chemical shift) would be the most likely samples to have a P-P bond because these samples had the highest relative concentration of P.

The chemical shift of 18.7 ppm for "$KP_{1.5}Se_{6.3}$" is within the range of what would be expected for a P-P bonded species, but the -1.0 ppm shift of "$KP_{1.3}Se_{5.2}$" was on the border between the regions where P-P and non P-P bonded species are found. One possibility is that there was rapid chemical exchange between a P-P bonded and a non P-P bonded species although there is no evidence for such exchange.

The chemical shift and peak width for the sample with the "PS_5" stoichiometry were also fit, and it was determined that the extrapolated chemical shift was 80.5 ppm, and the extrapolated peak width was ~2400 Hz. The raw chemical shift, longitudinal relaxation time and peak width data are displayed in Table 9-5. A room temperature ^{31}P MAS NMR spectrum of "PS_9" contained a dominant peak at 110 ppm that was about 5000 Hz wide.[21] The extrapolated chemical shift for "PS_5" is ~30 ppm away from the experimentally determined peak for "PS_9". Either these two compositions result in

fundamentally different ^{31}P coordination environments or the extrapolation of the chemical shift is inaccurate for this sample.

Table 9-5. The ^{31}P chemical shift and peak width of the "PS_5" sample over the 623 – 873 K temperature range.

Temp. (°C)[a]	^{31}P Shift (ppm)[b]	T_1 (ms)[c]	Line Width (Hz)[d]
623	80.4	114.5	4130
673	84.4	72.02	2520
723	86.8	36.71	2530
773	91.9	17.06	3530
823	98.0	9.08	5780
873	112.6	3.61	12350

[a] The uncertainty in temperature is estimated to be ± 5 °C.

[b] Chemical shifts were determined by fitting the spectral peaks to a 50% Gaussian 50% Lorentzian line function and the reported chemical shift was the peak center fitting parameter. The uncertainty in the chemical shift is estimated to be ± 0.5 ppm.

[c] The method of measuring the longitudinal relaxation time is described in the text. The uncertainty is estimated to be ± 12 %.

[d] Peak widths were determined by fitting the spectral peaks to a 50% Gaussian 50% Lorentzian line function and the reported line width measurement was the full width at half maximum (FWHM). A 50% Gaussian 50% Lorentzian line was chosen because it was in closer agreement with the experimental spectrum than a Gaussian or a Lorentzian line alone. Room temperature linewidths were measured under MAS conditions and high temperature linewidths were measured under static conditions. The estimated uncertainty in the line width is ± 5%.

Peak Width Extrapolation

In two selenophosphate samples it was possible to compare the extrapolated peak width to a known peak width of a crystalline solid. The peak width of the crystalline compound $Cs_4P_2Se_{10}$, was about 100 Hz.[6,10] Compared to the extrapolated peak width of the melt of "$Cs_4P_2Se_{16}$" (900 Hz), it appears that the broadness of the spectral line at high temperature cannot be ascribed to the presence of the free radicals alone. One likely contribution to the line width is some residual chemical shift anisotropy that is not fully averaged out by the random tumbling of the ^{31}P species that is present in the melt. The magnitude of the chemical shift anisotropy of $Cs_4P_2Se_{10}$ is 215 ppm at room temperature, and some of this anisotropy may remain even at 600 °C.

The extrapolated peak width of the "PS_5" sample was narrower than a comparable thiophosphate glass at room temperature, i.e. 2400 Hz versus 5000 Hz for "PS_9".[21] This is contradictory to the observations of the molten selenophosphate compounds where the extrapolated high temperature peak widths were still significantly broader than their room-temperature crystalline counterparts.

In a room temperature glass, there is a range of chemical environments. Unlike in a crystal where all of the coordination geometries are in the most energetically favorable configuration, in a glass, many different coordination geometries are present with slightly different bond lengths and angles. This lack of order distinguishes amorphous solids from crystalline solids. These energetically disfavored geometries are trapped because motion in the solid is restricted. The range of coordination geometries gives rise to the broadness of NMR spectral features of glasses because each geometry has a corresponding chemical shift. The chemical shifts are not resolved but instead are

overlapped into a broad spectral feature. The narrowness of the high temperature NMR peak relative to the room temperature NMR peak of the amorphous glass suggests that in the melt, motional averaging is increased such that contributions from the less energetically favorable configurations are somewhat diminished and sharper lines result.[22] The restricted coordination geometries of the amorphous solid are free to relax into more energetically favorable arrangements. This rearrangement occurs because of a decrease in the viscosity of the melt relative to the amorphous solid resulting in an increase in motional freedom.

For the sample "$KPSe_7$", the transverse relaxation time (T_2) was measured, and was approximately 420 μs, 200 μs, and 190 μs, respectively, at 350 °C, 450 °C, and 550 °C. In the T_2 broadened limit,[23] the predicted line widths would be 760 Hz, 1550 Hz, and 1700 Hz. The experimentally determined line widths were 1680 Hz, 2224 Hz, and 2734 Hz, respectively. The T_2 broadening therefore only accounts for 45%, 70%, or 62% of the linewidth, respectively. The additional line broadening is likely to be the residual chemical shift anisotropy or some contributions from less energetically favored coordination geometries.

Estimation of the Enthalpy of Formation of the Radical Species

The enthalpy of the formation of the radical species in the Se-containing samples was approximately 34.6 kJ/mol. The corresponding enthalpy of formation of S-containing radicals was approximately 48.1 kJ/mol. These data are displayed in Table 9-6, and an example fit using the "$KP_{1.5}Se_{6.3}$" sample is displayed in Figure 9-3. The calculated bond energies of Se-Se bonds in Se_6 was reported to be 50 kJ/mol and the

bond energy of S-S bonds in S_6 was reported to be 42 kJ/mol.[24] Although there is some debate about the true value of the chalcogen-chalcogen bond energy in the literature, the similarity of the reported bond energies to the enthalpy calculated in the present work provide some indication that the observed paramagnetic shift is correlated with radicals that are formed upon chalcogen bond scission. If a biradical species was formed (i.e. $[D] \leftrightarrow 2[P]$) as is thought to be the case for the pure chalcogens,[25,26] the calculated values if the enthalpy change would be half of the values reported here. This can be determined by substitution of the above equilibrium into equation (6) which would become

$$K' = [P]^2/[D] \tag{13}$$

where K' is the equilibrium between $[D] \leftrightarrow 2[P]$. This could also be expressed as

$$K' = K^2 \tag{14}$$

Equation (10) with the biradical equilibrium would therefore be modified to

$$2\ln K' = \frac{-\Delta G}{RT} = \frac{-\Delta H}{RT} + \frac{\Delta S}{R} \tag{15}$$

By combining (15) and (11), and plotting the natural logarithm of the change in chemical shift versus the reciprocal of the absolute temperature, the slope of the line is $\frac{-\Delta H}{2R}$. This results in a change in the reported enthalpies of formation by a factor of 2. For example, the enthalpy of "PS_5" would change to 96 kJ/mol.

Table 9-6. The enthalpy of radical formation. The ^{31}P chemical shift was extrapolated to 0 K. The uncertainties are given in parenthesis.

	^{31}P Shift (ppm) T = 0 K	M	B	ΔH (kJ/mol)
"$KP_{1.5}Se_{6.3}$"	17.2	-3446(91)	8.23(13)	30.2(8)
"$Cs_4P_2Se_{16}$"	-45.1	-4256(9)	9.121(11)	36.4(1)
"$KPSe_7$"	-25.6	-3872(30)	8.729(40)	32.2(2)
"$K_2PSe_{7.5}$"	-56.2	-3705(261)	8.19(37)	31(2)
"$KP_{1.3}Se_{5.2}$"	-2.3	-4481(670)	9.67(95)	37(6)
$K_2Cu_2P_4Se_{10}$	58.3	-4923(9)	9.926(11)	40.9(1)
"PS_5"	80.5	-5783(300)	9.917(40)	48(3)

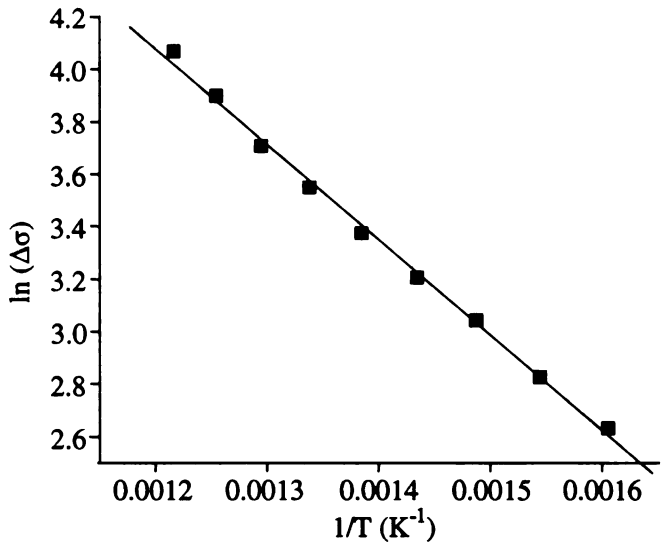

Figure 9-3. Plot of the data of the sample with the stoichiometry "$KP_{1.5}Se_{6.3}$" with the ordinate as the reciprocal of temperature and the abscissa as the natural logarithm of the change in chemical shift. The fit had a slope of -3446 and a *y*-intercept of 8.228 which indicated an enthalpy change of 30.2 kJ/mol. The R value was 99.743%.

CONCLUDING REMARKS

The nonlinear change of the chemical shift and peak width in chalcogenide-containing melts has been modeled, and the chemical shift and peak width in the absence of this effect has been calculated for several different samples. In the case of the crystalline compounds $K_2Cu_2P_4Se_{10}$ and $Cs_4P_2Se_{10}$, the extrapolated chemical shift from the high temperature data was near the known chemical shifts of the room temperature crystalline sample. Additionally, this chemical shift was correlated with the known presence and absence, respectively, of a P-P bonded species. This methodology will likely be useful in further characterization of chalcophosphate melts. Furthermore, it may be possible to look for samples that contain multiple types of anion (i.e. $[PSe_4]^{3-}$ and $[P_2Se_6]^{4-}$) and after correcting for the effects of the free radicals, characterization of such an equilibrium may be rationalized.

Additionally, the change in enthalpy that was derived from the NMR spectra shows reasonable agreement with one set of the reported bond enthalpies for chalcogen-chalcogen bonds. This provides support for the hypothesis that the mechanism that produces the radical species is a homolytic cleavage of a chalcogen-chalcogen bond.

One other NMR observable that was not considered in the present work was the extrapolation of the longitudinal relaxation time T_1. In the case of the chemical shift and peak width, the extrapolated values were always within about an order of magnitude of the high temperature values. In the case of the relaxation times, several orders of magnitude separate the room temperature samples which have relaxation times ranging from several hundred to several thousand seconds and the high temperature samples which have relaxation times that are frequently sub-millisecond. The failure of the

extrapolation of the relaxation rates to a comparable value of the room temperature relaxation rates is likely because relaxation rates depend strongly on motional rates and amplitudes. Presumably, the differences in the relaxation rates at high temperature and at room temperature could be explained considering these differences in motion and also the presence of the free radicals.

REFERENCES

1. Gave, M.; Kanatzidis, M. G.; Weliky, D. P. **2007,** In preparation.

2. Warren, W. W.; Dupree, R. *Phys. Rev. B.* **1980,** 22, 2257-2275.

3. Freeman, R.; Pachler, K. G. R.; Lamar, G. N. *J. Chem. Phys.* **1971,** 55, 4586-4593.

4. Dechter, J. J.; Levy, G. C. *J. Magn. Reson.* **1980,** 39, 207-215.

5. Bagley, B. G.; Waszczak, J. V.; Disalvo, F. J. *Solid State Commun.* **1972,** 11, 89-92.

6. Canlas, C. G.; Kanatzidis, M. G.; Weliky, D. P. *Inorg. Chem.* **2003,** 42, 3399-3405.

7. Gave, M.; Bilc, D.; Mahanti, S.; Breshears, J.; Kanatzidis, M. *Inorg. Chem.* **2005,** 5293-5303.

8. McCarthy, T. J.; Kanatzidis, M. G. *Inorg. Chem.* **1995,** 34, 1257-1267.

9. Fehér, F. Handbuch der Präparativen Anorganischen Chemie; Ferdinand Enke Verlag: Stuttgart, Germany, 1954; Vol. 1, pp 280-281.

10. Gave, M.; Canlas, C.; Iyer, R. G.; Kanatzidis, M. G.; Weliky, D. P. *J. Solid State Chem.* **2007,** 180, 2877-2884.

11. Gave, M.; Weliky, D. P.; Kanatzidis, M. G. *Inorg. Chem.* **2007,** 46, 11063-11074.

12. Chondroudis, K.; Kanatzidis, M. G. *Inorg. Chem.* **1998,** 37, 2098-2099.

13. Gave, M.; Malliakas, C. D.; Weliky, D. P.; Kanatzidis, M. G. *Inorg. Chem.* **2007,** 46, 3632-3644.

14. Chung, I.; Do, J.; Canlas, C. G.; Weliky, D. P.; Kanatzidis, M. G. *Inorg. Chem.* **2004,** 43, 2762-2764.

15. Chung, I.; Karst, A. L.; Weliky, D. P.; Kanatzidis, M. G. *Inorg. Chem.* **2006,** 45, 2785-2787.

16. Canlas, C. G.; Muthukumaran, R. B.; Kanatzidis, M. G.; Weliky, D. P. *Solid State Nucl. Magn. Reson.* **2003,** 24, 110-122.

17. Carr, H. Y.; Purcell, E. M. *Phys. Rev.* **1954,** 94, 630-638.

18. Meiboom, S.; Gill, D. *Rev Sci Instrum* **1958,** 29, 688-691.

19. Prosser, R. S.; Luchette, P. A. *J. Magn. Reson.* **2004,** 171, 225-232.

20. Canlas, C. G. Ph.D. Thesis, Michigan State University, East Lansing, MI, 2004.

21. Mutolo, P. F.; Witschas, M.; Regelsky, G.; Guenne, J. S. A. D.; Eckert, H. *J. Non-Cryst. Solids* **1999,** 257, 63-72.

22. Adamy, S. T.; Grandinetti, P. J.; Masuda, Y.; Campbell, D.; Jonas, J. *J. Chem. Phys.* **1991,** 94, 3568-3576.

23. Harris, R. K. Nuclear Magnetic Resonance Spectroscopy; Longman Scientific and Technical: New York, NY, 1983; pp 70-71.

24. Huggins, M. L. *J. Am. Chem. Soc.* **1953,** 75, 4124-4126.

25. Koningsberger, D.; Van Wolput, J.; Rieter, P. *Chem. Phys. Lett.* **1971,** 8, 145-147.

26. Sampath, P. I. *J. Chem. Phys.* **1966,** 45, 3519-3525.

CHAPTER 10

THE SOLID SOLUTIONS $Cu_3PSe_{4-x}S_x$ AND $Fe_2P_2Se_{6-x}S_x$.

INTRODUCTION

Solid solutions are materials where at least one crystallographic site has a random substitution of one element for another. For example, after cooling a molten liquid containing various proportions of copper and silver, the copper and silver randomly occupy the positions in the crystal structure.[1] In other cases, this substitution does not occur and rather, the room temperature solid contains domains of each metal. Hume-Rothery developed a set of empirical rules to determine if a given set of atoms will randomly substitute for one another: (1) the atomic sizes of the atoms should be within 15% of one another, (2) the atoms must not have too great of an electronegativity difference, and (3) the valency must be similar.[1] Solid solutions can, in many cases, be targeted by choosing species that adhere to this set of rules.

Solid solutions are industrially relevant because control of the stoichiometry in a solid solution often allows for tuning of various physical properties. Chalcogenide-based solid solutions have been shown to possess such tunability, and a number of potential applications of these materials exist. For example, there have been a number of chalcogenide-based light emitting diodes (LEDs) that have been produced, and the color of the light emitted from those diodes can be varied by changing the stoichiometry of the solid solution. Slight changes in the composition of the solid solution can have a marked effect on the band gap, and therefore the color of emission can be tailored.[2-4] Solid solutions are also relevant in data storage applications because the temperature of glass to crystalline phase transitions can be tuned by modifying the composition of the solid solution. A glass-to-crystalline phase transition is the basis for storing binary data on optical storage media like CDs and DVDs, and the ability to tune the melt and

crystallization temperatures is beneficial in the pursuit of next-generation data storage materials.[5-7]

In this study, solid solutions of $Cu_3PSe_{4-x}S_x$ and $Fe_2P_2Se_{6-x}S_x$ were formed. The parent compounds Cu_3PSe_4[8] and Cu_3PS_4[9] were chosen because they are isomorphic and $Fe_2P_2Se_6$[10] and $Fe_2P_2S_6$[11] were chosen because they are non-isomorphic, Table 10-1. Additionally, the parent compounds can be synthesized in pure form without significant contributions from competing impurity phases.

Table 10-1. Literature crystallographic parameters for the parent compounds of the solid solutions.

	Cu_3PSe_4[a]	Cu_3PS_4[b]	$Fe_2P_2Se_6$[c]	$Fe_2P_2S_6$[d]
a Å	7.685(2)	7.2817(11)	6.265(6)	5.947(1)
b Å	6.656(1)	6.3387(10)	6.265(6)	10.300(1)
c Å	6.377(1)	6.0746(10)	19.80(2)	6.7222(8)
α°	90	90	90	90
β°	90	90	90	107.16(1)
γ°	90	90	120	90
Space group	$Pmn2_1$	$Pmn2_1$	*R-3H*	*C2/m*

[a] Ma, H. W.; Guo, G. C.; Zhou, G. W.; Wang, M. S.; Lin, S. H.; Dong, Z. C.; Huang, J. S., *Chinese J. Struc. Chem.* **2002,** 21, 288-291.

[b] Pfitzner, A.; Reiser, S., Z. *Kristall.* **2002,** 217, 51-54.

[c] Klingen, W.; Eulenber.G; Hahn, H., Z. *Anorg. Allg. Chem.* **1973,** 401, 97-112.

[d] Ouvrard, G.; Brec, R.; Rouxel, J., *Mater. Res. Bull.* **1985,** 20, 1181-1189.

It was hypothesized that the $Cu_3PSe_{4-x}S_x$ compounds would form a solid solution wherein the cell parameters would vary linearly as a function of the chalcogen content. This hypothesis is justified on the basis of the Hume-Rothery rules as follows: (1) S^{2-} has a radius of 184 pm, and Se^{2-} has a radius of 198 pm (7% difference)[12] (2) the S and Se electronegativity difference is small (2.5 and 2.4 Pauling units for S and Se, respectively),[12] and (3) S and Se both carry a 2- charge in these compounds. Therefore, this system is predicted to form solid solutions. The linear dependence of the cell

parameters is predicted by Vegard's law.[13] This law states that the size of the unit cell depends only upon the radii of the constituent atoms. For this law to hold true, it is necessary that the bonding properties of the constituent elements do not vary as a function of the stoichiometry, a condition that might reasonably hold true under tenets (2) and (3) of the Hume-Rothery rules.

In the case of the $Fe_2P_2Se_{6-x}S_x$ compounds, however, the symmetry of the unit cell changes from *R*-3*H* (hexagonal) for $Fe_2P_2Se_6$ to *C*2/*m* (monoclinic) for $Fe_2P_2S_6$. The electronegativity difference between S and Se is constant as well as the divalency and so by comparison of the $Fe_2P_2Se_{6-x}S_x$ compounds to the $Cu_3PSe_{4-x}S_x$ system, the effect of the similarity of the parent unit cells in terms of cell symmetry could be explored. In this case, Vegard's law cannot hold because the cell parameters must not vary linearly because the substitution of S for Se results in substantial changes to the unit cell including a change in symmetry.

EXPERIMENTAL SECTION

Reagents

All reagents were used as received unless otherwise noted. Chemicals were used as obtained unless otherwise noted: selenium shot (99.999%, Tellurex Inc, Traverse City, MI), sulfur (sublimed flowers, Alfa Aesar, Ward Hill, MA), phosphorous (amorphous red, MCB Reagents, Gibbstown, NJ), electrolytic copper dust (Fisher Scientific, Pittsburgh, PA), iron filings (CCI, Columbus, WI). The selenium shot was ground in an agate mortar and pestle to ~100 mesh.

Synthesis

The compounds $Cu_3PSe_{4-x}S_x$ and $Fe_2P_2Se_{6-x}S_x$ were formed by combining the appropriate stoichiometric ratio of the elements in a fused silica ampoule. The total sample mass was held constant at 0.5 g. After sealing under a reduced pressure of ~100 mTorr, the samples were loaded into protective ceramic sheaths and then allowed to react by heating to 950 °C over 12 h, holding there for 12 h, and then cooling back to room temperature over 12 h.

Powder X-ray Diffraction

Powder X-ray diffraction was performed with a Rigaku-Denki RW400F2 (Rotaflex) diffractometer equipped with a Cu *K*α rotating anode operating at 45 kV and 100 mA with a 2°/min scan rate. The resultant powder patterns were indexed using the Jade 6.0 software package.[14] The indexing was performed by overlaying the powder pattern of the compound that was known to be an isomorphic analog, then refining the cell parameters to graft the overlayed peaks onto the experimental powder pattern.

Single Crystal X-ray Diffraction of Cu_3PSeS_3 and $Fe_2P_2Se_2S_4$

Single crystals of Cu_3PSeS_3 and $Fe_2P_2Se_2S_4$ were manually isolated from the reaction ampoule and were mounted onto a glass fiber. Intensity data were collected on a Bruker SMART platform CCD diffractometer using Mo Kα radiation operating at 40 kV and 40 mA. A full sphere of data was collected and individual frames were acquired with a 10 s exposure time and a 0.3° omega rotation. The SMART software was used for data collection, and SAINT software was used for data extraction and reduction. An

analytical absorption correction to the data was performed and direct methods were used to solve and refine the structures with the SHELXTL[15] software package. The details of data collection and refinement are summarized in Table 10-2. Fractional atomic coordinates are displayed in Tables 10-3 and 10-4, and selected bond lengths and angles are displayed in Tables 10-5 and 10-6 respectively for Cu_3PSeS_3 and $Fe_2P_2Se_2S_4$. These structures closely resemble Cu_3PSe_4 and $Fe_2P_2S_6$, respectively, with the only major change being the isomorphic substitution of the chalcogen. Detailed descriptions of the parent structures can be found elsewhere.[10,11]

Table 10-2. Summary of the details of the crystallographic refinement of Cu_3PSeS_3 and $Fe_2P_2Se_2S_4$.

	Cu_3PSeS_3	$Fe_2P_2Se_2S_4$
Crystal system	Orthorhombic	Monoclinic
Space group	$Pmn2_1$	$C2/m$
λ, Å (Mo Kα)	0.71073	0.71073
a, Å	7.381(4)	6.031(1)
b, Å	6.397(3)	10.458(2)
c, Å	6.136(3)	6.816(2)
α, °	90	90
β, °	90	106.972(3)
γ, °	90	90
Z	2	2
Crystal dimensions, mm	0.8 x 0.4 x 0.2	0.4 x 0.3 x 0.1
D_{calc} g/cm^3	4.429	3.638
μ, mm^{-1}	17.098	12.857
R_{int}, %	2.5	5.2
total reflections/independent	3023/714	2219/496
final R/Rw, %[a]	2.7%/6.2%	3.5/7.6
Largest peak/hole, e$^-$/Å^3	0.423/-0.708	0.686/-0.911

[a] $R = \Sigma(|F_o| - |F_c|)/\Sigma|F_o|$. $R_w = [\Sigma w(|F_o| - |F_c|)^2/\Sigma w|F_o|^2]^{1/2}$

Table 10-3. Fractional atomic coordinates for Cu_3PSeS_3 with standard uncertanties in parenthesis.

	x	y	z	U(eq)[a]	Occupancy
Cu(1)	0	0.6440(2)	0.0955(2)	22(1)	100%
Cu(2)	0.7460(1)	0.1816(1)	0.0870(1)	21(1)	100%
P	0	0.3238(4)	0.5961(6)	7(1)	100%
Se(1)|S(1)	0	-0.6831(4)	0.2553(4)	19(1)	75%/25%
Se(2)|S(2)	0	0.6320(3)	0.7176(4)	16(1)	75%/25%
Se(3)|S(3)	0.7369(2)	0.8338(2)	0.2109(2)	8(1)	75%/25%

[a] $U_{(eq)} = (\Sigma_i\Sigma_j U_{ij} a_i^* a_j^* a_i \cdot a_j)/3 \times 1000$

Table 10-4. Fractional atomic coordinates for $Fe_2P_2Se_2S_4$ with standard uncertanties in parenthesis.

	x	y	Z	U(eq)[a]	Occupancy
Fe(1)	0	0.3326(1)	0	17(1)	100%
Se(1)|S(1)	0.2509(1)	0.1677(1)	0.2522(1)	17(1)	33%/66%
Se(2)|S(2)	0.7467(1)	0	0.2498(1)	18(1)	33%/66%
P	0.0555(2)	0	0.1673(2)	13(1)	100%

[a] $U_{(eq)} = (\Sigma_i\Sigma_j U_{ij} a_i^* a_j^* a_i \cdot a_j)/3 \times 1000$

Table 10-5. Selected bond lengths (Å) and angles (°) for Cu_3PSeS_3. Standard uncertainties are displayed in parenthesis.

Cu1—Se1|S1^{i}	2.311(3)	Se1|S1^{i}—Cu1—Se2|S2^{ii}	113.20(11)
Cu1—Se2|S2^{ii}	2.320(2)	Se1|S1^{i}—Cu1—Se3|S3^{iii}	109.46(6)
Cu1—Se3|S3^{iii}	2.3970(17)	Se2|S2^{ii}—Cu1—Se3|S3^{iii}	108.19(6)
Cu1—Se3|S3^{iv}	2.3970(17)	Se1|S1^{i}—Cu1—Se3|S3^{iii}	109.46(6)
Cu2—Se1|S1^{v}	2.3081(16)	Se2|S2^{ii}—Cu1—Se3|S3^{iii}	108.19(6)
Cu2—Se3|S3^{vi}	2.3131(19)	Se1|S1^{i}—Cu1—Se3|S3^{iv}	109.46(6)
Cu2—Se2|S2^{vii}	2.3149(17)	Se2|S2^{ii}—Cu1—Se3|S3^{iv}	108.19(6)
Cu2—Se3|S3^{viii}	2.3523(18)	Se3|S3^{iii}—Cu1—Se3|S3^{iv}	108.22(9)
		Se1|S1^{i}—Cu1—Se3|S3^{iv}	109.46(6)
P—Se1|S1^{i}	2.092(5)	Se2|S2^{ii}—Cu1—Se3|S3^{iv}	108.19(6)
P—Se2|S2	2.108(4)	Se3|S3^{iii}—Cu1—Se3|S3^{iv}	108.22(9)
P—Se3|S3^{ix}	2.137(2)	Se1|S1^{v}—Cu2—Se3|S3^{vi}	114.69(7)
P—Se3|S3^{x}	2.137(2)	Se1|S1^{v}—Cu2—Se2|S2^{vii}	106.81(7)
		Se3|S3^{vi}—Cu2—Se2|S2^{vii}	114.19(8)
		Se1|S1^{v}—Cu2—Se2|S2^{vii}	106.81(7)
		Se3|S3^{vi}—Cu2—Se2|S2^{vii}	114.19(8)
		Se1|S1^{v}—Cu2—Se3|S3^{viii}	103.50(8)
		Se3|S3^{vi}—Cu2—Se3|S3^{viii}	106.48(5)
		Se2|S2^{vii}—Cu2—Se3|S3^{viii}	110.67(8)
		Se1|S1^{v}—Cu2—Se3|S3^{viii}	103.50(8)
		Se3|S3^{vi}—Cu2—Se3|S3^{viii}	106.48(5)
		Se2|S2^{vii}—Cu2—Se3|S3^{viii}	110.67(8)
		Se1|S1^{i}—P—Se2|S2	111.90(18)
		Se1|S1^{i}—P—Se3|S3^{ix}	108.64(12)
		Se2|S2—P—Se3|S3^{ix}	108.94(11)
		Se3|S3^{ix}—P—Se3|S3^{x}	109.77(14)

(i) x, 1+y, z; (ii) x, y, -1+z; (iii) 1-x, y, z; (iv) -1+x, y, z; (v) 1+x, 1+y, z; (vi) 1.5-x, 1-y, -0.5+z; (vii) 0.5-x, 1-y, -0.5+z; (viii) x, -1+y, z; (ix) 0.5-x, 1-y, 0.5+z; (x) -0.5+x, 1-y, 0.5+z; (xi) -1+x, -1+y, z; (xii) 1-x, -1+y, z; (xiii) x, y, 1+z; (xiv) 1.5-x, 1-y, 0.5+z; (xv) 1+x, y, z.

Table 10-6. Selected bond lengths (Å) and angles (°) for $Fe_2P_2Se_2S_4$. Standard uncertainties are displayed in parenthesis.

Fe1—Se1|S1	2.5885(8)	Se2|S2^{i}—Fe1—Se2|S2^{ii}	94.88(4)
Fe1—Se1|S1^{iii}	2.5885(8)	Se2|S2^{i}—Fe1—Se1|S1	84.34(2)
Fe1—Se1|S1^{ii}	2.5924(7)	Se2|S2^{ii}—Fe1—Se1|S1^{iii}	84.34(2)
Fe1—Se1|S1^{iv}	2.5924(7)	Se1|S1—Fe1—Se1|S1^{iii}	96.44(3)
Fe1—Se2|S2^{i}	2.5881(8)	Se2|S2^{i}—Fe1—Se1|S1^{ii}	95.97(3)
Fe1—Se2|S2^{ii}	2.5881(8)	Se2|S2^{ii}—Fe1—Se1|S1^{ii}	84.14(3)
P—Se1|S1	2.0982(8)	Se1|S1—Fe1—Se1|S1^{ii}	95.74(2)
P—Se2|S2^{vii}	2.0965(14)	Se1|S1^{iii}—Fe1—Se1|S1^{ii}	84.16(2)
P—Se1|S1^{viii}	2.0983(8)	Se1|S1—Fe1—Se1|S1^{ii}	95.74(2)
P—P^{ix}	2.181(2)	Se2|S2^{i}—Fe1—Se1|S1^{iv}	84.14(3)
		Se2|S2^{ii}—Fe1—Se1|S1^{iv}	95.97(3)
		Se1|S1—Fe1—Se1|S1^{iv}	84.16(2)
		Se2|S2^{vii}—P—Se1|S1	113.41(4)
		Se2|S2^{vii}—P—Se1|S1^{viii}	113.41(4)
		Se1|S1—P—Se1|S1^{viii}	113.44(6)

(i) -0.5+x, 0.5+y, z; (ii) 0.5-x, 0.5-y, -z; (iii) -x, y, -z; (iv) -0.5+x, 0.5-y, z; (v) 1+x, y, z; (vi) 0.5+x, -0.5+y, z; (vii) -1+x, y, z; (viii) x, -y, z; (ix) -x, -y, -z.

Raman Spectroscopy

Raman (750-100 cm^{-1}) spectra were collected using a BIO-RAD FT spectrometer equipped with a Spectra-Physics Topaz T10-106c 1.064 nm YAG laser and a Ge detector. Samples were ground into a fine powder and loaded into fused silica tubes and 64 scans were averaged.

NMR Spectroscopy

Room temperature solid-state NMR spectra of the $Cu_3PSe_{4-x}S_x$ compounds were collected on a 9.4 T spectrometer (Varian Infinity Plus) using a double resonance magic angle spinning (MAS) probe. Samples were spun at frequencies ranging from 5 kHz to 15 kHz in zirconia rotors of 4 mm outer diameter and with a maximum of a ~50 μL sample volume. Bloch decay spectra were taken with a 3.6 μs 90° pulse (calibrated using 85% H_3PO_4) and with relaxation delays of 1000 s. Each spectrum was processed with ≤

100 Hz line broadening and up to a 10^{th} order polynomial baseline correction. The spectra were referenced to 85% H_3PO_4 at 0 ppm.

For the samples Cu_3PSe_3S, $Cu_3PSe_2S_2$ and Cu_3PSeS_3, it was not possible to spin the samples with the full ~50 μL of sample with the probe inserted into the NMR magnet. The samples would spin stably without the external magnetic field present, however, when the probe was subsequently inserted into the magnet spinning became erratic or stopped altogether. To circumvent this problem, approximately equal volumes of the $Cu_3PSe_{4-x}S_x$ sample and talc were ground together in an agate mortar and pestle, and this mixture was loaded into the zircona rotor. This resulted in stable spinning for all compositions. For these samples, spectra with lower signal-to-noise were collected because of the decreased sample mass.

RESULTS AND DISCUSSION

X-ray Diffraction of $Cu_3PSe_{4-x}S_x$

Compounds with the stoichiometry $Cu_3PSe_{4-x}S_x$ were formed and the powder patterns were indexed following powder X-ray diffraction. The X-ray diffraction patterns are displayed in Figure 10-1, the indexed cell parameters are displayed in Table 10-7, and a plot of the cell parameters as a function of composition is displayed in Figure 10-2. In each case, every peak in the powder X-ray diffraction pattern was indexed to a single compound, and there was no evidence for the presence of, for example, mixtures of Cu_3PSe_4 and Cu_3PS_4 at the intermediate compositions.

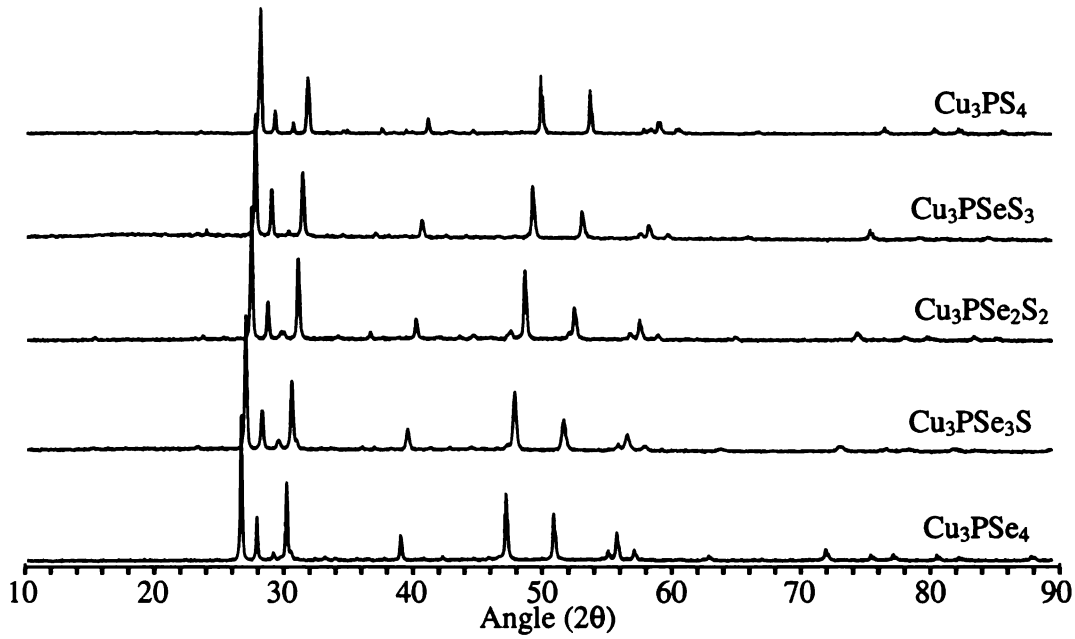

Figure 10-1. The X-ray diffraction patterns of the $Cu_3PSe_{4-x}S_x$ compounds. Each peak could be indexed to the parent structure of either Cu_3PSe_4 or Cu_3PS_4 and the cell parameters were subsequently refined.

Table 10-7. The cell parameters of each of the $Cu_3PSe_{4-x}S_x$ compounds as indexed from the powder X-ray diffraction data.

	Cu_3PS_4	Cu_3PSe_3S	$Cu_3PSe_2S_2$	Cu_3PSeS_3	Cu_3PSe_4
a (Å)	7.280(5)	7.344(10)	7.489(9)	7.592(3)	7.691(3)
b (Å)	6.317(4)	6.401(4)	6.313(11)	6.589(3)	6.663(2)
c (Å)	6.069(4)	6.127(3)	6.203(5)	6.286(3)	6.384(2)
Symmetry	Ortho.	Ortho.	Ortho.	Ortho.	Ortho.

The cell parameters do not smoothly vary from one extreme to the other as predicted by Vegard's law, and this indicates the possibility that the nature of the bonding in these compounds does not remain unperturbed as the switch from Se to S occurs. Instead of a linear dependence, there is a minimum in the cell parameter *b* and cell volume at the compound $Cu_3PSe_2S_2$.

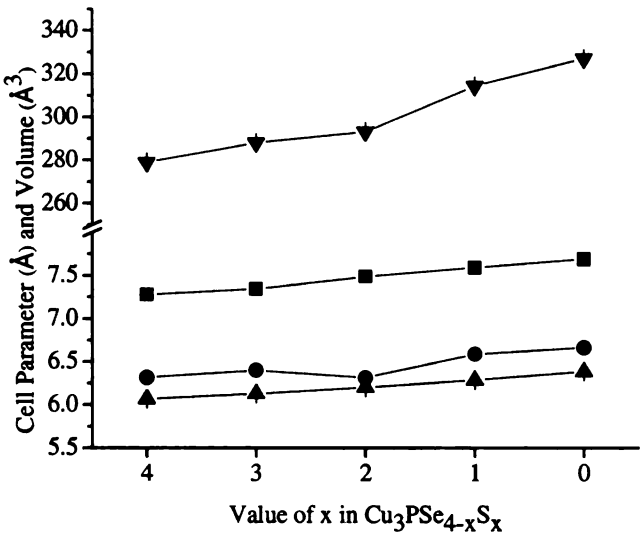

Figure 10-2. The cell parameters *a* (squares), *b* (circles), and *c* (upwards pointing triangles) of each of the $Cu_3PSe_{4-x}S_x$ compounds, as well as the cell volume (downwards pointing triangles). The uncertainties were smaller than the indicators used.

In a true solid solution, the types of atoms forming the solid solution are randomly substituted for one another. One possibility that could explain the nonlinearity of the cell parameters was that a true solid solution was not formed, but rather that there was some site preference for the S and Se atoms. The deviation from linearity was most pronounced in the cell parameter *b*, and therefore, the possibility existed that some ordering of the S and Se atoms along the *b*-axis might reasonably result in an alternation of bond lengths. To explore this possibility, a single crystal of Cu_3PSeS_3 was chosen and X-ray diffraction data were collected, solved, and refined. The crystallographic refinement contained no indication that a site preference existed for Se or S, and that each chalcogen atomic site was had a 25% probability of being occupied by an Se atom, and a 75% probability of being occupied by an S atom. No long range order in the form of satellite reflections were observed, and significant contributions of a structural modulation are therefore unlikely.

An additional possibility that was explored was that there was no long range ordering of the chalcogen atoms, but rather only short range ordering. From the single crystal X-ray diffraction data, the probability of each chalcogen site being an Se or an S atom is fixed at 25%, and 75%, respectively. Therefore, most of the $[PQ_4]^{3-}$ (Q = S or Se) moities would have the formula $[PSeS_3]^{3-}$. In contrast, it was hypothesized that the formation of $[PSe_4]^{3-}$ and $[PS_4]^{3-}$ may be favored over the mixed species, and it was these moities that were distributed in a 25% to 75% ratio. The crystallographic solution was incapable of distinguishing between these two possibilities.

X-ray Diffraction of $Fe_2P_2Se_{6-x}S_x$

The powder X-ray diffraction patterns of the $Fe_2P_2Se_{6-x}S_x$ compounds are displayed in Figure 10-3. The parent members $Fe_2P_2Se_6$ and $Fe_2P_2S_6$ have hexagonal and monoclinic cells, respectively.[10,11] The intermediate members that contained both S and Se could be indexed based off of one of these cells. The results of this indexing are displayed in Table 10-8. The members $Fe_2P_2SeS_5$ $Fe_2P_2Se_2S_4$ and $Fe_2P_2Se_3S_3$ were indexed to a monoclinic cell, and the remaining $Fe_2P_2Se_4S_2$ and $Fe_2P_2Se_5S$ were indexed with the hexagonal cell. For the S-rich compounds $Fe_2P_2SeS_5$ $Fe_2P_2Se_2S_4$ all of the peaks in the diffraction pattern could be indexed. In the case of the Se-rich compounds $Fe_2P_2Se_4S_2$ and $Fe_2P_2Se_5S$ there were some peaks that could not be indexed with the hexagonal unit cell.

One possibility is that the Se-rich compounds were not pure but were rather mixtures of phases with different unit cells. The extra peaks are putatively assigned to a

more S-rich compound that has monoclinic symmetry. This suggests that the S-rich anions are formed preferentially. This may be the result of increased stability of the P-S bond over the P-Se bond, and electronic structure calculations may verify this prediction. For the peaks that were successfully indexed for each compound, the size of the unit cell per formula unit (i.e. V/Z) there was a trend towards a larger unit cell with increased Se content, as would be expected for the substitution of the larger Se for the smaller S, Table 10-6.

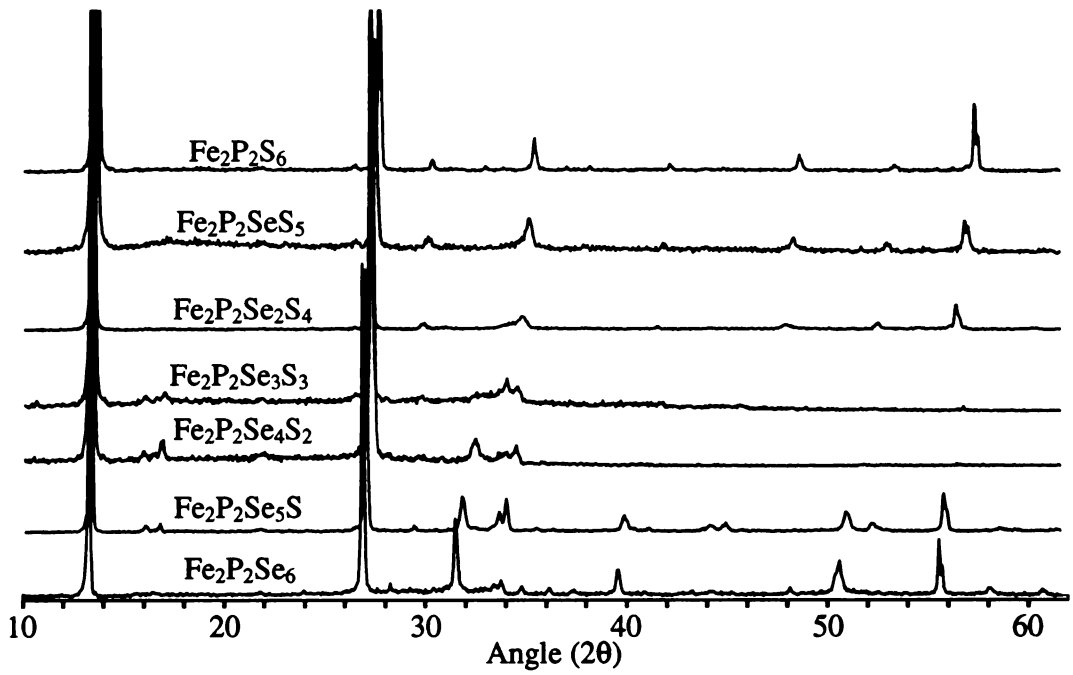

Figure 10-3. The powder diffraction patterns of the $Fe2P_2Se_{6-x}S_x$ compounds. The two strongest peaks are off scale to show the smaller peaks at higher angle 2θ.

Table 10-8. The cell parameters of each of the $Fe_2P_2Se_{6-x}S_x$ compounds as indexed from the powder X-ray diffraction data.

	$Fe_2P_2S_6$	$Fe_2P_2SeS_5$	$Fe_2P_2Se_2S_4$	$Fe_2P_2Se_3S_3$	$Fe_2P_2Se_4S_2$	$Fe_2P_2Se_5S$	$Fe_2P_2Se_6$
a (Å)	5.99(1)	6.03(1)	6.039(7)	6.11(5)	6.10(3)	6.203(1)	6.268(3)
b (Å)	10.29(2)	10.37(2)	10.454(8)	10.50(2)	6.10(3)	6.203(1)	6.268(3)
c (Å)	6.77(2)	6.81(1)	6.803(4)	6.83(2)	19.52(6)	19.753(1)	19.83(4)
α	90	90	90	90	90	90	90
β	108.0(3)	108.0(3)	106.6(3)	107.3(4)	90	90	90
γ	90	90	90	90	120	120	120
V ($Å^3$)	396.9	404.9	411.6	418.8	629.1	658.3	674.8
Z	2	2	2	2	3	3	3
V/Z	198.45	202.45	205.8	209.4	209.7	219.4	224.9
Sym.	Mono.	Mono.	Mono.	Mono.	Mono.	Hex.	Hex.

Like the single crystal refinement of the compound Cu_3PSeS_3, the refinement of a single crystal of $Fe_2P_2Se_2S_4$ contained no indication that there was a site preference for one chalcogen atom over the other, and each of the sites had an equal probability of containing each chalcogen atom.

Raman Spectroscopy

In order to determine whether or not the chalcogen atoms were randomly distributed in the $Cu_3PSe_{4-x}S_x$ compounds, Raman spectroscopy was used to determine the identity of the chalcophosphate moities present. It has been shown that $[PS_4]^{3-}$ and $[PSe_4]^{3-}$ have totally symmetric stretching modes that are commonly at ~420 cm^{-1} and ~240 cm^{-1}, respectively.[16,17] For the mixed $[PSe_{4-x}S_x]^{3-}$ it would be expected that with the loss of the tetrahedral symmetry, that the totally symmetric stretching modes would be fundamentally different and therefore readily distinguishable.

The Raman spectra for the $Cu_3PSe_{4-x}S_x$ are displayed graphically in Figure 10-4, and a list of the strongest peaks is displayed in Table 10-9. The features at 390 cm^{-1} and 213 cm^{-1} in the Cu_3PS_4 and Cu_3PSe_4 spectra can be assigned to the $[PS_4]^{3-}$ and $[PSe_4]^{3-}$ totally symmetric stretch, respectively.[16,17] In the case of the Cu_3PSeS_3 and Cu_3PSe_3S compounds, a spectral peaks at 384 cm^{-1} and 218 cm^{-1}, respectively, are observed, and these are likely attributable to the totally symmetric stretch of the $[PS_4]^{3-}$ and $[PSe_4]^{3-}$ anions. The slight energy change in the totally symmetric stretch is likely affected by nearby anions that are not homogeneously occupied by either an S or an Se. This change in energy is further evidence that the sample is not a mixture of various species, but rather a homogenous crystalline solid solution.

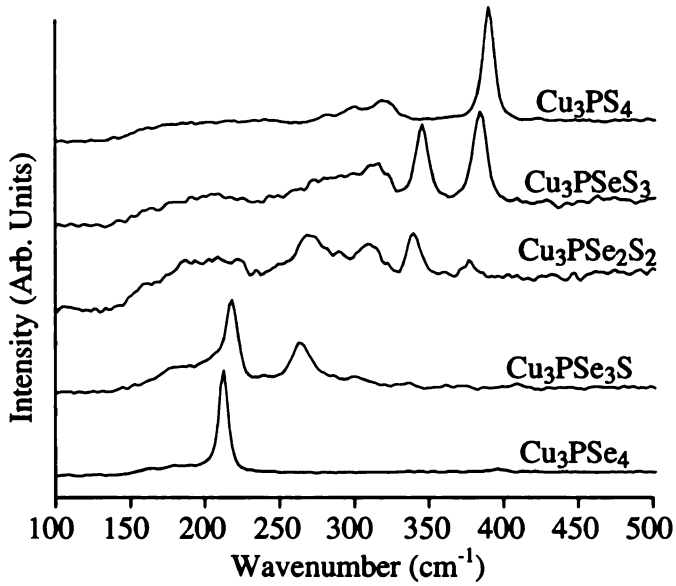

Figure 10-4. Raman spectra of the $Cu_3PSe_{4-x}S_x$ compounds. The spectra were sums of 64 scans.

The peaks at 345 cm^{-1} and 262 cm^{-1} in the Cu_3PSe_3S and the Cu_3PSeS_3 compounds, respectively, might reasonably be assigned to mixed chalcogen-containing anions. In the case of the Cu_3PSe_3S compound this may be the $[PSe_3S]^{4-}$ anion, and in the case of the

Cu_3PSeS_3 compound it may be the $[PSe_3S]^{4-}$ anion. It is unlikely that significant contributions from the $[PSe_2S_2]^{3-}$ anion is present in either case because the Raman spectrum for the compound where such a feature would be expected to be the most pronounced, namely $Cu_3PSe_2S_2$, contains only very weak intensity signals. Instead, the spectrum for this compound contains some features that closely resemble those in the spectra of the other compounds.

Table 10-9. The energy in wavenumber (cm^{-1}) of the strongest spectral features in the Raman spectra of the $Cu_3PSe_{4-x}S_x$ compounds.

Cu_3PS_4	Cu_3PSeS_3	Cu_3PSe_3S	Cu_3PSe_4
390	384	218	213
	345	262	

Nuclear Magnetic Resonance

In order to confirm the Raman assignments, NMR spectra were collected, Figure 10-5. The chemical shifts are displayed in Table 10-10. The parent compounds Cu_3PS_4 and Cu_3PSe_4 contained sharp ^{31}P spectral features at 55.9 ppm and -82.7 ppm, respectively. The chemical shift of Cu_3PSe_4 has been reported previously, and is well within the range of what is expected for a compound containing a $[PSe_4]^{3-}$anion.[18,19] The spectrum of Cu_3PS_4 contained an crystalline impurity phase with a chemical shift of 66.5 ppm. One possible assignment of this peak is to the compound Cu_7PS_6. The compounds Cu_3PS_4 and Cu_7PS_6 have been simultaneously produced previously.[20]

Table 10-10. The ^{31}P NMR spectral features observed for the $Cu_3PSe_{4-x}S_x$ compounds, in ppm. The peaks corresponding to the Cu_7PS_6 impurity have been omitted for clarity. The peaks common to different stoichiometry compounds have been grouped horizontally.

Cu_3PS_4	Cu_3PSeS_3	$Cu_3PSe_2S_2$	Cu_3PSe_3S	Cu_3PSe_4
55.9	55.9		-82.7	-82.7
	26.6	28.0		
		-34.8	-40.8	
	-5.5	-3	-6	

The spectra of the mixed S and Se compounds had much broader spectral lines. This broadness is evidence for microscopic inhomogeniety as a result of having a random distribution of the different anions rather than a perfectly ordered crystalline arrangement. The spectrum of Cu_3PSeS_3 contained the same two spectral features that have been assigned to the $[PS_4]^{3-}$ anions of Cu_3PS_4 and Cu_7PS_6. It also contained a spectral feature at 26.6 ppm and one at -5.5 ppm. These spectral features are reasonably assigned to the $[PSe_3S]^{3-}$ and the $[PSe_2S_2]^{3-}$ anions, respectively. The intensity of the 55.9 ppm peak is comparable to that of the 26.6 ppm peak, and both of these peaks are significantly more intense than the -5.5 ppm peak. The relative intensities of these three peaks are comparable to the respective peaks in the Raman spectrum of for this compound, with the weakest NMR spectral feature likely corresponding to a Raman feature that can barely be seen above the level of the noise. A weakness of this assignment is that if the concentrations of the $[PS_4]^{3-}$ and the $[PSeS_3]^{3-}$ anions are approximately equivalent with only a small amount of $[PSe_2S_2]^{3-}$, it would not be possible to account for the target stoichiometry of $CuPSeS_3$ but instead would indicate some more Se-rich stoichiometry. This discrepancy is presently unexplained.

A similar argument for the assignment of the NMR spectrum of Cu_3PSe_3S can be made. The -82.7 ppm is assigned to the P in the $[PSe_4]^{3-}$ anion, and the -40.8 ppm peak can reasonably be assigned to the $[PSe_3S]^{3-}$ anion. A weak third spectral feature is present at -6.0 ppm, which is assigned to the $[PSe_2S_2]^{3-}$ anion. Again the NMR spectral features agree with the previously proposed Raman assignment. The $Cu_3PSe_2S_2$ compound contains two strong spectral features at 28.0 ppm and -3.0 ppm, with a weaker feature at -34.8 ppm. These have already been assigned to the $[PSeS_3]^{3-}$, the $[PSe_2S_2]^{3-}$ and the $[PSe_3S]^{3-}$ anions.

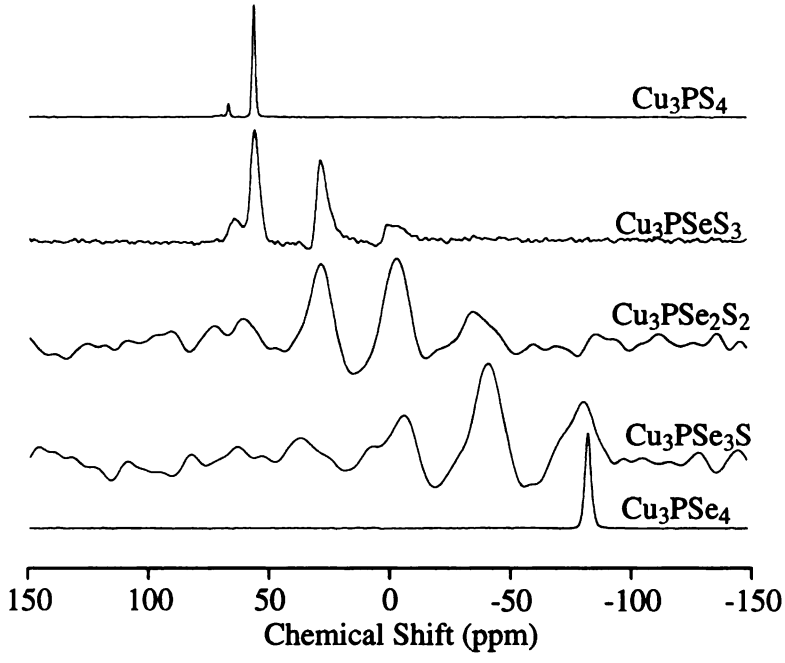

Figure 10-5. The ^{31}P NMR spectrum of the $Cu_3PSe_{4-x}S_x$ compounds. The spectra were sums of 4 individual scans with a pulse delay of 1000 s and the spinning frequency was 12 kHz, and spinning sidebands were not observed.

Observation of multiple anions within a single crystalline compound

It is somewhat surprising that the anion that is predicted by the stoichiometry of the compound (i.e. $[PSeS_3]^{3-}$ in the compound Cu_3PSeS_3) is not necessarily the dominant ion, but instead the anion with only one type of chalcogen atom is also present in significant amounts. The compounds Cu_3PSeS_3 and Cu_3PSe_3S compounds contain significant numbers of $[PSe_4]^{3-}$ and $[PS_4]^{3-}$ ions, respectively.

The P-S bond has an enthalpy of 444 kJ/mol, and the P-Se bond has an enthalpy of 364 kJ/mol.[21] The formation of a P-S bond is therefore more exothermic than the formation of a P-Se bond, and perhaps there is a relative difference in thermodynamic stability of the anions containing only P-S and only P-Se bonds. In the melt, P-S and P-Se bonds may break and form again in a dynamic equilibrium. Because of the increased enthalpy of the P-S bond over the P-Se bond, perhaps the P-S bonds are not as readily sundered as the P-Se bonds, and therefore S-rich anions are preferentially formed. Support for this hypothesis is provided by the NMR spectra wherein the peaks that are assigned to the more S-rich species are more intense than the Se-rich species whenever both S and Se are present. For example, in the spectrum of Cu_3PSeS_3 the peak that is assigned to the $[PS_4]^{3-}$ anion is more intense than the one for the $[PSe_2S_2]^{3-}$ anion. Also, in the NMR spectrum of $Cu_3PSe_2S_2$ the peak assigned to $[PSeS_3]^{3-}$ is more intense than the peak assigned to $[PSe_3S]^{3-}$. One weakness of this hypothesis is that for Cu_3PSe_3S, the intensity of the peaks assigned to $[PSe_2S_2]^{3-}$ and $[PSe_4]^{3-}$ are nearly equivalent. The exact peak intensities are not trivially measured given the significant nonlinearity of the baseline and the relatively low signal to noise ratio. These preliminary data should be

recollected to ensure that the effects observed are not the result of deviations from the nominal stoichiometry. Additionally, the summation of greater than four spectra for each sample will be useful to increase the signal to noise ratio and make a measurement of the relative peak intensities possible.

In each case where both S and Se are present, broad lines are observed whereas in the S-only and Se-only compounds, the lines are substantially narrower. The broadness of the NMR spectral features for each compound containing both S and Se provide some evidence that the microscopic inhomogeniety plays a significant role in the crystalline structure for these compounds. It is hypothesized that in the compounds with both S and Se, the different anions are randomly distributed, thus making a range of possible ^{31}P chemical environments. For example, with the compound $Cu_3PSe_2S_2$, the $[PSeS_3]^{3-}$, $[PSe_2S_2]^{3-}$, and $[PSe_3S]^{3-}$ are perhaps randomly distributed around a given P atom. Because the distribution is random, a different P atom that is not proximate to the former may have a different distribution of the different anions and therefore have a different chemical shift. There are many possible arrangements of each of the different anions near a given P atom within the crystalline solid, and this range of chemical environments results in a range of chemical shifts. This is manifested in the NMR spectra as broad lines because the different chemical shifts for each arrangement are not resolved and are rather significantly overlapped. This provides evidence for the hypothesis that the different anions are randomly distributed is correct.

CONCLUDING REMARKS

The compounds with the formula $Cu_3PSe_{4-x}S$ appear to form solid solutions as predicted by adherence to the Hume-Rothery rules.[1] Interestingly, a significant number of single chalcogen-containing chalcophosphate anions are present in the mixed solids. That is, the stoichiometry Cu_3PSe_3S does not produce a crystalline solid that contains only the $[PSe_3S]^{3-}$ anion, but also contains a significant amount of $[PSe_4]^{3-}$. The $Fe_2P_2Se_{6-x}S_x$ compounds may also demonstrate a similar preference to form the single chalcogen anions, and further Raman and NMR studies could be used to test this hypothesis. If such a propensity to preferentially form anions containing only a single type of chalcogen, it would be expected that the $Fe_2P_2Se_{6-x}S_x$ compounds would also demonstrate a similar behavior. One interesting possibility is that in addition to the single chalcogen atom anions being preferentially formed, that the $[P_2Se_3S_3]^{4-}$ ion might be preferentially formed. This possibility is justified because a single type of chalcogen atom might reasonably be attached to each P-atom, i.e. $[Se_3P\text{-}PS_3]^{4-}$.

REFERENCES

1. Hume-Rothery, W. *J. Inst. Metals* **1926,** 35, 295-348.

2. Abe, S.; Masumoto, K. *J. Cryst. Growth* **2000,** 220, 126-129.

3. Karczewski, G.; Klimkiewicz, M.; Glass, I.; Szczerbakow, A.; Behrendt, R. *Appl. Phys. A-Mater.* **1982,** 29, 49-52.

4. Ramos, A.; Levelut, C.; Petiau, J.; Villain, F. *J. Phys.-Condens. Mat.* **1993,** 5, 3507-3518.

5. Ahn, D. H.; Kang, D. H.; Cheong, B. K.; Kwon, H. S.; Kwon, M. H.; Lee, T. Y.; Jeong, J. H.; Lee, T. S.; Kim, I. H.; Kim, K. B. *IEEE Electr. Device L.* **2005,** 26, 286-288.

6. Ahn, D. H.; Lee, T. Y.; Lee, D. B.; Yim, S. S.; Wi, J. S.; Jin, K. B.; Lee, M. H.; Kim, K. B.; Kang, D. H.; Jeong, H. J.; Cheong, B. K. *Jpn. J. Appl. Phys.* **2007,** 46, 5719-5723.

7. Wachter, J. B.; Chrissafis, K.; Petkov, V.; Malliakas, C. D.; Bilc, D.; Kyratsi, T.; Paraskevopoulos, K. M.; Mahanti, S. D.; Torbrugge, T.; Eckert, H.; Kanatzidis, M. G. *J. Solid State Chem.* **2007,** 180, 420-431.

8. Ma, H. W.; Guo, G. C.; Zhou, G. W.; Wang, M. S.; Lin, S. H.; Dong, Z. C.; Huang, J. S. *Chinese J. Struc. Chem.* **2002,** 21, 288-291.

9. Pfitzner, A.; Reiser, S. *Z. Kristall.* **2002,** 217, 51-54.

10. Klingen, W.; Eulenber.G; Hahn, H. *Z. Anorg. Allg. Chem.* **1973,** 401, 97-112.

11. Ouvrard, G.; Brec, R.; Rouxel, J. *Mater. Res. Bull.* **1985,** 20, 1181-1189.

12. Greenwood, N. N.; Earnshaw, A. Chemistry of the Elements; 2nd ed.; Butterworth-Heinemann: Boston, MA, 1997; pp 662, 754.

13. Vegard, L. *Z. Phys.* **1921,** 5, 17-26.

14. *Jade 6.0*, Materials Data, Inc. Livermore, CA.: 2003.

15. *SMART, SAINT, SHELXTL V-5 and SADABS*, Bruker Analytical X-ray Instruments, Inc.: Madison, 1998.

16. Evenson, C. R.; Dorhout, P. K. *Inorg. Chem.* **2001,** 40, 2884-2891.

17. Evenson, C. R.; Dorhout, P. K. *Inorg. Chem.* **2001,** 40, 2875-2883.

18. Canlas, C. G. Ph.D. Thesis, Michigan State University, East Lansing, MI, 2004.

19. Canlas, C. G.; Muthukumaran, R. B.; Kanatzidis, M. G.; Weliky, D. P. *Solid State Nucl. Magn. Reson.* **2003,** 24, 110-122.

20. Blachnik, R.; Gather, B.; Andrae, E. *J. Therm. Anal.* **1991,** 37, 1289-1298.

21. Weast, R. C.; Astle, M. J., *CRC Handbook of Chemistry and Physics*. 60th ed.; CRC Press, Inc.: Boca Raton, 1980.

CHAPTER 11

CONCLUSIONS AND FUTURE DIRECTIONS.

Prior to this work, there were many known examples of alkali metal-containing chalcophosphate materials,[1-21] and now there are a number of new materials that contain pseudo alkali metals (i.e. Cu, Ag, and Tl).[22,23] These new compounds were found to have potentially relevant physical properties like spontaneous antiferroelectric ordering and glass to crystalline phase transitions (Chapter 2) and also to possess a wide range of chemical bonding motifs (Chapter 3). This also led to the discovery of several new alkali metal containing compounds during attempts to rationalize the pseudo alkali metal chemistry with the alkali metal chemistry (Chapter 5). Several new argyrodite-like compounds that contain a pseudo alkali metal were also discovered, and these compounds were found to have a composition-dependent phase transition (Chapter 6). Temperature dependent phase transitions for related argyrodite materials have previously been observed,[24-29] and variable temperature neutron diffraction experiments on the new argyrodite materials of this work are presently underway to look for similar phase transitions.

There are undoubtedly many other compounds that are yet to be discovered that contain a pseudo alkali metal and various chalcophosphate anions. Most of the new pseudo alkali metal containing chalcophosphate compounds presented herein also contained bismuth. The choice of another element in lieu of bismuth may be selected to target particular structural or physical properties. For example, targeting phases with Sb instead of Bi may more readily form vitreous products. Another possibility is to replace the Bi atom with various 2+ metal cations such as Ti^{2+} and Sn^{2+}. This may result in compounds that have structures similar to the other pseudo alkali metal chalcophosphate compounds with bismuth except with site vacancies to maintain charge neutrality.

An additional contribution that this work makes is some elucidation of the properties of the molten mixtures that ultimately result in the formation of crystalline compounds. In Chapter 7, it was proposed that a small molecular species such as $[P_2Se_{10}]^{4-}$ may exist in the melt,[30] and further support was given to this hypothesis in Chapter 9. Only very general conclusions about the nature of the melt, for example the viscosity, approximate molecular radius of the species present, and likelihood of containing a P-P bonded versus non P-P bonded species were discussed.[31,32] The presence of a significant concentration of a radical species was also demonstrated, although the chemical identities of the species are not yet known.

One significant limiting factor to the high temperature NMR experiments is that in almost all cases only a single peak was present at high temperature.[30] The high temperature NMR spectrum of $Hg_2P_2Se_6$ is the only example so far where multiple peaks have been observed once the sample is molten, Figure 11-1. There were peaks noted in the chemical shift regions that have, at room temperature, been assigned to P-P and non P-P bonded species. No known $[PSe_4]^{3-}$ ternary compound with Hg has yet been discovered, and this high temperature spectrum may provide evidence that the synthesis of such a material may be possible.

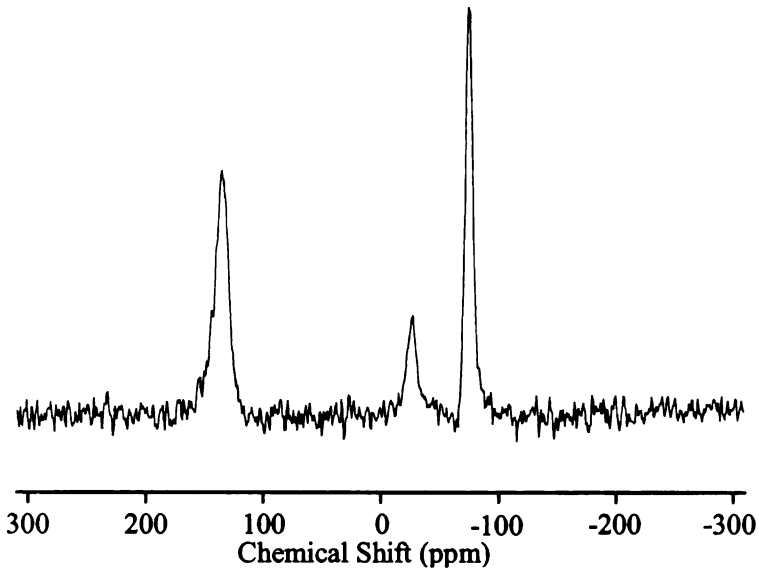

Figure 11-1. High temperature ^{31}P NMR spectrum of $Hg_2P_2Se_6$ at 525 °C. The melting point of the crystalline compound is 510 °C. The spectral features are presently unassigned and this is the first known example where speciation was observed in a molten sample.

New compound discovery with the high temperature NMR experiments has already been successful for the compound $Cs_4P_2Se_{10}$[30] (Chapter 7) and it is likely that this technique will allow for the discovery of other new compounds as well. NMR spectral collection at high temperature is possible in a matter of minutes (Chapter 8) and therefore screening various temperature ranges to look for new compound formation is potentially orders of magnitude faster than traditional methodology that combines high temperature synthesis and subsequent characterization by diffraction.

Another limitation to the high temperature NMR spectra is that other than the present works, there is no means by which to interpret the high temperature spectra of these melts. In the case of the room temperature NMR experiments, the interpretation of the resultant spectra is greatly assisted by known X-ray crystallographic refinements of the structure of the compound. In this manner, it is feasible to, in many cases, assign the

^{31}P NMR spectra to the known chemical environments of the crystalline solid. In a molten liquid, it is not possible to obtain crystal structures so the interpretation of the high temperature NMR spectra is substantially hindered. One type of method that may provide significant insights into the high temperature NMR spectra is *ab initio* electronic structure calculations.

The software package Gaussian 03 contains a routine to estimate NMR chemical shifts of small molecules[33] and such a calculation may be useful to interpret the high temperature NMR spectra. A first step would be to validate the method for these types of materials to ensure that the experimental chemical shifts correspond to the predicted ones. In preliminary trials, attempts to calculate the chemical shifts of the crystalline solids have failed. Calculations of NMR parameters are currently not implemented with 3D periodic structures like the chalcophosphate compounds of the present study, so it was necessary to use a molecular approximant of the 3D structure. In all cases, these calculations crashed and no chemical shift was predicted.

Calculations of the relative chemical shifts of isolated $[P_2Se_6]^{4-}$ and $[PSe_4]^{3-}$ anions (Q = S or Se) also did not provide useful information. Compounds containing these two anions resonate at chemical shifts separated by perhaps hundreds of ppm, but the calculation predicted a difference in chemical shift of only several ppm for the isolated anions. Calculations performed on larger clusters that also contained nearby metals were not successful in predicting chemical shifts that were comparable to those of the crystalline compounds. Again, the difference in chemical shifts between $[P_2Se_6]^{4-}$ and $[PSe_4]^{3-}$ containing species was much smaller than what is experimentally observed. Further work on improving the modeling techniques and the method of calculation may

circumvent these problems, and if this can be done, this technique will likely be very useful to interpret the high temperature NMR spectra.

There is also great potential to characterize the chalcophosphate melts by other means. An EPR heating apparatus was designed and fabricated, and temperatures of ~400 °C have been measured at the sample location in the NMR cavity. Unfortunately, to date high temperature EPR spectra have contained noise but not signal. The EPR spectra of Chapter 8 were all collected on samples that had been rapidly quenched from the melt. The high temperature NMR data have conclusively shown that radicals are present in the melt, and yet, they have not been observed directly with EPR measurements.

One possibility is that thermal noise is preventing the observation of a signal. Another possibility is significant electron-electron spin coupling. This may result in spectral features that are extremely broad, perhaps several thousand Gauss.[34] Electron-electron interaction is plausible in the molten mixture because of the high concentration of radicals, and the putative mobility of those species in a relatively non-viscous liquid. Furthermore, it has been proposed that the pure chalcogens form biradicals chains and an additional possibility is that in the melt, these chains can align in such a way that the radicals on each end are proximate. This is consistant with the formation of the various *cyclo-* species that are known to exist in the different room temperature chalcogen allotropes (i.e. *cyclo*-S_8 and *cyclo*-Se_6). An interesting test of this hypothesis would be to monitor the EPR peak width from room temperature to the melt. Presumably, with an increase in the number and mobility of the radical species, the EPR spectra will increasingly broaden as a function of temperature. It may be possible to collect spectra

below the temperature where this electron-electron coupling makes the lines unreasonably broad, if this hypothesis is correct.

Optical spectroscopy may also provide some useful information about the species that exist at room temperature. Sulfur radicals trapped in Zeolite cages have been characterized using visible spectroscopy.[35-37] It has been shown that the length of the S chain is correlated with the color of the radical species. This may allow the identification of the structure of the radical if it is indeed dominated by chalcogen chains of various lengths. High temperature Raman spectroscopy may also be useful in determining the species that exist in the melt. The Raman features in the high temperature melts are likely to be significantly broader than the room temperature crystalline counterparts. Glasses and aqueous solutions that do not have long range order have been shown to have Raman features that are broader than those in well ordered crystals.[38] Although the peaks would be significantly broadened by the loss of crystalline ordering, it may be possible to observe whether or not these species persist in the melt since various crystalline chalcophospate compounds have distinct Raman features.

REFERENCES

1. Belkyal, I.; El Azhari, M.; Wu, Y. D.; Bensch, W.; Hesse, K. F.; Depmeier, W. *Solid State Sci.* **2006,** 8, 59-63.

2. Chondroudis, K.; Hanko, J. A.; Kanatzidis, M. G. *Inorg. Chem.* **1997,** 36, 2623-2632.

3. Chondroudis, K.; Kanatzidis, M. G. *Inorg. Chem.* **1995,** 34, 5401-5402.

4. Chondroudis, K.; Kanatzidis, M. G.; Sayettat, J.; Jobic, S.; Brec, R. *Inorg. Chem.* **1997,** 36, 5859-5868.

5. Chondroudis, K.; McCarthy, T. J.; Kanatzidis, M. G. *Inorg. Chem.* **1996,** 35, 840-844.

6. Chung, I.; Do, J.; Canlas, C. G.; Weliky, D. P.; Kanatzidis, M. G. *Inorg. Chem.* **2004,** 43, 2762-2764.

7. Chung, I.; Karst, A. L.; Weliky, D. P.; Kanatzidis, M. G. *Inorg. Chem.* **2006,** 45, 2785-2787.

8. Coste, S.; Kopnin, E.; Evain, M.; Jobic, S.; Payen, C.; Brec, R. *J. Solid State Chem.* **2001,** 162, 195-203.

9. Evenson, C. R.; Dorhout, P. K. *Inorg. Chem.* **2001,** 40, 2884-2891.

10. Gauthier, G.; Evain, M.; Jobic, S.; Brec, R. *Solid State Sci.* **2002,** 4, 1361-1366.

11. Gieck, C.; Tremel, W. *Chem.-Eur. J.* **2002,** 8, 2980-2987.

12. Iordanidis, L.; Bilc, D.; Mahanti, S. D.; Kanatzidis, M. G. *J. Am. Chem. Soc.* **2003,** 125, 13741-13752.

13. Iordanidis, L.; Brazis, P. W.; Kyratsi, T.; Ireland, J.; Lane, M.; Kannewurf, C. R.; Chen, W.; Dyck, J. S.; Uher, C.; Ghelani, N. A.; Hogan, T.; Kanatzidis, M. G. *Chem. Mat.* **2001,** 13, 622-633.

14. Iordanidis, L.; Schindler, J. L.; Kannewurf, C. R.; Kanatzidis, M. G. *J. Solid State Chem.* **1999,** 143, 151-162.

15. Kanatzidis, M. G. *Chem. Mat.* **1990,** 2, 353-363.

16. Loken, S.; Tremel, W. *Eur. J. Inorg. Chem.* **1998,** 283-289.

17. McCarthy, T. Ph.D. Thesis, Michigan State University, East Lansing, MI, 1994.

18. McCarthy, T.; Kanatzidis, M. G. *J. Alloys Compd.* **1996,** 236, 70-85.

19. McCarthy, T. J.; Kanatzidis, M. G. *Chem. Mat.* **1993,** 5, 1061-1063.

20. McCarthy, T. J.; Kanatzidis, M. G. *J. Chem. Soc. Chem. Commun.* **1994,** 1089-1090.

21. McCarthy, T. J.; Kanatzidis, M. G. *Inorg. Chem.* **1995,** 34, 1257-1267.

22. Gave, M.; Bilc, D.; Mahanti, S.; Breshears, J.; Kanatzidis, M. *Inorg. Chem.* **2005,** 5293-5303.

23. Gave, M.; Malliakas, C. D.; Weliky, D. P.; Kanatzidis, M. G. *Inorg. Chem.* **2007,** 46, 3632-3644.

24. Evain, M.; Gaudin, E.; Boucher, F.; Petricek, V.; Taulelle, F. *Acta. Crystallogr. B* **1998,** 54, 376-383.

25. Gaudin, E.; Boucher, F.; Petricek, V.; Taullele, F.; Evain, M. *Acta. Crystallogr. B* **2000,** 56, 402-408.

26. Gaudin, E.; Petricek, V.; Boucher, F.; Taulelle, F.; Evain, M. *Acta. Crystallogr. B* **2000,** 56, 972-979.

27. Kuhs, W. F.; Nitsche, R.; Scheunemann, K. *Mater. Res. Bull.* **1979,** 14, 241-248.

28. Onoda, M.; Chen, X. A.; Ishii, M.; Wada, H. *Solid State Ionics* **2000,** 136, 415-418.

29. Onoda, M.; Wada, H.; Sato, A.; Ishii, M. *J. Alloys Compd.* **2004,** 383, 113-117.

30. Gave, M.; Canlas, C.; Iyer, R. G.; Kanatzidis, M. G.; Weliky, D. P. *J. Solid State Chem.* **2007,** 180, 2877-2884.

31. Canlas, C. G. Ph.D. Thesis, Michigan State University, East Lansing, MI, 2004.

32. Canlas, C. G.; Kanatzidis, M. G.; Weliky, D. P. *Inorg. Chem.* **2003,** 42, 3399-3405.

33. Frisch, M. J.; Trucks, G. W.; Schlegel, H. B.; Scuseria, G. E.; Robb, M. A.; Cheeseman, J. R.; Montgomery, J., J. A.; Vreven, T.; Kudin, K. N.; Burant, J. C.; Millam, J. M.; Iyengar, S. S.; Tomasi, J.; Barone, V.; Mennucci, B.; Cossi, M.; Scalmani, G.; Rega, N.; Petersson, G. A.; Nakatsuji, H.; Hada, M.; Ehara, M.; Toyota, K.; Fukuda, R.; Hasegawa, J.; Ishida, M.; Nakajima, T.; Honda, Y.; Kitao, O.; Nakai, H.; Klene, M.; Li, X.; Knox, J. E.; Hratchian, H. P.; Cross, J. B.; Bakken, V.; Adamo, C.; Jaramillo, J.; Gomperts, R.; Stratmann, R. E.; Yazyev, O.; Austin, A. J.; Cammi, R.; Pomelli, C.; Ochterski, J. W.; Ayala, P. Y.; Morokuma, K.; Voth, G. A.; Salvador, P.; Dannenberg, J. J.; Zakrzewski, V. G.; Dapprich, S.; Daniels, A. D.; Strain, M. C.; Farkas, O.; Malick, D. K.; Rabuck, A. D.; Raghavachari, K.; Foresman, J. B.; Ortiz, J. V.; Cui, Q.; Baboul, A. G.; Clifford, S.; Cioslowski, J.; Stefanov, B. B.; Liu, G.; Liashenko, A.; Piskorz, P.; Komaromi, I.; Martin, R. L.; Fox, D. J.; Keith, T.; Al-Laham, M. A.; Peng, C. Y.; Nanayakkara, A.; Challacombe, M.; Gill, P. M. W.; Johnson, B.; Chen, W.; Wong, M. W.; Gonzalez, C.; Pople, J. A. *Gaussian 03, Revision C.02*, Gaussian, Inc., Wallingford CT, 2004.

34. Vanvleck, J. H. *Phys. Rev.* **1948,** 74, 1168-1183.

35. Kowalak, S.; Jankowska, A.; Laczkowska, S. *Stud Surf Sci Catal* **2005,** 158, 215-222.

36. Kowalak, S.; Jankowska, A.; Laczkowska, S. *Recent Advances in the Science and Technology of Zeolites and Related Materials, Pts a - C* **2004,** 154, 1633-1640.

37. Kowalak, S.; Jankowska, A.; Zeidler, S.; Wieckowski, A. B. *J. Solid State Chem.* **2007,** 180, 1119-1124.

38. Kapitan, J.; Baumruk, V.; Kopecky, V.; Pohl, R.; Bour, P. *J. Am. Chem. Soc.* **2006,** 128, 13451-13462.

APPENDIX A

OPERATION AND MAINTENANCE OF THE HIGH TEMPERATURE FURNACES.

Replacement heating elements can be purchased from Applied Test Systems (http://www.atspa.com/) for the furnaces with a serial number beginning with C or CH. For the furnaces with serial numbers beginning with an H, the heating element is a single strand of nicrome wire wrapped around a large diameter mullite tube. Replacement K-type thermocouples can be ordered from Omega Engineering (http://www.omega.com/). The Omega website also includes detailed user manuals for more advanced controls not described here. Reaction ampoules should always be placed in a protective sheath prior to insertion into the furnace. This prevents any reactants from leaking out and contaminating the furnace when a reaction ampoule loses structural integrity. Mullite tubes for this purpose can be ordered from CoorsTek (http://www.coorstek.com/). Additionally, fire brick can be cut and drilled by the glass shop.

When inserting or removing samples from the furnace, it is essential that care be taken to avoid contact with the exposed heating element. Over time, the ceramic that is used to embed the heating element coils can wear away leaving the heating element coil exposed, and contact with this exposed wire could result in a shock or burn. Whenever the furnace is above room temperature, the ends of the furnace should be plugged up with an appropriate insulation material such as quartz wool to prevent excessive heat from escaping.

The C and CH furnaces have heating elements that are rated to 1200 °C, although operation at this temperature significantly decreases the lifetime of the heating element. Temperatures in excess of 1000 °C should only be used minimally if heating element life is to be maximized. The H furnaces have homemade heating elements and there is therefore no rating of a maximum temperature. However, temperatures exceeding 800 °C

have been avoided entirely and this temperature is a reasonable maximum for these furnaces.

Programming of the Omega CN4800 controllers can be completed as follows:

(1) Press and hold the leftmost key (select) to enter into programming mode.

(2) Press the down arrow key until "ProG" is displayed, and check that the value for this variable is set to "off". If it is not "off" press the rightmost key (return), then use the up or down arrows to change to "off" then press the return key again.

(3) Using the down arrow, the different programming points can be accessed. The definitions of these are as follows. "Sv 1" is the first temperature to reach in °C, "rn1r" is the amount of time to reach the temperature of "Sv 1" in hours, and "rn 1s" is the amount of time to stay at that temperature in hours. There are 4 different points that can be set, i.e. "Sv 2", "rn2r" and "rn2s" follow.

(4) To change the values, go to the program point to be modified and then press the return key. Each column of the display is changed separately. To input 550 °C into "Sv 2", press the return key twice to select the hundreds column, and then press the up arrow to change the hundreds place to a five. Press the return key again to select the tens column, and then change it to a 5. Then press the return key two more times to return out of editing mode.

(5) When the program has been successfully entered, press the up arrow several times until the display reads "ProG" and change "off" to "run".

APPENDIX B

OPERATION AND MAINTENANCE OF THE DOTY HIGH TEMPERATURE NMR PROBE.

The Doty high temperature NMR probe and temperature controller should be treated with utmost care because experience has shown that both are extremely fragile. Typically, the samples sealed in fused silica ampoules are inserted into a protective fused silica sheath that also functions to hold the sample at the center of the coil. The bell jar and probe casing than then be replaced. The probe should be inserted into the NMR magnet prior to making any connections.

Connections from the controller to the probe should be made as follows. The order that the connections is made is not important as long as all connections are made prior to probe heating.

(1) Ensure that the temperature controller is powered off, and connect the heater and sensor leads.

(2) Connect the "drive" gas output from the MAS controller to the "drive" port on the probe. The pressure of the gas should be manually set to about 40 psi. WARNING: failure to provide sufficient gas flow could result in permanent damage to the heating elements in the probe.

(3) The "upperstack gas" and frame cooling gas should be attached to the "electronic and bell dewar" and "body tube" ports on the probe and then a flow rate of 200 SFCH should be set manually. The hot gas outlet should also be equipped with the insulated outlet tube.

(4) The cooling stack for the Chemagnetics probes should be removed, and the bearing gas hose should be placed a few inches down into the bore of the magnet. A flow of gas will help to keep the bore cool.

(5) The proton and X-channel RF cables should be attached.

(6) After opening the controller software on the computer, the power switch on the controller can be safely switched on. The temperature of all three sensors should be near room temperature.

(7) The heating rate should be set to 10 °C / minute by selecting "setup → VT controller". Significantly faster heating rates should be used with extreme caution because heating quickly will require substantially more power to be passed through the heating elements, and their life spans will be shortened.

(8) The "heater on" button can then be pressed, and the target temperature set by clicking in the "setpoint" box and then typing the desired temperature. After pressing the return key, the temperature display should begin changing within several seconds.

Because of a fault, one of the safety interlocks for the probe has been intentionally defeated. There is a 4^{th} thermocouple that monitors the temperature of the gas that enters the probe. For reasons that are unclear, the temperature being read at this thermocouple was excessive even when the probe was at room temperature, and so this thermocouple has been shorted. An electrical short on pins 12 and 13 of the sensor cable provides a room temperature reading for this thermocouple, and allows for operation of the probe. It is likely that a break in the thermocouple is causing this problem, and if this thermocouple is ever replaced the short at pins 12 and 13 should be removed to restore this safety feature. The building N_2 is very unlikely to ever reach unacceptable temperatures, and so this safety feature is not essential.

APPENDIX C

OTHER SYNTHETIC ATTMPTS.

In addition to the new compounds reported herein, there were several other systems that were explored in attempts to produce new compounds, Table A-1. The results listed here were in most cases only attempted once, and the identification was only quickly screened by attempting to overlay known powder patterns with the experimental one. The purpose of these results is to provide a starting point for some related systems.

Table A-1. Other synthetic attempts with the reactants, maximum temperature, cooling time, lab notebook page number, and the major products as identified by X-ray diffraction. In cases where the powder diffraction peaks had no matches, the product is listed as "Unknown." When the powder pattern matched a known diffraction pattern but with slightly shifted peaks, the product is given in italics.

Reactants	Max Temp (°C)	Cool time (h)	Notebook Page	Products
Cu/Ga/P/Se	800	48	1MG85	$CuGaSe_2$, Unknown
Cu/Sb/P/Se	800	48	1MG85	Unknown
Ag/Ga/P/Se	800	48	1MG92	$AgGaSe_2$
Ag/Sb/P/Se	800	48	1MG92	*$Ag_2P_2Se_3$*
Zn/Hg/P/Se	700	91	1MG187	$Hg_2P_2Se_6$, ZnP
Cd/Hg/P/Se	700	91	1MG187	*$Cd_2P_2Se_6$*
Ni/Hg/P/Se	700	91	1MG187	$Hg_2P_2Se_6$
Pb/Hg/P/Se	700	91	1MG187	$Pb_2P_2Se_6$
Cu/Mg/Bi/P/Se	800	24	1MG202	*$CuBiP_2Se_6$*, Bi_2Se_3, $Mg_2P_2Se_6$
Cu/Ca/Bi/P/Se	800	24	1MG202	*$CuBiP_2Se_6$*, Bi_2Se_3, Ca
Ag/Mg/Bi/P/Se	800	24	1MG202	$AgBiP_2Se_6$, $Mg_2P_2Se_6$
Ag/Ca/Bi/P/Se	800	24	1MG202	$AgBiP_2Se_6$, Ca
Cu/Ce/P/Se	750	140	1MG209	$CeSe_2$, Cu_3PSe_4
Cu/Eu/P/Se	750	140	1MG209	Cu_3PSe_4, Unknown
Cu/Yb/P/Se	750	140	1MG209	Yb_2Se_3, Cu_3PSe_4, CuSe
Ag/Ce/P/Se	750	140	1MG209	$AgCeP_2Se_6$
Ag/Eu/P/Se	750	140	1MG209	$Ag_4P_2Se_6$, Unknown
Ag/Yb/P/Se	750	140	1MG209	Unknown
Ce/Cr/P/S	750	140	1MG213	$CePS_4$, $Cr_2P_2Se_6$
Ce/Mn/P/S	750	140	1MG213	$CePS_4$, $Mn_2P_2Se_6$
Ce/Fe/P/S	750	140	1MG213	$CePS_4$, $Fe_2P_2Se_8$
Ce/Co/P/S	750	140	1MG213	$CePS_4$, Unknown
Cu/Mg/P/Se	800	48	1MG220	Cu_3PSe_4, *$Mg_2P_2Se_6$*, Unknown
Cu/Sm/P/Se	750	140	1MG223	$SmSe_{1.8}$, Cu_3PSe_4
Cu/Fe/P/Se	800	48	1MG224	Cu3PSe4, $Fe_2P_2Se_6$, Se
Ba/Bi/P/S	950	48	1MG242	Unknown
Ba/Bi/P/S/BaBr2	950	48	1MG242	*$BaBr_2$*, *$BiPS_4$*, Unknown
BaS/Fe2P2S6	1050	12	1MG278	$Fe_2P_2S_6$, FeS, Unknown
BaS/Co2P2S6	1050	12	1MG278	Unknown

In several cases, there were no powder patterns that could be found to match the peaks in the experimental powder pattern, and in these cases, the products have been listed in table A-1 as "Unknown." In several cases, the peaks in the experimental powder pattern were closely related to a known compound, except there was some shift in the peaks. This may be evidence for a new compound with a structure that is closely related but with a different unit cell size. These products have been listed in the table as italics. There were also several cases where the resultant crystalline products matched with known crystalline products but that not all of the reactant elements could be accounted for. One possibility is that the sample chosen for the X-ray diffraction experiments was not representative of the bulk, and the other possibility is that the compound that was produced was isostructural to the known compound, but contained all of the reactant elements. In these cases The "Unknown" and italicized products are the ones that most likely contain as-yet unidentified crystalline products and merit further consideration. It is also worth considering the cases where some of the reactant elements could not be accounted for to look for isostructural compounds with different sets of elements.

APPENDIX D

FILE LOCATIONS OF SPECTRA

Figure 7-1. Ambient temperature ^{31}P magic angle spinning NMR spectra of the final products of: (A) a "$Cs_4P_2Se_{16}$" reaction stoichiometry indicating $Cs_4P_2Se_{10}$ as the dominant ^{31}P-containing species at -52.8 ppm; (B) a "$Cs_4P_2Se_8$" reaction stoichiometry indicating $Cs_4P_2Se_9$ as the dominant ^{31}P-containing species at -39.9 ppm; and (C) a "$Cs_4P_2Se_{12}$" reaction stoichiometry that produced $Cs_4P_2Se_9$ and $Cs_4P_2Se_{10}$ in a ~3:5 ratio. Panel D displays the static ^{31}P NMR spectrum of a 350 °C melt of the products in C. The peak with a chemical shift of -22.0 ppm in panels B and C was not assigned and the peak at -99.8 ppm in panel B was not assigned. For spectra A-C, the spinning frequency was 14 kHz and spinning sidebands are grouped with the corresponding isotropic peak using like symbols with * ≡ $Cs_4P_2Se_{10}$, + ≡ $Cs_4P_2Se_9$, and o ≡ unassigned peak with -22.0 ppm isotropic shift 173

(A) /home/gavematt4c/data/Cs4P2Sex_Fast/spec_121306
(B) /home/gavematt4c/data/Cs4P2Se9/spec_121206
(C) /home/gavematt4c/data/Cs4P2Sex/Cs4P2Se12/spec4x_022507
(D) /home/gavematt4c/data/HT/Cs4P2Sex/Cs4P2Se12/spec4k_350C/022807

Figure 7-4. The room temperature ^{31}P NMR spectrum of a mixture with "$Cs_4P_2Se_{16}$" stoichiometry that was cooled over 24 h to produce crystalline $Cs_4P_2Se_{10}$ and $Cs_4P_2Se_9$. The MAS frequency was 7 kHz. The intensities of peaks corresponding to $Cs_4P_2Se_{10}$ were used for the determination of CSA principal values of this compound 185

/home/gavematt4c/Cs4P2Sex/6_6_24/csa4x_011907

Figure 8-1. NMR spectra of a melt mixture with the nominal ratio "PS_5" showing the increase in chemical shift and peak width as a function of temperature. Spectra at 450, 500, 550, and 600 °C were acquired with acquisition delays of 2 s and represent the sums of 16 scans 200

/home/gavematt4c/data/HT/PS5/t1inv_500C_052607
/home/gavematt4c/data/HT/PS5/t1inv_550C_052607
/home/gavematt4c/data/HT/PS5/t1inv_600C_052607

Figure 8-3. High temperature ^{31}P NMR spectra of (A) $K_2Cu_2P_4Se_{10}$ at 550 °C and (B) a sample with the nominal composition "$KPSe_7$" at 350 °C. The spectra were acquired with acquisition delays of 10 ms and 200 ms, respectively and represent the sums of 50 scans 203

(A) /home/gavematt4b/data/HT/K2Cu2P4Se10/T1inv_550_110406
(B) /home/gavematt4c/data/HT/118/T1buildup_350_092506

Figure 8-4. EPR spectra at room temperature of rapidly quenched "PS_5" samples. Prior to quenching, the sample temperature in the furnace was (A) 1000 °C or (B) 550 °C. Acquisition parameters were: (A) 10 G modulation amplitude, 2000 G sweep width and (B) 0.1 G modulation amplitude, 50 G sweep width 208

(A) jlm-e680/home/mattg/071907_PS51000_3.spc
(B) jlm-e680/home/mattg/071907_PS5550_4.spc

Figure 8-5. Room temperature EPR of (A) "SnS_5" quenched from 550 °C (B) "PSe_5" quenched from 550 °C and (C) $K_{1.5}Bi_{2.5}(PS_4)_3$ quenched from 1000 °C. Acquisition paramaters were: (A) 1 G modulation amplitude, 40 G sweep width; (B) 1 G modulation amplitude, 500 G sweep width; and (C) 10 G modulation amplitude, 3000 G sweep width. Each spectrum was a single acquisition.....208

(A) /jlm-e680/home/mattg/061807_SnS5_9451.spc
(B) /jlm-e680/home/mattg/061807_PSe5_94485.spc
(C) /jlm-e680/home/mattg/quK15Bi25_295mg.spc

Table 9-2. The ^{31}P chemical shifts, longitudinal relaxation times (T_1), and line widths of various chalcophosphate-containing materials as well as the final product determined from powder X-ray diffraction.....227

Stoichiometry	Temp. (°C)	File Location
"$KPSe_7$"	350	gavematt4c/data/HT/118/T1inv_350_092506
	450	gavematt4c/data/HT/118/T1inv_450_092506
	550	gavematt4c/data/HT/118/T1inv_550_092506
"$K_2PSe_{7.5}$"	350	gavematt4c/data/HT/218/T1inv_350_092706
	450	gavematt4c/data/HT/218/T1inv_450_092706
	550	gavematt4c/data/HT/218/T1inv_550_092706
"$KP_{1.3}Se_{5.2}$"	350	gavematt4b/data/HT/348/T1inv_350_110106
	450	gavematt4b/data/HT/348/T1inv_450_110106
	550	gavematt4b/data/HT/348/T1inv_550_110106
"$KP_{1.5}Se_{6.3}$"	350	gavematt4b/data/HT/238/T1inv_350_110306
	450	gavematt4b/data/HT/238/T1inv_450_110306
	550	gavematt4b/data/HT/238/T1inv_550_110306
"$Cs_4P_2Se_{16}$"	350	gavematt4c/data/HT/2synth_Cs4P2Sex/spec3k_cool350C_121606
	450	gavematt4c/data/HT/2synth_Cs4P2Sex/spec3k_cool450C_121606
	550	gavematt4c/data/HT/2synth_Cs4P2Sex/spec3k_cool550C_121606
"PS_5"	350	gavematt4c/data/HT/PS5/T1inv_350_052607
	450	gavematt4c/data/HT/PS5/T1inv_450_052607
	550	gavematt4c/data/HT/PS5/T1inv_550_052607
$K_{1.5}Bi_{2.5}(PS_4)_3$	550	gavematt4c/data/HT/K15Bi25/T1inv_550_092606
	575	gavematt4c/data/HT/K15Bi25/T1inv_575_092606
	600	gavematt4c/data/HT/K15Bi25/T1inv_600_092606
$K_2Cu_2P_4Se_{10}$	500	gavematt4b/data/HT/K2Cu2P4Se10/T1inv_500_110406
	550	gavematt4b/data/HT/K2Cu2P4Se10/T1inv_550_110406
	600	gavematt4b/data/HT/K2Cu2P4Se10/T1inv_600_110406
$TlBiP_2Se_6$	525	gavematt4c/data/HT/TlBiP2Se6/T1inv_525_092606
	550	gavematt4c/data/HT/TlBiP2Se6/T1inv_550_092606
	600	gavematt4c/data/HT/TlBiP2Se6/T1inv_600_092606
KH_2PO_4	350	gavematt4c/data/HT/KH2PO4/T1buildup_350_092806
KH_2PO_4/S	350	gavematt4c/data/HT/KH2PO4_S/T1inv_350_093006

Figure 10-5. The ^{31}P NMR spectrum of the $Cu_3PSe_{4-x}S_x$ compounds. The spectra were sums of 4 individual scans with a pulse delay pulse delay of 1000 s and the spinning frequency was 12 kHz, and spinning sidebands were not observed.....260

/home/gavematt4c/data/Carly/Cu3PSe4/spec4x_030907
/home/gavematt4c/data/Carly/Cu3PSe3S/spec4x_030807
/home/gavematt4c/data/Carly/Cu3PS2Se2/spec4x_030807
/home/gavematt4c/data/Carly/Cu3PSeS3/spec4x_030807
/home/gavematt4c/data/Carly/Cu3PS4/spec4x_030807

Figure 11-1. High temperature ^{31}P NMR spectrum of $Hg_2P_2Se_6$ at 525 °C. The melting point of the crystalline compound is 510 °C. The spectral features are presently unassigned and this is the first known example where speciation was observed in a molten sample. 269

/home/gavematt4c/data/HT/Hg2P2Se6/spec16x_525C_052507